COMPLEX ADSORPTION MODELING FOR NUCLEAR ENERGY APPLICATIONS

A Thesis
Presented to
The Academic Faculty

by

Austin Pittman Ladshaw

In Partial Fulfillment
of the Requirements for the Degree
Doctor of Philosophy in the
School of Civil and Environmental Engineering

Georgia Institute of Technology
May 2017

COMPLEX ADSORPTION MODELING FOR NUCLEAR ENERGY APPLICATIONS

Approved by:

Dr. Sotira Yiacoumi, Advisor
School of Civil and Environmental Eng.
Georgia Institute of Technology

Dr. Spyros Pavlostathis
School of Civil and Environmental Eng.
Georgia Institute of Technology

Dr. Costas Tsouris
School of Civil and Environmental Eng.
Georgia Institute of Technology
Energy and Transportation Science Division
Oak Ridge National Laboratory

Dr. David Sherrill
School of Chemistry and Biochem.
Georgia Institute of Technology

Dr. James Mulholland
School of Civil and Environmental Eng.
Georgia Institute of Technology

Date Approved: April 3rd, 2017

This work is dedicated to my grandfathers, Robert E. Pittman and Thomas G. Ladshaw.

ACKNOWLEDGEMENTS

There have been many individuals who have helped me during this undertaking, both in research and in life. First of all, I must thank my advisor, Professor Sotira Yiacoumi, and our research collaborator, Dr. Costas Tsouris, for their wealth of support and advice that got me to this point. Even in times of great stress, Dr. Yiacoumi always provided me with the most effective guidance.

I must also give thanks to the organizations that have helped fund my PhD program throughout the years: Georgia Engineering Foundation, Nuclear Energy University Program, Idaho National Laboratory, Georgia Power, and Georgia Institute of Technology. In addition, I would also like to thank each of my other PhD committee members for providing useful and insightful comments during the development of this work: Dr. Jim Mulholland, Dr. Spyros Pavlostathis, and Dr. David Sherrill.

A great deal of this work was built upon collaborative efforts between myself and many other students, post-docs, and researchers from around the country. I would like to extend my thanks to each of those individuals who personally helped make this work possible: (i) David DePaoli, Bob Jubin, Vyacheslav Bryantsev, Aleksandr Ivanov, and Sadananda Das from Oak Ridge National Laboratory, (ii) Lawrence Tavlarides, Yue Nan, and Ronghong Lin from Syracuse University, (iii) Jack Law, Amy Welty, Kevin Lyon, and Veronica Rutledge from Idaho National Laboratory, and (iv) Li-Jung Kuo and Gary Gill from Pacific Northwest National Laboratory.

Lastly, I must thank my friends and family: Tom Ladshaw, Vicki Ladshaw, Allison Freeman, Brycen Freeman, Jackie Ladshaw, Josephine Pittman, Christopher Bayruns, and many others. Without their encouragement and guidance I may have lost my sanity a long, long time ago. The accomplishment I have made here is all because of their continued, unwavering support in the face of both the best of times and the worst of times. Thank you.

TABLE OF CONTENTS

LIST OF TABLES

LIST OF FIGURES

LIST OF COMMON SYMBOLS

A	specific surface area of an adsorbent
He	Henry's law constant
MW	molecular weight
P^o	standard state pressure, 100 kPa
q	adsorbed surface concentration
q_{max}	maximum capacity of adsorption
Q^{st}	isosteric heat of adsorption
Re	Reynolds number
Sc	Schmidt number
T	temperature
ΔG	change in free energy
ΔH	change in enthalpy
ΔS	change in entropy
γ	activity coefficient
ρ	density of a medium
AST	Adsorbed Solution Theory
GPAST	Generalized Predictive Adsorbed Solution Theory
GSTA	Generalized Statistical Thermodynamic Adsorption
IAST	Ideal Adsorbed Solution Theory
INL	Idaho National Laboratory
MAGPIE	Multicomponent Adsorption Generalized Procedure for Isothermal Equilibria
MSL	Marine Science Laboratory

MSPD	Modified Spreading Pressure Dependent
ORNL	Oak Ridge National Laboratory
PNNL	Pacific Northwest National Laboratory
PRAST	Predictive Real Adsorbed Solution Theory
SPD	Spreading Pressure Dependent
UNIQUAC	Universal Quasi-Chemical

SUMMARY

Adsorption is a complex physical-chemical phenomenon by which molecules are attached to surfaces of solid particles. The type of adsorption that occurs may often depend on the media the phenomenon is occurring in, making the design of models for various adsorption systems an arduous task. Regardless of the media, however, the basic mechanisms of the adsorption process are the same. Therefore, a plausible approach to the development of adsorption models in different systems would be to design a generalized mathematical framework with all the necessary methods built in that will be used as a platform to develop system specific adsorption models. In this work, the investigation and development of such a structure will be discussed and a host of system specific adsorption models that have been developed on top of that framework will be detailed. The applications of interest are all related to nuclear energy and specifically the availability of uranium in the Nuclear Fuel Cycle. To this end, the work here is divided into two parts: (i) modeling the treatment of off-gases produced from recycling uranium and (ii) modeling the recovery of raw uranium material from seawater.

In the entirety of the first part of this work, each subsequent model will be built upon the successes of the previous models, and maintaining with the theme of framework design and generality, each set of models will be incorporated into more complex adsorption tools. The initial investigation begins with research into a Generalized Statistical Thermodynamic Adsorption (GSTA) isotherm model for analysis of gas-solid adsorption data. For this model, we develop a comprehensive optimization routine to analyze large sets of adsorption data and provide isotherm parameters needed for macro-

scale adsorption modeling. Due to the flexibility and generality of this approach, we are able to demonstrate its applicability to a wide variety of adsorbate-adsorbent systems.

Building upon the prior work, we seek to utilize the GSTA isotherm in theories for mixed-gas adsorption, such as the Ideal Adsorbed Solution Theory (IAST). However, IAST forces one to assume an ideal surface, which may be unrealistic. To accommodate non-ideality, we develop a new approach to predicting mixed-gas adsorption equilibria based on combing the Adsorbed Solution Theory (AST) system of equations with the Henry's law behavior of pure gas species to estimate the non-ideal surface characteristics of the system. The new Generalized Predictive Adsorbed Solution Theory (GPAST), coupled with the GSTA isotherm, showed noticeable improvement in predictive capabilities over the IAST model.

After demonstrating that the models for gas-solid adsorption equilibria can predict both ideal and non-ideal systems, we move on to diffusion kinetics. In real world applications, the operation time of an engineered capture system will depend on the kinetics of adsorption. As such, it is paramount that we are able to predict not just how much material is adsorbed, but how fast that adsorption occurs. To achieve this goal, we develop a mass transfer and conservation law framework off of which we can create specific models for adsorption. The development of this modeling framework is validated for adsorption diffusion kinetics in various adsorbent particles through comparisons with adsorption data. In addition, we demonstrate how this framework could be utilized in transport modeling as well, which has implications for adsorption column design for off-gas treatment systems in the Nuclear Fuel Cycle.

For the second part of this work, we transition into adsorption modeling in aqueous systems. Here, the problems that we seek to solve are very different from those of the first part of this work. However, we are able to connect much of the mathematics to our prior work in gaseous systems and recycle existing framework code for development of models for uranium recovery from seawater.

To start, we discuss the development of a preliminary uranium adsorption model based on speciation and complexation of uranyl ions with amidoxime ligands in solution. Utilizing this approach, we are able to demonstrate how such a model could account for changing solution conditions such as ionic strength and bicarbonate presence. This relatively simple model, however, is not intended for real world applications. Instead, this model acts more as a framework giving us a stepping stone for further development of the more realistic adsorption model.

Building upon the metal-complexation modeling framework, we seek to develop a closed-loop computation design process for adsorbent materials. In collaboration with molecular modelers at Oak Ridge National Laboratory (ORNL), *ab initio* methods are used to predict binding strengths between uranium and vanadium with different amidoxime ligands. Then, from those quantum studies, we create a multi-ligand adsorption model for uranium and vanadium uptake by amidoximated fibers. Based on this combined approach, we are able to successfully predict the adsorption behavior of the ORNL adsorbent material for uranium uptake across a wide range of pH. In addition, we also use this same methodology, with minor modifications, to predict the competition between vanadium and uranium for the adsorption sites of the material.

Lastly, we begin to explore some more application driven adsorption models for predicting uranium uptake rates in real seawater and how ocean currents impact those rates. While the model we develop in this chapter is not particularly fundamental, it is very practical as an analytical tool and is used to estimate optimal ocean current conditions for deployment. Utilizing this model, we are able to determine that linear current velocities beyond 8 cm/s would eliminate a majority of the mass transfer limitations created by the braiding of the fibers. Using this information as a design parameter, engineers can plot out oceanic locations based on current velocity to optimize the mass transfer kinetics of the deployed adsorbent material.

The culmination of the adsorption models developed in this research will provide tools for scientists and engineers to better understand adsorption phenomena in the applications of interest and subsequently design the necessary capture systems at both the front and back ends of the Nuclear Fuel Cycle.

CHAPTER 1. INTRODUCTION

1.1 Background

Adsorption is the physicochemical phenomenon by which molecules, often referred to as adsorbates, are attached to the surface of a particle, referred to as an adsorbent.[1,2] The adsorption process can be sub-categorized into physi-sorption and/or chemi-sorption.[2,3] For physi-sorption, molecules are attached to the surface via intermolecular forces, such as van der Waals forces. In general, the interaction energy of this process is similar to the energy of condensation of the adsorbate, and attached molecules will be chemically identical to adsorbates in the fluid phase. As such, there is little change in the electronic states of the adsorbed species.[4]

Conversely, chemi-sorption involves the chemical binding of adsorbates to the adsorbent surface. In this case, the adsorbates actually undergo a site-specific, valence bonding interaction with the surface to produce an adsorbed species that is chemically distinct from the adsorbate in the bulk phase.[4,5] As a result, at maximum capacity, chemi-sorption will generally only involve the formation of a mono-layer of adsorbates, i.e., additional molecules will not bind to form a secondary layer of adsorption. In addition, the activation energy for chemi-sorption is typically larger than that of physi-sorption, which may result in irreversibility of the adsorption process.[4] Figure 1.1 provides a visualization of the difference between physi- and chemi-sorption.

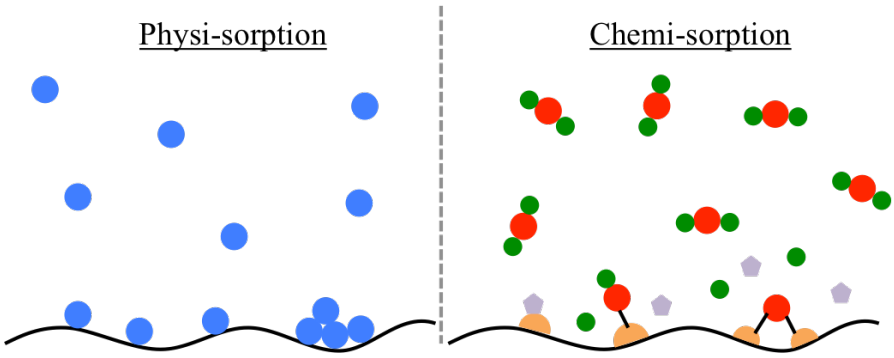

Figure 1.1 - Schematic showing the differences between physi- (left) and chemi-sorption (right). In physi-sorption, adsorbed molecules maintain the same chemical form as the species in the bulk solution and may even form multiple layers of adsorption if the concentration is high enough. For chemi-sorption, molecules undergo binding interactions at specific surface sites and are chemically different from the adsorbates in the fluid phase.

Although adsorption is a somewhat narrow field of study, it is a process that has broad implications in a wide variety of applications. As a separation process, adsorption is especially equipped to purify a bulk fluid phase by capturing and removing dilute contaminants from solution. Some of the applications of adsorption include: (i) removal of water vapor from ethanol via molecular sieving,[6] (ii) oxygen generation and purification from standard air,[1] and (iii) metal ion capture from tap water using commercial activated carbon filters.[7] In this work, we seek to investigate and develop modeling tools for the application of adsorption technologies in the Nuclear Fuel Cycle.

1.2 Motivation

Nuclear energy will remain a sustainable energy source if an economically viable supply of nuclear fuel remains available. The currently estimated availability of uranium from land mining is approximately 48.5 million tons, including known and yet to be

discovered resources.[8,9] Although this amount can support the current worldwide nuclear energy production for nearly 100 years, additional uranium sources could allow expansion of nuclear energy to reduce greenhouse gas emissions and counteract global warming.[10]

In addition, nuclear power is undergoing a revival of late and as a result, nuclear energy demand is expected to increase by up to 60% over the next 15 years.[11] Coupled with this increase will be a rise in demand for uranium, the fuel source of nuclear energy. The traditional methods of mining uranium ore such as open pit, underground, and *in situ* leach mining, however, cause severe environmental pollution.[12] Therefore, although the power generation portion of the nuclear fuel cycle is relatively benign to the environment, the increase in mining activities to acquire the needed fuel could potentially lead to adverse impacts on the environment.

Facilitating the expansion of nuclear energy, without causing environmental harm, will require technological innovations in the life cycle of our current fuel resources or an alternative to conventional uranium mining. To this end, we must examine the Nuclear Fuel Cycle[13] (Figure 1.2) in order to discover where scientific advances in separation processes may be applied to meet our goals. In this diagram, there are two nodes that have greatest impact on the availability of nuclear fuel: (1) the reprocessing or recycling facilities for spent fuel rods and (2) the cultivation and extraction of raw uranium material. Engineering enhancements in these two areas would extend the life of our current uranium reserves by providing new uranium to the cycle and by reusing the leftover uranium produced after power generation.

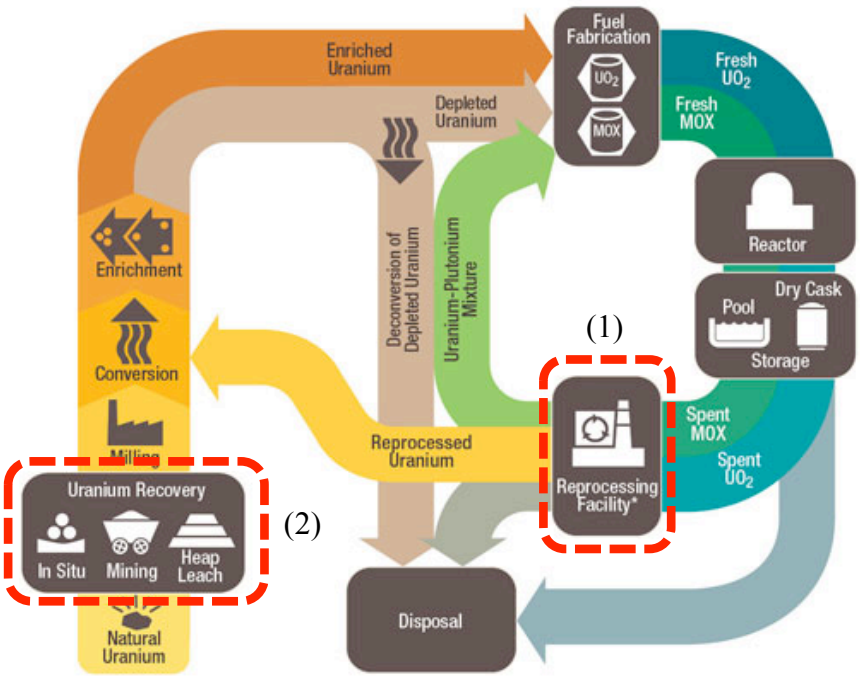

Figure 1.2 - Diagram of the Nuclear Fuel Cycle.[13] Node (1) represents reprocessing facilities for recycling spent fuel, and node (2) represents the addition of new uranium to the cycle through mining or other means.

First, consider the back end of the Nuclear Fuel Cycle (Figure 1.2: Node (1)). Spent uranium fuel rods from power generation still contain roughly 96% uranium, while the remaining 5% are unwanted fission products. Currently, this material is considered as waste and is typically being stored on-site in large concrete containers. If those fuel rods were to be reprocessed and recycled, however, they could reduce nuclear waste volume by around 70%, while also providing additional uranium resources to the fuel cycle.[14]

While the technology necessary to recycle the spent uranium already exists, that reprocessing procedure produces many different volatile radioisotopic gases as by-products: $^{129}I_2$, ^{3}HHO, ^{85}Kr, ^{135}Xe, and $^{14}CO_2$. These off-gases can be harmful to the environment and human health, which has prompted the U.S. Environmental Protection

Agency (EPA) to adopt exposure and release limits through 40 CFR 190.[15] This creates the need for engineered adsorption systems that can capture and remove those gas species from the off-gas stream of reprocessing facilities.

At the front end of the Nuclear Fuel Cycle (Figure 1.2: Node (2)) is where new raw uranium material is cultivated, typically through mining activities. If spent nuclear fuel is not recycled, it may become necessary to extract raw uranium in order to add additional fuel to the cycle. Since these actions can cause severe environmental damage,[12] however, it would be advantageous to explore the possibility of exploiting an unconventional source of uranium, such as seawater.

There is an estimated 4.5 billion tons of uranium dissolved in the world's oceans, which is nearly 1,000 times more than in all terrestrial reserves.[16] Tapping into this unused source of fuel could serve our nuclear energy needs while also preserving the environment for future generations. The concentration of uranium is seawater is very low (~3.3 ppb), however, and there is a lot of variability in ocean conditions (temperature, currents, salinity, etc.), which makes extraction of the uranium fairly complex.[17] Therefore, there is a need to develop and design adsorbent materials that can selectively capture uranium from seawater in an economically viable manner.

1.3 Scope and Objectives

The scope of the work presented here is to research and develop adsorption-models in order to better understand adsorption phenomena and to provide tools to be used in the design of the necessary capture systems applied in the Nuclear Fuel Cycle. Since the subjects that are to be investigated are separated by their medium (i.e., gaseous

and aqueous systems), the work has been divided into two parts. In Part I, adsorption in gaseous systems is covered and details research into the creation of off-gas treatment models. In Part II, adsorption in aqueous systems is discussed for the development of uranium from seawater capture models.

In CHAPTER 2, we introduce the concept of adsorption isotherms for modeling the gas-solid equilibrium partition of a particular adsorbate-adsorbent pair. Gas phase adsorption modeling inevitably requires the use of such models as a component of more practical modeling applications, such as multi-species separations and diffusion kinetics. In this chapter, we will discuss a particular isotherm called the Generalized Statistical Thermodynamic Adsorption (GSTA) model and its relationship with more common isotherm models. In addition, we will present an optimization algorithm for the GSTA model that is capable of taking in large quantities of isotherm data for a particular system and finding the temperature independent parameters necessary to describe that system.

CHAPTER 3 is a direct continuation from the previous chapter, wherein we seek to integrate the GSTA model into a multi-species model framework. In real adsorption applications, any system that we must model is inherently multi-species because adsorption is a separation process (i.e., we are separating some species from a set of other species). Therefore, it is paramount to develop models that can predict adsorption behavior of mixed-gas systems. In this chapter, we introduce the development of a Generalized Predictive Adsorbed Solution Theory (GPAST) as an extension of prior research in the field of mixed-gas adsorption, and then apply this theory to demonstrate its predictive capabilities for various gas mixtures.

To finish off Part I, CHAPTER 4 discusses the development of a modeling framework based on conservation laws. Regardless of the system of interest, adsorption models will always be based on some form of mass and/or energy balance on some domain. Therefore, by approaching the modeling of space-time dependent problems from a generic conservation law approach, we can develop a modeling framework off of which many different system specific models can be formulated. In this chapter, we derive the numerical methods and discretization techniques necessary for such a framework, and then demonstrate its applicability to diffusion kinetic and mass transport problems in gas phase adsorption.

While Part I of this work is very fundamental and generalized in its methodology, Part II is more application driven, with the focus on uranium from seawater. In CHAPTER 5, we examine the impact of aqueous speciation and ionic strength on the complexation between uranyl ions (UO_2^{2+}) and amidoxime ligands. Experiments were performed at Oak Ridge National Laboratory (ORNL) to measure how the addition of bicarbonate ($NaHCO_3$) and sodium chloride (NaCl) affects the adsorption capacity and rates of uranium uptake from batch solutions. Coupled with these experiments was the development of a preliminary chemi-sorption model that would implicitly include the influence of variations in ionic strength, pH, temperature, and speciation in the aqueous phase.

CHAPTER 6 provides an extension to the preliminary model developed in the preceding chapter, which had previously only considered adsorption as a generic metal-ligand complexation reaction. In this chapter, we detail the development of a site-specific, adsorption model that is capable of including the effects of surface charge

accumulation and non-ideal surface interactions among a variety of different adsorbing species. In addition, this new model is capable of considering an adsorbent surface that is composed of any number of different active ligands. Coupled with this adsorption model is an *ab initio* methodology to estimate the binding strengths of various reactions between uranium and vanadium with amidoxime ligands. To validate this model and approach, adsorption data for uranium and vanadium solutions were gathered at ORNL across a wide range of pH. Additionally, competitive adsorption experiments were also conducted to quantify the effect that competing metal ions, such as vanadium, will have on the uranium capacity of the adsorbents.

The last chapter of Part II (CHAPTER 7) branches away from the more fundamental aspects of aqueous adsorption and delves into the real application of the technology. This chapter discusses actual seawater experiments performed at Pacific Northwest National Laboratory (PNNL) to measure the impact of current velocity on braided adsorbent fibers. Mechanical mixing caused by the flow of water over the braids will effect the rate of mass transfer of material into the adsorption domain, which is critically important as this will impact how fast the adsorbent can take up uranium from seawater in real deployment scenarios. To supplement the experimental work from PNNL, a simple adsorption model was developed to couple reaction rates and mass transfer limitations to the adsorption rate of uranium from seawater. This model was then utilized to quantify how current velocity affects the rate of mass transfer for braided fibers.

Lastly, in Part III (CHAPTER 8) we offer up our closing remarks for all of the models developed in this work and discuss how these models can be applied in the

Nuclear Fuel Cycle or other adsorption systems. Finally, we will review the shortcomings and/or limitations of the models introduced and examine how they can be further improved and developed. In addition, the software tools that have been created throughout the entirety of this work will be presented in the Appendices of this thesis, and the mechanisms to acquiring and using those tools shall be described.

1.4 References

[1] C. Tien, *Adsorption Calculations and Modeling*, Butterworth-Heinemann, Newton, MA, 1994.

[2] J. Tóth (Ed.), *Adsorption Theory Modeling and Analysis*, Marcel Dekker, Inc. New York, NY, 2002.

[3] M.M. Benjamin, *Water Chemistry*, Waveland Press, Inc., Illinois, 2010.

[4] D.H. Everett, L.K. Koopal (Ed.), *Manual on Definitions, Terminology and Symbols in Colloid and Surface Chemistry*, IUPAC Council, Washington, DC, 2001, http://old.iupac.org/reports/2001/colloid_2001/manual_of_s_and_t/. (Accessed on March 8th, 2017).

[5] S. Yiacoumi, C. Tien, *Kinetics of Metal Ion Adsorption from Aqueous Solutions*, Kluwer Academic Publishers, Boston, MA, 1995.

[6] M. Llano-Restrepo, M.A. Mosquera, *Fluid Phase Equilibria*, 283 (**2009**) 73-88.

[7] M. Ahmedna, W.E. Marshall, A.A. Husseiny, R.M. Rao, I. Goktepe, *Water Research*, 38 (**2004**) 1062-1068.

[8] E.A. Schneider, B. Carlsen, E. Tavrides, C. van der Hoeven, U.B. Phathanapirom, *Energy Economics*, 40 (**2013**) 911-926.

[9] *Uranium 2014: Resources, Production and Demand*, Technical Report NEA 7209, OECD Nuclear Energy Agency: Paris, FR, 2014.

[10] J. Kim, C. Tsouris, R.T. Mayes, Y. Oyola, T. Saito, C.J. Janke, S. Dai, E. Schneider, D. Sachde, *Sep. Sci. Technol*, 48 (**2013**) 367–387.

[11] International Atomic Energy Agency, *Energy, Electricity and Nuclear Power Estimates for the Period up to 2050*, IAEA-RDS-1/36, Vienna, 2016.

[12] U.S. Nuclear Regulatory Commission*, Final Generic Environmental Impact Statement on Uranium Milling*, USNRC-NUREG-0706, Washington, DC, 1980.

[13] U.S. Nuclear Regulatory Commission, *Stages of the Nuclear Fuel Cycle*, www.nrc.gov, (Accessed on October 26th, 2014).

[14] World Nuclear Association, *Processing of Used Nuclear Fuel*, www.world-nuclear.org, (Accessed on September 28th, 2014).

[15] R.T. Jubin, G.D. DelCul, B.D. Patton, R.S. Owens, D.W. Ramey, B.B. Spencer, *WM2009 Conference*, Phoenix, AZ, March 1-5, 2009.

[16] R. V. Davies, J. Kennedy, R. W. McIlroy, R. Spence, K. M. Hill, *Nature*, 203 (**1964**) 1110.

[17] T.-L. Ku, K.G. Knauss, G.G. Mathieu, *Deep Sea Research*, 24 (**1977**) 1005-1017.

PART I. ADSORPTION IN OFF-GAS TREATMENT

CHAPTER 2. SINGLE-SPECIES EQUILIBRIA MODELING

2.1 Introduction

Gas-solid adsorption equilibria can be classified under a number of different categories depending on the details of the physical phenomena, such as physical adsorption versus chemical adsorption, or the topography of the adsorbent material (i.e., whether heterogeneous or homogeneous). Each of these various categories may require a different isotherm model to be used to describe the equilibrium between adsorbed (q) and gas phases (p) of a particular adsorption system.[1] From a scientific stand point, this is not only logical, but also a reasonable level of complexity as no single model can ever describe all possible systems. As a result, the most frequent approach for describing adsorption is through the utilization of one of the many common isotherm equations such as the Freundlich, Langmuir, and Tóth models.[1,2] Unfortunately, from an engineering point-of-view, the added complexity of having to seek out applicable models to a system makes it very difficult to standardize adsorption for design purposes and practical applications.

2.1.1 Common Isotherm Models

2.1.1.1 Freundlich

The Freundlich isotherm model, shown on Table 2.1, is typically regarded as the simplest model that can be used to represent adsorption equilibrium.[1] This is due in part to the ease in linearizing this equation in order to make correlations between the model and data to obtain the optimum parameters for that data set. Additionally, the parameters of the model have a simple interpretation: K_F being relative of the capacity of adsorption and a being relative to the strength of adsorption. However, this model is empirically

derived[2] and would not represent any fundamental description of the adsorption phenomena.

2.1.1.2 Langmuir

While the Freundlich model is generally considered to be an empirical expression, the Langmuir model, also shown on Table 2.1, can be derived fundamentally by considering the following four assumptions: (i) there exist a fixed number of sites at which adsorption takes place, (ii) all sites are identical, (iii) each site only accommodates one adsorbate molecule, and (iv) adsorbate molecules do not interact with each other. This derivation of the Langmuir model leads to the following physical interpretation of the parameters: K_L is the equilibrium constant between the gas and adsorbed phases and q_{max} is the monolayer adsorption capacity of the adsorbent material. In addition, this equation can also be linearized, as shown on Table 2.1, in order to find the optimum parameter values for a given set of data. The simplicity of use combined with the clear physical significance of its parameters makes the Langmuir isotherm one of the most popular expressions of adsorption.[1]

2.1.1.3 Tóth

Unlike the Freundlich and Langmuir models, which contained two adjustable parameters, the Tóth isotherm, shown on Table 2.1, is a three-parameter model that was extended from the Langmuir equation to consider the heterogeneity of adsorbent surfaces.[2] It is based on the experimental observation that heterogeneous adsorbents, of the same specific surface area, tend to uptake more adsorbate than an equivalent homogeneous adsorbent at the same pressure.[3] Under the circumstance in which the

parameter b is equal to one, the relative energies of the different adsorption sites are the same and the Tóth isotherm becomes the Langmuir isotherm.

While the exact physical interpretation of b is unclear, it is believed to reflect the heterogeneity of the adsorbent, as well as the lateral interactions between adsorbed molecules.[2,3] The K_T parameter is a function of the monolayer saturation pressure while q_{max} has the same meaning as in the Langmuir equation. Because of the similarities between the Langmuir and Tóth equations, the Tóth model is often utilized to correlate adsorption equilibrium data when the Langmuir model itself does not yield satisfactory results.[1,4]

2.1.1.4 Heterogeneous Langmuir

Similar to the Tóth isotherm, another heterogeneous adsorption model can be formulated as an extension of the Langmuir equation. If it can be assumed that the adsorbent surface acts as a patchwork of numerous, discrete homogeneous adsorption sites, then the Langmuir equation could apply separately to each individual site.[1,5] As a consequence, this means that each n^{th} site is associated with its own equilibrium constant ($K_{L,n}$) and adsorption capacity (q_n). The resulting equation is referred to as the Heterogeneous Langmuir model, as shown on Table 2.1.

Although the Heterogeneous Langmuir model provides a simple and fundamental description of adsorption on heterogeneous surfaces, it is seldom used in practice due to the complexity involved in correlating this model with data and determining the number of discrete patches that make up the adsorbent material. As the number of patch sites (m) increases, the number of necessary parameters to determine doubles and it becomes

progressively more difficult to correlate the model with data. Furthermore, the Tóth isotherm model provides a simpler equation for describing the heterogeneity of surfaces by introducing only one additional parameter to the Langmuir model.

Table 2.1 - A Summary of Common Adsorption Models

Model	Equation	Linear Form	Parameters
Freundlich	$q = K_F p^{1/a}$	$\log(q) = \log(K_F) + \frac{1}{a}\log(p)$	K_F, a
Langmuir	$q = \frac{q_{\max} K_L p}{1 + K_L p}$	$\frac{1}{q} = \frac{1}{q_{\max} K_L}\frac{1}{p} + \frac{1}{q_{\max}}$	K_L, $q_{\max}$
Tóth	$q = \frac{q_{\max} K_T p}{(1 + (K_T p)^b)^{1/b}}$	None	K_T, $q_{\max}$, b
Heterogeneous Langmuir	$q = \sum_{n=1}^{m} \frac{q_n K_{L,n} p}{1 + K_{L,n} p}$	None	$K_{L,1}$, $K_{L,2}$, … $K_{L,m}$ q_1, q_2, … q_m

2.1.2 Thermodynamic Considerations

In addition to the dozens of isotherm models discussed in literature, there are also certain thermodynamic criteria, such as low- and high-pressure behavior, to be evaluated when considering the usage of a particular isotherm model. This behavior may dictate whether or not the model used in the correlation of the single-component data can be extended into theories for predicting multicomponent behavior.[1,2,6] Since any real adsorption application is likely to be with mixed gases, it is critical that single-component equilibria models meet the necessary set of criteria for extension into multicomponent models.

2.1.2.1 Low Pressure Limits

As the gas pressure in an adsorption system approaches zero, the relationship between the gas and solid phases should behave linearly. The low-pressure zone of adsorption is commonly referred to as the Henry Regime because the isotherm model becomes equivalent to Henry's Law (i.e., $q = K_H p$), where K_H is the Henry's Law constant.[1,6] This behavior is particularly important with regards to the evaluation of the spreading pressure (π) of the adsorbed phase, which must be evaluated between the limits of zero pressure and system pressure as follows:

$$\frac{\pi A}{RT} = \int_0^P \frac{q}{p} dp \qquad \textbf{Equation 2.1}$$

where A is the specific surface area of the adsorbent, R is the gas constant, T is the temperature of the system, and P is the total pressure of the system. If the adsorption isotherm does not have a finite limit at low pressure, then the spreading pressure of the system cannot be accurately determined, especially when considering low-pressure systems.[6]

2.1.2.2 High Pressure Limits

Many monolayer adsorption theories, such as Langmuir, express the adsorbed phase quantity in terms of a theoretical maximum adsorption capacity.[6] In other words, using these theories, the amount adsorbed approaches the finite monolayer limit only if the pressures of the system become infinitely large (i.e., $\lim_{p\to\infty} q = q_{\max}$). This type of behavior is considered to be thermodynamically inconsistent and contrary to the Gibbs'

thermodynamic expression of gas-solid adsorption.[2] Realistically, the monolayer capacity should be obtainable at a finite saturation pressure as in the Tóth model. However, in practice it has been shown that the Langmuir model, and other monolayer theories, may still be applicable in describing equilibrium systems at pressures as high as 65 atmospheres (~6.5 MPa).[7]

2.1.3 Overview

There are still dozens of more isotherm models available beyond what was discussed in Section 1.1, and each model has its own set of parameters that may all have different physical meanings and require a different correlation or regression method to provide the optimum values.[1,2] This makes adsorption modeling very impractical, as one would have to plan for nearly every possible scenario that could be encountered in natural and/or engineered systems. Furthermore, the extension of single-component models into multicomponent theories would be made extraordinarily difficult if different equilibrium models described each single-component isotherm, each with different parameters whose correlations with temperature are all different. Therefore, it is vital that adsorption modeling be generalized in a way that can accommodate the most variability reasonable within real and engineered systems.

In order to accomplish this objective, a generalized isotherm model must be adopted that can account for physical or chemical adsorption on either heterogeneous or homogeneous adsorbents. One particular model of interest is the Generalized Statistical Thermodynamic Adsorption (GSTA) isotherm model proposed by Llano-Restrepo and Mosquera.[8] In Section 2.2, the GSTA model derivation and significance will be briefly

discussed. Furthermore, from its physical interpretation, we will provide an alternate derivation of the GSTA model based on the Heterogeneous Langmuir model. Since the GSTA model allows for a variable number of adjustable parameters, it could be utilized to correlate with a variety of different data sets. However, this flexibility makes it difficult to determine the number of parameters that would be most suitable in describing the data. In Section 2.3, the advantages and complications with using the GSTA model will be discussed, as well as the methodologies adopted to deal with these complications and make the GSTA model more readily usable by engineers and scientists. Lastly, Section 2.4 will show results from the GSTA model for an assortment of different gas-solid adsorption systems as a demonstration of the model versatility and generality.

2.2 Generalized Statistical Thermodynamic Adsorption Model

The GSTA model presented by Llano-Restrepo and Mosquera[8] was originally presented as an alternate form of Hill's statistical model. Their aim was to provide a physical significance and reinterpretation of the parameters of Hill's model in such a way that they could be correlated with temperature to obtain site-specific enthalpies and entropies. The GSTA model and its parameters are summarized below:

$$q = \frac{q_{\max}}{m} \frac{\sum_{n=1}^{m} nK_n p^n}{1 + \sum_{n=1}^{m} K_n p^n} \qquad \textbf{Equation 2.2}$$

$$K_n = K_n^o / (P^o)^n \qquad \textbf{Equation 2.3}$$

$$\ln K_n^o = -\frac{\Delta H_n^o}{RT} + \frac{\Delta S_n^o}{R} \qquad \textbf{Equation 2.4}$$

where m is the number of different types of adsorption sites available to adsorbate molecules, K_n is the equilibrium constant relative to the adsorption of n molecules in a network of available adsorption sites, K_n^o is the dimensionless equilibrium constant, P^o is standard state pressure (100 kPa), ΔH_n^o is the standard enthalpy of adsorption of n molecules in a network of sites, and ΔS_n^o is the standard entropy of adsorption of n molecules in a network of sites. The model contains 2 + m parameters (q_{max}, m, and K_n) that must be determined through correlations with equilibrium data, but if some information is known about the adsorbent, such as theoretical capacity and heterogeneity, then one could independently provide the q_{max} and m parameters.[8]

2.2.1 Relation with the Heterogeneous Langmuir Model

From the physical interpretation of the GSTA model provided by Llano-Restrepo and Mosquera,[8] it can be inferred that this model is analogous to a heterogeneous site model in which each adsorption site is energetically distinct, but has the same capacity. To explore this idea further, consider a simple two-site Heterogeneous Langmuir model shown below in Equation 2.5. If it is assumed that each adsorption site has the same capacity, as in the GSTA model, then it can be concluded that $q_1 = q_2 = q_s$ and therefore $q_{max} = q_1 + q_2$ or $q_{max} = 2q_s$.

$$q = \frac{q_1 K_{L,1} p}{1 + K_{L,1} p} + \frac{q_2 K_{L,2} p}{1 + K_{L,2} p} \qquad \textbf{Equation 2.5}$$

Expanding out Equation 2.5, while utilizing the assumption of site capacity equivalence, results in the following:

$$q = q_s \frac{K_{L,1}p + K_{L,2}p + 2K_{L,1}K_{L,2}p^2}{1 + K_{L,1}p + K_{L,2}p + K_{L,1}K_{L,2}p^2} \qquad \textbf{Equation 2.6}$$

By further reducing and grouping like terms from Equation 2.6, the model can be rewritten as:

$$q = q_s \frac{(K_{L,1} + K_{L,2})p + 2(K_{L,1}K_{L,2})p^2}{1 + (K_{L,1} + K_{L,2})p + (K_{L,1}K_{L,2})p^2} \qquad \textbf{Equation 2.7}$$

From Equation 2.7, the grouped terms can be renamed to formulate the equivalent terms from the GSTA model as the following: $K_1 = (K_{L,1} + K_{L,2})$ and $K_2 = (K_{L,1}K_{L,2})$. Lastly, by replacing the q_s term with its $q_{\max}$ equivalent, Equation 2.7 becomes Equation 2.8 below, which is exactly equal to the GSTA model when $m = 2$ (i.e., two-site adsorption).

$$q = \frac{q_{\max}}{2} \frac{K_1 p + 2K_2 p^2}{1 + K_1 p + K_2 p^2} \qquad \textbf{Equation 2.8}$$

This same derivation can be applied to any number of sites in the Heterogeneous Langmuir model and the results would be the same. Each K_n term in the GSTA model results in a combinatorial factor of the $K_{L,n}$ parameters in the Heterogeneous Langmuir. For example, the K_n parameters for the GSTA model for three adsorption sites would be as follows:

$$K_1 = \sum_n K_{L,n}$$
$$K_2 = \frac{1}{2}\sum_{n \neq k} K_{L,n} K_{L,k} \qquad \textbf{Equation 2.9}$$
$$K_3 = \prod_n K_{L,n}$$

Therefore, the GSTA model is basically a special case of the Heterogeneous Langmuir isotherm in which each adsorption site has the same capacity for adsorption, but different energy characteristics.

2.2.2 Physical Significance

Considering that the GSTA model can be derived from the Heterogeneous Langmuir isotherm, constructing a physical interpretation of its parameters would be relatively straightforward. It can be concluded from Section 2.2.1 that both the q_{max} and m parameters from the GSTA model were correctly defined by Llano-Restrepo and Mosquera[8] as the maximum adsorbent capacity and number of different types of adsorption sites, respectively. However, creating the link between the K_n parameters and the standard enthalpy and entropy, as in Equation 2.4, will require a deeper investigation.

For the Heterogeneous Langmuir model, the $K_{L,n}$ parameters are defined as the equilibrium constants associated with the adsorption of molecules at the n^{th} site. As such, each site would have a different energy associated with it[1,9] and could be correlated with temperature according to the van't Hoff equation (Equation 2.10), in which $K_{L,n}{}^{o}$ is the dimensionless equilibrium constant of the Heterogeneous Langmuir model and $\Delta H_{L,n}{}^{o}$ is the standard enthalpy associated with the n^{th} site.

$$\left(\frac{\partial \ln K_{L,n}^{o}}{\partial T}\right)_{n} = \frac{\Delta H_{L,n}^{o}}{RT^{2}} \qquad \textbf{Equation 2.10}$$

Integration of Equation 2.10 will result in an equation, which takes the same form as Equation 2.4, relating the K_n parameters with temperature. Since the K_n parameters are a function of the $K_{L,n}$ parameters as in Equation 2.9, a direct leap between Equation 2.10 and Equation 2.4 cannot be made for the GSTA parameters. However, the relationship can be inferred through consideration of the particular combinations of $K_{L,n}$ that result in the K_n parameters.

Recall from Section 2.2.1 the two-site Heterogeneous Langmuir model that resulted in the equivalent GSTA model. Each $K_{L,n}$ parameter is associated with a specific adsorbate-site interaction that can accommodate the same number of molecules. Therefore, for a pure gas with a two-site adsorbent, there are two distinct ways in which the interaction of a single molecule may occur: one molecule interacts with site one ($K_{L,1}$) or one molecule interacts with site two ($K_{L,2}$). Based on combinatorial mathematics,[10] this particular event may be represented by the Rule-of-Sum, which states that any event whose tasks cannot be performed simultaneously can be accomplished as a sum of those tasks. In other words, the event which corresponds to the adsorption of a single molecule from the two-site model can be represented as the sum of $K_{L,1}$ and $K_{L,2}$ (i.e., Event 1 = $K_{L,1} + K_{L,2}$).

The second event to consider is when two molecules of adsorbate are adsorbed, one to each available site (i.e., one molecule adsorbed to site one and site two or one molecule adsorbed to site two and site one). By combining the Rule-of-Sum with the

Rule-of-Product,[10] the second event can be represented as the sum of the product of the individual tasks. This results in the following: $K_{L,1}K_{L,2} + K_{L,2}K_{L,1}$. However, since the two products are indistinguishable from each other (i.e., $K_{L,1}K_{L,2} = K_{L,2}K_{L,1}$), they would be considered the same task and the duplicate must be eliminated. Therefore, the event is reduced to the following: Event 2 = $K_{L,1}K_{L,2}$.

From these definitions, it can be seen that events one and two correspond directly with the K_1 and K_2 parameters that were formulated in Section 2.2.1 from the Heterogeneous Langmuir model. This stands to reaffirm the physical interpretation of those parameters offered by Llano-Restrepo and Mosquera,[8] who had claimed that the K_n parameters represented the equilibrium constants associated with the adsorption of *n* molecules into a collection of adsorption sites. Furthermore, because the parameters of the GSTA model are established as equilibrium constants, it is suitable to utilize the van't Hoff equation (Equation 2.10) in order to formulate their dependence with temperature as shown in Equation 2.4. However, it is noteworthy to point out that the energy terms, which correspond to the equilibrium constants of the GSTA model, are not associated with site specific energies as in the Heterogeneous Langmuir model, but are instead representative of the event energies, which result from the adsorption of *n* molecules in the site network of the adsorbent.

2.3 Utilization of the GSTA Model in Equilibrium Data Correlations

2.3.1 Advantages and Complications

The greatest advantage of the GSTA model is in the fact that the equation contains an adjustable number of equilibrium parameters that may be used to describe the

system. Logically, the more parameters a model is allowed to have, the better it can describe the system it is being applied to. However, this advantage leads to a number of complications with regards to the utilization of the model. Such complications include determining the maximum number of parameters allowed and the minimum number of parameters needed to describe the system.

Another advantage of the GSTA model is in the physical interpretation of the parameters themselves. After obtaining the appropriate equilibrium parameters from the system, a simple linear regression across temperature for the corresponding K_n parameters will yield the relevant energy terms (Equation 2.4) necessary to predict the adsorption behavior between the temperatures for which experimental data are available. Therefore, as an additional complication, this requires that the model have the same number of parameters for each isotherm in a given adsorbate-adsorbent system. These complications and others were dealt with by using the techniques discussed in Section 2.3.2 below. The application of these techniques was accomplished in the development of a comprehensive C/C++ computer code (APPENDIX A. GSTA Optimization) to handle the variability of systems through a generalized treatment of each problem including whether or not $q_{\max}$ is known, the adsorbent's heterogeneity or homogeneity, and agnostic treatment of the units of adsorption capacity.

2.3.2 Solution Techniques

2.3.2.1 Non-Linear Least Squares Regression

The form of the GSTA equation is indefinite and non-linear and therefore requires the use of a non-linear regression technique to accommodate the optimization of the

parameters within the model. There are a number of non-linear optimization routines available (e.g., Newton's method, steepest-decent, trust region, ect.), but for the specific purpose of data correlation, a least squares method would be most applicable.[11]

In any least squares method, the objective is to minimize the Euclidean norm, or vertical displacement, between the y-axis data points and the result of the model function given the parameters and corresponding x-axis points. The mathematical form of the Euclidean norm is as follows:

$$\Phi = \sqrt{\sum_i (y_i - f(x_i, \mathbf{t}))^2} \qquad \textbf{Equation 2.11}$$

where Φ is the euclidean norm, y_i is the i^{th} y-axis data point, $f(x_i, \mathbf{t})$ is the model, x_i is the i^{th} x-axis data point, and $\mathbf{t}$ is the parameter vector of the model.

2.3.2.2 Determining the Number of Parameters

The size of the solution vector for the GSTA equation represents the number of equilibrium parameters of the model. Note that the q_{max} parameter is not considered to be adjustable as it represents the theoretical maximum adsorption capacity for a particular adsorbate-adsorbent system. Without any knowledge as to the heterogeneity of the adsorbent, the logical course of action is to search for all parameter solutions for every applicable size of the solution vector and compare each solution to determine which describes the data best. Computationally this is very time consuming, but can be optimized by careful elimination of unnecessary solution searches and setting up an objective function whose purpose is to minimize the size of the solution vector.

An obvious approach to limiting the number of parameters in the model is to consider the number of data points that the model is attempting to describe. Mathematically, it is impossible to describe any set of data with a number of parameters that exceeds the number of data points (M), but this can be taken a step further by considering that the number of parameters should be only a fraction of the number of data points. One could adopt a Two-Fifths compromise to place an absolute limit on the number of parameters to two-fifths of the total number of data points (e.g., $m \leq 2/5\ M$). However, this method is entirely arbitrary.

An alternate method to limit the total number of parameters could be adopted by using the Gibbs' Phase Rule.[12,13] Equation 2.12 below can be used to determine the degrees of freedom (D) for an equilibrium system from the number of components (N), phases (F), and intensive variables (I). For gas-solid adsorption systems there are two components (adsorbate and adsorbent), three phases (gas, solid, and adsorbed), and three intensive variables (pressure, temperature, and spreading pressure), therefore the number of degrees of freedom would be two.[12] Additionally, the Gibbs' Phase Rule can also be applied in determining the number of equilibrium parameters (m) applicable to describe the system. From Equation 2.13, it can be concluded that the maximum number of allowable equilibrium parameters to describe a gas-solid adsorption system is six. However, this rule does not yield any information as to the minimum number of parameters that may be able to describe the system.

$$D = N - F + I \qquad \textbf{Equation 2.12}$$

$$m = (N-1)F + I \qquad \textbf{Equation 2.13}$$

Minimizing the number of parameters in the GSTA model will simply reduce the calculations and the possibility of over-fitting or over describing a data set with unnecessary parameters. This can be accomplished by creating an objective function that serves to penalize data correlations that have a large number of parameters or a small number of data points. Such an objective function would be as follows:

$$F_{obj} = \sqrt{\frac{\sum_i [(y_i - f(x_i, \mathbf{t}))/y_i]^2}{M - m - 1}} \qquad \textbf{Equation 2.14}$$

whose parameters are the same as in the Euclidean norm of Equation 2.11. While the overall adequacy of the model to represent the data would be determined by the Euclidean norm, the most suitable solution with the least number of parameters would be determined by the objective function. Therefore, the objective function would serve as the final criterion in determining the number of parameters in the GSTA model.

A systematic procedure necessary to find the most suitable number of parameters is to start with the minimum number of parameters (m = 1), find an applicable solution via non-linear least squares regression, then increment the number of parameters by one. At each stage, the values of the Euclidean norm and objective function are observed and compared to the previous stage. This process is continued until the maximum number of parameters applicable to the system has been reached (i.e., when m = 2/5 M or m = 6, whichever is smaller). Finally, the most suitable solution is determined by locating the smallest F_{obj} from all solutions found.

2.3.2.3 Educated Initial Value Guessing

Unlike linear least squares regression, a non-linear regression analysis must start with an initial guess being made to the solution vector (**t**). Then, gradient observations must be made through the use of Jacobian matrices ($\mathbf{J} = \partial f/\partial \mathbf{t}$) in order to establish a magnitude and direction in which to shift the parameters of the model. This procedure is repeated until a reasonable solution is located, but due to the nature of non-linear regression, the ability to obtain solutions can be dependent on the initial values given in the solution vector.[11] To combat this issue, a number of techniques are adopted to ensure that the initial guess vector is as close to the solution as possible and that guesses being made are not arbitrary or irrelevant in magnitude.

The first guess is realized when considering that the GSTA model is exactly equal to the Langmuir equation when the number of equilibrium parameters (m) is equal to one. Under this condition, it is possible to linearize the equation (see Table 2.1) and perform a standard linear regression to obtain the parameters. The optimized parameters from the linear regression are then used in the non-linear analysis as the initial guess for the parameter vector.

The previously optimized parameters from the one-parameter solution found are then used as a basis for making the initial guess for the two-parameter model. Using that information, the two unknown parameters are given an initial value equal in magnitude to the previously found one parameter. Maintaining the relative magnitudes in all parameters will ensure that no parameter is seen as irrelevant in the current iteration and will therefore be treated as equally important in the overall model.

All subsequent guesses, for three parameters and beyond, are made as order-of-magnitude slope projections from two previously optimized parameters and the new parameter in the vector is a slope projection from the other parameters within the vector. For example, if the current iteration is meant to find a three-parameter (m = 3) solution, then the initial guess for the K_1 parameter will be based on the optimized K_1 parameters from the two- and one-parameter solutions, the K_2 parameter will also be based on that slope, and the K_3 parameter will be based on the slope between the K_1 and K_2 parameters that for the current iteration. Figure 2.1 provides a visualization of this procedure.

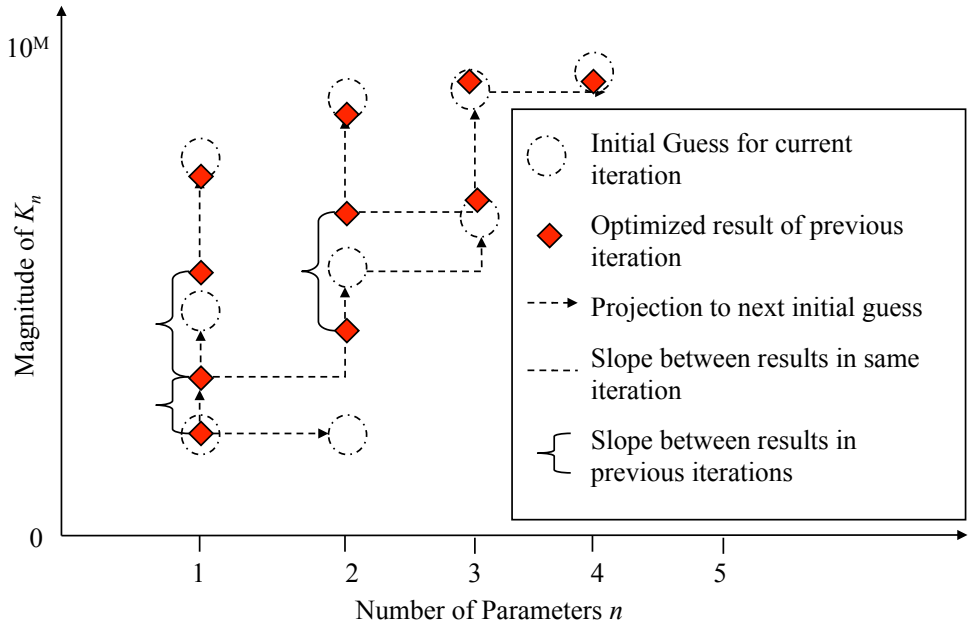

Figure 2.1 - Visualization of the *Educated Initial Value Guessing* procedure used by the GSTA code to estimate the initial values of the parameters. A good estimate is needed to ensure that the non-linear solution algorithm optimizes the parameters appropriately and can reliably find a solution. By using information gained from previously optimized sets of parameters, a more educated guess can be made for the next set.

2.3.2.4 Handling Multiple Isotherms

All previously mentioned techniques (Section 2.3.2) have been applied to a single isotherm set of data, but most gas-solid adsorption equilibria data for a system are composed of many isotherms. Each isotherm within the same system must have the same value for q_{max} and be described by the same number of parameters in order to make any correlations with temperature (recall Section 2.3.1) to obtain the relevant energy terms (ΔH_n^o and ΔS_n^o). Accomplishing this feat requires an additional procedure that can work alongside all other techniques.

From Section 2.3.2.2, the number of parameters that best describes each isotherm can be determined independently, but there needs to be a way to determine the number of parameters that can describe all isotherms. Each isotherm begins searching for solutions to the simplest model (m = 1), then continues to add complexity ($m = m + 1$) until solutions are no longer considered applicable. Therefore, there are a maximum number of parameters at which an applicable solution was found for each isotherm. For example, if isotherms one and three were described by up to five parameters, but isotherm two was only described by up to four parameters, then the maximum number of parameters that can describe all isotherms is four.

Continuing from that same example, each of the four solutions (i.e., the solutions for one, two, three, and four parameters) for the three isotherms is associated with an objective function value (F_{obj}) from which the best solution can be determined, and therefore the corresponding number of parameters that is most suitable for all isotherms. If the best solutions for each isotherm are different (i.e., isotherms one and three are best

described with three parameters, but isotherm two is best described with two parameters), then the weighted average of the number of parameters, rounded down to the nearest integer, is taken as the best solution for all isotherms.

If the maximum adsorption capacity (q_{max}) of a system is known, then there is no need for an additional procedure. However, this information may not always be available and such a case needs to be prepared for accordingly. First, the q_{max} is treated as an adjustable parameter and the procedures in Sections 2.3.2.2 through 2.3.2.4 would all still apply. Once the final solution is obtained, the optimized q_{max} parameters for each isotherm are compared alongside the respective Euclidean norms of that solution. A weighted average of the q_{max} parameters is then taken and the entire procedure is rerun from the beginning to find a solution, which has the same q_{max} for each isotherm.

2.4 Results of GSTA Optimization with Various Data Sets

2.4.1 Water Vapor on Zeolite 3A

The first set of results was developed to describe the equilibrium behavior between water vapor and zeolite 3A. Data for these isotherms were determined experimentally by Grace Davison,[15] a manufacturer of zeolite, and presented in a graphical format that had to be digitized in order to formulate the appropriate input data. An open-source software called Plot Digitizer[16] was used to digitize the Grace Davison plots. This was a very large data set with many data points and many isotherms, so it served as a vigorous test of the ability of the codes to handle big data.

For this set of data, the q_{max} parameter was known (22.8 kg/ 100 kg)[8] and was therefore given to the code as an input. Final results from the code are displayed in Figure 2.2, which shows the digitized data points with the model results from the temperature dependent parameters shown on Table 2.2. The optimum number of equilibrium parameters to describe this system was found to be six (m = 6). However, it should be noted that the original authors of the GSTA model[8] had concluded that the best solution to this system required seven parameters (m = 7).

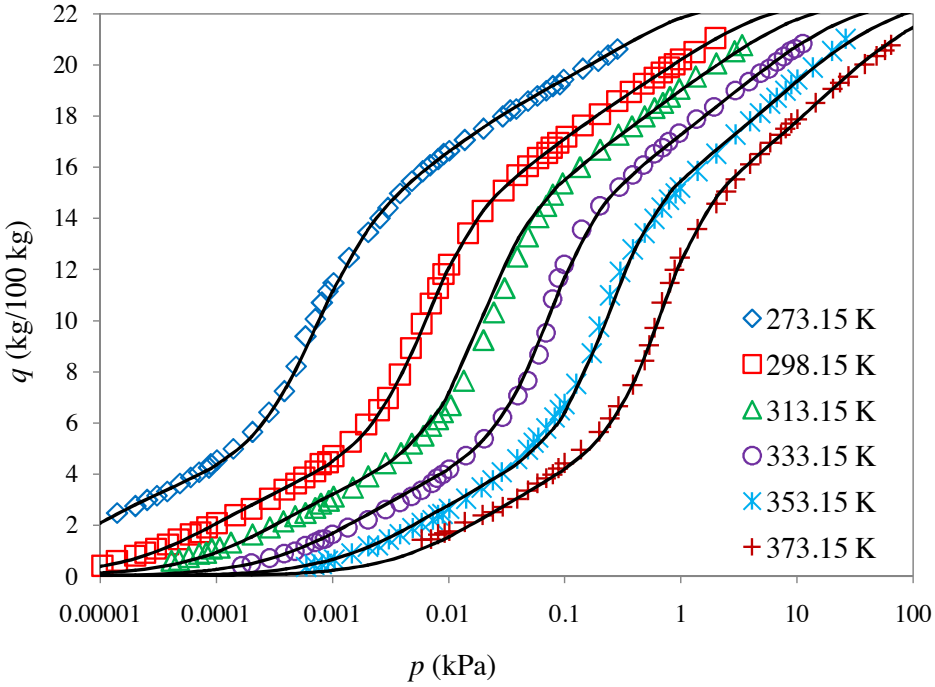

Figure 2.2 - Equilibrium adsorption isotherms of water vapor on zeolite 3A at various temperatures. The symbols represent experimental data points which were digitized while the solid lines show the result of the GSTA model using the temperature dependent equilibrium parameters formulated from the enthalpies and entropies reported on Table 2.2 for the 6-parameter solution.

Table 2.2 - Comparison of the relevant energy terms for the water vapor isotherms optimized at six and seven parameters. The units of ΔH_n^o and ΔS_n^o are kJ/mol and J/(K mol), respectively.

	Our Code Results			Modified Code Results			Llano-Restrepo & Mosquera [8]		
n	ΔH_n^o	ΔS_n^o	R^2	ΔH_n^o	ΔS_n^o	R^2	ΔH_n^o	ΔS_n^o	R^2
1	-63.5	-97.3	0.998	-64.8	-99.6	0.998	-64.7	-98.0	0.998
2	-120.6	-204.2	0.999	-121.4	-197.9	0.999	-122.0	-198.0	0.999
3	-184.5	-339.5	0.994	-321.0	-783.8	0.540	-187.8[a]	-342.0[a]	0.999[a]
4	-233.4	-423.0	0.999	-236.1	-421.4	0.998	-236.0	-420.0	0.998
5	-287.9	-548.1	0.999	-292.7	-539.9	0.999	-292.5	-535.0	0.999
6	-329.6	-653.3	0.999	-343.5	-657.2	0.999	-343.8	-654.0	0.999
7	---	---	---	-385.2	-764.3	0.999	-385.7	-763.0	0.999

[a] The correlation reported in literature was obtained by disregarding the value of K_3^o which lay outside of the of the linear regression (see Fig. 3).

It was found that the both the maximum allowable parameter and smoothness criteria, mentioned in the Appendix and seen in Figure A. 1, was the cause of the algorithms being unable to recreate the results given by the original authors of the model. By disabling these criteria, the code was able to find an applicable solution at seven parameters that was comparable to the solution given in literature[8] (see Table 2.2). Note that Llano-Restrepo and Mosquera[8] report their linear regression (Table 2.2) only after eliminating an outlying data point (K_3) at 60 ^oC. The code reconstructed the same outlying data point that was observed by Llano-Restrepo and Mosquera[8] shown in Figure 2.3. Without removing this point, the linear regression of the data to obtain the energy terms (ΔH_n^o and ΔS_n^o) is significantly and negatively impacted (see Table 2.2), but if that point were eliminated from the code's regression as well, then the results would essentially be the same.

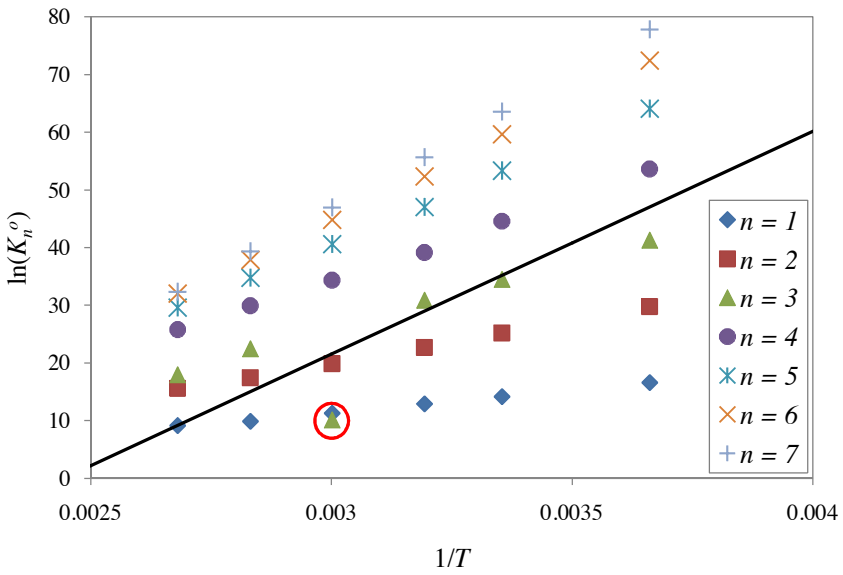

Figure 2.3 - Relationship between the dimensionless equilibrium constants of the GSTA isotherm and the system temperature for the 7-parameter solution to the water vapor and zeolite equilibrium data. The outlying data point for the third equilibrium point ($n = 3$) is circled and the solid line shows its influence on the linear interpolation. Correlation coefficients for all the linear regressions can be viewed on Table 2.2 under the Modified Code header.

To further investigate the effect of the K_3 parameter on this set of data, a sensitivity analysis was performed using the code's regression of that parameter without removing the outlier. The solid line in Figure 2.4 shows the result of the 7-parameter GSTA temperature dependent model if the outlying point from Figure 2.3 is not removed. What this demonstrates is that the first isotherm (273.15 K) is very sensitive to the K_3 parameter, while the other isotherms do not appear sensitive at all. To verify the 7-parameter model sensitivity, the results were recreated at seven parameters, but all K_3 parameter values were set to zero. The dotted line in Figure 2.4 shows the result from this and confirms that while the first isotherm is sensitive to the value of K_3, all other isotherms are not. Because the majority of the model lacks sensitivity to K_3, it may be

unnecessary to consider this parameter in the solution. However, this parameter cannot simply be thrown out just because it does not follow the linear trends in Figure 2.3. Therefore, the 6-parameter solution obtained by the GSTA algorithms may be more applicable to this data than the 7-parameter recorded in literature.[8]

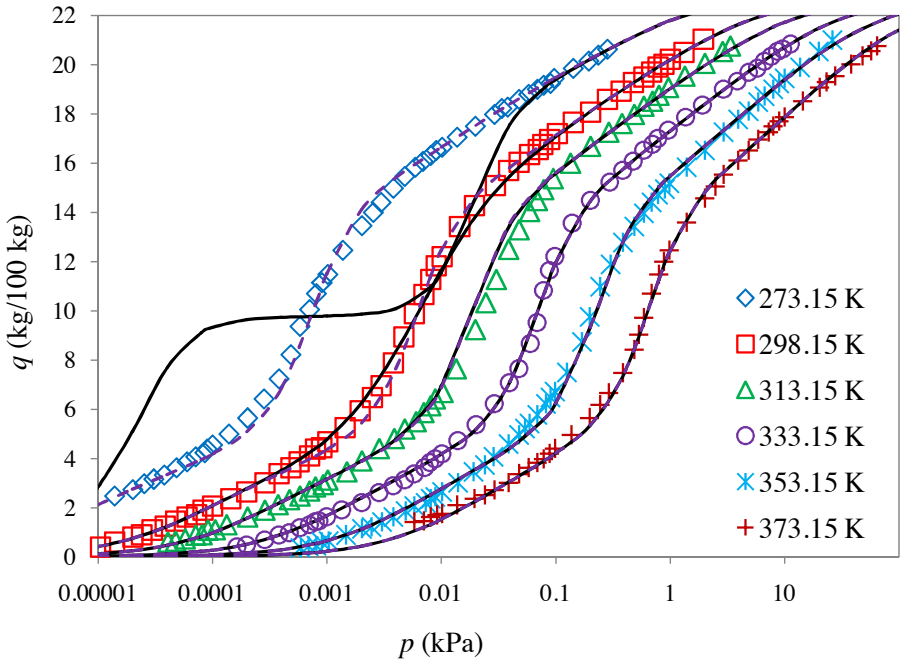

Figure 2.4 - Equilibrium adsorption isotherms of water vapor on zeolite 3A at various temperatures. The symbols represent the experimental data points and the solid lines show the result of the GSTA model using the temperature dependent parameters formulated from the enthalpies and entropies reported on Table 2.2 for the 7-parameter solution found under the Modified Code header. The dotted line shows the result of the GSTA model using those same parameters, except the third parameter (K_3) is replaced with zeros for all isotherms. This shows that the first isotherm (273.15 K) is very sensitive, while all others are barely, or not at all, sensitive to the third parameter.

2.4.2 CO_2, H_2S, and C_3H_8 on H-mordenite

The next series of equilibrium data employed in this study was published by Talu and Zwiebel,[17] whom had experimentally measured several gas-solid adsorption isotherms for CO_2, H_2S, and C_3H_8 on an H-mordenite adsorbent. Each adsorbate-adsorbent system displayed a slightly different equilibrium behavior and in no case was the maximum adsorbent capacity (q_{max}) known. Therefore, this set of data would test how well the code could estimate the capacity for each system and the versatility of the model to describe different behaviors.

Parameter results from the GSTA code are shown on Table 2.3 along with the correlation coefficients (R^2). The optimal number of parameters for each system was found to be six parameters for the CO_2 isotherms and two parameters for the H_2S and C_3H_8 isotherms. Maximum adsorption capacities were optimized to approximately 2.88 mmol/g, 3.02 mmol/g, and 1.48 mmol/g for CO_2, H_2S and C_3H_8 isotherms, respectively. Figure 2.5 through Figure 2.7 show the results of the temperature dependent GSTA model using the parameters found on Table 2.3. Although Talu and Zwiebel[17] did not provide parameters for their own correlations with these single component isotherms, they did comment on the order of preferential adsorption: $H_2S > CO_2 > C_3H_8$. This behavior was replicated by model and reflected in the estimation of the q_{max} parameter.

Table 2.3 - Relevant energy terms for the gas phase adsorption isotherms on an H-mordenite adsorbent. The units of ΔH_n^o and ΔS_n^o are kJ/mol and J/(K mol), respectively.

Gas Component	n	ΔH_n^o	ΔS_n^o	R^2
CO_2	1	-36.67	-76.86	0.999
	2	-82.98	-207.66	1.000
	3	-105.44	-266.22	0.997
	4	-145.36	-391.34	0.999
	5	-169.19	-474.27	0.994
	6	-195.59	-558.59	0.999
H_2S	1	-34.30	-67.57	0.996
	2	-67.15	-164.09	0.999
C_3H_8	1	-39.24	-87.05	0.997
	2	-69.36	-185.83	0.999

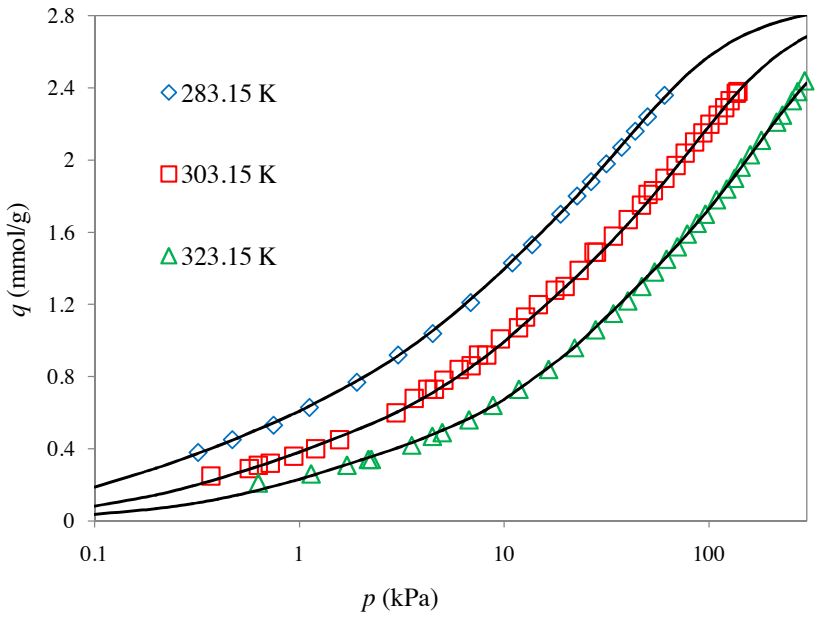

Figure 2.5 - Equilibrium adsorption isotherms of CO_2 on H-mordenite at various temperatures. The symbols represent the experimental data points and the solid lines show the results of the GSTA model using the temperature dependent parameters formulated from the enthalpies and entropies reported on Table 2.3.

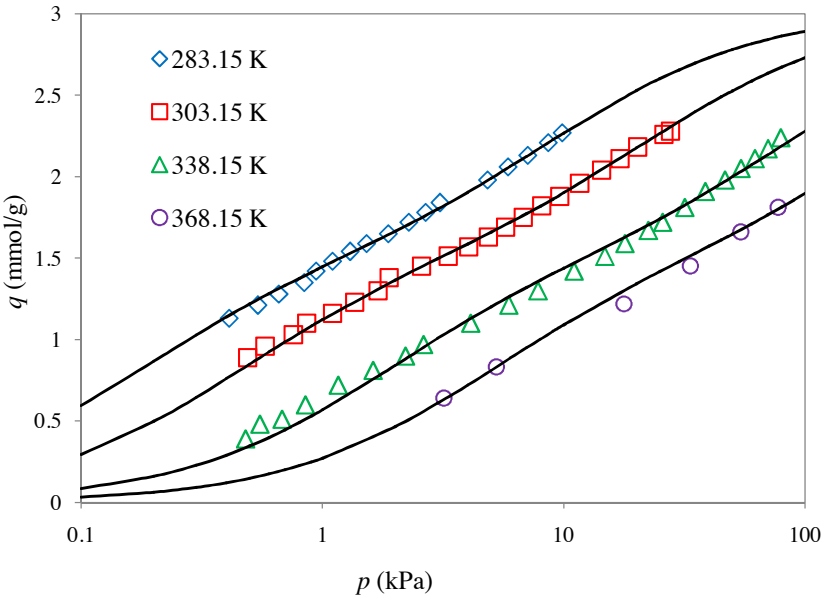

Figure 2.6 - Equilibrium adsorption isotherms of H_2S on H-mordenite at various temperatures. The symbols represent the experimental data points and the solid lines show the results of the GSTA model using the temperature dependent parameters formulated from the enthalpies and entropies reported on Table 2.3.

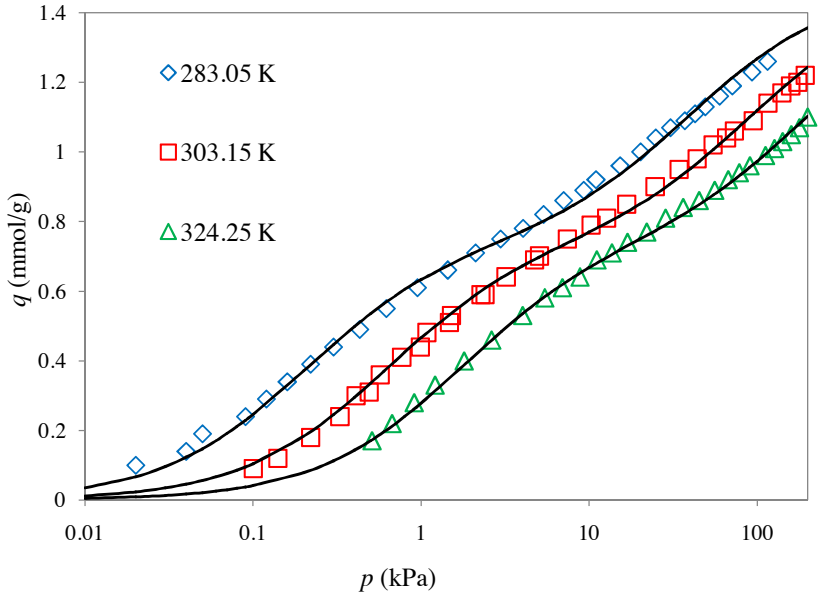

Figure 2.7 - Equilibrium adsorption isotherms of C_3H_8 on H-mordenite at various temperatures. The symbols represent the experimental data points and the solid lines show the results of the GSTA model using the temperature dependent parameters formulated from the enthalpies and entropies reported on Table 2.3.

2.4.3 CH_4, CO, CO_2, H_2, and H_2S on Activated Carbon

The final set of data examined was a series of five single-species systems on an activated carbon adsorbent. Isothermal data were measured experimentally by Ritter and Yang[7] and published along with their own correlated parameters for the data using a modified Langmuir isotherm model, which provided an empirical relationship between the Langmuir isotherm capacity (q_{max}) and temperature. All isotherms are reported at the high-pressure regimes (0.1 to 6.5 MPa), as opposed to the previous data tested in Sections 2.4.1 and 2.4.2, which were all low pressure. This will test the ability of the algorithms and model to adapt to high-pressure isothermal behaviors.

Table 2.4 shows the results for the energy terms found through the optimization of the GSTA model parameters with the equilibrium data. As on Table 2.2 and Table 2.3, all parameters show a very orderly and well-behaved correlation across the temperature range. Interestingly, the code had found that the optimal number of parameters for all systems was one, which means that the GSTA model took the form of the Langmuir model, which Ritter and Yang[7] had used in their own correlations. However, a direct comparison between the GSTA parameters and the Ritter and Yang parameters was not possible due to some differences in utilization of the two models.

Recall in Section 2.1.1.2 that the derivation of the Langmuir model included four basic assumptions to be applied to the adsorbate-adsorbent system.[1] Of these four assumptions, statements (i) and (iii) formulate the fundamental definition of the q_{max} parameter, which defines it as a constant for the particular adsorption system (i.e., it should not vary with temperature). This is how the q_{max} parameter is treated in the GSTA

model, but not how Ritter and Yang[7] treated the parameter in their correlations. Ritter and Yang allowed the maximum capacity to vary with each isotherm and declared an empirical relationship between their obtained q_{max} and temperature.

Table 2.4 - Relevant energy terms for the gas phase adsorption isotherms on an Activated Carbon adsorbent. The units of ΔH_n^o and ΔS_n^o are kJ/mol and J/(K mol), respectively.

Gas Component	n	ΔH_n^o	ΔS_n^o	R^2
CH_4	1	-20.35	-81.84	0.996
CO	1	-16.66	-74.48	0.997
CO_2	1	-22.56	-85.10	0.996
H_2	1	-13.42	-84.89	0.992
H_2S	1	-20.64	-72.61	1.000

Although a direct comparison of parameters is not possible, the Euclidean norm of each model can still be directly compared. Table 2.5 shows the average Euclidean norms and errors between each model and the data for each isotherm. The Ritter and Yang[7] model was able to better describe the data than the original GSTA model overall, but it did so at the cost of more parameters. Because the q_{max} was allowed to vary with temperature, each isotherm of Ritter and Yang was described with four temperature parameters, two for q_{max} and two for K. On the other hand, the GSTA code found constant maximum capacities for each system and therefore could describe the data with only two temperature parameters, ΔH_1^o and ΔS_1^o.

Table 2.5 - Euclidean Norms and Error Percentages for Gas-Solid Isotherms on Activated Carbon

Gas Component	T (K)	Ritter and Yang [7]		Original Code		Modified Code	
		Norm	Error %	Norm	Error %	Norm	Error %
CH_4	296	0.38	2.39	0.38	3.43	0.10	0.65
	373	0.38	4.68	0.63	9.28	0.11	1.62
	480	0.12	4.17	0.26	7.57	0.06	2.81
CO	296	0.22	4.21	0.40	4.51	0.20	4.00
	373	0.29	7.45	0.12	4.60	0.04	1.80
	473	0.10	4.77	0.14	9.24	0.02	1.74
CO_2	296	0.32	3.25	0.42	2.63	0.25	2.51
	373	0.58	7.65	0.52	11.40	0.12	2.69
	480	0.08	3.19	0.24	11.72	0.06	2.93
H_2	296	0.17	6.99	0.17	9.41	0.16	7.92
	373	0.03	1.95	0.02	1.64	0.01	0.88
	480	0.03	5.51	0.03	4.16	0.03	6.14
H_2S	296	0.30	1.85	0.74	5.15	0.30	2.01
	373	0.16	1.93	0.31	4.78	0.10	1.57
	480	0.07	1.67	0.19	6.97	0.03	1.25
Averages		0.22	4.11	0.30	6.43	0.11	2.70

In an attempt to recreate the Ritter and Yang[7] results, the code was temporarily modified to allow the q_{max} parameter to vary with temperature and then the code was rerun. Those results can also be viewed on Table 2.5 and are shown to be the best overall description of the data. However, this temporary modification to the GSTA model did not find the same empirical relationship that Ritter and Yang[7] had used to correlate the maximum capacities with temperature. This lack of any cohesive relationship between q_{max} and temperature is a good indication that no such relationship should actually exist for this type of isotherm model.

Other variations in these results could be explained by the different techniques used for obtaining the optimum parameters. Ritter and Yang used a linear least squares method[7] combined with the linearized form of the Langmuir model (see Table 2.1) to obtain the model parameters, while the GSTA code used a Levenberg-Marquardt non-linear optimization routine[14] to optimize the model parameters. Variations between the model parameters and overall description are a direct result of the transformation of the Langmuir model to a linear form.[18] When a model is transformed, or linearized, the relative error is also transformed which may result in a deviation between obtained and real solutions.

To gain a better understanding of the differences between the GSTA model and the Ritter and Yang[7] model, Figure 2.8 through Figure 2.12 show the temperature dependent GSTA model (solid line) and the temperature dependent Ritter and Yang[7] results (dotted line) against the experimental data recorded in literature. Between the pressure regions that contained data, the two models are very close to each other, but at the higher pressures the two models start to diverge. This is because the Ritter and Yang model will approach a different limit for each isotherm, while the GSTA model will approach the same limit. That limiting behavior is defined by the constant q_{max} parameters which the GSTA code had optimized for at approximately 5.88 mmol/g, 5.15 mmol/g, 9.27 mmol/g, 4.59 mmol/g, and 10.03 mmol/g for the CH_4, CO, CO_2, H_2, and H_2S isotherms, respectively.

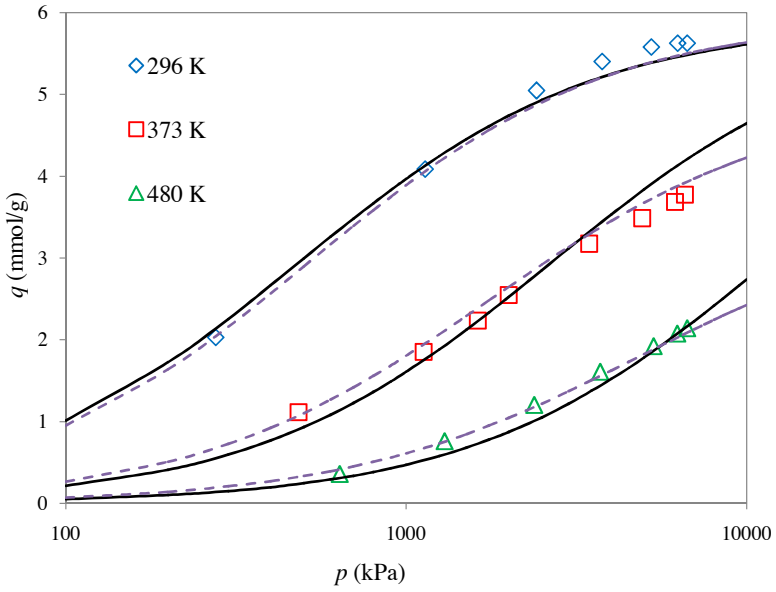

Figure 2.8 - Equilibrium adsorption isotherms of CH_4 on activated carbon at various temperatures. The symbols represent the experimental data points and the solid and dashed lines show the GSTA and Ritter and Yang[7] model results, respectively, using the temperature dependent parameters formulated from the enthalpies and entropies reported on Table 2.4.

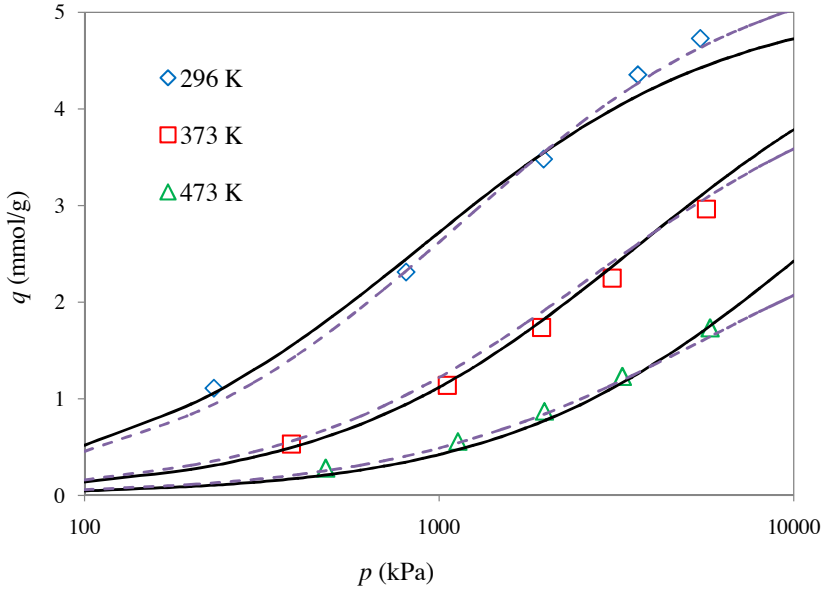

Figure 2.9 - Equilibrium adsorption isotherms of CO on activated carbon at various temperatures. The symbols represent the experimental data points and the solid and dashed lines show the GSTA and Ritter and Yang[7] model results, respectively, using the temperature dependent parameters formulated from the enthalpies and entropies reported on Table 2.4.

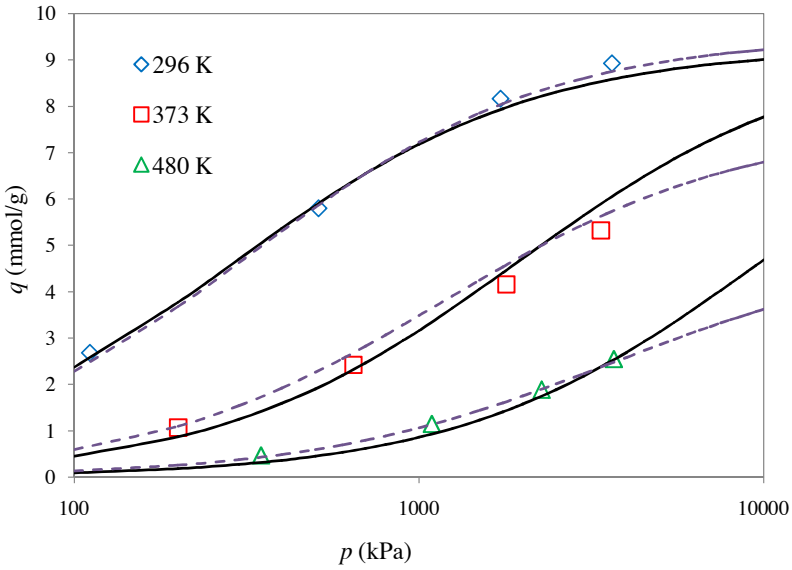

Figure 2.10 - Equilibrium adsorption isotherms of CO_2 on activated carbon at various temperatures. The symbols represent the experimental data points and the solid and dashed lines show the GSTA and Ritter and Yang[7] model results, respectively, using the temperature dependent parameters formulated from the enthalpies and entropies reported on Table 2.4.

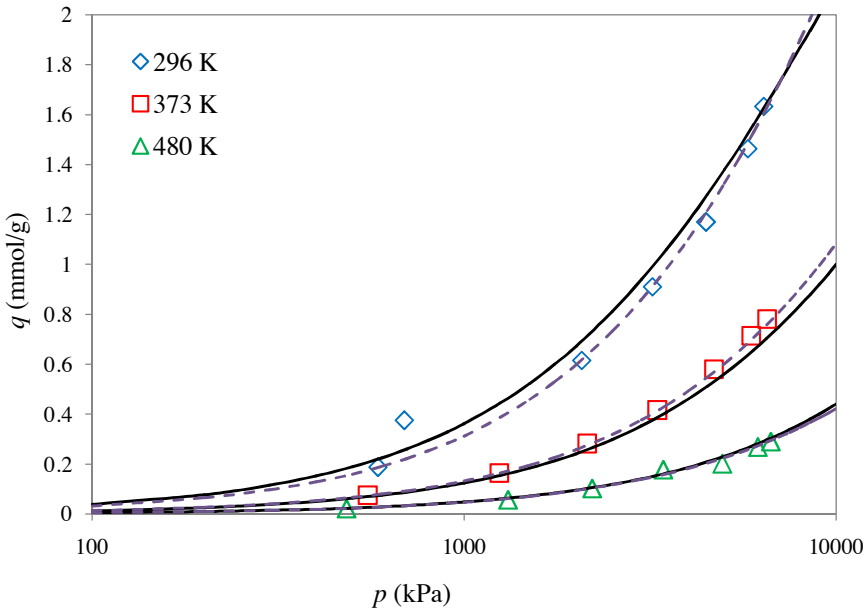

Figure 2.11 - Equilibrium adsorption isotherms of H_2 on activated carbon at various temperatures. The symbols represent the experimental data points and the solid and dashed lines show the GSTA and Ritter and Yang[7] model results, respectively, using the temperature dependent parameters formulated from the enthalpies and entropies reported on Table 2.4.

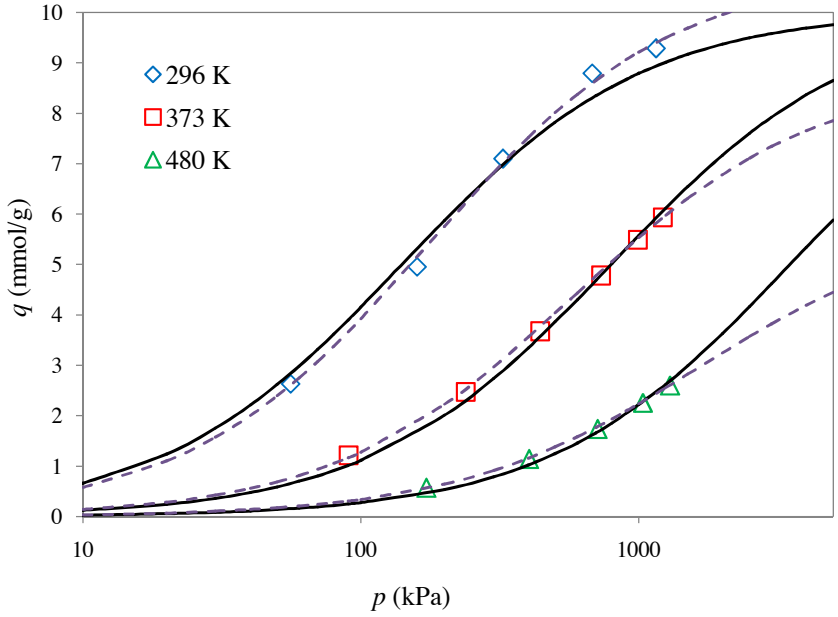

Figure 2.12 - Equilibrium adsorption isotherms of H_2S on activated carbon at various temperatures. The symbols represent the experimental data points and the solid and dashed lines show the GSTA and Ritter and Yang[7] model results, respectively, using the temperature dependent parameters formulated from the enthalpies and entropies reported on Table 2.4.

2.5 Discussion and Conclusions

2.5.1 Verification and Validation

The verification of the GSTA modeling and optimization algorithms has been routinely performed throughout its development to ensure that no steps in its execution or routine utilized have been broken. Each different set of data, with additional test cases, was used to search out errors in code that may be revealed through the variability of the input that the code may be faced with. Although there may still be improvements to data handling routines that can be made, in the current version of the code no errors exist in any of the routines that are implemented.

Validation of the GSTA code was accomplished through the comparison of the results with those reported in Llano-Restrepo and Mosquera,[8] which was the only known literature source that also used the GSTA model. Recall from Section 2.4.1 that the code, in its unaltered form, found a different solution than the solution in literature. However, the code was able to recreate the 7-parameter solution when some specific functionality of the code and the outlying K_3 point was neglected. Llano-Restrepo and Mosquera[8] had also found valid solutions between six and ten parameters, but did not report those parameters found. Their 7-parameter solution was chosen for two reasons: (i) it resulted in fewer oscillations in the isosteric heat of adsorption and (ii) they could physically define a set of seven sites where water molecules could adsorb in a fully utilized zeolite.

However, it should be noted that the validity of the 7-parameter solution that Llano-Restrepo and Mosquera proposed[8] could only be attained by selectively disregarding an outlying data point to formulate the enthalpies and entropies associated with the third parameter (K_3). Additionally, through the sensitivity analysis of the third parameter in Figure 2.4 it is demonstrated that the 7-parameter model does not rely on all seven parameters in most cases. Only one of the isotherms (273.15 K) shows an affinity to that parameter, while all others are nearly unaffected by its magnitude.

Furthermore, Llano-Restrepo and Mosquera[8] acknowledge that the 7-parameter solution represents only a maximum plausible number of sites for the adsorbate-adsorbent system. It is therefore possible that the actual number of sites be lower than this maximum, which may imply that certain sites within the adsorbent matrix are unavailable or unattainable by the adsorbate molecules. Such restrictions could be due to space or diffusion limitations. In any case, the 6-parameter solution obtained from the GSTA code

developed here could therefore also be valid and possibly more significant due to the lack of sensitivity observed in the 7-parameter solution.

2.5.2 Versatility and Reliability

Through the results obtained in Section 2.4, it has been demonstrated that the developed algorithms can accommodate a wide range of variability in the adsorption behavior. This is likely due to the versatility of the GSTA model itself. Since the GSTA model contains an adjustable number of parameters, it could be utilized in describing any number of systems. Furthermore, the optimal number of parameters obtained could potentially reveal information regarding the adsorbate-adsorbent system, such as heterogeneity.

Recall that in 2.2.1 the GSTA model could be derived from the Heterogeneous Langmuir model and consider that the code was designed to find the optimal value for the number of parameters (m). In the case in which the optimal number of parameters was found to be one, the GSTA model would take the form of the Langmuir model (i.e., a homogeneous adsorption model). For all other cases, the GSTA model would be a special case of the Heterogeneous Langmuir model. The m parameter yields information as to the heterogeneity of the system (i.e., larger m is a more heterogeneous system, while a smaller m is more homogeneous). Therefore, the GSTA model would be valid for both heterogeneous and homogeneous isothermal data because it has the versatility to fit in both situations.

Additionally, both the Langmuir and Heterogeneous Langmuir models have been widely used and accepted models for describing both physical and chemical adsorption

[1]. Having made the connection between the GSTA model and those isotherm models it would be reasonable to conclude that the GSTA model could also be used to describe both physical and chemical adsorption. However, this may have an impact on the physical interpretation of the parameters of the model.

All of the results obtained in Section 4 articulate the reliability of the GSTA model and the code developed for it. Recall the correlation coefficients (R^2) for the enthalpies and entropies on Table 2.2 through Table 2.4. Every parameter optimized was found to have a nearly perfect linear relationship with temperature as evident from all R^2 values being 0.992 or better. The accuracy of these correlations dictates the ability of the model to reliably predict the adsorption behavior between the applicable ranges of temperature. This feature is especially important if the model is to be applied to real systems in which isothermal conditions are rarely achieved.

2.5.3 Extensions and Improvements

As discussed in Section 2.1.2.1, in order to evaluate the spreading pressure of an adsorption system, the isotherm model must display linear behavior at low pressure.[1,6] To extend the GSTA model into other models, such as the Ideal Adsorbed Solution Theory (IAST) for predicting multicomponent behavior of gas mixtures, the spreading pressure must be accurately evaluated.[6,13] Llano-Restrepo and Mosquera also recognized the need for this Henry's Law like behavior and demonstrated themselves that the GSTA isotherm does have a finite limit at very low pressure.[8] This would be logical since the GSTA isotherm behaves similarly to the Langmuir model.

Unfortunately, this also means that the GSTA model is thermodynamically inconsistent with the Gibbs' expression for gas-solid adsorption, as there is a finite limit of q_{max} as the pressure increases infinitely.[2] However, it may be possible to formulate a new, modified version of the GSTA model, which is thermodynamically consistent. There is a two-step procedure discussed by Tóth[2] in which inconsistent isotherms can be modified through a general mathematical approach. This method has been used before to derive a three-parameter modified Langmuir model in which the monolayer capacity is achievable at a given saturation pressure.

Additionally, this inconsistent behavior of the GSTA model may account for some of the errors and divergence observed in the results obtained for the Ritter and Yang[7] data in Section 2.4.3. Since all of these isotherms are measured and analyzed at high pressures, the GSTA and Langmuir models may not be the most applicable equilibrium models to describe that set of data. Although the data were described reasonably well, discrepancies observed could be the result of going beyond the actual monolayer capacity of the adsorbent material. Therefore, while the GSTA model may be general enough to be utilized for nearly any low to mid-range pressure systems, modifications may be necessary in order for results to be considered significant and consistent for higher-pressure systems.

In conclusion, the GSTA model proposed by Llano-Restrepo and Mosquera[8] and the code developed in this paper have performed admirably for the variety of systems tested. Each different adsorbate-adsorbent isotherm was described with high accuracy and the largest of the errors were observed only in the highest-pressure ranges. All solutions obtained showed a well-behaved linear behavior with temperature, allowing

predictions to be reliably made for the temperature for which data were not available. Although there were many complications with using the GSTA model, the culmination of careful programming with today's modern computing languages have made the utilization of such a complex adsorption model not only feasible, but also robust and reliable as well.

2.6 Acknowledgement

The development of this chapter was a collaborative effort between my co-authors and myself and was the main subject of the following publication: A. Ladshaw, S. Yiacoumi, C. Tsouris, D. DePaoli, "Generalized Gas-Solid Adsorption Modeling: Single-Component Equilibria," *Fluid Phase Equilibria*, 338 (**2015**) 169-181.

2.7 References

[1] C. Tien, *Adsorption Calculations and Modeling*, Butterworth-Heinemann, Newton, MA, 1994.

[2] J. Tóth (Ed.), *Adsorption Theory Modeling and Analysis*, Marcel Dekker, Inc. New York, NY, 2002.

[3] J. Tóth, *Adv. Colloid Interf. Sci.* 55 (**1995**) 1-239.

[4] D.P. Valenzuela, A.L. Myers, *Adsorption Equilibrium Handbook*, Prentice-Hall, Englewood Cliffs, NJ, 1989.

[5] A.L. Myers, *AIChE J.* 29 (**1983**) 691-693.

[6] O. Talu, A.L. Myers, *AIChE J.* 34 (**1988**) 1887-1893.

[7] J.A. Ritter, R.T. Yang, *Ind. Eng. Chem. Res.* 26 (**1987**) 1679-1686.

[8] M. Llano-Restrepo, M.A. Mosquera, *Fluid Phase Equilibria*, 283 (**2009**) 73-88.

[9] H. Moon, C. Tien, *Chem. Eng. Sci.* 43 (**1988**) 2967-2980.

[10] R.P. Grimaldi, *Discrete and Combinatorial Mathematics*, Pearson Education, Inc. New York, NY, 2004.

[11] K. Madsen, H.B. Nielsen, O. Tingleff, Methods for Non-Linear Least Squares Problems, *Informatics and Mathematical Modeling*, Technical University of Denmark, 2004.

[12] R.M.A. Roque-Malherbe, *Adsorption and Diffusion in Nonporous Materials*, CRC Press, Taylor & Francis Group, Boca Raton, FL, 2007.

[13] A.L. Myers, J.M. Prausnitz, *AIChE J.* 11 (**1965**) 121-127.

[14] J. Wuttke, Version <lmfit-3.4>, <http://joachimwuttke.de/lmfit>, Accessed January 21, 2013.

[15] W.R. Grace & Co. Grace Davison, *Sylobead Adsorbents for Process Applications*, Columbia, MD, 2002.

[16] Plot Digitizer, <http://plotdigitizer.sourceforge.net/>, Accessed October 16, 2013.

[17] O. Talu, I. Zwiebel, *AIChE J.* 32 (**1986**) 1263-1276.

[18] D.G. Kinniburgh, *ES&T*, 20 (**1986**) 895-904.

2.8 Nomenclature

Latin Symbols

a	parameter of the Freundlich isotherm for to adsorption strength, Table 2.1
A	specific surface area of an adsorbent, Equation 2.1
b	parameter of the Tòth isotherm relative to heterogeneity and lateral interactions of molecules, Table 2.1
D	number of degrees of freedom in an equilibrium system, Equation 2.12
F	number of phases in an equilibrium system, Equation 2.12
$f(x_i,\mathbf{t})$	generic representation of a model function, Equation 2.11
F_{obj}	objective function used to penalize optimization with many parameters and/or few data points, Equation 2.14
I	number of intensive variables in an equilibrium system, Equation 2.12

$\mathbf{J}$ Jacobian matrix of a model function

K_F parameter of the Freundlich isotherm relative to adsorption capacity, Table 2.1

K_H Henry's Law constant at low pressure regime of an isotherm

K_L equilibrium constant of the Langmuir isotherm, Table 2.1

$K_{L,n}$ equilibrium constant at the n^{th} adsorption site for the Heterogeneous Langmuir isotherm, Table 2.1

$K_{L,n}^{o}$ dimensionless equilibrium constant at the n^{th} adsorption site for the Heterogeneous Langmuir isotherm, Equation 2.10

K_n equilibrium constant of the GSTA model associated with the adsorption of n adsorbate molecules, Equation 2.2

K_n^{o} dimensionless equilibrium constant of the GSTA model associated with the adsorption of n adsorbate molecules, Equation 2.3

m number of equilibrium parameters and adsorption sites, and/or adsorbed molecules, in the Heterogeneous Langmuir and GSTA models, Table 2.1

M power representing the magnitude of the K_n parameter of the GSTA model, Figure 2.1

M number of equilibrium points of an experimental isotherm, Equation 2.14

n index for the number of parameters and adsorption sites, and/or adsorbed molecules, in the Heterogeneous Langmuir and GSTA models, Table 2.1

N number of components in an equilibrium system, Equation 2.12

p partial pressure of adsorbate species in the gas phase, Equation 2.1

P total pressure of the system, Equation 2.1

P^{o} standard state pressure, 100 kPa, Equation 2.3

q amount of adsorbate adsorbed at equilibrium, Equation 2.1

$q_{\max}$ monolayer capacity of the adsorbate-adsorbent system, Table 2.1

q_n monolayer capacity of the n^{th} adsorption site in the Heterogeneous Langmuir isotherm, Table 2.1

q_s monolayer capacity of each site in the Heterogeneous Langmuir isotherm if all sites have the same capacity

R gas law constant, 8.314 J/K/mol, Equation 2.1

R^2 correlation coefficient for a linear regression

T temperature of the system in Kelvin, Equation 2.1

t parameter vector of a generic model function, Equation 2.11

x_i independent variable of a model function at the i^{th} data point, Equation 2.11

y_i dependent variable of the i^{th} data point, Equation 2.11

Greek Symbols

$\Delta H_{L,n}^{o}$ standard molar enthalpy of adsorption at the n^{th} adsorption site from the Heterogeneous Langmuir isotherm, Equation 2.10

ΔH_n^o standard molar enthalpy of the adsorption of n molecules, Equation 2.4

ΔS_n^o standard molar entropy of the adsorption of n molecules, Equation 2.4

π spreading pressure of the system, Equation 2.1

Φ euclidean norm of the model function versus the data points, Equation 2.11

Abbreviations

GSTA Generalized Statistical Thermodynamic Adsorption

IAST Ideal Adsorbed Solution Theory

Other Symbols

iso index for the isotherms given on input, Figure A. 1

m_dat number of data points for an experimental isotherm, Figure A. 1

max maximum number of parameters plausible for any isotherm of a system given the maximum number of parameters found applicable from the previous isotherm, Figure A. 1

n_iso number of experimental isotherms for a given adsorbate-adsorbent system, Figure A. 1

n_par number of adjustable parameters being optimized for in the GSTA model, Figure A. 1

QMAX Boolean expression to check for the existence of the q_{max} parameter on input, Figure A. 1

qmax estimated value of the q_{max} parameter when not known, Figure A. 1

CHAPTER 3. MULTI-SPECIES EQUILIBRIA MODELING

3.1 Introduction

Adsorption isothermal equilibrium has been the cornerstone of adsorption modeling and separation process design for decades. For simple, single-component systems, it is generally sufficient to represent adsorption equilibria in terms of a series of isotherms. This type of data describes the equilibrium partition between the gas and solid phases at a constant temperature. A series of isotherms, each at a different temperature, would then allow for interpolation of the adsorption equilibrium behavior expected at any temperature and pressure that falls within that applicable temperature range. In real separation processes, however, there are multiple gas species involved. Therefore, one needs to be capable of predicting how each species would behave and interact with other species and the adsorbent surface. To accomplish this feat, proposed here is a procedure, which can be utilized in the prediction of multicomponent adsorption equilibria for any number of gas species. The aim is to provide a theory that is general enough to allow other scientists and engineers to extend the basic ideas developed in this work by simply applying different isotherm and activity models.

3.1.1 Adsorbed Solution Theory

One of the most well-known multicomponent adsorption theories is the Adsorbed Solution Theory (AST) proposed by Myers and Prausnitz and shown below in Equation 3.1 through Equation 3.6.[1]

$$\Pi = \frac{\pi A}{RT} = \int_0^{p_i^o} \frac{q_i^o}{p_i^o} dp_i^o \qquad \textbf{Equation 3.1}$$

$$P_T y_i = p_i^o x_i \gamma_i \qquad \textbf{Equation 3.2}$$

$$q_T = \left[\sum_{i=1}^{N} \frac{x_i}{q_i^o} + \sum_{i=1}^{N} x_i \left(\frac{\partial \ln \gamma_i}{\partial \Pi} \right)_{T,x} \right]^{-1} \qquad \textbf{Equation 3.3}$$

$$\sum_{i=1}^{N} x_i = 1 \qquad \textbf{Equation 3.4}$$

$$q_i = q_T x_i \qquad \textbf{Equation 3.5}$$

$$q_i^o = f(p_i^o) \qquad \textbf{Equation 3.6}$$

This theory was derived from the Gibbs thermodynamic expression for physical adsorption and assumes that the adsorbent is thermodynamically inert and contains a specific surface area (A) that is shared by all adsorbates. Intensive properties of the system are temperature (T), spreading pressure (π), and adsorbed phase composition (x_i, x_j, …, x_N) while the extensive property of the mixture is the total surface loading (q_T).[1]

For any given mixture, the surface energy per unit area (i.e. spreading pressure) must be a constant. Therefore, it is often lumped into a combined spreading pressure term (Π) for convenience. Additionally, since this term is constant for the mixture, each pure species isotherm integral (Equation 3.1) must evaluate to the same value, which places a constraint in the system of equations. To obtain the pure species (i.e. reference state) pressure (p_i^o), Raoult's Law is applied between the gas and solid phases (Equation 3.2),

which couples the activity (γ_i) and adsorbed mole fraction (x_i) to the gas phase partial pressure ($P_T y_i$).[1]

The primary advantage of AST was that it allowed for the prediction of the mixed gas adsorption equilibria for any pure gas isotherm, $q_i^o = f(p_i^o)$. Furthermore, if the adsorbed phase was assumed to behave like an ideal solution, then the activity coefficients for each species would be equal to one ($\gamma_i = 1$, for all i). This simplification made the system of equations solvable and could then be used to predict adsorption equilibria for any number of components (N).

3.1.2 Including Non-ideal Surface Effects

Unfortunately, the assumption of ideality in the adsorbed phase has been shown to produce fairly large errors when the model is compared against experimental data.[2-4] Largely, these errors are attributed to the activity coefficients, though other explanations suggest they may stem from surface heterogeneity of the adsorbents.[4-5] Either way, it has become common practice to propose various activity models to account for the non-ideality of real mixed gas systems. Some models that have been utilized include the Flory-Huggins[6] and Wilson[7] equations, as well as the UNIQUAC[8-9] and UNIFAC[10] models. However, all these models lack a relationship between the spreading pressure (π) and activity coefficient (γ_i) as Equation 3.3 above requires.

In order for an activity model to be considered thermodynamically consistent, it must abide by three criteria[2-3] detailed below in Equation 3.7 through Equation 3.9.

$$\lim_{x_i \to 1} \gamma_i = 1 \qquad \textbf{Equation 3.7}$$

$$\lim_{\pi \to 0} \gamma_i = 1 \qquad \textbf{Equation 3.8}$$

$$\lim_{x_i \to 0} \gamma_i = \gamma_i^{\infty} \qquad \textbf{Equation 3.9}$$

Equation 7 states that the activity of a particular component must become unity when the adsorbed mole fraction (x_i) of that component approaches one. In addition, the activity must also approach unity as the spreading pressure approaches zero. When the mole fraction of a component approaches zero in the adsorbed phase, then there is some infinite dilution activity (γ_i^{∞}) attained,[11] which usually displays a negative deviation from Raoult's Law.[5]

Unlike the other activity models mentioned above, the Spreading Pressure Dependent (SPD) model proposed by Talu and Zwiebel[3] and shown below in Equation 3.10 through Equation 3.14, does abide by the thermodynamic criteria in Equation 3.7 through Equation 3.9.

$$\ln \gamma_i = s_i \left[1 - \ln\left(\sum_{j=1}^{N} \theta_j \tau_{ji} \right) - \sum_{j=1}^{N} \frac{\theta_j \tau_{ij}}{\sum_{k=1}^{N} \theta_k \tau_{kj}} \right] \qquad \textbf{Equation 3.10}$$

$$\theta_i = \frac{s_i x_i}{\sum_{j=1}^{N} s_j x_j} \qquad \textbf{Equation 3.11}$$

$$\tau_{ji} = \exp\left[-\frac{z(e_{ji} - e_{ii})}{2RT}\right] \qquad \textbf{Equation 3.12}$$

$$e_{ii} = \frac{2(Q_i^{st} - Q_{i,o}^{st})}{zs_i} \qquad \textbf{Equation 3.13}$$

$$e_{ji} = \sqrt{e_{ii}e_{jj}}(1 - \beta_{ji}) \qquad \textbf{Equation 3.14}$$

This model was developed as an adaptation of the UNIQUAC activity model, and included lateral interaction potentials (e_{ji}) that were related to surface coverage through the difference between the isosteric heat of adsorption (Q_i^{st}) at the spreading pressure of the mixture and the isosteric heat of adsorption at zero spreading pressure ($Q_{i,o}{}^{st}$). A quick verification of the SPD model's adherence to Equation 3.8 can be shown by recognizing that when the spreading pressure is zero, the interaction potentials all become zero, which in turn causes all the Boltzmann weighting factors (τ_{ji}) to equal one. By substituting this information into Equation 3.10, it can be shown that the activity coefficients will always evaluate to unity for zero spreading pressure. A similar analysis can be performed to verify the SPD model's adherence to Equation 3.7 and Equation 3.9 as well.

Although the SPD model does stay consistent with the criteria outlined in Equation 3.7 though Equation 3.9 above, it still contains multiple adjustable parameters, including molecular shape factors (s_i) and a cross-lateral correction parameter (β_{ji}). In that case, an N component mixture will contain a total of $N + N(N - 1)/2$ adjustable parameters, which must be determined through binary adsorption experiments.[3] Additionally, as it is impossible to run any adsorption experiments at a constant spreading

pressure, it can be extraordinarily difficult to accurately quantify the activities of each species.[5] This drives the need to develop a purely predictive approach to estimating the parameters of the activity model.

3.1.3 Predicting Non-ideal Surface Effects

In 1998, Sakuth et al. had proposed an extension of AST, called Predictive Real Adsorbed Solution Theory (PRAST), that intended to estimate the binary interaction parameters of an activity model by looking at the limiting behavior of each component's pure isotherm and using that information to calculate the infinite dilution activities.[11] As a result, each of the pure-component isotherms must obey Henry's Law at low pressure (Equation 3.15), which is a thermodynamic expectation for gas adsorption.[2] The infinite dilution activities for each component can then be evaluated from Equation 3.16 and combined with the activity model to set up a system of equations in which the adjustable parameters of the model can be explicitly solved for.[11]

$$\lim_{p_i^o \to 0} \frac{q_i^o}{p_i^o} = He_i \qquad \textbf{Equation 3.15}$$

$$\gamma_i^{\infty}(\pi_j) = \frac{q_j^o(\pi_j)}{He_i p_i^o(\pi_j)} \qquad \textbf{Equation 3.16}$$

However, this formulation is only valid for a binary mixture because it must be assumed that the adsorbed mole fraction of the other species becomes one ($x_j = 1$) as the mole fraction of the first becomes zero ($x_i = 0$). Additionally, PRAST requires that the activity model itself only have two adjustable parameters for a binary mixture, such as

UNIQUAC, in order for the equations to be solvable. Therefore, PRAST would not be applicable for use with SPD because SPD has three adjustable parameters and PRAST only formulates two equations, one for each component.

In an attempt to expand upon and overcome the limitations of PRAST, there is a need to modify the SPD model such that the binary interaction parameters of that model can be determined through the system of equations developed in PRAST. However, modification of SPD alone will not suffice in creating a generalized multicomponent adsorption theory. PRAST itself must also be extended to allow equilibria predictions of mixtures that contain more than just two adsorbable components.

The proposed extension to PRAST is geared towards outlining how one can systematically determine the infinite dilution activities for an *N*-component mixture, thus generalizing the PRAST system into what will be referred to as the Generalized Predictive Adsorbed Solution Theory (GPAST). Additionally, the lateral interaction potentials of the SPD model will be redefined to allow the model to fit within the GPAST procedure without altering the significance or behavior of the model itself. This reformulated SPD model will be called the Modified Spreading Pressure Dependent (MSPD) model. Application of these models and theories will be carried out in a computer code developed in C/C++ for the purpose of single and multicomponent adsorption data analysis. A series of adsorption data from literature will serve as a test case for GPAST. GPAST will then be compared against Ideal Adsorbed Solution Theory (IAST) under the same conditions with the intent to demonstrate a significant improvement in predictive capabilities.

3.2 Generalized Predictive Adsorbed Solution Theory

In many semi-predictive approaches to multicomponent adsorption equilibria, it is common practice to calibrate an activity model for an *N*-component system using binary adsorption data from each unique pair of species in that system.[3,7,8,12] The calibrated parameters of those activity models are then used for the prediction of the ternary and higher systems. However, this calibration approach, based on experimental measurements, is problematic for two main reasons: (i) there is an exponential increase in the number of binary experiments required for calibration as the number of species in a system increases and (ii) it is impossible to carry out adsorption under constant spreading pressure and therefore very difficult to accurately measure the activity of each species in the adsorbed phase.[5]

3.2.1 Extending the PRAST System of Equations

The principal idea governing GPAST is to predict the parameters of the activity model, without experiments, using each unique binary pair of species within the overall system. By looking at each species pair-wise, as opposed to altogether, the PRAST estimate of the infinite dilution activity (Equation 3.16) can be used directly and applied serially to each unique pair. This is now possible because, for a given binary pair, the adsorbed mole fraction of species *j* will approach unity ($x_j = 1$) as the adsorbed mole fraction of species *i* approaches zero ($x_i = 0$).

To visualize this concept, consider a system that has three adsorbable species: A, B, and C. In this system, there are three unique binary pairs whose infinite dilution activities must be determined: A+B, A+C, and B+C. Note that the reverse of these

pairings (i.e. B+A, C+A, and C+B) is not considered because they are not unique. The infinite dilution activities are determined by Equation 3.16 for each species in a pair, such that each pair results in two infinite dilution activities: $\gamma^{\infty}{}_A(\pi_B)$ & $\gamma^{\infty}{}_B(\pi_A)$, $\gamma^{\infty}{}_A(\pi_C)$ & $\gamma^{\infty}{}_C(\pi_A)$, and $\gamma^{\infty}{}_B(\pi_C)$ & $\gamma^{\infty}{}_C(\pi_B)$. When this idea is extended to an N-component system, the number of unique pairs to that system becomes $N(N\text{-}1)/2$ and the number of infinite dilution activities to determine is $N(N\text{-}1)$.

From here, GPAST becomes a combinatorial and serial application of the PRAST system. Recall that in the PRAST method, a system of equations involving the activity model and the calculated infinite dilution activities is set up in order to solve for the parameters of the activity model for that binary system.[11] This same procedure is used in GPAST, but is applied sequentially over each binary set within the overall system, such that all of the activity model parameters for each pair of species can be determined.

To demonstrate this concept, consider Equation 3.10 and Equation 3.11 from the SPD model to be the activity model chosen to describe the non-ideal behavior at the surface of the adsorbent. To simplify this example, it will be assumed that the molecular shape factors (s_i) can be independently determined based on the adsorbing molecule size characteristics and that the only model parameters to be determined are the Boltzmann weighting factors: τ_{ij} and τ_{ji}. Then, continuing from the previous ternary example, a system of equations for each binary pair can be formulated as shown below in Equation 3.17 through Equation 3.22.

$$\lim_{\substack{x_A \to 0 \\ x_B \to 1}} \left(\ln \gamma_A\right) = \ln \gamma_A^{\infty}(\pi_B) = s_A\left(1 - \ln \tau_{BA} - \tau_{AB}\right) \qquad \textbf{Equation 3.17}$$

$$\lim_{\substack{x_B \to 0 \\ x_A \to 1}} \left(\ln \gamma_B\right) = \ln \gamma_B^{\infty}(\pi_A) = s_B \left(1 - \ln \tau_{AB} - \tau_{BA}\right) \qquad \textbf{Equation 3.18}$$

$$\lim_{\substack{x_A \to 0 \\ x_C \to 1}} \left(\ln \gamma_A\right) = \ln \gamma_A^{\infty}(\pi_C) = s_A \left(1 - \ln \tau_{CA} - \tau_{AC}\right) \qquad \textbf{Equation 3.19}$$

$$\lim_{\substack{x_C \to 0 \\ x_A \to 1}} \left(\ln \gamma_C\right) = \ln \gamma_C^{\infty}(\pi_A) = s_C \left(1 - \ln \tau_{AC} - \tau_{CA}\right) \qquad \textbf{Equation 3.20}$$

$$\lim_{\substack{x_B \to 0 \\ x_C \to 1}} \left(\ln \gamma_B\right) = \ln \gamma_B^{\infty}(\pi_C) = s_B \left(1 - \ln \tau_{CB} - \tau_{BC}\right) \qquad \textbf{Equation 3.21}$$

$$\lim_{\substack{x_C \to 0 \\ x_B \to 1}} \left(\ln \gamma_C\right) = \ln \gamma_C^{\infty}(\pi_B) = s_C \left(1 - \ln \tau_{BC} - \tau_{CB}\right) \qquad \textbf{Equation 3.22}$$

Since the infinite dilution activities have already been calculated by Equation 3.16, and the shape factors are independently determined, these equations represent a uniquely solvable, non-linear system of six equations and six unknowns. Each τ_{ji} determined from these equations is then used back in the original activity model to represent the non-ideality that occurs at the surface for the ternary system. From this point on, the standard AST system of equations (Equation 3.1 through Equation 3.6) can be used to predict the adsorbed amounts in the system under various conditions of temperature and pressure, using the activity model with the parameters (τ_{ji}) calculated from GPAST.

It is important to note that GPAST is essentially a direct extension of the PRAST method with the purpose of generalizing the approach to be applicable to systems containing more than two adsorbable species. As such, if the number of adsorbable

species in a system is only two, then GPAST is exactly the same as PRAST. However, GPAST has a clear advantage over PRAST in its ability to go beyond just a binary system and instead consider an *N*-component system.

3.2.2 Modifying the SPD Activity Model

It was shown previously that the SPD activity model proposed by Talu and Zwiebel[3] abides by the three thermodynamic criteria outline in Equation 3.7 through Equation 3.9, which makes it a viable model to use for gas-solid adsorption. However, this model contains a set of three parameters (s_i, s_j, and β_{ij}) for each binary pair of adsorbing molecules (i and j). Note that the $\beta_{ij} = \beta_{ji}$ so that it only counts as one parameter instead of two. Therefore, the SPD model does not fit within the GPAST system because GPAST, like PRAST, requires that there be two parameters per binary pair in order for the resulting system of equations to be solvable.

Much like in the GPAST example considered previously (Section 3.2.1), the SPD model can be modified by assuming the shape factors are not model parameters, but instead are values that can be determined independently based on the characteristics of the adsorbing molecules. Bondi,[13] Abrams and Prausnitz,[8] and Vera et al.[14] proposed several methodologies for determining the shape factor of a molecule based on the van der Waals volume (v_i) of that molecule and the lattice coordination number (z), which is typically taken to be a constant. For simple, non-aromatic molecules, the shape factor (s_i) can be calculated simply from Equation 3.23. Note that v^o is a constant that depends on the chosen coordination number. For a coordination number of 10, $v^o = 18.92$ cm^3/mole. Other values of v^o for various coordination numbers are tabulated in Vera et al.[14]

$$s_i = \frac{v_i(z-2)}{v^o z} + \frac{2}{z} \qquad \textbf{Equation 3.23}$$

This relationship, or another similar method, may be used to eliminate the shape factors as parameters of the SPD model leaving β_{ij} as the only adjustable parameter. However, the GPAST system under these conditions still remains unsolvable because it needs the activity model to have exactly two parameters per binary pair. By having only one model parameter per binary pair, the system of equations is not uniquely solvable since there may be many values of that parameter that could minimize the residuals of the system, but not eliminate those residuals. Therefore, the SPD model must be further modified to fit into the GPAST system.

In the original SPD model, the β_{ij} parameter shows up in the equation for the lateral interaction potentials (e_{ij}) between molecules *i* and *j* (Equation 3.14) and serves as a correction parameter for the geometric averaging of each molecules' interaction potential with itself (e_{ii}). However, this simple geometric average is only valid if both e_{ii} and e_{jj} have the same sign, positive or negative. This may not necessarily be the case since each adsorbing molecule is likely to have different energy characteristics with the surface loading and spreading pressure.

To correct this issue, a shifted geometric mean should be used for the lateral interaction potentials to eliminate the possible advent of imaginary numbers. In this type of averaging, the values being averaged are first shifted to the positive region of the domain by some factor such that all values underneath the square root are positive. Once the geometric average of the shifted values has been determined, the actual geometric

average is back calculated out by undoing the initial shifting. A common use of this type of averaging is seen in financial economics in determination of the average rate-of-return (g) on an investment (Equation 3.24). In this example, the shift factor is taken to be 1 (or 100%) for all returns (r_t) in a series of investments.[15] This equation can be generalized further by allowing the shift factor for each return to be any constant (C), such that the geometric mean then takes the form of Equation 3.25.

$$g = \sqrt[G]{\prod_t (1 + r_t)} - 1 \qquad \textbf{Equation 3.24}$$

$$g = \sqrt[G]{\prod_t (C + r_t)} - C \qquad \textbf{Equation 3.25}$$

Comparing Equation 3.25 to Equation 3.14, it can be seen that the β_{ij} parameter of the activity model is essentially acting as a correction to the shift factor in the geometric mean. As such, we can redefine Equation 3.14 to Equation 3.26 below using a shifted geometric mean of the interaction potentials (e_{ii}) and using a new correction parameter α_{ij} to replace the β_{ij} correction parameter used by Talu and Zwiebel.

$$e_{ji} = \sqrt{\left(\mu + e_{ii}\right)\left(\mu + e_{jj}\right)} - \alpha_{ji}\mu \qquad \textbf{Equation 3.26}$$

$$\mu = \max\left\{\max_{\forall \pi}\left|e_{ii}\right|, \max_{\forall \pi}\left|e_{jj}\right|\right\} \qquad \textbf{Equation 3.27}$$

In this formulation, the variable μ is the maximum absolute value of the maximum of e_{ii} and e_{jj} at any spreading pressure (Equation 3.27).

To stay consistent with the original SPD model, the correction parameters α_{ij} and α_{ji} must be equivalent. However, to fit within the GPAST system, there must be exactly two adjustable parameters per binary pair. In order to satisfy these two conditions, a simple mixing rule is adopted in which the lateral interaction potentials, through the new correction parameters, depend on the mole fractions (x_i) of the adsorbed molecules relative to the other adsorbing molecule for that particular binary pair as shown in Equation 3.28 and Equation 3.29 below.

$$\alpha_{ji} = \left(\eta_{ij} - \eta_{ji}\right)\left(\frac{x_j}{x_i + x_j}\right) + \eta_{ji} \qquad \textbf{Equation 3.28}$$

$$\alpha_{ij} = \left(\eta_{ji} - \eta_{ij}\right)\left(\frac{x_i}{x_i + x_j}\right) + \eta_{ij} \qquad \textbf{Equation 3.29}$$

From this relationship, it can be shown that $\alpha_{ij} = \alpha_{ji}$ for any values of x_i and x_j and is therefore consistent with the original SPD model and contains two adjustable parameters (η_{ij} and η_{ji}) per binary pair.

The Modified SPD (MSPD) model replaces Equation 3.14 from the original SPD model with Equation 3.26 through Equation 3.29 outlined above. These modifications still maintain the overall significance and behavior of the original SPD model, but allow it to fit within the GPAST system by having exactly two adjustable parameters. Additionally, much like the original SPD model, the MSPD model maintains the three criteria shown in Equation 3.7 through Equation 3.9 above, making it a thermodynamically consistent model. When the MSPD model is combined with the

GPAST system and the original six equations from AST (Equation 3.1 through Equation 3.6), a closed system of equations can be developed in which one can predict the non-idealities and adsorbed amounts of an *N*-component system under various conditions of pressure and temperature.

3.2.3 Single-species Isotherm Considerations

The final step to consider before solving the resulting system of equations is the form of the pure component isotherm model that appears in Equation 3.6 of the AST system. This model can technically take any form, so long as the pure adsorbed amount (q_i^o) can be expressed as an explicit function of the pure gas partial pressure (p_i^o). However, there are a few thermodynamic considerations to reflect upon prior to choosing a particular isotherm model.

One major criterion for the isotherm model is that it must obey Henry's law at low pressure. This is required not only by the GPAST system (Equation 3.15 and Equation 3.16), but is also necessary for the evaluation of the spreading pressure in AST (Equation 3.1). The most common isotherm model that obeys this behavior is the Langmuir isotherm (Equation 3.30). However, this model is somewhat limited in its ability to describe a wide variety of pure gas adsorption data and is theoretically only applicable to homogenous adsorbent surfaces. For the GPAST system, a more general isotherm model that can be applicable to homogeneous and heterogeneous surfaces may be more desirable.

$$q_i^o = q_{\max,i} \frac{K_i p_i^o}{1 + K_i p_i^o} \qquad \textbf{Equation 3.30}$$

Recall from CHAPTER 2, we discussed the Generalized Statistical Thermodynamic Adsorption (GSTA) isotherm model developed by Llano-Restrepo and Mosquera (Equation 3.31 and Equation 3.32).[16] This model considered the adsorbed phase to be an ensemble of subsystems that are all energetically distinct from each other (i.e., surface sites of various energy characteristics), and had a unique relationship to the Heterogeneous Langmuir model (Section 2.2.1).[17] Because of the generality and flexibility that this isotherm demonstrated in the previous chapter, we want to utilize this model within our GPAST framework.

$$q_i^o = \frac{q_{\max,i}}{m_i} \frac{\sum_{n=1}^{m_i} n K_{n,i}^o \left(p_i^o / P^o\right)^n}{1 + \sum_{n=1}^{m_i} K_{n,i}^o \left(p_i^o / P^o\right)^n} \qquad \textbf{Equation 3.31}$$

$$\ln K_{n,i}^o = -\frac{\Delta H_{n,i}^o}{RT} + \frac{\Delta S_{n,i}^o}{R} \qquad \textbf{Equation 3.32}$$

Another advantage of using this isotherm model is that it can account for both surface homogeneity, as well as heterogeneity, depending on the surface characteristics of the particular adsorbent. Under the condition that there is only one type of adsorption site (m_i = 1), this model reverts down to the standard Langmuir model. Additionally, since this model has many adjustable equilibrium parameters, it has the potential to describe a wide variety of different pure species isotherms. Llano-Restrepo and Mosquera[16] have also derived an expression for the isosteric heat of adsorption (Equation

3.33) as a function of the loading ($\varphi_i = q_i^o / q_{\max,i}$) of the adsorbent, which is needed for determining the interaction potentials (e_{ii}) of the MSPD model (Equation 3.13).

$$Q_i^{st} = \frac{\sum_{n=1}^{m_i} (m_i\varphi_i - n) K_{n,i}^o \left(p_i^o / P^o\right)^n \left(-\Delta H_{n,i}^o\right)}{\sum_{n=1}^{m_i} (m_i\varphi_i - n) n K_{n,i}^o \left(p_i^o / P^o\right)^n} \qquad \textbf{Equation 3.33}$$

3.2.4 GPAST Model Application

The culmination of the GPAST system together with the MSPD activity model and GSTA isotherm creates a fully closed, solvable, non-linear system of equations for which one can predict the non-ideal adsorption behavior of a mixed gas system containing any number of adsorbable components. However, this system has become significantly more involved than AST and will require a comprehensive software code to handle these added complexities. The code developed here preforms a series of stepwise actions to setup the system and solve for either the adsorbed phase or gas phase composition of the mixed system depending on what information it is initially supplied with. This software is referred to as the Multicomponent Adsorption Generalized Procedure for Isothermal Equilibria or MAGPIE for short.

Prior to the development and execution of MAGPIE, the GPAST system can be simplified by forming an analytical solution to the evaluation of the spreading pressure in Equation 3.1. To quantify this integral requires use of the isotherm expression, which in this case is the GSTA model (Equation 3.31). The analytical solution to this integral can be obtained by use of a simple substitution technique, which results in the expression

below in Equation 3.34. Additionally, the values of the Henry's law constant (He_i) for the GSTA isotherm can be formulated as in Equation 3.35, such that these limits do not need to be estimated numerically in the software routines.

$$\Pi = \frac{q_{\max,i}}{m_i} \ln\left(1 + \sum_{n=1}^{m_i} K_{n,i}^{o} \left(p_i^o / P^o\right)^n\right) \qquad \textbf{Equation 3.34}$$

$$He_i = \frac{q_{\max,i} K_{1,i}^{o}}{m_i P^o} \qquad \textbf{Equation 3.35}$$

Before MAGPIE can evaluate the GPAST system of equations, each infinite dilution activity for each unique binary pair of species in the overall system must be determined by using Equation 3.16. This is accomplished by recognizing that the spreading pressure of the system, under infinite dilution conditions, is only being contributed to by the component whose adsorbed mole fraction is unity (x_j = 1). In addition, from Equation 3.7, the activity of that component must also be unity (γ_j = 1). Therefore, from Equation 3.2, the reference state pressure for that component (p_j^o) is exactly equal to the partial pressure of that component in the gas phase ($P_T y_i$).

Using that reference state pressure for the j^{th} component, MAGPIE can solve directly for the spreading pressure at infinite dilution (π_j) using Equation 3.34 and the reference amount adsorbed (q_j^o) with Equation 3.31. Then, because the spreading pressure of the system must be equivalent for all species in the mixture, MAGPIE solves for the reference state pressure of the i^{th} component at the j^{th} spreading pressure, $p_i^o(\pi_j)$, using Equation 3.34. However, the solution at this particular step requires a non-linear, iterative technique because the variables are not separable.

After these steps are completed, MAGPIE can directly calculate the infinite dilution activities of the system for each binary pair. That information is stored and used in the GPAST system of equations to determine the interaction parameters (η_{ij} and η_{ji}) of the MSPD model in a similar fashion to the GPAST example shown in Equation 3.17 through Equation 3.22. However, for this particular application, the τ_{ij} and τ_{ji} parameters from Equation 3.17 through Equation 3.22 would be replaced with their actual expressions in the MSPD model, such that the parameters being solved for in this system are the interaction parameters (η_{ij} and η_{ji}).

After the interaction parameters (η_{ij} and η_{ji}) of MSPD have been calculated and stored, they can then be used to solve the AST system (Equation 3.1 through Equation 3.6) without neglecting the activity coefficients. Again, this step requires a non-linear, iterative technique. The solution to this final system of equations will yield the predicted adsorbed amounts for each adsorbable species as well as the total amount being adsorbed. Evaluation of the gradient of activity to spreading pressure in Equation 3.3 is carried out numerically using a centered difference approach for second order accuracy (Equation 3.36). An analytical solution to this derivative cannot be formed because the activity is an implicit function of spreading pressure in the MSPD model.

$$\frac{\partial \ln \gamma_i}{\partial \Pi} = \frac{\ln \gamma_i(\Pi + \Delta\Pi) - \ln \gamma_i(\Pi - \Delta\Pi)}{2\Delta\Pi} + O(\Delta\Pi^2) \qquad \textbf{Equation 3.36}$$

Many of the steps involved in solving this system require the use of a non-linear solver. To accommodate this need, MAGPIE makes use of a small, standalone C library called *lmfit*[18], which is used to solve non-linear systems of equations using a Levenberg-

Marquardt algorithm. This library has demonstrated respectable convergence over a variety of test cases and is used throughout MAGPIE for all non-linear systems.

3.2.5 MAGPIE Special Case

Because the MAGPIE application is the culmination of the GPAST system with the GSTA isotherm and MSPD activity model, there is a special circumstance under which this application will revert down to the extended Langmuir model for multicomponent adsorption. To demonstrate this, consider a binary gas system composed of molecules A and B, with the pure gas isotherms of both species being described by the GSTA model. In addition, if isotherms are homogenous in form (i.e., $m_A = 1$ and $m_B = 1$), then the GSTA model itself reverts to the standard Langmuir model for both species (Equation 3.37 and Equation 3.38).

$$q_A^o = \frac{q_{\max,A} K_{1,A}^o \left(p_A^o / P^o\right)}{1 + K_{1,A}^o \left(p_A^o / P^o\right)} \qquad \textbf{Equation 3.37}$$

$$q_B^o = \frac{q_{\max,B} K_{1,B}^o \left(p_B^o / P^o\right)}{1 + K_{1,B}^o \left(p_B^o / P^o\right)} \qquad \textbf{Equation 3.38}$$

By considering the equation for isosteric heat of adsorption (Equation 3.33) derived for the GSTA isotherm, it can be shown that, under the homogeneous case, this energy term is equivalent to the enthalpy[16] (Equation 3.39). Therefore, for molecules A and B, the isosteric heat (Q_i^{st}) would not be changing with the spreading pressure. That being the case, the lateral interaction parameters (e_{AB}, e_{AA}, and e_{BB}) from MSPD will all be zero, which in turn causes all the Boltzmann weighting factors (τ_{AB} and τ_{BA}) to become

one. If all of these weighting factors are always one, then the activity for each adsorbing species will always be unity ($\gamma_A = 1$ and $\gamma_B = 1$).

$$Q_i^{st}\Big|_{m_i=1} = (-\Delta H_{1,i}^o) \qquad \textbf{Equation 3.39}$$

Under these exact circumstances, the GPAST system will revert down to IAST. In addition, since the GSTA isotherm for molecules A and B both take the form of the Langmuir equation, the IAST system of equations can then be solved analytically, instead of numerically. The solution to IAST when all isotherms obey the Langmuir model results in the standard extended Langmuir model (Equation 3.40).[4] This conclusion could also be obtained qualitatively by reasoning that the primary assumption behind the extended Langmuir model is that the different adsorbate molecules do not interact with each other, [4] which was determined in the MSPD model for this case by having all the lateral interaction potentials (e_{ij}) equal to zero.

$$q_i = \frac{q_{\max,i} K_{1,i}^o \left(p_i / P^o\right)}{1 + \sum_{j=1}^{N} K_{1,j}^o \left(p_j / P^o\right)} \qquad \textbf{Equation 3.40}$$

3.3 Results and Discussion

3.3.1 Comparison with IAST

To quantify the predictive capabilities of MAGPIE requires use of actual multicomponent adsorption data, either obtained experimentally or found in literature.

Two sets of adsorption data available in literature will serve as test cases for MAGPIE: (i) Talu and Zwiebel data for binary and ternary mixtures of CO_2, H_2S, and C_3H_8 on an H-mordentite adsorbent[3] and (ii) Ritter and Yang data for various mixtures of CH_4, CO_2, CO, H_2, and H_2S on activated carbon.[19] The results of MAGPIE will then be compared against the results of IAST for the same data sets. It is expected that MAGPIE will show a significant improvement in predictive capabilities over IAST.

In order to eliminate as much bias in the analysis as possible, both MAGPIE and IAST will use the GSTA model for the pure component isotherms. Therefore, the only differences in the system of equations will be the activity model and the GPAST procedure used to adjust that model to the infinite dilution activities. After the GSTA model has been calibrated to each set of single component data, the parameters of that model can be used in the evaluation of both the MAGPIE and IAST system.

The comparison between MAGPIE and IAST will be examined by studying the differences in the distribution of error between each numerical result and the actual data. There are two predicted quantities to be compared from MAGPIE and IAST: (i) the adsorbed mole fractions (x_i) and (ii) the total amount adsorbed (q_T), of which there are 214 and 86 observations, respectively. Because the adsorbed mole fractions are a bounded quantity (Equation 3.4), the errors associated with predicting those values will be determined as an absolute difference (absolute error = predicted – actual). However, the total amount adsorbed is unbounded, so its error will be quantified in terms of a relative difference (relative error = (predicted – actual) / actual), which would be analogous to a percent error in this quantity.

These errors are formulated such that a positive error represents an overestimate, while a negative error reflects an underestimate. This allows us to show how the error is distributed and where any error bias may occur. However, these error distributions would not capture total error since a positive error could be offset by an equal negative error. Therefore, we will also compare the average Euclidean errors (E_{avg}) of both predicted quantities (x_i and q_T) for each method (MAGPIE and IAST) by taking the square root of the sum of the squares of the errors divided by the number of observations made (M).

$$E_{avg} = \frac{1}{M}\sqrt{\sum_{i=1}^{M}(\text{predicted}_i - \text{actual}_i)^2} \qquad \textbf{Equation 3.41}$$

Results for the adsorbed mole fractions can be seen in the histogram on Figure 3.1. The size of each bin in the histogram is 0.05 in absolute error and each bin is named after its median error for that bin (i.e., bin 0.025 ranges from 0 to 0.05 in absolute error). At a glance, it can be seen from this figure that MAGPIE has a relatively standard distribution of error, but IAST appears to have two outer peaks at bins -0.175 and 0.175. These particular error bins are being filled mostly from IAST errors associated with predicting the Talu and Zwiebel data, but cannot be pinpointed to any particular mixture or species.

Additionally both MAGPIE and IAST errors follow roughly a normal-type distribution centered near zero error. However, MAGPIE appears to have a greater number of results occurring closer to zero than IAST. Note that in reality neither MAGPIE nor IAST can have a normal distribution of absolute error for this observation because it is a bounded observation wherein the maximum errors are +/- 1. A real normal

distribution is an unbounded observation, so we are idealizing the error distribution of MAGPIE and IAST as a normal distribution to more easily study the error quantitatively.

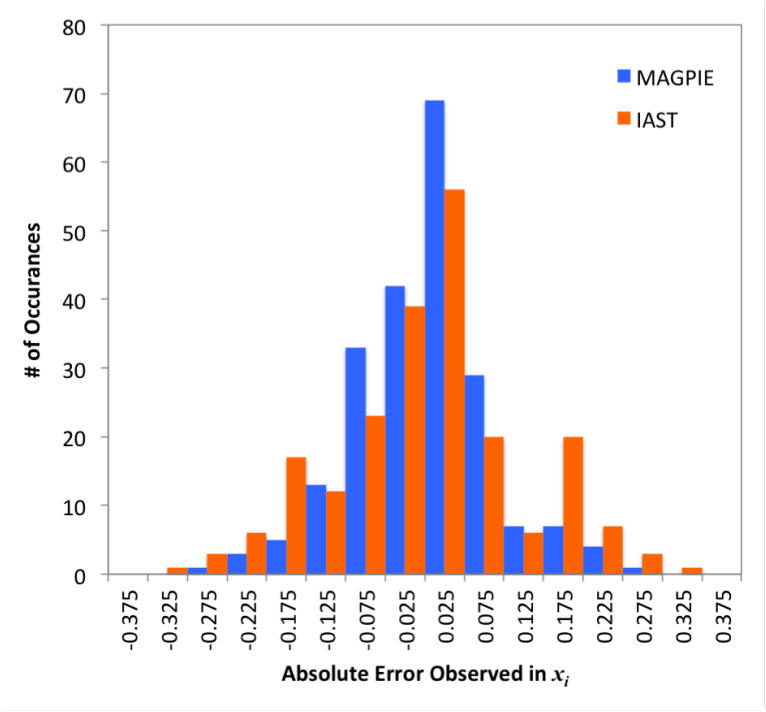

Figure 3.1 - Error distribution histogram for the absolute errors observed in the adsorbed mole fractions predicted from both MAGPIE and IAST.

For the total adsorbed amounts (Figure 3.2), the distribution is much wider spread. Here, the bin sizes are 0.05 in relative error and each bin is again named after its median error. Immediately apparent is what appears to be a large outlying peak for MAGPIE errors in bin 0.125. Nearly all (8 out of 11) of these error observations come from a single mixture in the Talu and Zwiebel data set: CO_2 and H_2S on H-mordenite. Both CO_2 and H_2S show very high affinity towards H-mordenite, from their single

component isotherms, and are highly polar molecules[3], which may contribute to the overestimations in the adsorption capacities for this mixture.

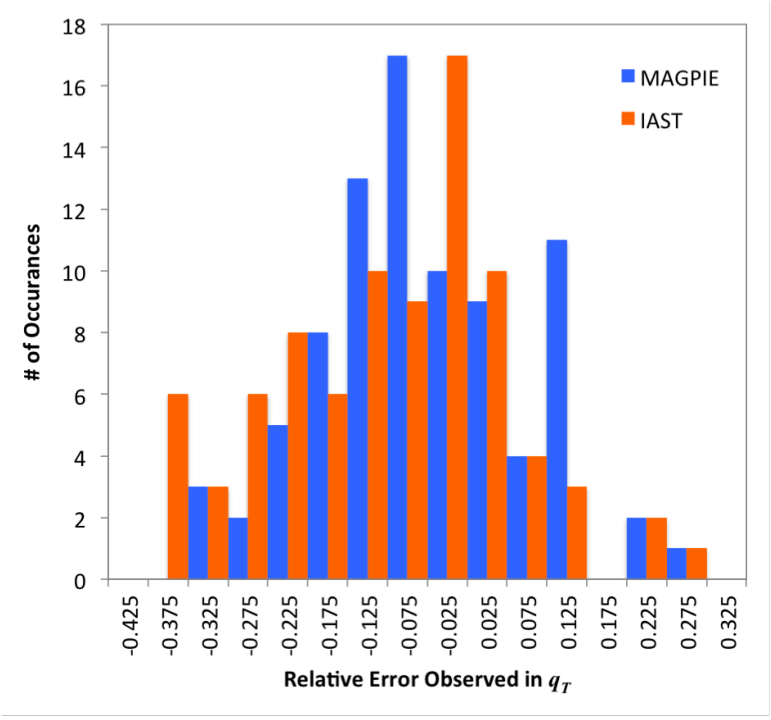

Figure 3.2 - Error distribution histogram for the relative errors observed in the adsorbed totals predicted from both MAGPIE and IAST.

Looking at Figure 3.2 it is difficult to determine precisely which methodology has produced better results. Unlike the fairly standard distributions of error observed from Figure 3.1, Figure 3.2 appears to be more irregular in shape with little peaks and valleys moving from left to right, especially for IAST. However, overall the general trends observed do create the bell shaped curve we expect to see for distributions of random variables. To precisely determine which method has resulted in a better distribution of

error, a more quantitative analysis will be necessary, but it can at least be seen from this figure that both MAGPIE and IAST show a slight negative bias in the errors. This means that both methods, on average, have predicted adsorbed amounts lower than the actual measured data.

In order to compare the performance between MAGPIE and IAST, a statistical analysis is performed on the error distributions from Figure 3.1 and Figure 3.2. For this analysis, we will idealize these actual error distributions as normal distributions and quantify properties such as average values and standard deviations, which can be used to plot probability density functions associated with each error histogram. Each histogram is first normalized using the observations of each bin and the total number of observations such that the total area underneath each corresponding probability density function will be 1. Then, from those normalized curves, we approximated the average values and standard deviations of each distribution of observations.

Table 3.1 summarizes the results of this analysis. For the errors in adsorbed mole fractions, MAGPIE showed no improvement in the average error bias. However, both MAGPIE and IAST had almost no error bias in this quantity, which is primarily attributed to the bounding of the mole fractions (Equation 3.4). Due to this bounding, any negative error in adsorbed amount x_j would be offset by an equal positive error in x_i, such that the sum of all mole fractions equals one. As such, there is not expected to be any error bias in this average quantity to begin with.

Table 3.1 - Summary of the Statistical Analysis of the Error

	MAGPIE	IAST	*Improvement (%)*
Absolute Error of Mole Fractions			
Average	0.001	0.001	0.00
Standard Deviation	0.062	0.097	-36.14
E_{avg} (Equation 3.41)	5.76E-3	7.98E-3	-27.87
Relative Error of Adsorbed Totals			
Average	-0.048	-0.092	-48.43
Standard Deviation	0.114	0.139	-17.72
E_{avg} (Equation 3.41)	0.050	0.053	-5.26

In all other regards, Table 3.1 demonstrations that MAGPIE results show dramatic improvement over IAST. There was a 36% reduction in the standard deviation of the absolute error in the adsorbed mole fractions, meaning that the MAGPIE predictions of this quantity are grouped more closely around the actual data than IAST results. Additionally, MAGPIE shows a near 28% reduction in the average Euclidean error of the mole fractions, which indicates that the magnitude of the errors observed from MAGPIE were on average 28% smaller than those observed for IAST.

For the adsorbed totals, both IAST and MAGPIE still showed a tendency to underestimate adsorption, as indicated by the negative values for average error, but MAGPIE showed a resounding 48% reduction in that negative error basis. This means that, on average, MAGPIE results were significantly closer to the real adsorption totals compared to the IAST results. However, the standard deviations of these errors were relatively similar, 0.114 for MAGPIE compared to 0.139 for IAST, which resulted in the average Euclidean errors being very similar, 0.050 for MAGPIE compared to 0.053 for IAST. In both cases, MAGPIE did yield better results, but the gains were marginal,

roughly 18% improvement in standard deviations and only a 5% improvement in average Euclidean error.

To visualize this information, the average and standard deviations from Table 3.1 are used to plot probability density functions for each distribution of error in Figure 3.3 and Figure 3.4. These plots show the dramatic difference in the idealized error distributions between MAGPIE and IAST. In both figures, MAGPIE error is grouped more tightly around the average as a result of the reduction in the standard deviation for both distributions. For Figure 3.4, MAGPIE also shows a shift in the average error towards zero error, which demonstrates a reduction in the negative bias of the adsorbed totals found in IAST.

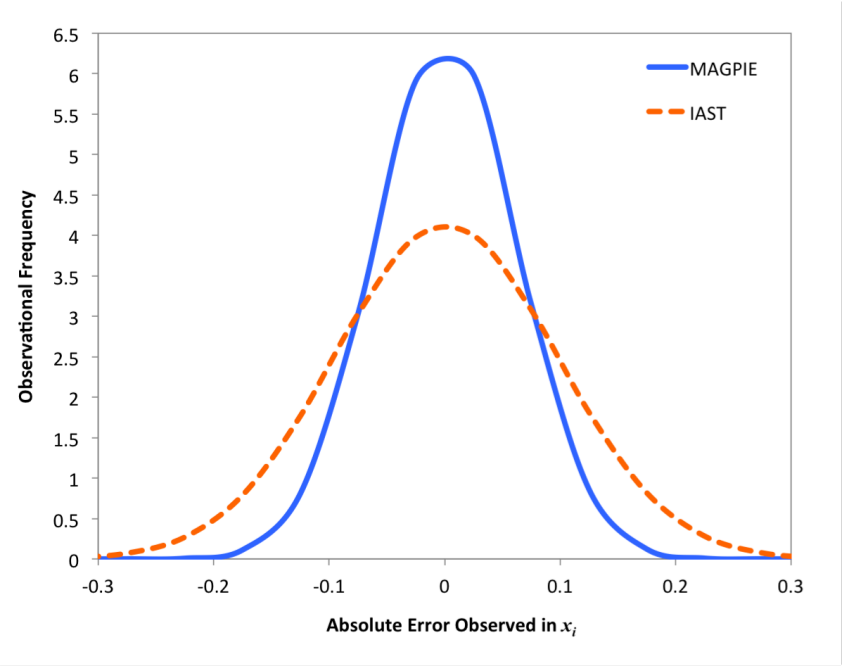

Figure 3.3 - Idealized normal probability density functions for the absolute error in the adsorbed mole fractions generated from the averages and standard deviations of Table 3.1 that were based on the statistical analysis of the error histograms from Figure 3.1.

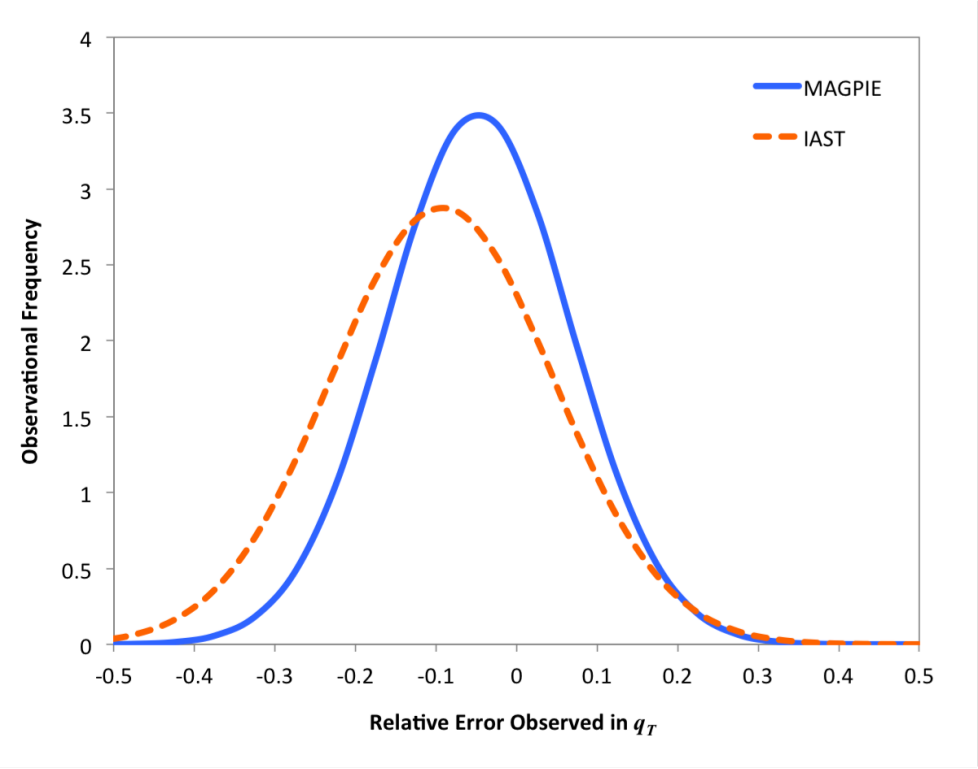

Figure 3.4 - Idealized normal probability density functions for the relative error in the adsorbed totals generated from the averages and standard deviations of Table 3.1 that were based on the statistical analysis of the error histograms from Figure 3.2.

3.3.2 Comparison with Literature Data

The actual MAGPIE results and literature data are plotted in Figure 3.5 and Figure 3.6 for the adsorbed mole fractions and in Figure 3.7 and Figure 3.8 for the adsorption totals. In these plots, the solid lines represent the equivalence line at which the result from the MAGPIE simulation (y-axis) is exactly equal to the measured value recorded in literature (x-axis). The dashed lines show the boundaries, determined by the statistical analysis, in which 95% of all points lay between (i.e., +/- twice the standard deviations). Note that the dashed lines for Figure 3.5 and Figure 3.6 are parallel while the dashed lines

fan outwards for Figure 3.7 and Figure 3.8. This is because the error distribution analyzed for the adsorbed mole fractions was done in terms of an absolute error (Figure 3.1), but the error distribution for adsorption totals was performed on the relative error (Figure 3.2).

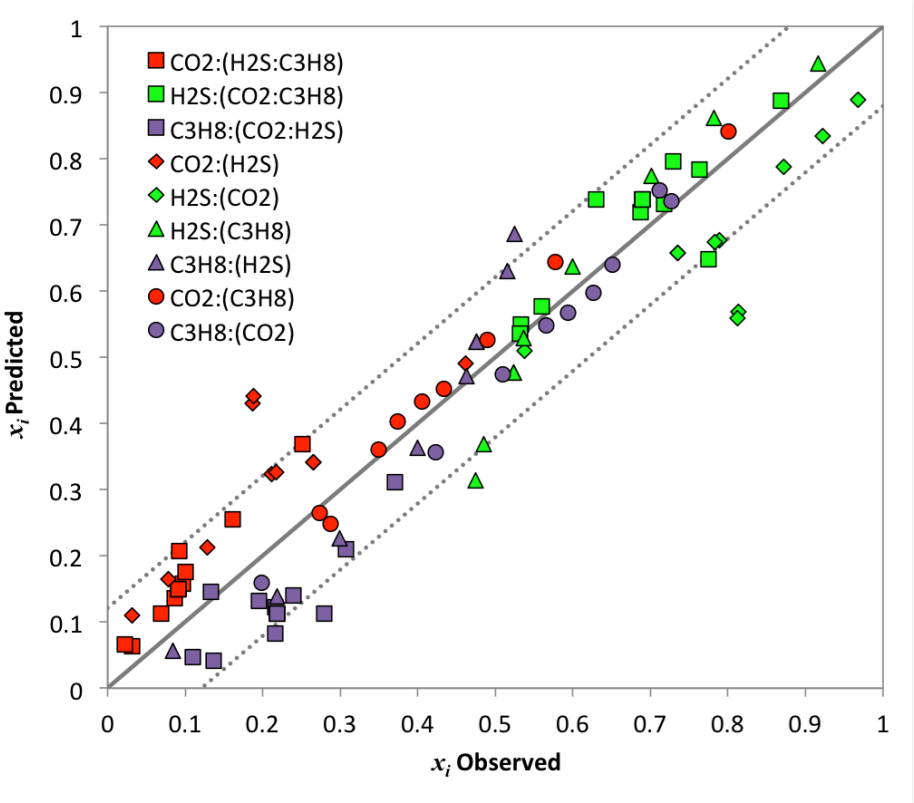

Figure 3.5 - MAGPIE results versus the Talu and Zwiebel[3] reported adsorbed mole fractions. Solid line represents the equivalence line between model and data, while the dashed lines show the 95% confidence intervals based on the statistical analysis. The different mixtures each has its own symbol and is labeled by which species is being observed, followed by the other species involved in the mixture in parentheses. Different colors are also used to denote which species is being observed (i.e. red = CO_2, green = H_2S, and purple = C_3H_8).

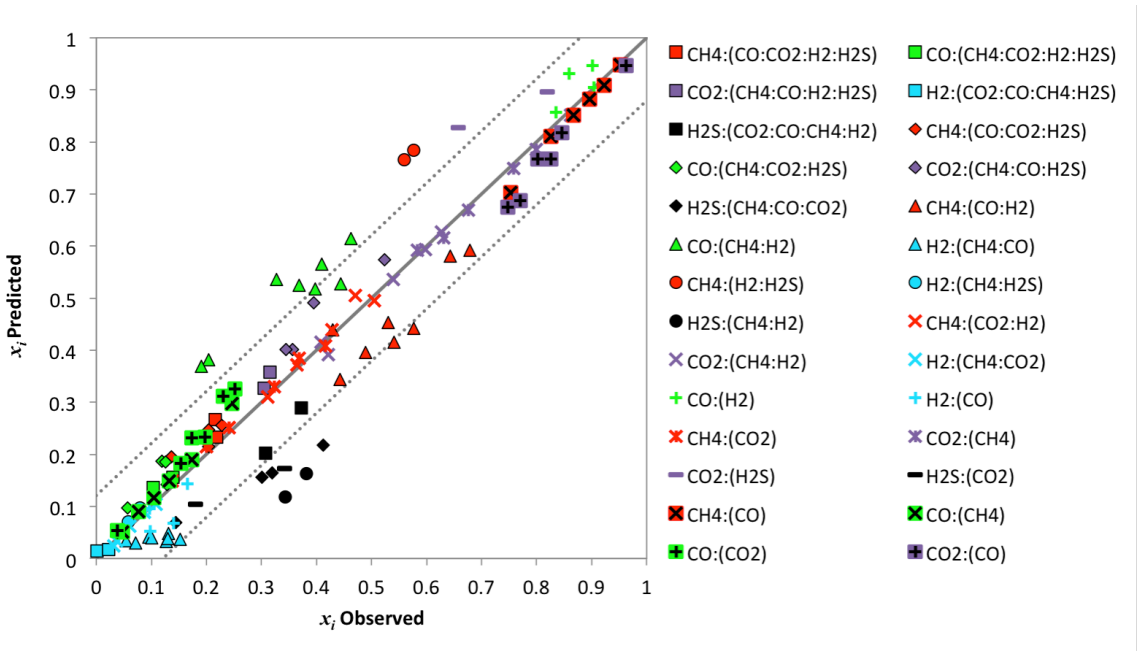

Figure 3.6 - MAGPIE results versus the Ritter and Yang[19] reported adsorbed mole fractions. Solid line represents the equivalence line between model and data, while the dashed lines show the 95% confidence intervals based on the statistical analysis. The different mixtures each has its own symbol and is labeled by which species is being observed, followed by the other species involved in the mixture in parentheses. Different colors are also used to denote which species is being observed (i.e. red = CH_4, green = CO, purple = CO_2, blue = H_2, and black = H_2S).

The results shown in Figure 3.5 and Figure 3.6 generally show very good agreement with the observations made by Talu and Zwiebel[3] and Ritter and Yang[19]. However, there are some notable outliers in both sets of results. For instance, in Figure 3.5 it can be seen that MAGPIE has consistently over estimated the CO_2 adsorbed mole fractions (red diamonds) and under estimated the H_2S mole fractions (green diamonds) for the binary mixtures. This may be caused by the highly polar nature of these two species, which is a factor that the activity model does not take into account. Also in Figure 3.5, for the ternary mixtures of CO_2, H_2S, and C_3H_8, the mole fractions of H_2S (green squares) are very close to the equivalent line, while CO_2 (red squares) is

consistently over estimated and C_3H_8 (purple squares) consistently under estimated. This is most likely a result of the relative adsorption strengths of CO_2 and C_3H_8. CO_2 has a much higher affinity to adsorb to the H-mordenite than the C_3H_8[3] and therefore would be expected to show a larger mole fraction than C_3H_8 in the adsorbed phase.

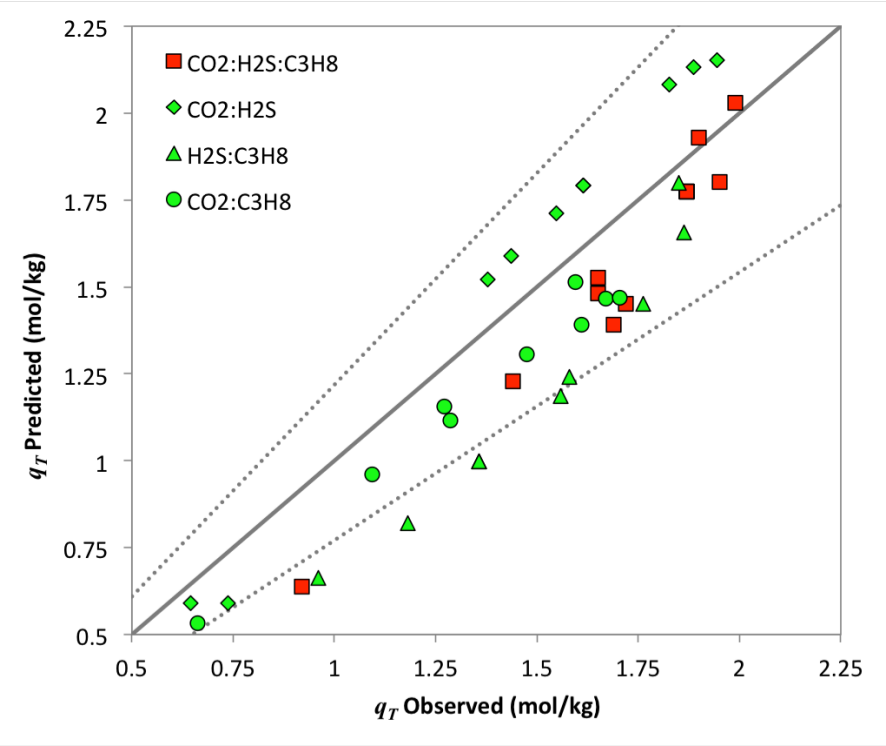

Figure 3.7 - MAGPIE results versus the Talu and Zwiebel[3] reported adsorbed totals. Solid line represents the equivalence line between model and data, while the dashed lines show the 95% confidence intervals based on the statistical analysis. Each symbol denotes a different mixture and those same symbols correspond to the mixtures in Figure 5. Colors identify whether the mixture is binary, ternary, etc. (i.e. red = ternary and green = binary).

Figure 3.6 showed fewer outliers than Figure 3.5, but still had some points and species that were consistently outside of the expected values. Most notable of those species was H_2S (all black shapes), whose mole fractions were under estimated by

MAGPIE for nearly all mixtures and experiments. It is unclear as to why this is compared to what was seen in Figure 3.5, because the mixtures for the Ritter and Yang[19] data are much more varied. However, many of those mixtures do involve other polar components (CO and CO_2), which themselves are usually being over estimated (green triangles and purple dashes). Based on the consistency of these observations, an improvement to MAGPIE could be made by including factors for polarization of species in the activity model.

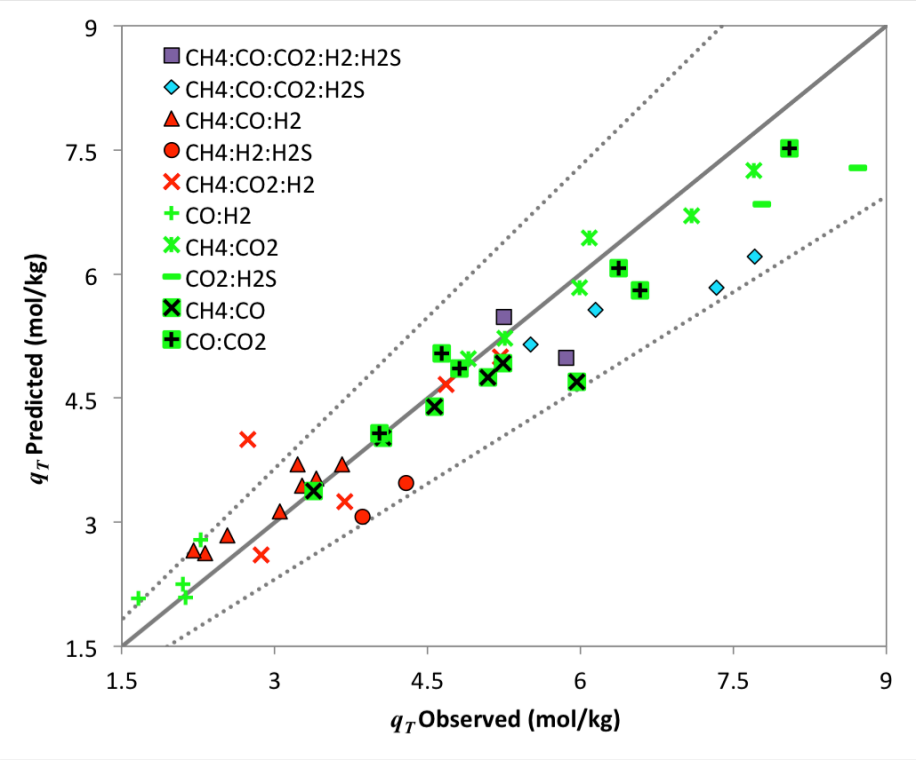

Figure 3.8 - MAGPIE results versus the Ritter and Yang[19] reported adsorbed totals. Solid line represents the equivalence line between model and data, while the dashed lines show the 95% confidence intervals based on the statistical analysis. Each symbol denotes a different mixture and those same symbols correspond to the mixtures in Figure 6. Colors identify whether the mixture is binary, ternary, etc. (i.e. purple = quinary, blue = quaternary, red = ternary, and green = binary).

Figure 3.7 and Figure 3.8 also generally show good agreement with the adsorption totals observed from the Talu and Zwiebel[3] and Ritter and Yang[19] data sets. However, both sets of results show a negative bias, or a tendency for MAGPIE to under estimate the adsorption. This observation is especially true in the case of the Talu and Zwiebel[3] data set (Figure 3.7), which shows a negative bias for all mixtures except the CO_2 and H_2S mixtures. For that particular mixture, MAGPIE consistently over estimates the adsorption capacities by roughly 10%. This is the same mixture that caused the over and under estimations in the adsorbed mole fractions of Figure 3.5 so it is likely that these over estimations could also be attributed to the polarity of CO_2 and H_2S. The other mixtures from Figure 3.7 show a negative bias, which could be attributed to the low affinity of adsorption for C_3H_8 on H-mordenite[3], since all other mixtures involve this species.

The adsorption capacity results in Figure 3.8 for the Ritter and Yang[19] data show much better agreement than the results for the Talu and Zwiebel[3] data. In fact, MAGPIE shows almost no negative bias for these data sets as the majority of results are spread nearly equally around the equivalence line. The exceptions would be the quaternary mixture (blue diamonds) and the CO_2 and H_2S binary mixture (green dashes), which both show a consistent negative bias in the results. Each of these mixtures also contain all, or a majority, of polar species in the adsorbed phase.

3.4 Conclusions

The results from the above analysis indicate that MAGPIE has demonstrated a significant improvement in predictive capabilities over IAST for the data sample given.

However, it is important to note that MAGPIE is only a single application of GPAST and these results may have been different if another isotherm or activity model were used in place of the GSTA and MSPD models. Recall that GPAST itself only requires that the isotherm abides by Henry's law (Equation 3.15) and that the activity model obey a set of thermodynamic criteria (Equation 3.7 through Equation 3.9) while containing two adjustable parameters per binary pair, which are to be determined by the GPAST procedure. This means that it is possible to use any other isotherm or activity model that is found to be applicable, making GPAST a very generalized and flexible technique. It is this tremendous flexibility that makes GPAST such a powerful analytical tool for multicomponent adsorption equilibria.

Additionally, unlike its predecessor PRAST, GPAST is not limited to analyzing only binary adsorption systems. As was demonstrated with the Talu and Zwiebel[3] and Ritter and Yang[19] literature data, GPAST can be used to model and predict binary, ternary, quaternary, quinary, and larger adsorption systems. The generalization of the PRAST to GPAST is carried out in a combinatorial and serial fashion, such that it can apply to any number of adsorbable components in a mixture, thus further adding to the flexibility of GPAST.

Another advantage of GPAST is that this procedure does not require any calibration with binary adsorption data. It is a fully predictive model in which solutions to the adsorbed phase are determined by using only the adsorption behavior of each individual species in the mixture. The predictions being made are also fully reversible since the system of equations is deterministic. Therefore, when given a specific gas phase

composition A, the adsorbed phase solution will be B, and if given a specific adsorbed phase composition B, the gas phase solution will be A.

Due to the apparent flexibility of GPAST, it would be very simple to further extend upon this procedure to produce new applications simply by adding, removing, or changing the isotherm and activity models. MAGPIE was only one example of an application built on the GPAST procedure. With dozens of different isotherm and activity models available in literature, there are potentially hundreds of different applications of GPAST that could be developed and utilized for predicting thousands of different adsorption systems.

3.5 Acknowledgement

The development of this chapter was a collaborative effort between my co-authors and myself and was the main subject of the following publication: A. Ladshaw, S. Yiacoumi, C. Tsouris, "A Generalized Procedure for the Prediction of Multicomponent Adsorption Equilibria," *AIChE J.* 61 (**2015**) 2600-2610.

3.6 References

[1] A.L. Myers, J.M. Prausnitz, *AIChE J.* 34 (**1965**) 121-127.

[2] O. Talu, A.L. Myers, *AIChE J.* 34 (**1988**) 1887-1893.

[3] O. Talu, I. Zwiebel, *AIChE J.* 32 (**1986**) 1263-1276.

[4] C. Tien, *Adsorption Calculations and Modeling*, Butterworth-Heinemann, Newton, MA, 1994.

[5] A.L. Myers, *AIChE J.* 29 (**1983**) 691-693.

[6] T.W. Cochran, R.L. Kabel, R.P. Danner, *AIChE J.* 31 (**1985**) 268-277.

[7] E. Costa, J.L. Sotelo, G. Calleja, C. Marron, *AIChE J.* 27 (**1981**) 5-12.

[8] D.S. Abrams, J.M. Prausnitz, *AIChE J.* 21 (**1975**) 116-128.

[9] G. Maurer, J.M. Prausnitz, *Fluid Phase Equilibria*, 2 (**1978**) 91-99.

[10] A. Fredenslund, R.L. Jones, J.M. Prausnitz, *AIChE J.* 21 (**1975**) 1086-1099.

[11] M. Sakuth, J. Meyer, J. Gmehling, *Chemical Engineering and Processing*, 37 (**1998**) 267-277.

[12] D. Tondeur, F. Yu, K. Bonnot, L. Luo, *J. of Colloid and Interface Sci.* 293 (**2006**) 342-352.

[13] A. Bondi, *Journal of Physical Chemistry*, 68 (**1964**) 441-451.

[14] J.H. Vera, S.G. Sayegh, G.A. Ratcliff, *Fluid Phase Equilibria*, 1 (**1977**) 113-135.

[15] H. Markowitz, *Annals of Financial Economics*, 7 (**2012**) 1-30.

[16] M. Llano-Restrepo, M.A. Mosquera, *Fluid Phase Equilibria*, 283 (**2009**) 73-88.

[17] A. Ladshaw, S. Yiacoumi, C. Tsouris, D. DePaoli, *Fluid Phase Equilibria*, 338 (**2015**) 169-181.

[18] J. Wuttke, Version <lmfit-3.4>, <http://joachimwuttke.de/lmfit>, Accessed January 21, 2013.

[19] J.A. Ritter, R.T. Yang, *Ind. Eng. Chem. Res.* 26 (**1987**) 1679-1686.

3.7 Nomenclature

Latin Symbols

A	specific surface area of adsorbent (m^2/kg)
C	shift factor in the geometric mean
e	lateral interaction potential (J/mol)
E_{avg}	average Euclidean errors of predictions
$f(x)$	variable f as a function of variable x
g	geometric mean of a sample

G sample size for the geometric mean

He Henry's law constant (mol/kg/kPa)

K equilibrium constant (1/kPa)

K^o dimensionless equilibrium constant

m number of energetically distinct adsorption sites in GSTA

M number of observations or data points

N number of adsorbable species in a mixture

O mathematical error term or truncation error

p partial or reference state pressure (kPa)

P total or standard state pressure (kPa)

q adsorbed amount (mol/kg)

Q^{st} isosteric heat of adsorption (J/mol)

R ideal gas law constant (J/K/mol)

r return on investment

s molecular shape factor

T temperature of the system (K)

v van der Waals volume of a molecule (cm^3/mol)

x adsorbed mole fraction

y gas phase mole fraction

z coordination number of adsorbed phase lattice

Greek Symbols

α lateral interaction potential correction parameter of MSPD

β geometric mean correction parameter of SPD

γ activity coefficient of the adsorbed phase

ΔH	enthalpy of adsorption (J/mol)
ΔS	entropy of adsorption (J/K/mol)
η	binary interaction parameter of MSPD
θ	external contact fraction of molecules in adsorbed phase
μ	maximum lateral interaction potential (J/mol)
Π	lumped spreading pressure term (mol/kg)
π	spreading pressure of adsorbed phase (J/m^2)
τ	Boltzmann weighting factor
φ	fractional adsorption loading

Abbreviations

AST	Adsorbed Solution Theory
GPAST	Generalized Predictive Adsorbed Solution Theory
GSTA	Generalized Statistical Thermodynamic Adsorption
IAST	Ideal Adsorbed Solution Theory
MAGPIE	Multicomponent Adsorption Generalized Procedure for Isothermal Equilibria
MSPD	Modified Spreading Pressure Dependent
PRAST	Predictive Real Adsorbed Solution Theory
SPD	Spreading Pressure Dependent

Sub/superscripts

∞	infinite dilution
i,j,k	indices for adsorbable species
max	maximum adsorption capacity

n index of adsorption site

o standard or reference state

T total amount of some value

t index of investment returns

CHAPTER 4. DIFFUSION AND TRANSPORT MODELING

4.1 Introduction

In environmental and chemical engineering applications of adsorption, the majority of the physicochemical processes studied are governed by a conservation law.[1,2] Adsorption modeling typically involves the coupling of mass and energy balances of some material over a given domain. For example, if micro-porous diffusion of adsorbates into an adsorbent particle were to be investigated, the physical process would be described via a mass balance in a spherical coordinate system as in Equation 4.1:[1]

$$r^2\varepsilon\frac{\partial C}{\partial t}=\frac{\partial}{\partial r}\left[r^2 D\varepsilon\frac{\partial C}{\partial r}\right] \qquad \textbf{Equation 4.1}$$

In this system, the concentration of the adsorbate (C) is the conserved quantity, and the micro-pore diffusivity (D) and micro-porosity of the material (ε) are parameters of the model that describe how material moves through the radial space (r) of the particle in time (t).

Alternatively, if one were interested in observing the axial temperature profile of a gas stream through a column, then the mathematical description of that process would be an energy balance in Cartesian coordinates as in Equation 4.2:

$$(h\rho)\frac{\partial T}{\partial t}+\frac{\partial}{\partial z}(h\rho vT)=\frac{\partial}{\partial z}\left(K\frac{\partial T}{\partial z}\right) \qquad \textbf{Equation 4.2}$$

The parameters of this model equation include gas heat capacity (h), gas density (ρ), fluid velocity (v), and thermal conductivity (K) as the physical parameters and z represents the axial coordinate of the domain.

These two equations are mathematically very different, but are formulated from the same governing principles and are very common types of problems that one might encounter in adsorption. To dig deeper into the mathematics, consider the four primary mechanisms of adsorption as depicted in Figure 4.1. These mechanisms are all common to every type of adsorption problem that one may seek to model.

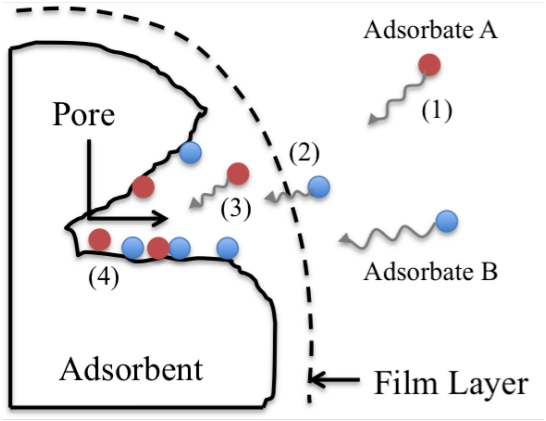

Figure 4.1 - Mechanisms of adsorption: (1) interparticle transport, (2) interphase mass-transfer, (3) intraparticle diffusion, and (4) surface reaction and equilibria. These mechanisms are common to all adsorption problems.

Adsorption, by its nature, is inherently a multi-species and multi-scale process involving (1) interparticle transport, (2) interphase mass transfer, (3) intraparticle diffusion, and (4) surface reactions and equilibria.[1] At the macro-scale, the primary

interest is in interparticle transport, which is how the adsorbates travel between adsorbent particles. This process is governed primarily by advection and molecular diffusion.[1,3] For the micro-scale, adsorption is governed by film mass transfer from bulk solution to the outside of the adsorbent, pore and surface diffusion inside the adsorbent domain, and surface reactions or adsorption equilibria.[4,5] To model these mechanisms requires a mass balance on each adsorbate as it travels between, around, and inside the particles. In other words, the model is required to include multiple mechanisms on multiple scales for multiple species.

This modeling undertaking is comprised of several parts. First, approaching this problem as generally as possible requires the development of a framework under which the majority of adsorption problems can be placed. For this to be accomplished, the model must be capable of describing the process under various geometrical domains, inherently allowing parameters to vary in space and time, and including terms for multiple physical processes that may be present in the system. Then, the model must be discretized into a solvable form using either direct or iterative techniques. Therefore, one must also incorporate linear and non-linear solvers into the framework that can be adapted into the generalized conservation law to solve the resulting system at each time step. The culmination of all these parts will provide a robust adsorption model.

4.2 Modeling Framework

4.2.1 Generalized 1-D Conservation Law

There are several terms that one may need to include in a general conservation law: advection, diffusion, reaction, etc. Each of these terms needs to be flexible enough

so that they can be allowed to vary in space and time. Additionally, there may also be a variety of spatial domains over which the problems exist in space (e.g., spherical, cylindrical, Cartesian). From Equation 4.1 and Equation 4.2, it has been shown that there are cases in which one wants to solve conservation laws in different geometries and may even leave out certain physical terms altogether. Based on these considerations, a Generalized 1-D Conservation Law Model (Equation 4.3) has been formulated in this work.

$$z^d R\frac{\partial u}{\partial t}+\frac{\partial}{\partial z}\left(z^d vu\right)=\frac{\partial}{\partial z}\left(z^d D\frac{\partial u}{\partial z}\right)-z^d ku-z^d S \qquad \textbf{Equation 4.3}$$

In this form of the conservation law, the conserved quantity is denoted by the variable u. This can be any conserved quantity that one wants to observe and will depend on a number of space-time dependent parameters, which all have a different physical interpretation. R is a retardation coefficient, v is an advective velocity, D is for dispersion, k is a reaction coefficient, and S can be some generic source/sink term or other forcing function.

The spatial quantity z, along with its exponent portion d, is used to change the geometry of the physical domain upon which observations of u are made. This is shown by a simple inspection: if d=0 in Equation 4.3 and the reaction and source terms are removed, then the form of the equation is exactly that of Equation 4.2. Likewise, if the advection term is removed and d=2, then the form of the equation now matches that of Equation 4.1. Therefore, one can easily switch between Cartesian, polar, and spherical coordinates just by changing the value of a single argument (d) from 0 to 1 to 2.

Similarly, different physical terms from Equation 4.3 can be neglected or removed simply by setting all space-time values of the corresponding coefficient to zero. For example, if one wanted to solve a steady-state reaction-diffusion problem in a cylindrical geometry, this would be accomplished by setting d=1 and then setting the R, v, and S parameters to all zeros. Solving the resulting system would then show the steady-state profile of u distributed radially in a cylinder. Therefore, by formulating the equations in this manner, one can set up a simple approach to modeling different adsorption processes.

4.2.2 Discretization of the Conservation Law

Since the problem (Equation 4.3) is one-dimensional, it will be easiest to use a finite difference approach to numerically solve the conservation law. In order to handle problems that may be advectively dominated, it is advantageous to use a particular finite difference method known as a Monotonic Upstream-centered Scheme for Conservation Laws (MUSCL). These discretization schemes were first introduced by Bram van Leer[6] in 1979, and have since been the leading approach for these types of problems. A particular MUSCL scheme of interest is the Kurganov and Tadmor (KT) scheme[7] for its high accuracy and applicability for both linear and non-linear conservation laws.

The KT scheme uses the concept of *slope limiting*, or *flux limiting*, to reconstruct the edge fluxes at the boundaries of each cell in the discretized mesh (Figure 4.2 and Equation 4.4). By taking this approach, one can ensure that the quantity u is conserved across the entire domain, as overflow from one cell would feed into the next cell. Additionally, to maintain a high resolution and accuracy, the KT scheme also includes a

correction term for numerical dispersion, which seeks to penalize the discretization based on the local maximum wave speed (Equation 4.5). This allows the scheme to better handle shocks and discontinuities that may be present in the solution.[7]

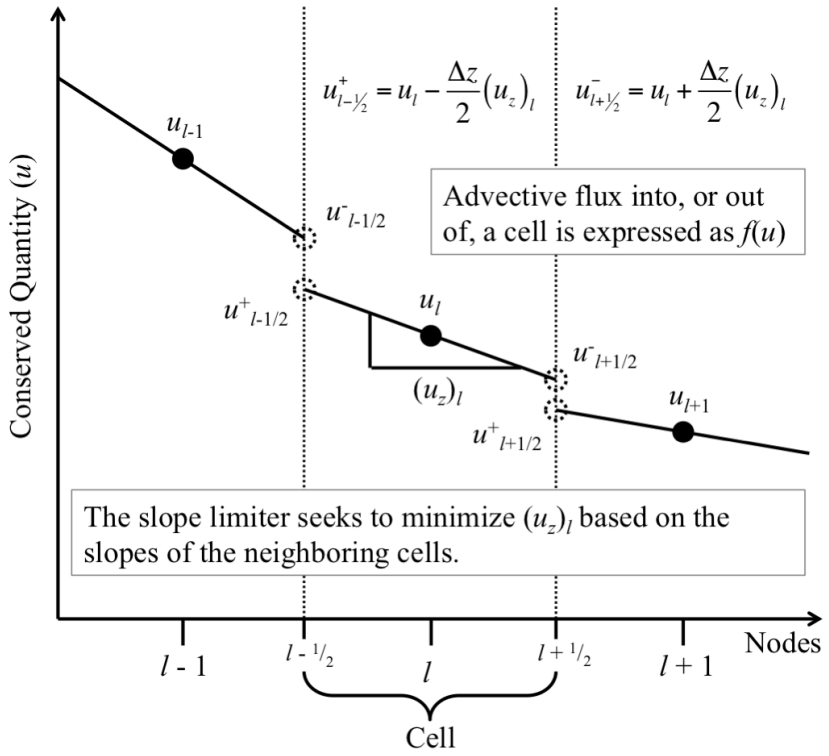

Figure 4.2 - Visualization of the process of flux reconstruction on a 1-D mesh.

$$H_{l+½} = \frac{1}{2}\left[f\left(u^+_{l+½}\right) + f\left(u^-_{l+½}\right)\right] \qquad \textbf{Equation 4.4}$$

$$p_{l+½} = \frac{a_{l+½}}{2}\left[u^+_{l+½} - u^-_{l+½}\right] \qquad \textbf{Equation 4.5}$$

In the above equations, $H_{l+1/2}$ is the average advective flux leaving cell l from the right, $p_{l+1/2}$ is the penalty term applied for the jump discontinuity at the right boundary of the cell, and $f(u)$ is the advective flux term into or out of the cell. Note that u_z in the figures and equations represent the derivative of u with respect to z (du/dz). The magnitude of that penalty is based on the jump, as well as the local maximum wave speed ($a_{l+1/2}$). Using the same procedure for the left side boundary of the cell and then applying a centered finite difference approximation to the derivative of the advective term will produce the overall advective flux discretization shown in Equation 4.6.[7]

$$\frac{\partial}{\partial z} f(u)_l \cong \frac{\left(H_{l+½} - p_{l+½}\right) - \left(H_{l-½} - p_{l-½}\right)}{\Delta z} \qquad \textbf{Equation 4.6}$$

According to Kurganov and Tadmor, the maximum local wave speed is equivalent to the maximum spectral radius of the Jacobian of $f(u)$ over all u within the discretized sub-domain.[7] In general, this may be difficult to estimate, especially if $f(u)$ is complex. Therefore, a simpler approximation to this term is provided within this framework. For the application considered here, the advective term is always of the form $f(u) = z^d v u$. From this formulation, one can make a simple observation; if the parameter v is not a function of u, then the Jacobian of the function will be constant with respect to u, and the maximum wave speed will always be of the form $a = z^d v$. This should work well for most of the problems of interest.

After discretizing the advective flux term of Equation 4.3, one can use a centered-difference discretization for the rest of the terms within the conservation law and develop a simple semi-discrete form, as shown in Equation 4.7. Note that, since the advective

coefficient (v) is a vector, the equations have been discretized in such a way as to allow for the direction of flow in the domain to change between positive and negative. Additionally, the terms in the discretization have been rearranged such that it is easy to differentiate between the nodal quantities (u) and their gradients (u_z). This is done so that it is easier to split the system between its pseudo-linear and non-linear parts, since the gradients of u are where the slope limiters will be applied.

$$
\begin{aligned}
& z_l^d R_l \frac{d}{dt}(u_l) = \\
& \left[\frac{z_{l-\frac{1}{2}}^d D_{l-\frac{1}{2}}}{\Delta z^2} + \frac{z_{l-\frac{1}{2}}^d \left(v_{l-\frac{1}{2}} + \left|v_{l-\frac{1}{2}}\right|\right)}{2\Delta z}\right] u_{l-1} \\
& -\left[\frac{z_{l+\frac{1}{2}}^d D_{l+\frac{1}{2}}}{\Delta z^2} + \frac{z_{l-\frac{1}{2}}^d D_{l-\frac{1}{2}}}{\Delta z^2} + \frac{z_{l+\frac{1}{2}}^d \left(v_{l+\frac{1}{2}} + \left|v_{l+\frac{1}{2}}\right|\right)}{2\Delta z} - \frac{z_{l-\frac{1}{2}}^d \left(v_{l-\frac{1}{2}} - \left|v_{l-\frac{1}{2}}\right|\right)}{2\Delta z} + z_l^d k_l\right] u_l - z_l^d S_l \\
& +\left[\frac{z_{l+\frac{1}{2}}^d D_{l+\frac{1}{2}}}{\Delta z^2} - \frac{z_{l+\frac{1}{2}}^d \left(v_{l+\frac{1}{2}} - \left|v_{l+\frac{1}{2}}\right|\right)}{2\Delta z}\right] u_{l+1} \\
& +\left[\frac{z_{l-\frac{1}{2}}^d \left(v_{l-\frac{1}{2}} + \left|v_{l-\frac{1}{2}}\right|\right)}{4}\right] (u_z)_{l-1} \\
& -\left[\frac{z_{l+\frac{1}{2}}^d \left(v_{l+\frac{1}{2}} + \left|v_{l+\frac{1}{2}}\right|\right)}{4} + \frac{z_{l-\frac{1}{2}}^d \left(v_{l-\frac{1}{2}} - \left|v_{l-\frac{1}{2}}\right|\right)}{4}\right] (u_z)_l \\
& +\left[\frac{z_{l+\frac{1}{2}}^d \left(v_{l+\frac{1}{2}} - \left|v_{l+\frac{1}{2}}\right|\right)}{4}\right] (u_z)_{l+1}
\end{aligned}
\qquad \textbf{Equation 4.7}
$$

Grouping the terms of Equation 4.7, one can simplify the semi-discrete form into parameters for left, center, and right side terms for nodal and gradient fluxes (N_L, N_C, N_R, G_L, G_C, and G_R) as shown in Equation 4.8. From this point, all that is needed is to apply boundary conditions and choose a time integration scheme. For this particular framework application, two different input boundary conditions are allowed: (i) Dirichlet and (ii) Neumann (Equation 4.9 and Equation 4.10). Those conditions are applied at the input of

the domain, while the output uses the zero flux boundary condition (Equation 4.11). The time integration scheme will either be Crank-Nicolson for the accuracy or Backwards Euler for the stability and will be chosen by the framework when a simulation is being run.

$$z_l^d R_l \frac{d}{dt}(u_l) = \left[N_L\right]_l u_{l-1} - \left[N_C\right]_l u_l + \left[N_R\right]_l u_{l+1} + \left[G_L\right]_l (u_z)_{l-1} - \left[G_C\right]_l (u_z)_l + \left[G_R\right]_l (u_z)_{l+1} - z_l^d S_l \quad \textbf{Equation 4.8}$$

$$u\big|_{z=0} = u_{in} = u_0 \quad \textbf{Equation 4.9}$$

$$D\frac{\partial u}{\partial z}\bigg|_{z=0} = -v(u_{in} - u_0) \quad \textbf{Equation 4.10}$$

$$\frac{\partial u}{\partial z}\bigg|_{z=L} = 0 \quad \textbf{Equation 4.11}$$

4.2.3 Applying Slope Limiter Functions

Slope limiters are functions applied to the gradient of the solution vector *u* in order to reduce the advent of oscillations around sharp or discontinuous portions of the solution. They are required for any high-resolution scheme for fluid dynamics or advectively dominant conservation laws. Unfortunately, there is no slope limiter function that is linear, thus one must introduce some non-linear portions into this simple scheme.

There are several different kinds of slope limiter functions available, each with its own advantages and disadvantages. Kurganov and Tadmor used a generalized minmod slope limiter for their own scheme (Equation 4.12).[7] This slope limiter includes a ϑ parameter that can vary between 1 and 2, 1 being most dispersive and most stable while 2 is least dispersive and least stable. The most attractive feature of this slope limiter is that it is optimal in the sense that it provides the true minimum of the gradient of u for the scheme. Since this slope limiter is non-differentiable, however, it may have very poor convergence properties when using an iterative solution method.

$$\left(u_z\right)_l = \text{minmod}\left\{\vartheta\frac{u_l - u_{l-1}}{\Delta z}, \frac{u_{l+1} - u_{l-1}}{2\Delta z}, \vartheta\frac{u_{l+1} - u_l}{\Delta z}\right\} \qquad \textbf{Equation 4.12}$$

To overcome any potential convergence issues that may arise requires the inclusion of a class of slope limiters that are differentiable and continuous on a given sub-domain. This can be represented by Equation 4.13 and Equation 4.14, wherein $\phi(g_l)$ is a slope limiter function that varies between 0 and 1 to convert the scheme from low to high resolution, depending on the slopes of the surrounding cells. If the neighboring slopes are smooth, then the scheme's resolution is high, whereas if the neighboring slopes are sharp or discontinuous, the scheme reverts to a lower order, upwind-like scheme to reduce oscillations around the sharp wave. For this particular application, both the minmod slope limiter (Equation 4.12) and the van Albada slope limiter will be considered (Equation 4.13 through Equation 4.15).[8]

$$(u_z)_l = \begin{cases} \left(1-\phi(g_l)\right)\left(\frac{u_l - u_{l-1}}{\Delta z}\right) + \phi(g_l)\left(\frac{u_{l+1} - u_{l-1}}{2\Delta z}\right) & v_l > 0 \\ \left(1-\phi(g_l)\right)\left(\frac{u_{l+1} - u_l}{\Delta z}\right) + \phi(g_l)\left(\frac{u_{l+1} - u_{l-1}}{2\Delta z}\right) & v_l \le 0 \end{cases}$$ **Equation 4.13**

$$g_l = \frac{u_l - u_{l-1}}{u_{l+1} - u_l}$$ **Equation 4.14**

$$\phi(g) = \frac{g^2 + g}{g^2 + 1}$$ **Equation 4.15**

4.2.4 Solution Methodology

After formulating the semi-discrete form (Equation 4.8) and choosing a slope limiter, one must still solve the resulting system of equations. Depending on the particular problem and the presence of, or lack thereof, an advective term, the resulting problem may be linear or non-linear. The exact form of the problem, however, will never actually be known until a particular simulation case is chosen. Therefore, it is best to solve the system with a non-linear scheme, which is the most generic approach.

For multi-physics problems derived from spatial discretizations, Newton methods can be computationally inexpensive and effective iterative approaches for non-linear problems.[9] This class of methods is particularly useful for the problem of interest because the linear iterations can be preconditioned, or solved approximately, based on the linearization of the semi-discrete model (Equation 4.8) in order to accelerate

convergence. In essence, the framework is solving the system linearly and using the linear solution as the basis for the non-linear iterations.

4.3 Models for Specific Systems

4.3.1 Bi-porous Pellet Model

One of the most common configurations for commercial adsorbent pellets is a two-phase, heterogeneous structure composed of a macro-porous binder material holding together a collection of micro-porous adsorbent crystals. The binder material typically behaves as an inert conduit by which adsorbates can travel through the pellet to reach the adsorption sites on the adsorbent crystals. Upon reaching the crystals, the adsorbates can adsorb and travel deeper into the crystals via a surface diffusion mechanism.[1] An idealized bi-porous adsorbent pellet is shown in Figure 4.3 below.

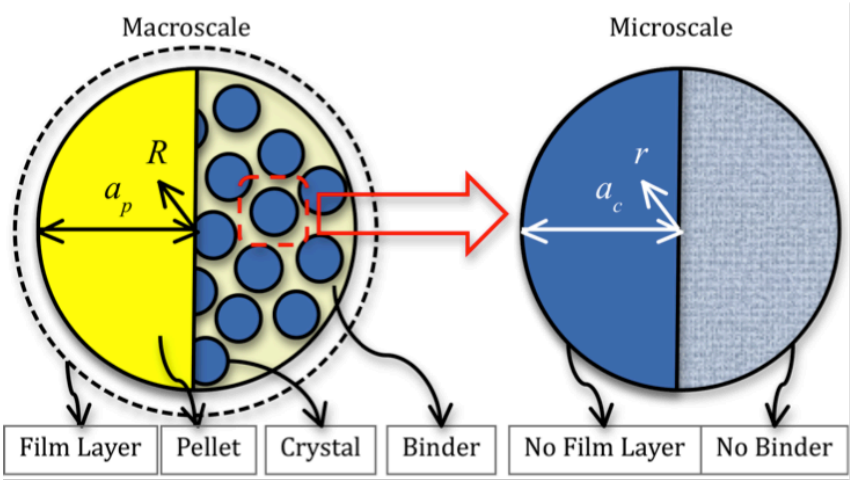

Figure 4.3 - Diagram showing the idealization of a commercial, bi-porous adsorbent made up of a collection of micro-porous adsorbent crystals held together by an inert, macro-porous binder. Dimensions *R* and *r* are the radial coordinates of the adsorbent pellet and micro-porous crystals, respectively.

The mechanisms involved with these types of adsorbents include (i) mass transfer across the film layer, (ii) macro-pore diffusion through the binder material, (iii) adsorption on the crystals, and (iv) surface diffusion through the micro-porous adsorbent crystals.[1] Because the different diffusion processes happen in separate regions of the adsorbent and on different physical scales, a multi-scale physics problem is created that must be resolved using multiple material balances. Each material balance resolves the transport of material on the different scales of the problem and requires a different partial differential equation. The system governing all these mechanisms is outlined in Equation 4.16 through Equation 4.20.

$$\frac{\partial q}{\partial t} = \frac{1}{r^2}\frac{\partial}{\partial r}\left[r^2 D_c \frac{\partial q}{\partial r}\right] \qquad \textbf{Equation 4.16}$$

$$q\big|_{r=a_c} = f(c) \qquad \textbf{Equation 4.17}$$

$$\overline{q} = \frac{3}{a_c^3}\int_0^{a_c} q r^2\, dr \qquad \textbf{Equation 4.18}$$

$$\varepsilon_p \alpha \frac{\partial c}{\partial t} + \rho_s \frac{\partial \overline{q}}{\partial t} = \frac{1}{R^2}\frac{\partial}{\partial R}\left[R^2 D_p \varepsilon_p \alpha \frac{\partial c}{\partial R}\right] \qquad \textbf{Equation 4.19}$$

$$D_p \frac{\partial c}{\partial R}\bigg|_{R=a_p} = k_f (C_b - c) \qquad \textbf{Equation 4.20}$$

On the micro-scale, the material balance (Equation 4.16) is governed by the diffusivity of adsorbates through the crystal (D_c). Each crystal is assumed to be spherical in shape with a nominal radius of a_c. Adsorption occurs on the outside domain of each

crystal (Equation 4.17) and is governed by the adsorption isotherm, which is some function of the local pore space concentration of the adsorbates (c). The average adsorption ($\overline{q}$) in each crystal is resolved as an integral over each crystal domain (Equation 4.18) and becomes part of the macro-scale problem in Equation 4.19.

The macro-scale problem is controlled by pore diffusion (D_p), film mass transfer (k_f), and mass removed through the average adsorption term that is being controlled by the micro-scale. The movement of adsorbate from bulk solution (C_b) to the interior of the pellet (c) is driven by the concentration difference at the boundary (Equation 4.20). Rates at which the adsorbates move throughout the macro-porous binder material are further modulated by the macro-porosity of that binder material (ε_p), the adsorbent density (ρ_s), and the fraction of the pellet that is binder material (α).

Although this bi-porous structure is common for many commercial pellets, it is not always necessary to model the adsorption mechanisms in this much detail. For instance, one may want to ignore the micro-scale diffusion portion of this problem and consider the average adsorption to just be a function of local equilibrium in the pellet, which is dictated by the isotherm. To do this only requires changing the micro-scale adsorption function to the adsorption isotherm (Equation 4.17). Or perhaps the pellets are actually extruded cylinders instead of compressed bi-porous spheres. Under the generalized framework, it is very simple to change coordinate systems from spherical to cylindrical. This is accomplished simply by changing the value of dimensional parameter d (Equation 4.3) from 2 to 1.

4.3.2 Mass and Energy Transport Model

This modeling framework is also well suited for simulating mass and energy transfer during adsorption in a fixed-bed column. Fixed beds are the typical engineered adsorption systems for the separation or recovery of dilute gases.[3,4] They are generally cylindrical columns packed with adsorbent pellets held in place by some form of screen so that gas is allowed to pass through the system. In some cases, the outer walls of those columns are thermally controlled and, often times, the length of those columns is much larger than their diameter. In these cases, it is very suitable to model the mass and energy balance in one-dimension, since there will be very minor changes in the radial distribution of mass and heat.[1]

The mass balance portion of the fixed-bed model is driven primarily by the interparticle transport mechanisms of advection and dispersion (Equation 4.21). Additionally, there is a sink term for gas phase losses caused by adsorption. Adsorption taking place in this model can be in terms of local equilibrium or in terms of the kinetics of adsorption, such as bi-porous kinetics in the case of engineered commercial pellets (Equation 4.16 through Equation 4.20). The parameters involved with mass transport include superficial gas velocity (v), bulk bed porosity (ε_b), axial dispersion (D_z), and bulk bed solids density (ρ_b). At the inlet boundary to the fixed-bed, mass flow into the problem domain is governed by the flow rate and the concentration gradient formed at the entrance to that domain between the inlet concentration (C_{in}) and the concentration inside the bed (Equation 4.22).

$$\varepsilon_b \frac{\partial C}{\partial t} + \frac{\partial}{\partial z}\left(\varepsilon_b v C\right) = \frac{\partial}{\partial z}\left(\varepsilon_b D_z \frac{\partial C}{\partial z}\right) - \rho_b \frac{\partial q}{\partial t} \qquad \textbf{Equation 4.21}$$

$$D_z \left.\frac{dC}{dz}\right|_{z=0} = v\left(C_{in} - C\right) \qquad \textbf{Equation 4.22}$$

For this model, one may also want to track how the temperature of the gas (T) changes with adsorption. This requires the development of an energy balance between gas and solid phases as material moves through the bed and as adsorption occurs.[1,3] The energy balance involves similar boundary conditions and mechanisms to that of the mass balance (Equation 4.23 and Equation 4.24), but also includes thermal conductivity, heat transfer from the walls of the columns, and heats of adsorption. Since radial changes in temperature and concentration are being neglected in the 1-D case, the effect of the heating of the wall is done on an average basis. The parameters in this energy balance include heat capacity of the gas (h_g), density of the gas (ρ), heat capacity of the adsorbents (h_s), axial thermal conductivity (K_z), heat of adsorption (Q_{st}), temperature of the wall (T_w), heat transfer coefficient between the wall and the interior gases (U_w), and the inner diameter of the column (d_{in}).

$$\left(h_g \rho \varepsilon_b + h_s \rho_b\right)\frac{\partial T}{\partial t} + \frac{\partial}{\partial z}\left(h_g \rho \varepsilon_b v T\right) = \frac{\partial}{\partial z}\left(\varepsilon_b K_z \frac{\partial T}{\partial z}\right) + \rho_b \frac{\partial (Q_{st} q)}{\partial t} + \frac{4U_w}{d_{in}}\left(T_w - T\right) \qquad \textbf{Equation 4.23}$$

$$K_z \left.\frac{dT}{dz}\right|_{z=0} = h_g \rho v\left(T_{in} - T\right) \qquad \textbf{Equation 4.24}$$

These material balances (Equation 4.21 through Equation 4.24) make up the bulk of the fixed-bed adsorption model. To resolve the actual amount of adsorption (q)

occurring in the column, one could either assume local equilibrium (i.e., apply the adsorption isotherm at each spatial location in the domain) or use an adsorption kinetics model, such as the bi-porous pellet model. Combining the actual adsorption kinetics with these equations for mass and energy transfer creates a fully coupled model for adsorption in engineered systems.

4.3.3 Estimating Model Parameters

All the models discussed involve many different physical parameters ranging from thermal capacities to various types of diffusion. Some of these values, such as pellet density (ρ_s) and wall heat transfer coefficients (U_w), can be found by looking at various tables or published data for similar systems or particular materials.[3,4] Other parameters, such as surface diffusion (D_c), may only be determined through experiments or listed in literature for a particular system. However, a bulk of the model parameters can be approximated through theoretical and semi-empirical considerations.

Many of the parameters involved in the bi-porous pellet kinetics model can be determined independently. Tien[1] offers several techniques and expressions for determining the pellet diffusivity (D_p) and mass-transfer coefficient (k_f) based on the system parameters (Equation 4.25 through Equation 4.28). The parameters for Equation 4.25 through Equation 4.28 are as follows: ε_p is macro-porosity, τ is tortuosity, D_m is molecular diffusivity, D_k is Knudsen diffusivity, $D^o{}_p$ is the idealized pore diffusivity, D_p is the corrected pore diffusivity, r_p is nominal pore radius, *MW* is molecular weight of adsorbing species, *Re* is the Reynolds number, and *Sc* is the Schmidt number.

Actual pore diffusivity (Equation 4.27) inside the adsorbent pellet is controlled by both Knudsen diffusion (Equation 4.26) and molecular diffusion, which is modified by the tortuous path that molecules take through the macro-porous binder material (Equation 4.25). The film mass-transfer coefficient can be approximated through empirical relationships with the dimensionless Reynolds (*Re*) and Schmidt (*Sc*) numbers, along with the molecular diffusivity in the gas phase (Equation 4.28).

$$D_p^o = \frac{\varepsilon_p D_m}{\tau} \qquad \textbf{Equation 4.25}$$

$$D_k = 9700 r_p \left(\frac{T}{MW} \right)^{1/2} \qquad \textbf{Equation 4.26}$$

$$\frac{1}{D_p} = \frac{1}{D_p^o} + \frac{1}{D_k} \qquad \textbf{Equation 4.27}$$

$$k_f = \frac{D_m}{2a_p} \left[2 + 1.1 Re^{0.6} Sc^{0.3} \right] \qquad \textbf{Equation 4.28}$$

Each species in a gas mixture will have a different molecular diffusivity ($D_{m,i}$) that can be determined from the binary diffusivities (D_{ij}) between all species present (Equation 4.29). The binary diffusivities vary theoretically with temperature and the viscosity (μ_i), density (ρ_i), and molecular weight (MW_i) of each species according to Equation 4.30.[10] Temperature relationships for the density of each species can be determined using the ideal gas law (Equation 4.31), and the Sutherland's equation[11] (Equation 4.32) can be used to relate the viscosity of each pure species with temperature using a reference state viscosity (μ_i^o) and reference temperature (T_i^o), as well as the

Sutherland's constant (X_i). Combining all these theoretical models, then, allows one to accurately estimate the influence of diffusivity on the kinetics of adsorption.

$$D_{m,i} = \frac{1 - y_i}{\sum_{j \neq i} \frac{y_j}{D_{ij}}} \qquad \textbf{Equation 4.29}$$

$$D_{ij} = \frac{(4/\sqrt{2})(MW_i^{-1} + MW_j^{-1})^{1/2}}{\left[\left(\frac{\rho_i^2}{1.92\mu_i^2 MW_i}\right)^{1/4} + \left(\frac{\rho_j^2}{1.92\mu_j^2 MW_j}\right)^{1/4}\right]^2} \qquad \textbf{Equation 4.30}$$

$$\rho_i = \frac{P_T MW_i}{RT} \qquad \textbf{Equation 4.31}$$

$$\mu_i = \mu_i^o \frac{T_i^o + \mathrm{X}_i}{T + \mathrm{X}_i}\left(\frac{T}{T_i^o}\right)^{3/2} \qquad \textbf{Equation 4.32}$$

The Reynolds and Schmidt numbers (Equation 4.33 and Equation 4.34) are also implicit functions of temperature and pressure because they relate the kinematic viscosity (v_g) and diffusivity of the gas with the gas velocity (v) and size of the particles (a_p).[12] To determine the kinematic viscosity of the mixed gas system requires the total dynamic viscosity of the gas (μ_g) and the total density of the gas phase (ρ). While the total density can be determined from the ideal gas law, the dynamic viscosity of the mixed gas must be determined from a theoretical model, such as that outlined in Equation 4.35 through Equation 4.37.[13] This model takes into account the mole fractions (y_i) of each species together with the binary diffusivities and a temperature correction factor (χ) to approximate the mixed gas viscosity.

$$Re = \frac{2u_s a_p}{\nu_g}$$ **Equation 4.33**

$$Sc_i = \frac{\nu_g}{D_{ij}}$$ **Equation 4.34**

$$\mu_g = \sum_{i=1}^{N} \frac{\mu_i}{1 + \frac{113.65\chi\mu_i T}{y_i MW_i} \sum_{\substack{j=1 \\ j \neq i}}^{N} \frac{y_i}{D'_{ij}}}$$ **Equation 4.35**

$$\chi = 0.873143 + (7.2375 \times 10^{-5})T$$ **Equation 4.36**

$$P^o D'_{ij} = P_T D_{ij}$$ **Equation 4.37**

Using all these relationships allows for reasonable approximation of many of the parameters involved in the bi-porous pellet kinetics model. For the fixed-bed model, many of the parameters of the energy balance (Equation 4.23), including wall heat transfer coefficient and heat capacities of materials, can be determined by looking up the properties of the specific materials involved. The heat of adsorption (Q_{st}) is typically determined through the isotherm (recall CHAPTER 3) or through experiments.[14,15]

For the mass balance portion of the fixed-bed model, the axial dispersion coefficient can be approximated through an empirical relationship with the Reynolds and Schmidt numbers (Equation 4.38) in a similar fashion to how the film mass transfer coefficient was determined.[3,16] Most other parameters in the fixed-bed model, notably the thermal parameters such as heat capacities, conductivities, and heat transfer coefficients, must be looked up in tables or determined experimentally.

$$D_z = 2va_p\left[\frac{20}{Sc \cdot Re} + \frac{1}{2}\right] \qquad \textbf{Equation 4.38}$$

4.3.4 Equilibrium Isotherm Model

The final piece of information necessary for modeling adsorption kinetics and transport is the isotherm. Isotherms describe the relationship between the adsorbed phase and the gas phase at equilibrium. There are a variety of different adsorption models available in literature: Langmuir, Freundlich, Tóth, etc. The individual choice of isotherm will depend on the suitability of the model for describing the partition between gas and solid phases across a variety of temperatures and pressures.[15]

For the work considered here, the Generalized Statistical Thermodynamic Adsorption (GSTA) isotherm model[14] was chosen as the equilibrium model (recall CHAPTER 2). This isotherm is very flexible and has been shown to be useful at describing the adsorption equilibrium of many different systems.[15,17] Additionally, this model has also been employed in mixed-gas adsorption equilibrium models with great success (recall CHAPTER 3).[18] Isotherm parameters for all systems that have been modeled in this work were determined through an iterative procedure described in Ladshaw et al.[15]

4.4 Data Acquisition

4.4.1 Materials

To demonstrate the capability of the model framework for different adsorption systems, kinetic data of water vapor adsorption with a zeolite molecular sieve 3A (MS3A) and iodine gas adsorption with a reduced silver mordenite (Ag^0Z) were analyzed. MS3A is one of the classic adsorbents for removing water in gas and liquid streams, and Ag^0Z is the most promising material for iodine capture in spent nuclear fuel reprocessing plants. Both solid adsorbents were micro-porous crystalline alumina silicates that have micro pores and channels in the crystals. The commercial MS3A that were used in prior studies[5] were spherical beads with a radius of 1.18 mm, and the Ag^0Z used in prior studies[19] were extruded cylinders with a radius of 0.8 mm.

The silver mordenite contained 11.9 wt.% silver and was reduced prior to adsorption experiments in a hydrogen/argon stream at 400 ^oC and for 24 hours to achieve a better iodine adsorption performance. Previous studies have shown that silver ions inside the mordenite crystals were reduced to metallic silver and formed silver nanoparticles on the surface of the crystals during the reduction by hydrogen.[19-22] Physical properties and chemical characteristics of the MS3A and Ag^0Z were described previously.[5,19] In addition to those reported properties, the average macropore radii of MS3A and Ag^0Z were measured in this work using mercury porosimetry, which were 35 nm and 26.5 nm, respectively. Table 4.1 and Table 4.2 below provide some important structural and physical parameters for modeling adsorption kinetics in both MS3A and Ag^0Z adsorbents.

Table 4.1 - Structural parameters for the MS3A zeolite

Description	Variable	Value	Units
Crystal Radius	a_c	1.5	μm
Pellet Radius	a_p	1.18	mm
Macro-pore Radius	r_p	35	nm
Adsorbent Density	ρ_s	1.69	g/cm^3
Macro-porosity	ε_p	0.272	-
Binder Fraction	α	0.175	-

Table 4.2 - Structure parameters for the Ag^{0}Z mordenite

Description	Variable	Value	Units
Pellet Radius	a_p	0.8	mm
Macro-pore Radius	r_p	26.5	nm
Adsorbent Density	ρ_s	3.06	g/cm^3
Macro-porosity	ε_p	0.384	-

4.4.2 Methods

Both the H_2O and I_2 uptake experiments were performed with continuous-flow gas adsorption systems, which have been reported previously.[5,19] Each of the systems had a H_2O/I_2 vapor generating unit, a microbalance unit, a heating unit, and a data acquisition system. Changing the temperature of the generating units and varying the flow rates of the carrier and dilution gas streams controlled the H_2O and I_2 vapor concentrations. A microbalance connected with a data acquisition system was used in each system for recording the mass changes of the adsorbents during the adsorption/desorption processes.

H_2O adsorption experiments were performed at temperatures between 25 to 80 ^oC, with H_2O concentrations (in terms of dew point) ranging from -69 to 17 ^oC, and I_2 adsorption experiments were conducted at 100 – 200 ^oC with I_2 vapor concentrations in the range of 9 – 52 ppmv. In each experiment, a few vacuum-dried adsorbent particles were loaded into a screen tray suspended from the microbalance. There were fairly large spaces between the particles so the adsorption data essentially represented the adsorption processes on each single particle. Details of the procedures were reported in previous papers.[5,19]

4.5 Results

4.5.1 H_2O on MS3A Modeling

The adsorption of water vapor on commercial MS3A zeolite adsorbents has a potential use for the capture of tritiated water (H^3HO) from the off-gas stream of nuclear fuel reprocessing facilities.[5,17] A prior study of the kinetics of water vapor on MS3A had utilized various simple kinetic models, such as linear driving force and shrinking core models.[5] Using the data from that study, a model analysis was performed using the bi-porous pellet kinetics model described in the section 4.3. The commercial MS3A zeolite used is the perfect structural candidate to validate the bi-porous pellet model. MS3A is a small, spherical adsorbent constructed from a macro-porous binder material that holds small zeolite crystals together, much like it was depicted in Figure 4.3. Important structural parameters for this pellet were given in Table 4.1.

For the purpose of modeling the adsorption of water vapor in this system, the relationships discussed from Equation 4.25 through Equation 4.37 were used to

approximate film mass transfer coefficients (k_f) and pore diffusivities (D_p) from the experimental conditions described by Lin et al.[5] The value of the micro-pore diffusion coefficient (D_c), however, is not known for this system. Therefore, it was decided to first treat this parameter as adjustable and determine its optimal value for each experiment. The results of that analysis are shown in Figure 4.4.

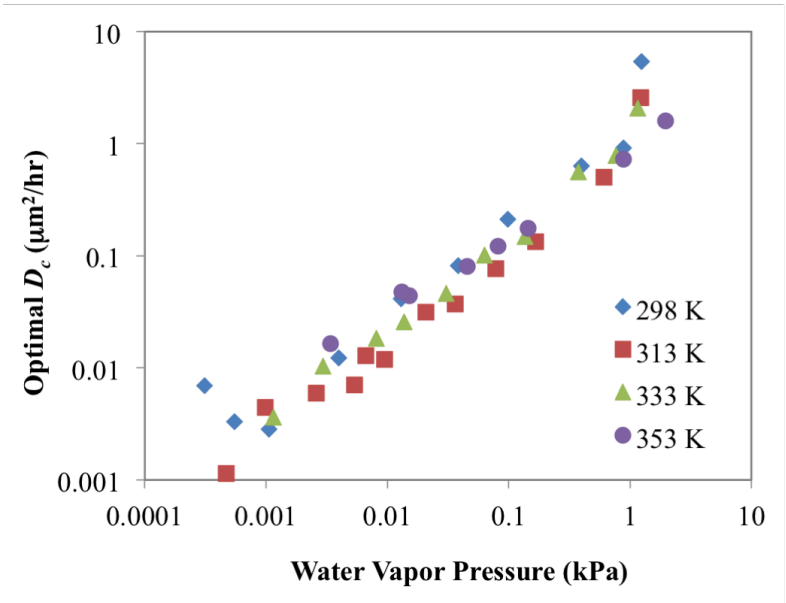

Figure 4.4 - Optimal micro-pore diffusivities versus water vapor pressures across different temperatures. Little or no relationship between diffusivity and temperature is observed, but there is a strong, linear relationship between vapor pressure and diffusivity on a log-log scale. The data analyzed to obtain these values came from Lin et al.[5]

It is fairly clear to see from Figure 4.4 that there exists a strong relationship between the micro-pore diffusivity and the ambient vapor pressure. Similar trends were also observed by Lin et al.[5] for the parameters of the kinetic models they had utilized. Comparisons between the optimized bi-porous model and select kinetic curves from the

water adsorption experiments are shown in Figure 4.5. These curves were normalized by their respective equilibrium capacities at the given experimental conditions. This was done so that no bias would be introduced in the optimization by differences that may exist between the model equilibrium value and the equilibrium value reported by Lin et al.[5] Overall, the bi-porous kinetic model works very well at describing the adsorption rate for water vapor on the MS3A adsorbent.

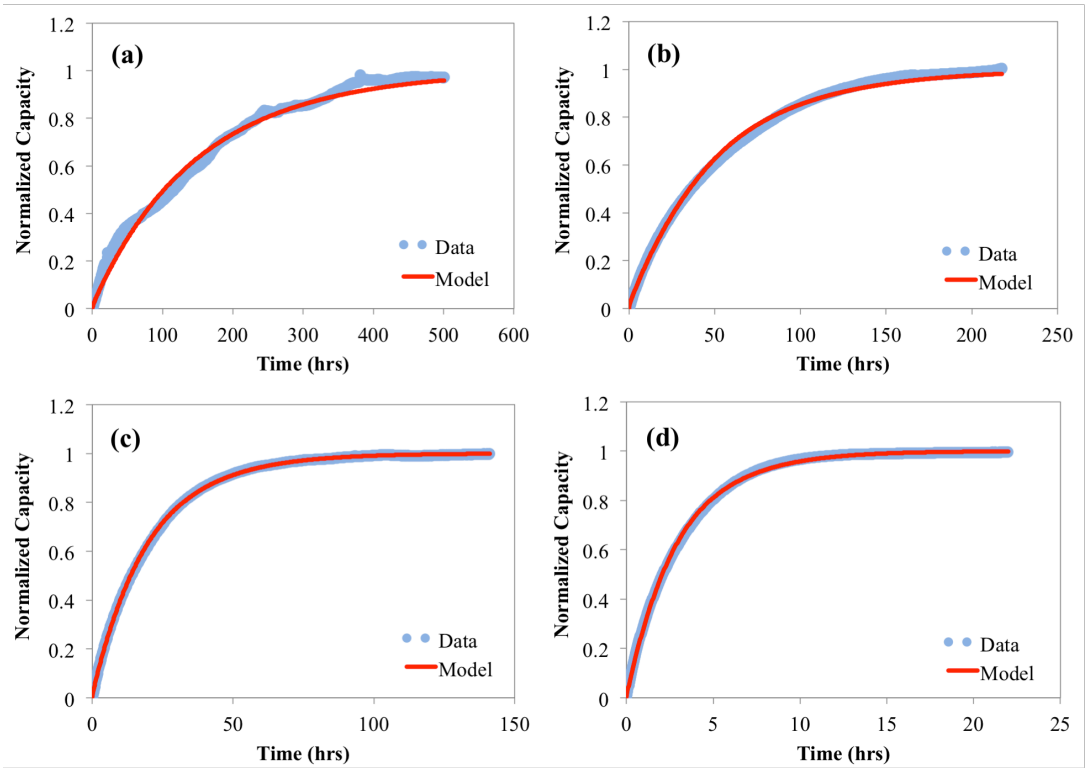

Figure 4.5 - Comparison between experimental data and optimized bi-porous pellet kinetic model results for four different uptake curves. The uptake curves were normalized to provide the amount adsorbed divided by the equilibrium adsorption value for each experiment. (a) gas temperature of 25 ^{o}C and vapor pressure of 3.1E-4 kPa, (b) gas temperature of 40 ^{o}C and vapor pressure of 5.4E-3 kPa, (c) gas temperature of 60 ^{o}C and vapor pressure of 8.1E-3 kPa, and (d) gas temperature of 80 ^{o}C and vapor pressure of 8.1E-2 kPa.

It is easy to see that the model performs well when modeling results are compared to the experimental data in order to determine the optimal micro-pore diffusivity (D_c). The mark of a good model, however, will be its ability to predict behavior and not just describe existing data. After the optimal values of the diffusivities have been determined (Figure 4.4), that information can be utilized to predict different adsorption curves for the same system at different temperatures and pressures. To accomplish this, adsorption and desorption cycling data were measured and then simulated to further validate the bi-porous model (Figure 4.6).

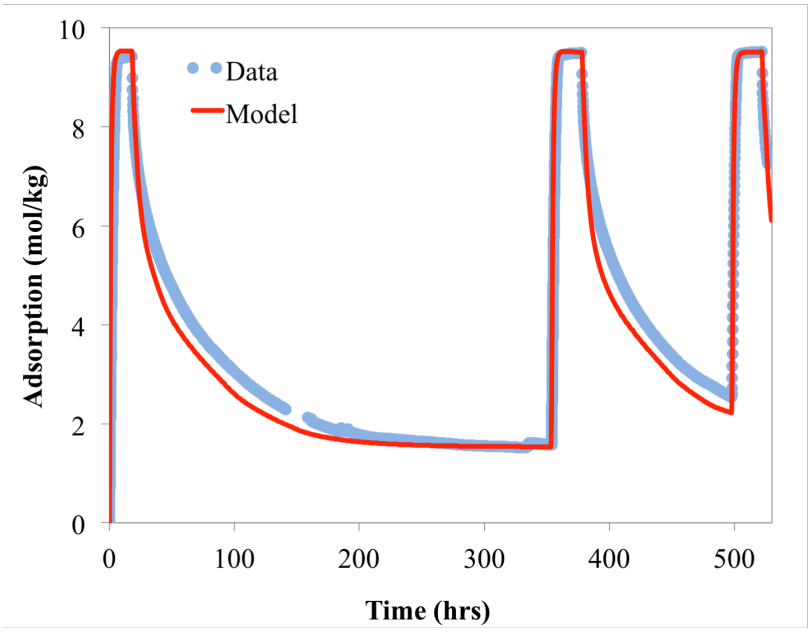

Figure 4.6 - Comparison between adsorption cycling data and bi-porous pellet model predictions. Adsorption occurs at 40 °C and a vapor pressure of 0.34 kPa. During desorption, the temperature remains the same, but the vapor pressure drops to 7.3E-4 kPa.

The adsorption was performed at the dew point of -10 ^{o}C followed by desorption in dry air (dew point: -70 ^{o}C) after the MS3A particles were equilibrated with H_2O vapor. Adsorption was restarted when desorption reached equilibrium, and that process continued for roughly two and a half cycles. The simulation of the cycling behavior compared to the adsorption/desorption data is shown in Figure 4.6. This result demonstrates the model's ability to predict the adsorption and desorption cycling behavior of water vapor on the MS3A adsorbent.

4.5.2 I_2 on Ag^0Z Modeling

To highlight the flexibility and generality of this modeling approach, it will be demonstrated that the bi-porous kinetics model is suitable for predicting adsorption uptake for a completely different system. Here, the bi-porous pellet kinetics model described above has been utilized to predict the uptake rates of I_2 on Ag^0Z pellets, using data reported in a previous paper.[19] The structural treatment of the problem is very different and some of the parameters of the model must be adjusted, as described below, to align with the physical problem.

As mentioned in section 4.4, the Ag^0Z pellets are cylindrical instead of spherical. This is not an issue for the modeling framework that was developed here. Recall that the framework is based on the generalization of a one-dimensional conservation law (Equation 4.3). Because of this framework approach, one can easily shift the model into different coordinate systems. This is done so by only changing the value of a single framework parameter (d) from a value of 2 to a value of 1.

The reducing process involved with preparing the Ag^0Z pellets creates nanoparticles of silver on the outer surface of the adsorbent crystals inside the pellets.[19] Since the I_2 adsorption occurs only at these silver sites, and those sites are formed on the outside of the micro-porous crystals, the pellet actually behaves more homogeneously. In other words, I_2 travels only through the binder of the pellets, and then adsorbs onto the crystals without entering the micro-porous regions.

This system can be represented mathematically in the bi-porous pellet model (Equation 4.16 through Equation 4.20) by neglecting the micro-porous diffusion equations and replacing them with just the adsorption isotherm. Therefore, the assumption being made is that the I_2 molecules travel through the pore space of the binder, reach a silver site, and then undergo local equilibrium reactions to adsorb to that site. In addition, the binder fraction (α) parameter is neglected by setting its value to 1. This will make it so that Equation 4.19 is exactly representative of homogenous diffusion kinetics for the case of the pore-diffusion controlled adsorption.[1]

Since the micro-porous diffusion mechanism is neglected, there is no need for the model of this system to be calibrated with the adsorption data. All system parameters can be approximated based on the relationships in Equation 4.25 through Equation 4.37, thereby making the model purely predictive. Then, the last pieces of information necessary to make predictions of the adsorption of I_2 by Ag^0Z pellets are the structural parameters, which were provided in Table 4.2.

Using the structural parameters from Table 4.2, as well as the diffusion and film mass transfer parameters calculated from Equation 4.25 through Equation 4.37, based on

the experimental conditions[19] described above, simulations were performed to predict the I_2 adsorption kinetics and compare the modeling results to the experimental data. Figure 4.7 below shows select results of that analysis at different gas temperatures and partial pressures of I_2 in the gas stream. These results show that the model did very well to predict the rate of I_2 adsorption; especially since no parameter optimization was performed. It does appear, however, that some of the model uptake curves predicted faster adsorption kinetics than the kinetics observed in the data.

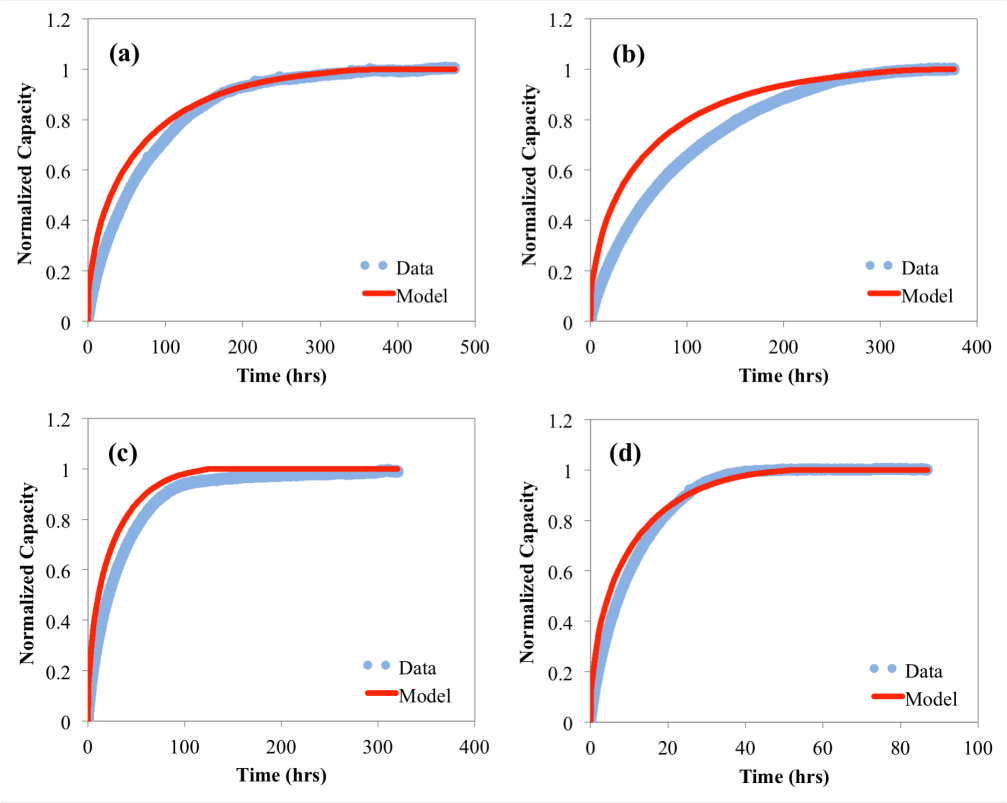

Figure 4.7 - Comparison between experimental data and kinetic model predictions for four different uptake curves. The uptake curves were normalized to represent the amount adsorbed divided by the equilibrium adsorption value for each experiment: (a) gas temperature of 100 °C and I_2 partial pressure of 1.3E-3 kPa, (b) gas temperature of 150 °C and I_2 partial pressure of 1.4E-3 kPa, (c) gas temperature of 150 °C and I_2 partial pressure of 3.7E-3 kPa, and (d) gas temperature of 200 °C and I_2 partial pressure of 8.8E-3 kPa. The data shown were collected by Nan et al.[19]

4.5.3 Column Modeling

Ultimately, the goal of adsorption process modeling is to utilize models in order to design adsorption capture systems. As previously stated, the most common configuration for removal and recovery of dilute species in gaseous streams is that of a fixed-bed adsorption column.[3,4] To demonstrate the framework's capacity to model adsorption in fixed-beds, a fictitious scenario was devised in which the concentration and temperature breakthrough curves for water vapor adsorption in a column packed with MS3A adsorbent pellets could be modeled using this modeling framework.

Structural parameters for the MS3A adsorbent are the same as those in Table 4.1, and the same isotherm parameters were used that were discussed in the analysis of the Lin et al.[5] data set (Figure 4.5 and Figure 4.6). The adsorption term (q) for the mass and energy balances of the fixed-bed model (Equation 4.21 and Equation 4.23) was resolved by performing simulations with the bi-porous pellet model (Equation 4.16 through Equation 4.20) to approximate the amount of water vapor adsorbed at different points in the column versus time. That result was then coupled into the fixed-bed equations as a mass or energy source/sink term. The heat of adsorption (Q_{st}) was determined through the isotherm relationships described by Ladshaw et al.[15] and Llano-Restrepo and Mosquera.[14]

Besides the isotherm parameters and physical characteristics relevant to the MS3A adsorbent, other structural and thermal parameters needed for the fixed-bed model were determined by looking up known values or estimating some constants to take the place of otherwise unknown parameters, such as the wall heat transfer coefficient (U_w) and axial thermal conductivity (K_z). Table 4.3 summarizes the remaining parameters for

the fixed-bed model (Equation 4.21 through Equation 4.24) and their corresponding values that were used in the model demonstration. Additionally, for the purpose of this demonstration it was assumed that the temperature of the wall (T_w) was constant.

Table 4.3 - Parameters for the Fixed-bed Adsorption Model Demonstration

Description	Variable	Value	Units
Bulk Bed Porosity	ε_b	0.36	-
Linear Gas Velocity	V	0.10	cm/s
Bulk Pellet Density	ρ_b	1.08	g/cm^3
Inlet Concentration	C_{in}	7.80E-5	mol/L
Gas Heat Capacity	h_g	1.01	J/g/K
Gas Density	ρ	1.23E-3	g/cm^3
Pellet Heat Capacity	h_s	1.05	J/g/K
Axial Conductivity	K_z	0.01	J/s/cm/K
Heat Transfer Coefficient	U_w	5.00E-3	J/s/cm^2/K
Column Inner Diameter	d_{in}	1.75	cm
Wall Temperature	T_w	313.15	K
Inlet Temperature	T_{in}	313.15	K

For the fixed-bed model demonstration, a 20-hour simulation was run for water vapor adsorption in a 9-cm long column given an inlet water vapor pressure of 0.203 kPa and inlet temperature of 313.15 K. Initial conditions for this simulation assumed there was no water vapor in the column prior to the simulation. After the first 10 hours, the inlet boundary conditions for the mass balance were changed to that of dry air such that the final 10 hours of the simulation would represent desorption.

The results of this simulation are summarized in Figure 4.8 and Figure 4.9. Figure 4.8 shows the vapor pressure at the exit of the column over time. It is worth noting here

that, in the absence of adsorption, the breakthrough should happen in about 90 seconds given the length of the column and the linear velocity of the gas. Therefore, the model demonstrates significant retardation of the flow, as mass is transferred from the gas phase to the surface sites of the adsorbent. Figure 4.9 shows the effect that adsorption has on the temperature of the gas stream. The model shows that the gas stream heats up above ambient levels as adsorption occurs, but decreases below ambient during desorption.

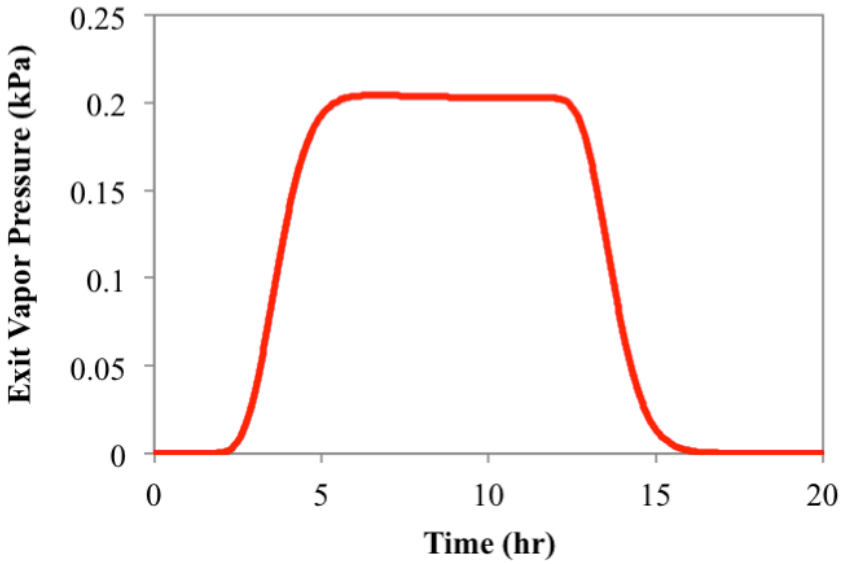

Figure 4.8 - Water vapor breakthrough history for the 20-hour sample simulation in a 9-cm long column packed with MS3A adsorbent. After 10 hours, dry air was given to the model as the inlet boundary condition to simulate desorption of water vapor from 10 to 20 hours.

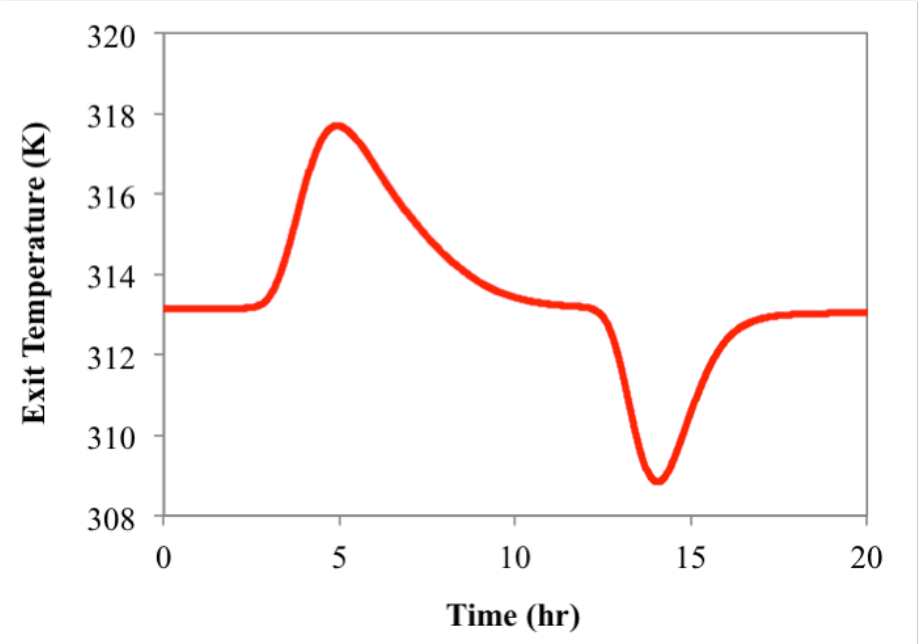

Figure 4.9 - Gas temperature breakthrough history for the 20-hour simulation in a 9-cm long column packed with MS3A adsorbent. After 10 hours, dry air was given to the model as the inlet boundary condition to simulate desorption of water vapor from 10 to 20 hours.

4.6 Discussion

4.6.1 H_2O on MS3A

It is clear to see from Figure 5 that the bi-porous pellet model describes well the adsorption kinetics of water vapor by the MS3A adsorbent. The simpler models investigated by Lin et al.[5], however, could also fit their data equally well. This comparison immediately brings up the question: Why use the more complex model, when the simpler models are just as good? The primary reason for the use of a complex model is that it will more accurately predict the cycling or desorption behavior of the system.

Let's consider the linear driving force (LDF) model (Equation 4.39) as a point of comparison against the bi-porous pellet model. This is a very common, very simple model for adsorption kinetics that relates the average equilibrium adsorption value (q_e) of an adsorbent pellet to a lumped mass transfer parameter (k_{LDF}) often referred to as the LDF parameter.[1,3,5] One can find the optimum values for the LDF parameter in a similar manner in which the optimum diffusivity parameters are found from Figure 4.4. Then, using those parameters, one can model the adsorption/desorption scenario as in Figure 4.6 and compare those LDF model results to both the data and the bi-porous model.

$$\frac{dq}{dt} = k_{LDF}(q_e - q) \qquad \textbf{Equation 4.39}$$

Recall from the data analysis in Figure 4.4 that there was a strong relationship between vapor pressure and the micro-pore diffusivity. This was also true for the optimized LDF parameters reported by Lin et al.[5] To compare LDF to the bi-porous model, LDF simulations considering two different scenarios were performed: (i) one in which there is a step change in the LDF parameter caused by the step change in the vapor pressure and (ii) one in which any change in the LDF parameter caused by changes in vapor pressure has been ignored. Comparison between the LDF model and the bi-porous model at predicting the cycling behavior of water vapor adsorbed by MS3A is shown in Figure 4.10.

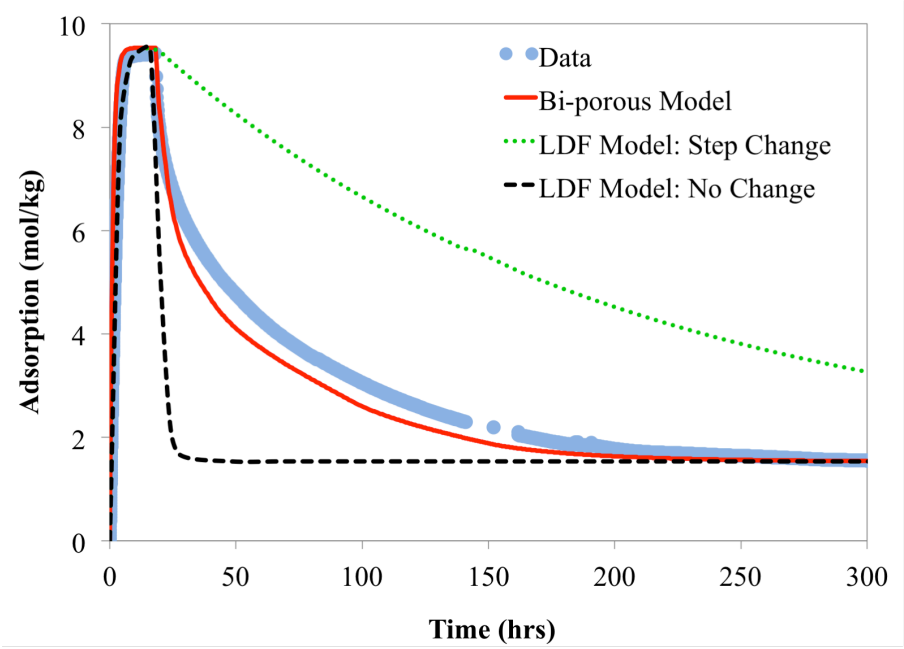

Figure 4.10 - Comparison between the adsorption/desorption cycle behavior for water vapor on MS3A and three different models: (i) the bi-porous pellet model described in this work, (ii) the LDF model with a step change in the LDF parameter, and (iii) the LDF model with no change in the LDF parameter. The bi-porous model works well to predict the adsorption and desorption behavior, while the LDF models can only predict the adsorption curve. The data are taken from Figure 4.6.

When a step change in the LDF parameter was considered based on the simulation step change from high to low vapor pressure, the LDF model showed slower desorption than adsorption, but it does not accurately reflect the data (Figure 4.10). In contrast, if one ignores a step change in the LDF parameter, then the rate of desorption is roughly the same as the rate of adsorption. Like the LDF model with the step change, the bi-porous model does consider how changes in vapor pressure change the micro-pore diffusion parameter according to the data analysis of Figure 4. This raises the question: why does the bi-porous model perform better than the LDF model?

The reason the bi-porous model performs better than the LDF models for desorption is because of how the simulations are actually carried out and what information is being tracked throughout the simulation. In the case of the LDF model, the adsorption amount is only calculated as an average, based solely on the driving equilibrium value (q_e) and the rate constant (k_{LDF}). The bi-porous model, however, tracks both the macro-pore gaseous concentration (c) and the micro-pore adsorption (q) as a function of time and space through the entire pellet. In this case, while the outside vapor pressure (C_b from Equation 4.20) undergoes a step change in the concentration level, the interior concentration of vapor in the macro-pore region of the pellet (c) starts relatively high at the time of the step change, and then decreases gradually as vapor exits the macro-pore space and leaves the pellet.

In the bi-porous model (Equation 4.17), the local adsorption (q) on the crystals is based on the interior concentration (c) and not the exterior concentration (C_b). This is not the case for the LDF model because it does not track the local interior concentrations; instead it bases the average adsorption only on the exterior concentration. Therefore, by tracking how the local interior concentration varies based on the macro-pore diffusion and losses/gains to adsorption/desorption, it is possible to more accurately portray how the overall adsorption process influences the amount of material adsorbing/desorbing as changes occur in the bulk gas phase.

4.6.2 I_2 on Ag^0Z

The model predictions for I_2 on Ag^0Z showed exceptional accuracy for the rates of adsorption at different concentrations and temperatures, but also showed some over-

estimates for how fast the system reached equilibrium (Figure 4.7). In these simulations, it was assumed that once I_2 had reached a silver site, it underwent adsorption instantaneously, thereby reaching its local equilibrium value within the pellet at a given location. It was noted by Nan et al.[19], however, that the reaction between the iodine and silver was one of the rate controlling mechanisms in the overall adsorption rate. This may explain why the model developed here showed faster adsorption kinetics, especially for images (b) and (c) from Figure 4.7.

If the rate of reaction were included, then the local adsorption of I_2, based on the interior concentration of iodine gas, would be smaller compared to the predicted concentration after assuming local equilibrium. This reduction in adsorption locally would suppress the overall rate of adsorption and could yield even better predictions for this system. Therefore, this model can be improved by including adsorption reaction rates at the silver sites instead of just applying the isotherm.

4.6.3 Column Model

The fixed-bed modeling results in Figure 4.8 and Figure 4.9 were produced with a fictitious adsorption scenario. This simulation was performed as a demonstration of the modeling capacity of the numerical framework developed in this work. Qualitatively, the model behaves exactly as expected for a simulation of this type. The rate at which the vapor exits the column (Figure 4.8) indicates that there is a strong retardation effect of adsorption as water vapor is taken out of the bulk gas phase and adsorbed on the pellets. This is known simply by observing that, in the absence of adsorption and mass-transfer, the breakthrough time for this simulation would be approximately 90 seconds. This value

is determined based on the length of the column (9 cm) and the linear velocity of the gas phase (0.1 cm/s).

Additionally, the simulated temperature breakthrough curve in Figure 4.9 behaves in a manner expected for adsorption. Since adsorption of water vapor on MS3A is an exothermic process, the gas temperature in the column is expected to rise as adsorption occurs and fall as desorption occurs.[3] The fixed-bed model demonstration shows this expected behavior (Figure 4.9).

4.7 Conclusions

While adsorption is a very complex process that can vary widely based on differences in adsorbents and adsorbates, the basic mechanisms that govern this physical-chemical process are generally the same. Regardless of the specifics of the problem, adsorption will always involve (i) interparticle transport, (ii) interphase mass-transfer, (iii) intraparticle diffusion, and (iv) surface reactions and equilibria. Therefore, the most effective and efficient way to model adsorption processes is to create a framework under which one can simulate all these mechanisms.

The basis of that framework comes from the fact that all adsorption models stem from conservation laws. Using that knowledge, a generalized conservation law model (Equation 4.3) was developed that serves as the basis of a framework to simulate a variety of different adsorption problems. Following this framework, the model problem is solved numerically to preserve its generality, as the numerical solution is valid regardless of whether or not the model is linear or non-linear and/or dominated by advection or diffusion.

As a demonstration of the generality and flexibility of this modeling framework, three different types of common adsorption problems were simulated: (i) spherical, heterogeneous adsorption kinetics, (ii) cylindrical, homogeneous adsorption kinetics, and (iii) one-dimensional, fixed-bed mass and energy transfer. Although these three systems are very different in terms of their structural characteristics, the same mechanisms and conservation laws govern them all. Therefore, they can all be modeled under the same framework approach.

Through comparisons of the modeling results produced in this work to experimental data, the validity of this modeling approach and numerical framework has been demonstrated (Figure 4.5 through Figure 4.7). This framework gives engineers and scientists a tool by which one can approach a variety of different adsorption problems. Building off from this basic framework, it will be possible to develop a variety of other adsorption models to provide a systematic and mechanistic approach to modeling engineered adsorption processes.

4.8 Acknowledgement

The development of this chapter was a collaborative effort between my co-authors and myself and was the main subject of the following manuscript: A. Ladshaw, S. Yiacoumi, R. Lin, Y. Nan, L.L. Tavlarides, C. Tsouris, "A Mechanistic Modeling Framework for Gas Phase Adsorption Kinetics and Fixed-Bed Transport," *AIChE J.*, Submitted February 5th, 2017.

4.9 References

[1] C. Tien, *Adsorption Calculations and Modeling*, Butterworth-Heinemann, Newton, MA, 1994.

[2] J. Tóth (Ed.), *Adsorption Theory Modeling and Analysis*, Marcel Dekker, Inc. New York, NY, 2002.

[3] M. Simo, S. Sivashanmugam, C.J. Brown, V. Hlavacek, *Ind. Eng. Chem. Res.* 48 (**2009**) 9247-9260.

[4] A. Gorbach, M. Stegmaier, G. Eigenberger, *Adsorption*, 10 (**2004**) 29-46.

[5] R. Lin, J. Liu, Y. Nan, D.W. DePaoli, L.L. Tavlarides, *Ind. Eng. Chem. Res.* 53 (**2014**) 16015-16024.

[6] B. Van Leer, *J. Comp. Physics*. 32 (**1979**) 101-136.

[7] A. Kurganov, E. Tadmor, *J. Comp. Physics*. 160 (**2000**) 241-282.

[8] G.D. Van Albada, B. Van Leer, W.W. Roberts, *Astronomy and Astrophysics*, 108 (**1982**) 76-84.

[9] D.A. Knoll, D.E. Keyes, *J. Comp. Physics*, 193 (**2004**) 357-397.

[10] C.R. Wilke, *J. Chem. Phys.* 18 (**1950**) 517-519.

[11] W. Sutherland, *Philosophical Magazine*, 36 (**1893**) 507-531.

[12] N. Wakao, T. Funazkri, *Chemical Engineering Science*, 33 (**1978**) 1375–1384.

[13] F.J. Krieger, *Calculation of the Viscosity of Gas Mixtures*, U.S. Air Force: Project RAND Research Memorandum, RM-649, 1951.

[14] M. Llano-Restrepo, M.A. Mosquera, *Fluid Phase Equilibria*, 283 (**2009**) 73-88.

[15] A. Ladshaw, S. Yiacoumi, C. Tsouris, D.W. DePaoli, *Fluid Phase Equilibria*, 338 (**2015**) 169-181.

[16] V. Rutledge, *OSPREY Model*, U.S. DOE: Separations and Waste Forms, FCRD-SWF-2013-000086, 2013.

[17] R. Lin, A. Ladshaw, Y. Nan, J. Liu, S. Yiacoumi, C. Tsouris, D.W. DePaoli, L.L. Tavlarides, *Ind. Eng. Chem. Res.* 54 (**2015**) 10442-10448.

[18] A. Ladshaw, S. Yiacoumi, C. Tsouris, *AIChE J.* 61 (**2015**) 2600-2610.

[19] Y. Nan, D.W. DePaoli, L.L. Tavlarides, *AIChE J.* 63 (**2016**) 1024-1035.

[20] K.W. Chapman, P.J. Chupas, T.M. Nenoff, *J. Am. Chem. Soc*. 132 (**2010**) 8897-8899.

[21] H. Zhao, T.M. Nenoff, G. Jennings, P.J. Chupas, K.W. Chapman, *J. Phys. Chem. Lett*. 2 (**2011**) 2742-2746.

[22] S.G. Aspromonte, M.D. Mizrahi, F.A. Schneeberger, J.M. López, A.V. Boix, *J. of Phys. Chem. C*. 117 (**2013**) 25433-42.

4.10 Nomenclature

Latin Symbols

a	local maximum wave speed, Equation 4.5
a_c	micro-sphere nominal radius, Equation 4.18
a_p	macro-sphere nominal radius, Equation 4.20
c	intrapellet pore space concentration, Equation 4.19
C	gas phase concentration in bed, Equation 4.21
C_b	bulk gas phase concentration, Equation 4.19
D	dispersion coefficient, Equation 4.3
D_c	micro-pore diffusion, Equation 4.16
D_{ij}	binary diffusivity (cm^2/s), Equation 4.30
d_{in}	inner diameter of the fixed-bed, Equation 4.23
D_k	Knudsen diffusivity (cm^2/s), Equation 4.26
D_m	molecular diffusivity, Equation 4.25
D_p	macro-pore diffusion, Equation 4.19
D_z	axial dispersion coefficient, Equation 4.21
$f(c)$	isotherm function, Equation 4.17
$f(u)$	advective flux function, $f(u) = z^d vu$, Equation 4.3

G gradient flux discretization term, Equation 4.8

g gap jump ratio in sub-domain, Equation 4.14

H average advective flux into or out of a cell, Equation 4.4

h_g heat capacity of the gas, Equation 4.23

h_s heat capacity of the solids, Equation 4.23

k reaction coefficient, Equation 4.3

k_f film mass-transfer coefficient, Equation 4.20

k_{LDF} linear driving force coefficient, Equation 4.39

K_z axial thermal conductivity, Equation 4.23

MW molecular weight (g/mol), Equation 4.26

N nodal flux discretization term, Equation 4.8

p penalty term for advective flux, Equation 4.5

P^o reference state pressure (100 kPa), Equation 4.37

P_T total gas pressure (kPa), Equation 4.31

q adsorption or surface concentration, Equation 4.16

q_e equilibrium adsorption, Equation 4.39

Q_{st} heat of adsorption, Equation 4.23

r micro-sphere radial dimension, Equation 4.16

R retardation coefficient, Equation 4.3

R macro-sphere radial dimension, Equation 4.19

R ideal gas constant (J/K/mol), Equation 4.31

Re Reynolds number, Equation 4.28

r_p nominal macro-pore radius (cm), Equation 4.26

S generic source/sink or forcing function, Equation 4.3

Sc Schmidt number, Equation 4.28

t time, Equation 4.3

T gas phase temperature (K), Equation 4.23

T_w temperature of the wall, Equation 4.23

u conserved quantity, Equation 4.3

u_s superficial gas velocity (cm/s), Equation 4.33

U_w heat transfer coefficient of the wall, Equation 4.23

v advective velocity, Equation 4.3

y gas phase mole fraction, Equation 4.29

z spatial dimensional quantity, Equation 4.3

Greek Symbols

α binder fraction for bi-porous pellet, Equation 4.19

χ temperature correction factor, Equation 4.36

X Sutherland's constant (K), Equation 4.32

Δ change in a quantity

ε_b bulk bed porosity, Equation 4.21

ε_p macro-porosity, Equation 4.19

$\phi(g)$ slope limiter function, Equation 4.13

ϑ minmod dispersion parameter, Equation 4.12

μ gas viscosity (g/cm/s), Equation 4.30

μ_g total gas viscosity (g/cm/s), Equation 4.35

ν_g kinematic viscosity (cm^2/s), Equation 4.33

ρ gas density (g/cm^3), Equation 4.23

ρ_b bulk bed solids density, Equation 4.21

ρ_s pellet density, Equation 4.19

τ tortuosity, Equation 4.25

Sub/superscripts

0 inlet boundary node, Equation 4.9

- approach value from the left, Figure 4.2

+ approach value from the right, Figure 4.2

C center node, Equation 4.8

d spatial exponent, Equation 4.3

i,j indices for different species in a mixture

in inlet or input value

l specific node in a domain

L left node, Equation 4.8

o ideal or reference state

R right node, Equation 4.8

z gradient of variable in z-dimension, Equation 4.7

PART II. URANIUM RECOVERY FROM SEAWATER

CHAPTER 5. IMPACT OF SPECIATION AND IONIC STRENGTH

5.1 Introduction

Uranium recovery from seawater faces a number of challenges, including capacity for uranium, selectivity over competing metals, and durability for deployment in the ocean. During the last few decades, poly(acrylamidoxime) (PAO) has been found to be a chemically suitable adsorbent for capturing uranium. PAO based adsorbents have been tested for uranium uptake from seawater in laboratory-scale[1-5] as well as in natural sea.[6-11] Amidoxime ligand is known to undergo complexation with various metal ions apart besides uranium.[1,12,13] Seawater is a vast source of uranium at a relatively low concentration of 3.3 ppb.[14] The presence of other ions[15] (Table 5.1) at overwhelmingly higher or similar concentrations complicates the recovery of uranium from seawater. Understanding the speciation of uranium in seawater environment is of great importance in the development of strategies for uranium extraction from seawater.

Table 5.1 - Concentration of selected elements in seawater

Element	Conc. (ppm)	Element	Conc. (ppm)
U	0.0033	Na	10,752
V	0.0019	Mg	1,295
Mo	0.01	Ca	416
Rb	0.12	Cl	19,345
Li	0.17	SO_4	2,701
Sr	8.10	HCO_3	145

Extraction of uranium from seawater is further complicated by uranium speciation which is mainly affected by uranyl hydrolysis products and carbonate complexes including $UO_2(CO_3)_3^{4-}$, $UO_2(OH)_3^-$, $UO_2(CO_3)_2^{2-}$, UO_2^+, $UO_2(OH)^+$ and $UO_2(OH)_2$ although the tricarbonate species [$UO_2(CO_3)_3^{4-}$] is the most dominant form by higher abundance (~84.9%).[9, 16-19] However, a recent study by Endrizzi et al.[20] reports that the ternary Ca-UO_2-CO_3 and Mg-UO_2-CO_3 species dominate the aqueous chemistry of uranium and the species, $Ca_2UO_2(CO_3)_3$ (aq) accounts for nearly 60% of uranium species in the ocean. Leggett et al.[21] claimed that calcium and magnesium are expected to occupy a significant fraction of the active sites of amidoxime-based adsorbents due to their overwhelmingly higher concentrations relative to uranium in seawater. Among the other metal ions present in seawater, vanadium not only reduces the uranium adsorption capacity, but also it binds so strongly that eluting this metal may irreversibly damage the adsorbent.[22,23]

Although uranium recovery from seawater is impacted by many factors, the focus of this chapter is mainly on the investigation of effects of speciation and ionic strength on adsorption. This study will explore those effects through both modeling and experimentation. To that end, sets of experiments have been performed at Oak Ridge National Laboratory (ORNL) that varies the concentrations of bicarbonate to quantify how the speciation of uranium with carbonates will affect adsorption. In addition, experiments have been done both in the presence and absence of NaCl to quantify the impact of ionic strength on uranium uptake. Coupled with those experiments is the development of a uranium speciation and adsorption model that will be utilized to explain and predict the observed behaviors.

5.2 Modeling Methods

5.2.1 Numerical Techniques

The system that we intend to model can be reasonably simplified based on the conditions of the laboratory-scale experiments. However, as we look further ahead to modeling a real uranium recovery from seawater system, we realize that the problem is extraordinarily complex. Seawater has specific solution characteristics such as pH (7.5-8.5),[24] temperature (12-40 ºC),[25,26] complex ion speciation,[18,27] and high salt concentration (0.6 – 0.7M)[18,28,29] among others. The overall problem involves multi-species complexation, precipitation, phase changes, adsorption reactions, mass transfer mechanisms, and may even include biological processes. Therefore, a model to handle these complexities must be carefully designed and implemented in a piece-by-piece, or object-oriented fashion.

To accomplish this task, we first divided the problem into its constituent parts and represent each part as a C++ object. For instance, since our problem will clearly involve chemical speciation reactions and several mass balances, we have devised and developed different objects to handle the tasks associated with each different chemical sub-problem. Each object will have an independent residual equation that must be resolved with each other objects' residual equations. Then, the culmination of all those objects and equations will be used to form the overall residual function that will be fed into a non-linear solver routine, which will find the solution to all variables simultaneously.

The underlying solver routine was based on the Jacobian-Free Newton Krylov (JFNK) method,[30] because it is tremendously efficient compared to traditional Newton

methods that require use of the full Jacobian matrix. Linear sub-problems for the non-linear iterations are then solved using either GMRES[31] or GMRESR[32] depending on the problem size and whether or not a linear preconditioner was supplied to the routine. Our implementation of the JFNK method also includes a simple backtracking line search subroutine[33] to ensure smooth convergence of the non-linear system.

5.2.2 Speciation Model

For the laboratory-scale model, we decided to represent the adsorption of uranium by amidoxime-functionalized fibers as standard metal-ligand complexation reactions[34] coupled with speciation reactions between all involved species in solution with mass balances between the major species' groups (i.e., uranium, carbonate, nitrate, etc.). To account for ionic strength, we used the Davies activity model,[35] which is used to account for non-idealities in solutions with ionic strengths up to 0.5 M.

The time evolution of adsorption uses a simple unsteady version of the metal-ligand complexation reactions between uranyl and carbonate ions and the amidoxime ligands (Equation 5.1 and Equation 5.2). Those reaction equations would then formulate the rate expressions for adsorption of the uranium (Equation 5.3 and Equation 5.4). Although this formulation of the problem idealizes the actual kinetics of adsorption, it will allow us to implicitly include the effects of carbonate concentration and pH into the overall adsorption model.

$$UO_2^{2+} + A(OH)_2 \Leftrightarrow UO_2AO_2 + 2H^+ \qquad \textbf{Equation 5.1}$$

$$UO_2^{2+} + CO_3^{2-} + A(OH)_2 \Leftrightarrow UO_2CO_3AO_2^{2-} + 2H^+$$ **Equation 5.2**

$$\frac{d\{UO_2AO_2\}}{dt} = k_{f,1}\{UO_2^{2+}\}\{A(OH)_2\} - k_{r,1}\{UO_2AO_2\}\{H^+\}^2$$ **Equation 5.3**

$$\frac{d\{UO_2CO_3AO_2^{2-}\}}{dt} = k_{f,2}\{UO_2^{2+}\}\{CO_3^{2-}\}\{A(OH)_2\} - k_{r,2}\{UO_2CO_3AO_2^{2-}\}\{H^+\}^2$$ **Equation 5.4**

To finish the construction of this speciation and complexation model, we must add in the equilibrium reactions between all the ions in solution and provide mass balances for all the major species. Equation 5.5 through Equation 5.20 below outline the most important reactions and mass balances for an aqueous system involving uranium, nitrate, and carbonate. Note that reactions involving sodium (Na^+) and/or chlorine (Cl^-) are not shown here. This is because those complexes will typically dissociate completely and are generally only important for ionic strength and electroneutrality calculations.

$$UO_2^{2+} + H_2O \Leftrightarrow UO_2OH^+ + H^+$$ **Equation 5.5**

$$UO_2^{2+} + 3H_2O \Leftrightarrow UO_2(OH)_3^- + 3H^+$$ **Equation 5.6**

$$2UO_2^{2+} + 2H_2O \Leftrightarrow (UO_2)_2(OH)_2^{2+} + 2H^+$$ **Equation 5.7**

$$3UO_2^{2+} + 5H_2O \Leftrightarrow (UO_2)_3(OH)_5^+ + 5H^+$$ **Equation 5.8**

$$UO_2^{2+} + NO_3^- \Leftrightarrow UO_2NO_3^+$$ **Equation 5.9**

$$UO_2^{2+} + 2NO_3^- \Leftrightarrow UO_2(NO_3)_2$$ **Equation 5.10**

$$UO_2^{2+} + CO_3^{2-} \Leftrightarrow UO_2CO_3$$ **Equation 5.11**

$$UO_2^{2+} + 2CO_3^{2-} \Leftrightarrow UO_2(CO_3)_2^{2-}$$ **Equation 5.12**

$$UO_2^{2+} + 3CO_3^{2-} \Leftrightarrow UO_2(CO_3)_3^{4-}$$ **Equation 5.13**

$$HNO_3 \Leftrightarrow H^+ + NO_3^-$$ **Equation 5.14**

$$H_2CO_3 \Leftrightarrow H^+ + HCO_3^-$$ **Equation 5.15**

$$HCO_3^- \Leftrightarrow H^+ + CO_3^{2-}$$ **Equation 5.16**

$$\begin{aligned} U_T = &\left[UO_2^{2+}\right] + \left[UO_2OH^+\right] + \left[UO_2(OH)_3^-\right] \\ &+ 2\left[(UO_2)_2(OH)_2^{2+}\right] + 3\left[(UO_2)_3(OH)_5^+\right] \\ &+ \left[UO_2NO_3^+\right] + \left[UO_2(NO_3)_2\right] + \left[UO_2CO_3\right] + \left[UO_2(CO_3)_2^{2-}\right] \\ &+ \left[UO_2(CO_3)_3^{4-}\right] + \left[UO_2AO_2\right] + \left[UO_2CO_3AO_2^{2-}\right] \end{aligned}$$ **Equation 5.17**

$$N_T = \left[NO_3^-\right] + \left[HNO_3\right] + \left[UO_2NO_3^+\right] + 2\left[UO_2(NO_3)_2\right]$$ **Equation 5.18**

$$\begin{aligned} C_T = &\left[CO_3^{2-}\right] + \left[HCO_3^-\right] + \left[H_2CO_3\right] + \left[UO_2CO_3\right] \\ &+ 2\left[UO_2(CO_3)_2^{2-}\right] + 3\left[UO_2(CO_3)_3^{4-}\right] + \left[UO_2CO_3AO_2^{2-}\right] \end{aligned}$$ **Equation 5.19**

$$A_T = \left[A(OH)_2\right] + \left[UO_2AO_2\right] + \left[UO_2CO_3AO_2^{2-}\right]$$ **Equation 5.20**

Each of these reactions and mass balances will contribute residual functions for the solver routine to work on. That routine solves the speciation/complexation reactions at each discrete time step for the transient problem. To step the simulation through time, we used a standard implicit discretization technique for greater numerical stability. While the routine is intended to run unsteady problems and seek out the system pH using the electroneutrality condition, it can also be run as a steady state simulation and/or hold the system pH constant to a specified value. Additionally, since the major speciation reactions are equilibrium reactions, the model is also implicitly temperature dependent since the stability/dissociation constants are related to temperature through the van't Hoff relationship.

5.3 Experimental Methods

5.3.1 Adsorbent Preparation

Adsorbent fibers were prepared by radiation-induced graft polymerization (RIGP) at the NEO Beam Electron Beam Cross-linking Facility (Middlefield, OH), as described by Das et al.[36] Prior to irradiation, the polylactic acid (PLA) that was protecting the polyethylene trunk fibers was removed by submerging the fibers in excess tetrahydrofuran (THF) at 60 °C overnight. The pre-weighed dry fiber samples were irradiated with the electron beam for 16 passes to a dose of approximately 200 ± 10 kGy using 4.4-4.8 MeV electrons and 1 mA current from an RDI Dynamitron electron beam machine. After irradiation, the fibers were immersed in a 300-mL flask containing previously de-gassed grafting solutions consisting of acrylonitrile (AN) and itaconic acid (ITA) in dimethyl sulfoxide and were then placed in an oven at 64 °C for 18 hours for

grafting. After grafting, the fibers were washed with N', N' dimethyl formamide DMF to remove unreacted monomers and homo polymers, followed by rinsing with methanol and dried at 50 °C under vacuum. The nitriles in the grafted fiber (AF1) samples were converted to amidoxime (AO) by reaction with 10 wt % hydroxylamine hydrochloride in 50/50 (w/w) water/methanol at 80 °C for 72 hours. The samples were then washed under vacuum filtration with deionized water followed by a methanol rinse and allowed to dry at 50 °C under vacuum. The amidoximated AF1 fibers were treated with 0.44 M KOH solution for 1 hour at 70 ºC. The KOH-treated samples were immediately filtered and washed with DI water until the pH was neutral, and then used for the uranium adsorption study.

5.3.2 Batch Experiments

Two different sized batch containers were used in the experiments: 1 L plastic bottles and 5 gallon plastic bottles. In all of the batch experiments, an initial solution sample of one milliliter was collected prior to addition of the adsorbent. The containers were shaken constantly at 100 rpm at room temperature. This agitation speed was proven sufficient for fluidized fibers to adsorb uranium in the reaction-limited regime, i.e., in the presence of bicarbonate ions.[7] One-milliliter aliquot samples were collected periodically over the whole period. The quantitative analysis of the aliquots was carried out using inductively coupled plasma mass spectroscopy (ICP-MS, Thermo Scientific X-Series II). Sample aspiration was performed at 100 μL/min with a Teflon SP nebulizer coupled to an Elemental Scientific Inc. PC^3 and Fast combination spray chamber. An internal standard solution containing Bi, In, Sc, Tb, Y (High Purity Standards ICP-MS-IS-2, Perkin-Elmer)

was added to eliminate the matrix effect. High-purity nitric acid (2%, Optima, Fisher Scientific) was used as the sample diluent and carrier phase and for wash out of the instrument, which was monitored between samples. The average of six replicate measurements per sample was used to quantify uranium-238 against a 6-point calibration curve. The standards, NASS-5 (seawater) and CASS-6 (seawater) supplied by the National Research Council of Canada, were used for seawater quality-control experiments.

5.3.2.1 Effect of Speciation and Salinity

AF1 adsorbents (~8 mg), conditioned with 0.44 M of KOH at 60 ºC for 1 hour, were added into three 5-gallon plastic containers with de-ionized water, where adsorbent fibers were freely suspended. Deionized water in container 1 was spiked only with 10 ppm uranium in the form of nitrate. Sodium bicarbonate (140 ppm) was added along with 10 ppm uranium, in the form of nitrate, in container 2. Sodium chloride (0.43M) was added in container 3 in addition to uranium nitrate and sodium bicarbonate at similar concentrations as in containers 1 and 2. The concentrations of sodium bicarbonate and sodium chloride were maintained as those in seawater. After adsorbent fibers were brought in contact with the solution, the experiments continued for a period of 57 days. During this period, samples of the solution were periodically taken to determine the uranium concentration vs time. Additionally, vanadium in the form of sodium orthovanadate (Na_3VO_4) was added in the 5-gallon plastic containers, after completion of these experiments. The objective was to investigate possible replacement of uranium adsorbed by the AF1 adsorbent by vanadium. These experiments lasted for another 43 days.

5.3.2.2 Effect of Bicarbonate Concentration

The study of the effect of bicarbonate concentration was carried out in 1 L bottles containing deionized water spiked with 0.43 M sodium chloride, 75 ppm uranium nitrate and different concentrations of sodium bicarbonate (i.e., 0, 35, 70, and 140 ppm). AF1 adsorbent fibers (~8 mg), conditioned with 0.44 M of KOH at 70 ºC for 1 hour, were added into 1 L plastic bottles, which underwent constant shaking at room temperature over a period of 28 days exposure.

5.4 Results and Discussion

5.4.1 Experimental Results

Uranium speciation has a strong effect on the adsorption kinetics. The results of 5-gallon batch reactor experiments on the effect of different uranium speciation on adsorption by AF1 adsorbent fibers are demonstrated in Figure 5.1. The uranium uptake kinetics from solution spiked only with uranyl nitrate is very fast. However, the kinetics is slowed down after addition of sodium bicarbonate and sodium chloride, indicating that: (i) salinity plays an important role on adsorption kinetics and (ii) bicarbonate strongly competes with amidoxime for uranium binding.

An investigation for the effect of bicarbonate concentration on uranium adsorption was also conducted. In these experiments, the uranium concentration was kept constant (75 ppb) and the bicarbonate concentration was varied the in the solution (from 0 to 140 ppm HCO_3^- by adding $NaHCO_3$). The results of this study are illustrated in Figure 5.2. As can be seen in this figure, increasing the bicarbonate concentration in the

solution gradually slowed the uranium adsorption kinetics down. This observation suggests that bicarbonate effectively competes with amidoxime ligand on the AF1 adsorbent for uranium complexation in seawater conditions.[37]

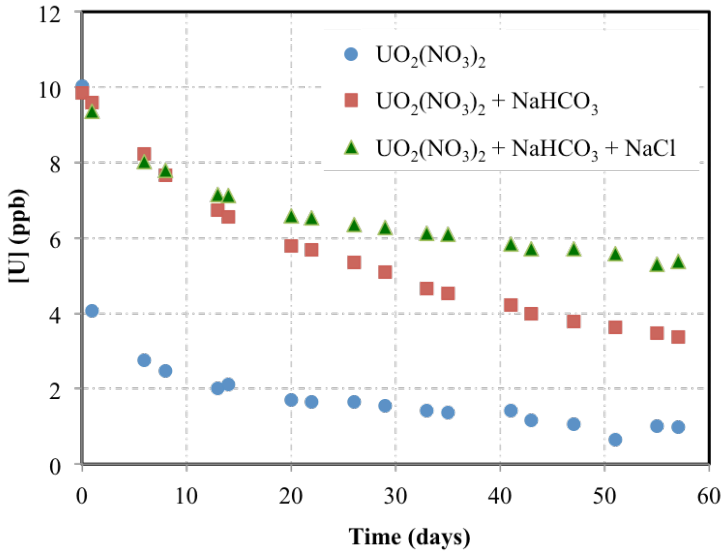

Figure 5.1 - The kinetics of uranium uptake by AF1 adsorbent under various conditions. The initial concentration of uranium in all solutions was 10 ppb.

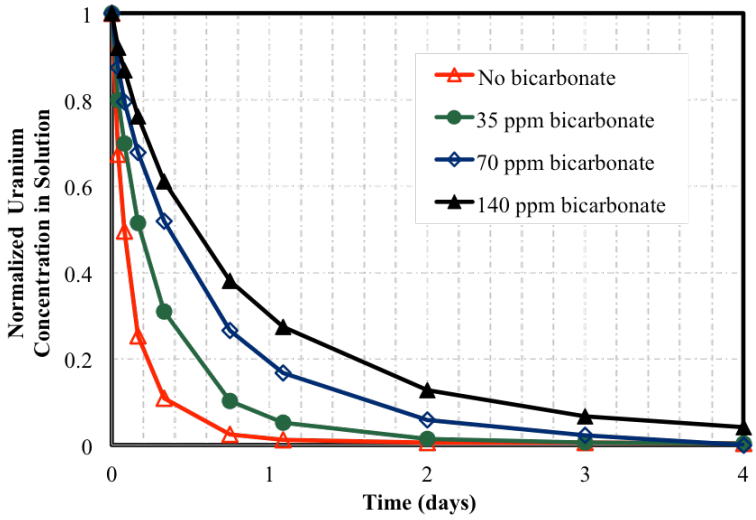

Figure 5.2 - Kinetics of uranium uptake by AF1 adsorbent in presence of different concentrations of bicarbonate. The uranium concentrations were kept constant at 75 ppb.

5.4.2 Model Calibration

To model the lab scale experiments, we need to have all the necessary chemical parameters that describe the system. These parameters include equilibrium constants for the speciation reactions from Equation 5.5 through Equation 5.16, as well as the rate constants for the metal-ligand complexation reactions from Equation 5.3 and Equation 5.4. For the basic speciation reactions (Equation 5.5 through Equation 5.16), the equilibrium parameters can be found recorded in various literature sources.[35,38] However, the thermodynamic and kinetic parameters for amidoxime complexation are not known. Therefore, those parameters are calibrated for based on the experimental data.

For parameter calibration, we used the 5-gallon batch experimental data sets (Figure 5.1) to find the optimum equilibrium and kinetic parameters for Equation 5.1 through Equation 5.4. Concentrations of adsorbed uranium from these experiments were determined from a mass balance based on the mass of fibers added and the concentration of aqueous uranium remaining. The experiment which did not involve carbonate in the system (blue diamonds: Figure 5.1) will be used to find the parameters for Equation 5.1 and Equation 5.3, while the experiments with 140 ppm of sodium bicarbonate, both with (red squares: Figure 5.1) and without 0.43 M of NaCl (green triangles: Figure 5.1), will be used to find the parameters for Equation 5.2 and Equation 5.4. Ideally, all experiments should be describable from the same set of equilibrium and kinetic parameters.

Calibration of the equilibrium constant for Equation 5.1 is fairly straightforward. This parameter is varied until we see an agreement between the model's steady-state solution and the projected adsorption equilibrium of 23.5 mg-U/g-adsorbent. However, to

calibrate the kinetics of the model requires a more detailed analysis of the data. We know that the reaction kinetics of uranyl with amidoxime, in the absence of carbonate, is very fast,[2] but the data show a sharp uptake after 1 day, which is then followed by a slow, gradual increase in adsorption capacity over time (blue diamonds: Figure 5.1). This indicates that the initial adsorption on the outer surface of the adsorbent fiber is likely reaction controlled, but the long-term adsorption of uranyl into the fiber is diffusion controlled.

To model this data more accurately, we devised a 2-part model in which the adsorption from experiment start to end of day 1 consisted of only the reaction expression from Equation 5.3. Then, after that initial loading, it is assumed that intraparticle diffusion dominates the kinetic uptake of uranyl ions. The diffusion portion of the model was done using a cylindrical diffusion equation where the concentration on the outer edge of the cylinder is assumed constant (Equation 5.21).[39] In this model, a is the radius of a single fiber, D is the diffusion coefficient of uranyl through the polyethylene, $q(t)$ and q_e are average fiber adsorption and equilibrium adsorption respectively, and α_n are roots of the zero order Bessel function[39], $J_o(a\alpha_n)=0$.

$$\frac{q(t)}{q_e} = 1 - \sum_{n=1}^{\infty} \frac{4}{\left(a\alpha_n\right)^2} \exp\left(-D\alpha_n t\right) \qquad \textbf{Equation 5.21}$$

The results of the calibrated reaction kinetic model and combined reaction/diffusion model are shown in Figure 5.3, and parameters used for this model are detailed in Table 5.2. These results clearly suggest that when carbonate is not present, reaction kinetics is extremely fast and the overall uptake of uranium becomes primarily

controlled by long-term intraparticle diffusion. Additionally, we see that by combining both reactions and diffusion into the model, we can significantly improve the model's description of the experimental data.

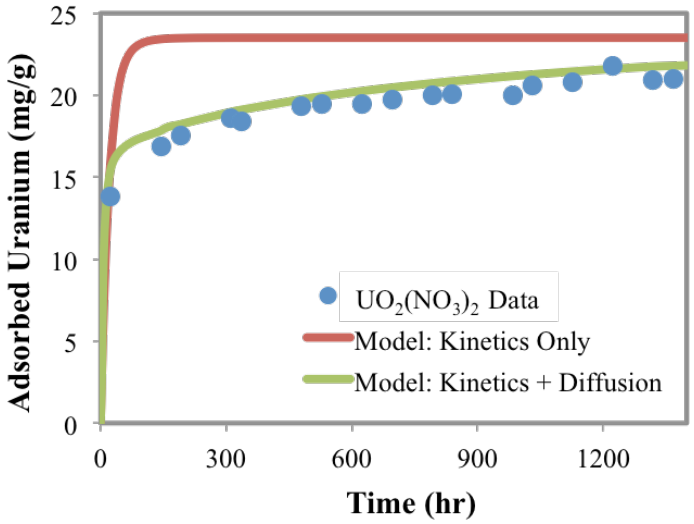

Figure 5.3 - Comparison between experimental data [from Figure 5.1] and the reaction-based and reaction/diffusion models. Results indicate that in the absence of carbonate, long-term uranyl uptake is primarily intraparticle-diffusion controlled.

Table 5.2 - Summary of model parameters

Equation/Model	**log(*K*)**	**k_f (L/mol)^m/hr**
Equation 5.1 & Equation 5.3	-1.35	4.50E+06
Equation 5.2 & Equation 5.4: *No Salt*	3.45	5.75E+15
Equation 5.2 & Equation 5.4: *0.43 M NaCl*	3.45	8.90E+15
Equation 5.2 & Equation 5.4: *Averaged*	3.45	7.30E+15
Equation/Model	***D*** **µm^2/hr**	***a*** **µm**
Equation 5.21	1.05	76.5

Five-gallon experiments with bicarbonate (Figure 5.1) were used to calibrate the model parameters associated with the uranyl, carbonate, and amidoxime complexation reactions of Equation 5.2 and Equation 5.4. While the optimum equilibrium parameters from each data set were found to be the same, the optimum kinetic parameters did vary slightly with salt content. To create a single set of parameters for all data sets used, a weighted average of the kinetic parameters optimized for the experiments both with and with out salt was created. All of the model parameters are summarized in Table 5.2.

Figure 5.4 shows the comparison between the complexation reaction models' with the experimental data both with and without added salt. The solid lines show the optimized model, while the dashed lines show the averaged model. Discrepancies between the models' optimum values with and without salt present are likely caused by errors introduced by the activity model. In both cases, the systems have the same uranium, carbonate, and amidoxime concentrations, but the introduction of NaCl into the system has a significantly raised the ionic strength. Therefore, the only difference mathematically between the two models would be the activity coefficients determined through the Davies activity model. Since the Davies model is a semi-empirical activity model that only calculates the average activity of each charged species in solution, it is possible that this is the primary cause of error in the model for this set of simulations.

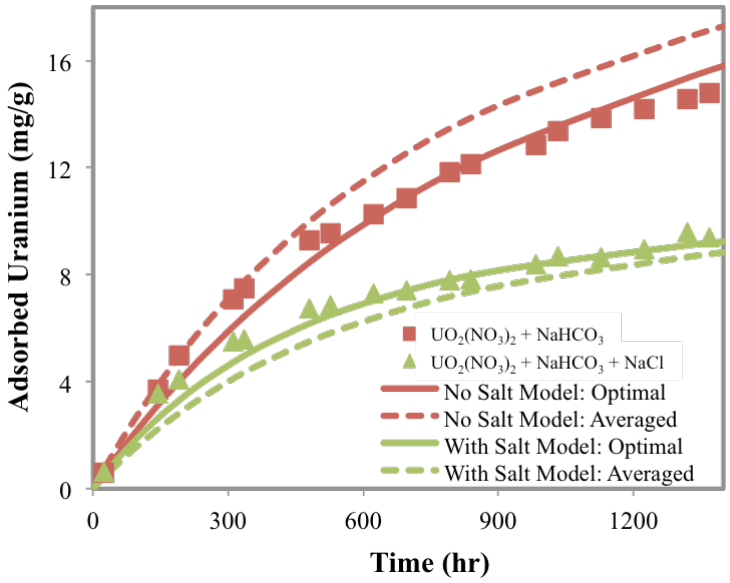

Figure 5.4 - Comparison between the complexation reaction models for adsorption and the data collected in 5-gallon batch reactors (Figure 5.1) with and without salt present. The total carbonate and uranium concentrations were 140 ppm and 10 ppb, respectively.

5.4.3 Model Validation

After calibrating the model with the experimental data from the 5-gallon experiments, we can use the optimal parameters to try to predict the behavior of the system at different conditions, i.e., different uranium and carbonate concentrations, as a validation step for our model. For this validation, we modeled attempted to predict the data observed in the 1 L system containing 0.43 M of NaCl, 75 ppb of uranium, 8 mg of amidoxime fibers, and various concentrations of carbonate (Figure 5.2). These predictions were based solely on our kinetic model described in Equation 5.1 through Equation 5.20 and the parameters from Table 5.2.

Figure 5.5 shows the comparisons between the experimental data and the model predictions based on the calibrations with the 5-gallon experiments. The model performed reasonably well to predict the aqueous uranium removal at a carbonate concentration of 35 and 70 ppm. Additionally, we can also see that the model qualitatively responded correctly to the stimuli: (i) faster overall kinetics, compared to the 5-gallon experiments, when uranium levels were increased and (ii) a reduction in the removal rates as the carbonate concentration increases. However, the model predictions at 140 ppm and 0 ppm showed kinetics that were too slow and too fast, respectively, resulting in a relatively poor overall prediction of the system at all conditions.

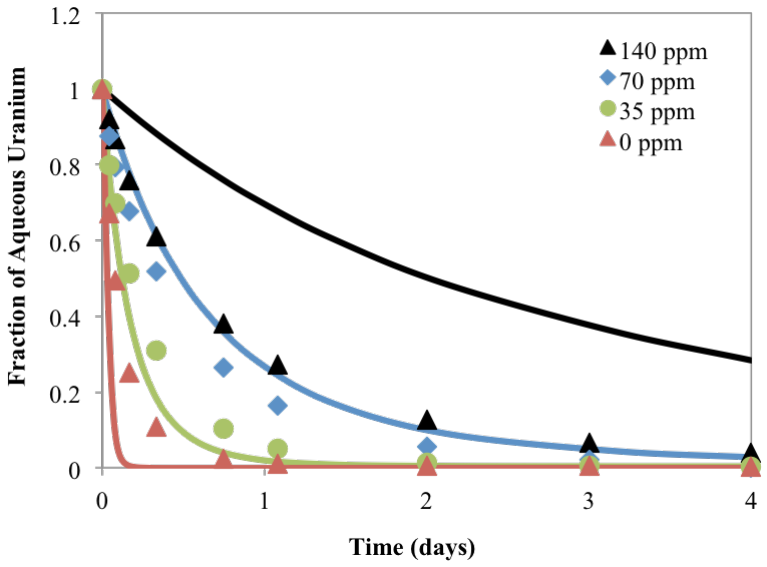

Figure 5.5 - Comparison between model predictions and experimental data at various carbonate concentrations. The model predicts the 35 and 70 ppm bicarbonate experimental data fairly well, but over estimates the kinetics at 0 ppm and underestimates the kinetics at 140 ppm.

There are two possible explanations for the errors observed between our model and the data in Figure 5.5: (i) as the carbonate concentration decreases, the controlling uptake mechanism switches from reaction controlled to diffusion controlled, as demonstrated in Figure 5.3, or (ii) the simple rate equations derived for the complexation reactions with amidoxime are too much of a simplification of the actual adsorption reaction kinetics. We know from our analysis of the data in Figure 5.3 that the diffusion process becomes dominant when no carbonate is present. Therefore, intraparticle diffusion may still be important even at low carbonate concentrations, which will contribute to the errors observed in the model results at 0 ppm of carbonate. Other errors are most likely introduced by our model only considering an overall, unsteady complexation reaction (Equation 5.3 and Equation 5.4) instead of a reaction mechanism. A better model would probably be to represent the adsorption process based on an actual adsorption mechanism coupled with intraparticle diffusion.

5.5 Conclusions

Investigations on how speciation and salinity affecting the kinetics of uranium adsorption from seawater were successfully demonstrated experimentally and theoretically. The speciation study revealed that bicarbonate strongly competes with amidoxime sites for uranium binding, and thus slowed down the uranium adsorption kinetics. The uranium uptake kinetics was initially much faster in the absence of bicarbonate, and gradually decreased with increasing bicarbonate concentration in the solution.

Although our simple kinetic model worked well to describe the uptake kinetics of the 5-gallon experiments, it was less adequate of accurately modeling systems in the absence of carbonate, where diffusion became important. Therefore, we must include mass transfer effects into the overall model. Additionally, we have shown that this simplified kinetic model did not perform well to quantitatively predict all of the 1 L experiments. This may be partially attributed to the lack of mass transfer in the model, but may also be attributable to the over simplification we made in the representation of the reaction kinetics from the complexation reactions in Equation 5.3 and Equation 5.4, instead of using a reaction mechanism for the kinetics.

From these results, we have a clear path forward for improvement of the model, but we also are able to show the strengths of this model as well. By representing the system with its full suite of species and thermodynamic speciation constants, the model is capable of implicitly including the effects of pH, ionic strength, temperature, and concentration of each species. This capacity was demonstrated through the model's kinetic results when the system parameters were altered from Figure 5.3 through Figure 5.5. When uranium concentration increased from 10 ppb (Figure 5.3 and Figure 5.4) to 75 ppb (Figure 5.5), the uptake kinetics became much faster, as indicated by the time scales on the figures. Additionally, when the carbonate concentration was reduced (Figure 5.5), the model responded accordingly and showed an increase in the rate of uranium removal. Therefore, the model does respond qualitatively correctly to external stimuli, but does need to include mass transfer effects and reaction mechanisms to fully describe our system.

5.6 Acknowledgement

The development of this chapter was a collaborative effort between my co-authors and myself and was the main subject of the following publication: A. Ladshaw, S. Das, W. Liao, S. Yiacoumi, C.J. Janke, R.T. Mayes, S. Dai, C. Tsouris, "Experiments and Modeling of Uranium Uptake by Amidoxime-Based Adsorbent in the Presence of Other Ions in Simulated Seawater," *Ind. Eng. Chem. Res.* 55 (**2016**) 4241-4248.

5.7 References

[1] A. Nilchi, R. Rafiee, A.A. Babalou, *Macromol. Symp.* 274 (**2008**) 101−108.

[2] S. Das, A.K. Pandey, A.A. Athawale, V.K. Manchanda, *J. Phys. Chem. B*, 131 (**2009**) 6328−6335.

[3] T. Caykara, F. Cakar, S. Demirci, *Polym. Int.* 60 (**2011**) 141−145.

[4] O. Hazer, S. Kartal, *Anal. Sci.* 25 (**2009**) 547−551.

[5] Y. Yue, R.T. Mayes, G. Gill, L.-J. Kuo, J. Wood, A. Binder, S. Brown, S. Dai, *RSC Advances*, 5 (**2015**) 50005-50010.

[6] J. Kim, C. Tsouris, Y. Oyola, C.J. Janke, R.T. Mayes, S. Dai, G. Gill, L.-J. Kuo, J. Wood, K.Y. Choe, E. Schneider, H. Lindner, *Ind. Eng, Chem. Res. 53* (**2014**) 6076-6083.

[7] J. Kim, Y. Oyola, C. Tsouris, C.R. Cole, R.T. Mayes, J.C. Janke, S. Dai, *Ind. Eng. Chem. Res.* 52 (**2013**) 9433-9440.

[8] T. Saito, S. Brown, S. Chatterjee, J. Kim, C. Tsouris, R.T. Mayes, L.-J. Kuo, G. Gill, Y. Oyola, C.J. Janke, S. Dai, *J. Mater. Chem. A,* 2 (**2014**) 14674-14681.

[9] K. Sekiguchi, K. Saito, S. Konishi, S. Furusaki, T. Sugo, H. Nobukawa, *Ind. Eng. Chem. Res.* 33 (**1994**) 662−666.

[10] A. Goto, K. Kusakabe, S. Morooka, T. Kago, *Sep. Sci. Technol.*, 28 (**1993**) 1273−1285.

[11] A. Zhang, T. Asakura, G. Uchiyama, *React. Funct. Polym.* 57 (**2003**) 67-76.

[12] J. Kim, C. Tsouris, R.T. Mayes, Y. Oyola, T. Saito, C.J. Janke, S. Dai, E. Schneider, D. Sachde, *Sep. Sci. Technol*. 48 (**2013**) 1−21.

[13] X. Liu, H. Chen, C. Wang, R. Qu, C. Ji, C. Sun, Q. Xu, *Polym. Adv. Technol.* 22 (**2011**) 2032−2038.

[14] K. Oguma, T. Suzuki, K. Saito, *Talanta*, 84 (**2011**) 1209–1214.

[15] K.K. Turekian, *Oceans*, Prentice Hall Inc., Englewood Cliffs , NJ, 1968.

[16] A. Zhang, G. Uchiyama, T. Asakura, *React. Funct. Polym.* 63 (**2005**) 143–153.

[17] T. Aihara, A. Goto, T. Kago, K. Kusakabe, S. Morooka, *Sep. Sci. Technol.* 27 (**1992**) 1655–1667.

[18] H. Yamashita, Y. Ozawa, F. Nakajima, T. Murata, *Bull. Chem. Soc. Jpn.* 53 (**1980**) 1331–1334.

[19] C. Gotz, G. Geipel, G. Bernhard, *J. Radioanal Nucl. Chem.* 287 (**2011**) 961-969.

[20] F. Endrizzi, L. Rao, *Chem. Eur. J*. 20 (**2014**) 14499-14506.

[21] C.J. Leggett, L. Rao, *Polyhedron*, 95 (**2015**) 54-59.

[22] S.P. Kelley, P.S. Barber, P.H. Mullins, R.D. Rogers, *Chem. Commun.* 50 (**2014**) 12504-12407.

[23] T. Suzuki, K. Saito, T. Sugo, H. Ogura, K. Oguma, *Anal. Sci.* 16 (**2000**) 429.

[24] A. Zhang, T. Asakura, G. Uchiyama, *React. Funct. Polym.* 57 (**2003**) 67–76.

[25] M. Tamada, N. Seko, F. Yoshii, *Radiat. Phys. Chem.* 71 (**2004**) 221–225.

[26] B. Zheng, S. Cai, M. Zhuang, L. Jiang, *Haiyang Xuebao.* 7 (**1985**) 34–39.

[27] H. Yamashita, Y. Ozawa, F. Nakajima, T. Murata, *Bull. Chem. Soc. Jpn.* 53 (**1980**) 1–5.

[28] B.B. Benson, D. Krause, Jr. *Limnol. Oceanogr.* 29 (**1984**) 620–632.

[29] K. Sugasaka, S. Katoh, N. Takai, H. Takahashi, Y. Imezawa, *Sep. Sci. Technol.* 16 (**1981**) 971–985.

[30] D.A. Knoll, D.E. Keyes, *J. Comp. Phys.* 193 (**2004**) 357-397.

[31] Y. Saad, M.H. Schultz, *SIAM J. Sci. Stat. Comp.* 7 (**1986**) 856-869.

[32] H.A. Vorst, C. Vuik, *GMRESR: A family of nested GMRES methods*, Faculty of Technical Mathematics and Informatics, Delft, ND, 1992.

[33] J.E. Dennis, R.B. Schanbel, *Numerical Methods for Unconstrained Optimization and Nonlinear Equations*, Prentice-Hall Inc., Englewood Cliffs, NJ, 1983.

[34] S. Yiacoumi, C. Tien, *Kinetics of Metal Ion Adsorption from Aqueous Solutions*, Kluwer Academic Publishers, Boston, MA, 1995.

[35] M.M. Benjamin, *Water Chemistry*, Waveland Press, Inc., Illinois, 2010.

[36] S. Das, Y. Oyola, R.T. Mayes, C.J. Janke, L.-J. Kuo, G.A. Gill, J.R. Wood, S. Dai, *Ind. Eng. Chem. Res*. 55 (**2016**) 4110-4117.

[37] G. Tian, S.J. Teat, Z. Zhang, L. Rao, *Dalton Trans.* 41 (**2012**) 11579-11586.

[38] R. Guillaumont, T. Fanghanel, V. Neck, J. Fuger, D.A. Palmer, I. Grenthe, M.H. Rand, *Update on the Chemical Thermodynamics of Uranium, Neptunium, Plutonium, Americium, and Technetium*, Elsevier B.V., Amsterdam, ND, 2003.

[39] J. Crank, *The mathematics of diffusion*, 2nd Ed., Oxford University Press, England, 1975.

5.8 Nomenclature

Latin Symbols

a	single fiber radius
A_T	total amidoxime concentration in system
C_T	total carbonate concentration in system
D	intraparticle diffusivity for uranyl in polyethylene
$k_{f,r}$	forward and/or reverse reaction rates for unsteady reactions
m	exponent for the units of the reaction rate constants
N_T	total nitrate concentration in system
q_e	equilibrium adsorption capacity for uranyl
$q(t)$	average uranyl adsorption on the fibers
U_T	total uranium concentration in system

Greek Symbols

α_n roots of the zero order Bessel function, $J_o(a\alpha_n)=0$

CHAPTER 6. EFFECT OF PH AND COMPETING METALS

6.1 Introduction

Uranium in seawater is naturally occurring and is found usually in the form of the stable uranyl tricarbonate ion[1] ($UO_2(CO_3)_3^{4-}$) or a neutrally charged derivative, such as $Ca_2UO_2(CO_3)_3$.[2] Part of the challenge of recovering uranium from seawater is in the development of materials that can dissociate the uranyl ion (UO_2^{2+}) from those stable aqueous species in order to capture the uranium. In addition, extraction of uranyl is further complicated due to uranium being present at very low concentrations (3.3 μg/L) in seawater.[3,4] Over the last several decades, many materials and methods have been developed[5-9] for the recovery of uranium from seawater, but polymers functionalized with amidoxime ligands have shown the greatest promise.[10,11]

One of the best performing adsorbent materials so far is a polyamidoxime-functionalized polyethylene (PAO) fiber developed by Oak Ridge National Laboratory (ORNL), which reportedly captured 3.3 mg-U/g-adsorbent after roughly 60 days in contact with natural seawater.[12] This material is the same one examined in CHAPTER 5. A major problem with this material seems to be in the selectivity for uranium over other metal ions in solution. In particular, high vanadium uptake[13] was observed in real seawater experiments with the PAO fiber, which suggests that vanadium ions (VO_2^+) may be competing with uranyl for adsorption sites. Additionally, other studies have shown that vanadium is so strongly bonded to the PAO fibers that the harsh elution process needed to remove vanadium can damage and lower the reusability of the material.[14,15] Therefore, it is expected that design of new ligands with a greater selectivity

for uranyl over vanadium ions will aid in the enhancement of uranium recovery without sacrificing material durability.

To design ligands with the desired selectivity properties for uranium requires a comprehensive computational approach starting from small molecule studies and scaling up into process level models for adsorption. In addition, that approach must be validated with known experimental values and experimental data for uranium and vanadium capture from bulk solution. In this work, quantum chemical methods are utilized to determine metal-ligand reaction schemes and binding strengths for the complexation between uranyl and vanadium ions with open-chain amidoxime and cyclic imide-dioxime ligands. Coupled with that *ab initio* approach is the development of an aqueous adsorption model that will evaluate how much uranium and vanadium can be captured by the adsorbent based on the reaction schemes and binding constants from quantum calculations, as well as other solution information such as pH, ionic strength, aqueous speciation, etc. The culmination of these computational methods in adsorption is intended to create a closed-loop design process for ligands that can predict the adsorption and selectivity of the materials.

6.2 Experimental Methods

6.2.1 Materials

The adsorbent used in this study was the AF1 PAO-PE fibers developed at ORNL (same material from CHAPTER 5).[16,17] This material is formed from high-surface-area hollow gear, poly-ethylene fibers that were grafted with poly-acrylonitrile and itaconic acid using radiation-induced graft polymerization (RIGP). Subsequently, the fibers were

amidoximated with hydroxylamine in a methanol/water mixture, whereby the nitrile group was converted to amidoxime groups. Prior to use in the experiment, the AF1 fibers were conditioned with 0.44 M KOH at 80 ^{o}C for 1 hour. Additional details regarding this material are described by Das et al.[16] and Kuo et al.[17]

6.2.2 Capacity Studies

Four different studies with the AF1 fibers were conducted in this work. The first study was performed to assess the maximum uranium uptake capacity of the AF1 fibers. In these experiments, adsorbent fibers were placed in a batch solution at 20 ^{o}C containing only uranyl nitrate ($UO_2(NO_3)_2$) and DI water. The pH of that solution was controlled using NaOH and/or HCl as needed to maintain a pH of 6 throughout each experiment. This was done because it has been previously determined that uranyl binds most favorably with amidoxime at the pH of 6, thus it is expected that the maximum adsorption capacity would occur at that pH.[18]

In each experimental run, the batch system was allowed to come to equilibrium before quantifying the uranium adsorption. The amount of uranyl adsorbed onto the fibers was measured based on the initial and final concentrations of uranium in solution, as well as acidification of the fibers to strip the adsorbed uranium. This was repeated four times at increasing concentrations of uranyl nitrate until we could approximate the maximum adsorption capacity of the material.

6.2.3 pH Studies

The next three studies were performed to determine the effect of pH on (i) the adsorption of uranium, (ii) the adsorption of vanadium, and (iii) the adsorption selectivity between uranium and vanadium for the AF1 fibers at various pH levels. In each of these studies, simulated seawater solutions at 20 ^{o}C were prepared in 750 mL batches containing 193 ppm of $NaHCO_3$ and 0.43 M NaCl to emulate the salinity and carbonate concentration of real seawater. HCl and NaOH were added to control the solution pH to a desired level during each experiment.

In each of the pH studies, roughly 15 mg of AF1 fibers were added to the batch solutions for adsorbing uranium and vanadium. For studies involving uranium, uranyl nitrate ($UO_2(NO_3)_2$) was added to solution to achieve an aqueous uranium concentration of 7.6 ppm, while studies with vanadium involved the addition of sodium orthovanadate (Na_3VO_4) to reach a vanadium concentration of 2.9 ppm. Table 6.1 below provides a summary of the experimental conditions for each of the pH studies performed in this work.

Table 6.1 - Summary of experimental conditions for the pH studies

All pH Studies	
Temperature	20 ^{o}C
Volume	750 mL
Adsorbent Mass	15 mg
$NaHCO_3$	193 ppm
NaCl	0.43 M
Uranium Adsorption Study	
U in form of $UO_2(NO_3)_2$	7.6 ppm
Vanadium Adsorption Study	
V in form of Na_3VO_4	2.9 ppm
U/V Selectivity Study	
U in form of $UO_2(NO_3)_2$	7.6 ppm
V in form of Na_3VO_4	2.9 ppm

6.3 Molecular Studies

6.3.1 Quantum Chemical Methods

The Gaussian 09 D.01 software was used to perform electronic structure calculations in this work.[19] Density functional theory (DFT) was applied using the B3LYP[20,21] and M06[22] functionals coupled with the Stuttgart small-core (SSC) potentials to account for relativistic effects. The basis sets used for vanadium and uranium were the Dunning correlation-consistent sets of [6s/5p/3d/1f] and [8s/7p/6d/4f], respectively. Solvent corrections for gas-phase geometries were computed at 25 ^{o}C using the solvation model based on density (SMD),[23] as implemented in the Gaussian 09 software. Additional details regarding the quantum chemical calculations are reported by Ivanov and Bryantsev.[24]

6.3.2 Stability Constant Calculations

Complexation free energy and stability constants (log K), for a given reaction between some aqueous metal and a free ligand, were calculated using the solvation model described by Vukovic et al.[25] This approach considers a thermodynamic cycle involving the calculation of the gas-phase free energies and the change in free energy upon transfer of 1 mole of a species from the gas to the aqueous phase. Once the various free energy terms of the cycle are calculated from the quantum chemical solvation model, then the change in free energy for the aqueous reaction (ΔG_{aq}) can be calculated and coupled with the van't Hoff equation to estimate the stability constants (Equation 6.1). This model has already been validated for uranyl and vanadium complexes and is described in greater detail by Ivanov and Bryantsev[24] and Vukovic et al.[25]

$$\log K = -\frac{\Delta G_{aq}}{2.303RT} \qquad \textbf{Equation 6.1}$$

6.3.3 Ligands of Interest

For this work, the ligands that are of greatest interest are those that are grafted to the AF1 fiber adsorbents from ORNL. A typical PAO adsorbent fiber will contain polyethylene or polypropylene as a trunk polymer, which contains amidoximated PAN that was copolymerized with some hydrophilic groups, e.g., itaconic acid (Figure 6.1). Prior studies[26,27] have identified that the conversion of PAN to PAO leads to the simultaneous formation of open-chain amidoxime and cyclic imide-dioxime ligands. Thus, comparison between the binding strengths of these two ligands with uranium and

vanadium could provide some insight for optimization of the grafting process and improve selectivity of new materials being developed.

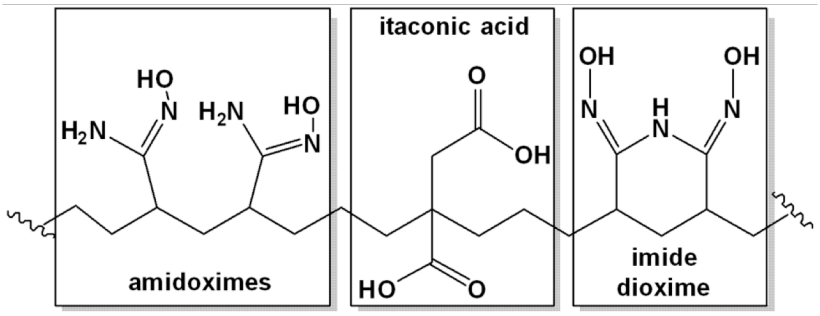

Figure 6.1 - Schematic depiction of a small subsection of the PAO polymer chain grafted onto the fibers.

To quantify the binding strengths between uranium, vanadium, and the identified ligands of interest, stability constants for two surrogate ligand molecules were examined: (i) acetamidoximate (Figure 6.2a) and (ii) glutarimidedioximate (Figure 6.2b). These ligands were the chosen for the molecular studies because they would most closely resemble the actual functional groups grafted on the polymer trunk of the AF1 fibers (Figure 6.1). In this work, reaction schemes between uranium and vanadium with these ligands were formulated based on the solvation model described above,[24,25] and stability constants were estimated for those reactions at 25 ^{o}C and zero ionic strength. Those reactions and parameters were then utilized in a process level adsorption model to predict the total uptake of uranium and vanadium by the AF1 fibers.

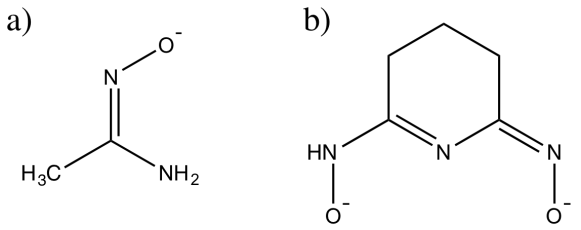

AO^- $HIDO^{2-}$

Figure 6.2 - Drawing of the (a) Acyclic acetamidoximate (HAO^-) and (b) cyclic glutarimidedioximate ($HIDO^{2-}$) ligands.

6.4 Adsorption Modeling

6.4.1 Model Basics

The adsorption model has been constructed in such a way that it can inherently include the various mechanisms and parameters that control the aqueous and surface reactions occurring in the system. Those effects include, but are not limited to, variations in pH, temperature, ionic strength, molar concentrations, and competing ions for the binding of uranium and vanadium.[28-30] As a result, our approach to the foundation of the adsorption model is similar to that of the MINEQL[31,32] software package, but with added flexibility and a focus on surface reaction modeling. Additional details regarding the basics of the model are given in APPENDIX B. Aqueous Adsorption Details.

6.4.2 Surface Reactions

To represent the adsorption reactions that occur on the adsorbent surface, consider the diagram in Figure 6.3. In this illustration of the surface phase, there are a number of reactive sites or ligands (semi-circles and triangles) that may bond with positive or

negative ions in solution (ovals and diamonds) to form new surface species. Additionally, those surface species may become involved in non-bonding interactions with other surface species or other salts in solution, as indicated by the dashed lines in Figure 6.3. These additional interactions may create non-idealities for surface adsorption[33] and/or charge neutralization of the adsorbent surface.[34]

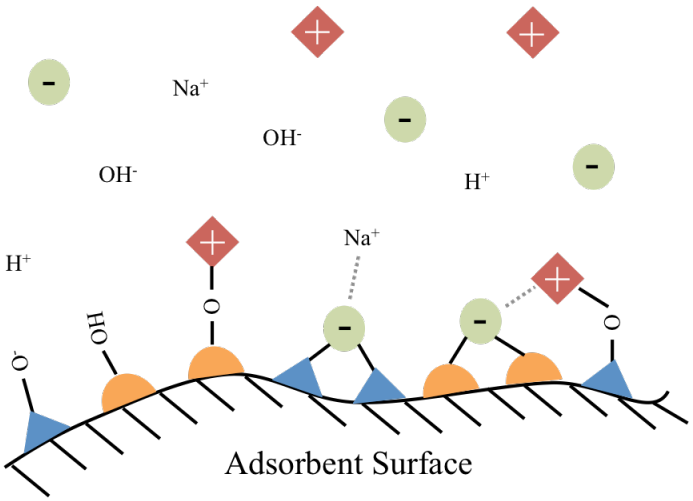

Figure 6.3 - Schematic diagram to represent adsorption of ions from bulk solution onto a surface that may be composed of multiple ligands or reactive sites. Bonding reactions are represented by solid lines to the ions (diamonds and/or ovals), and dashed lines represent the non-bonding interactions.

Surface reactions in our model are represented mathematically as shown in Equation 6.2. In this generalized expression, the specific adsorbate is identified by the *i* subscript, while any other aqueous ions involved in the reaction are denoted by *j* and *k* subscripts. Activities of the participating aqueous ion are denoted by curly bracket notation (i.e., $\{i\}$ is the activity of the i^{th} aqueous species), and the stoichiometry is

denoted by υ. The subscript l denotes a different ligand for each reaction, which can involve different numbers of sites ($m_{i,l}$) for the adsorbate/ligand pair. Molar concentration of available sites for the l^{th} ligand is represented by $[L\phi]_l$, and $\{q_{i,l}\}$ represents the adsorption activity of the i^{th} adsorbate to that site.[29,34] Note that the subscripts of i,l refer to the i^{th} adsorbate that is bonded with the l^{th} ligand.

$$\upsilon_i\{i\} + \sum_j \upsilon_j\{j\} + m_{i,l}[L\phi]_l \Leftrightarrow \{q_{i,l}\} + \sum_k \upsilon_k\{k\} \qquad \textbf{Equation 6.2}$$

The concentration of available ligands on the surface is the difference between the maximum surface density ($L_{\max,l}$) of the l^{th} ligand and the molar adsorption concentration ($q_{i,l}$) of the occupied ligand sites (Equation 6.3). Equilibrium constants for each adsorption reaction ($K_{i,l}$) are represented very similarly to those for aqueous reactions (Equation 6.4) except that they also include the surface activity coefficient ($\gamma^{s}_{i,l}$) and the Boltzmann factor ($\eta_{i,l}$). The surface activity coefficient is a parameter that can be used to account for non-ideal, non-bonding surface interactions,[33,35,36] while the Boltzmann factor is a correction parameter that accounts for changes in binding strength due to the accumulation of surface charge.[29,34]

$$[L\phi]_l = L_{\max,l} - \sum_{\forall i \in l} m_{i,l} q_{i,l} \qquad \textbf{Equation 6.3}$$

$$K_{i,l} \cdot \eta_{i,l} = \frac{\left(\gamma^{s}_{i,l} q_{i,l}\right) \cdot \prod \{k\}^{\upsilon_k}}{[L\phi]_l^{m_{i,l}} \cdot \{i\}^{\upsilon_i} \cdot \prod \{j\}^{\upsilon_j}} \qquad \textbf{Equation 6.4}$$

6.4.3 Surface Charging

Charging of the adsorbent surface occurs naturally as the ligands bind with ions in solution to form new surface species.[29,34] The impact of surface charging is accounted for through the Boltzmann factor, which acts as a correction parameter for the binding strength (Equation 6.4). This correction term is a function of the elementary electric charge constant (e = 1.6 x 10^{-19} C), Boltzmann constant (k_B = 1.38 x 10^{-23} J/K), electrical surface potential (ψ), temperature (T), and net charge exchange (N), which is itself a function of the ionic charges (n) of the aqueous species involved in the reaction (Equation 6.5 and Equation 6.6).

$$\eta_{i,l} = \exp\left(-\frac{N_{i,l} e \psi}{k_B T}\right) \qquad \textbf{Equation 6.5}$$

$$N_{i,l} = \upsilon_i n_i + \sum_j \upsilon_j n_j - \sum_k \upsilon_k n_k \qquad \textbf{Equation 6.6}$$

Determination of the electrical surface potential (ψ) can be very mathematically complex. Theoretically, the electrical potential varies with the distance from the surface of the adsorbent and the adsorbed ionic charge density at that distance away from the surface.[29,37] This variation can be represented by the Poisson equation below:

$$\nabla^2 \psi(\mathbf{r}) = -\frac{\rho(\mathbf{r})}{\varepsilon \varepsilon_0} \qquad \textbf{Equation 6.7}$$

where ε is the dielectric constant of the medium, ε_0 is the permittivity of free space, ρ is the volumetric ion charge density, and **r** is a vector representing a location in three-dimensional space.

Finding a solution to Equation 6.7 for the generalized representation of surface adsorption would require non-linear, numerical integration and add significant complexity to the model. We can simplify the approximation to the electrical potential by assuming that the adsorbent surface can be represented by a flat plane and applying the Gouy-Chapman theory to approximate the surface potential at the adsorption interface of the electrical double layer.[29,34,38] If this approximation is then coupled with the Grahame model[41] for the adsorbent surface charge density, then a simple approximation to the electrical surface potential can be formulated as shown in Equation 6.8 below:

$$\sqrt{8\varepsilon RTI}\sinh\left(\frac{e\psi}{2k_BT}\right)=\sigma=\frac{F}{A}\sum_{\forall(i,l)}n_{i,l}q_{i,l} \qquad \textbf{Equation 6.8}$$

where I is the ionic strength in the bulk aqueous phase, σ is the total surface charge density for the adsorbent, F is Faraday's constant (96.49 kC/mol), and A is the specific area of the adsorbent. Note that the summation over (i,l) means to iterate over all adsorbate (i) and ligand (l) pairs. One of the underlying assumptions of the Grahame model is that the double layer consists of an ideal 1:1 electrolyte ratio.[34] Although the majority of ions in the experiments are monovalent (Table 6.1), in the generalized model this may not always be the case, so Equation 6.8 is only an approximation of the electrical surface potential.

6.4.4 Surface Activity

In addition to surface charging effects on adsorption, the non-bonding interactions between the various surface species can also have an impact on adsorption of ions from solution. Similar to aqueous species, the activity of surface species can be included in the model through the activity coefficients (i.e., $\{q\} = \gamma^s q$). There are several different models available in literature (e.g. Flory-Huggins, Wilson, etc.) to estimate the activity coefficients of the adsorbed species.[33,35,36] For this particular application, our model utilizes the universal quasi-chemical (UNIQUAC) model developed by Abrams and Prausnitz.[33]

UNIQUAC is a semi-theoretical model of excess Gibbs energy that was derived from a generalization of the Guggenheim model.[33] The total expression for the activity coefficient for the i^{th} adsorbate bonded to the l^{th} ligand (Equation 6.9) is composed as a sum of an athermal combinatorial average area factor (Equation 6.10) and a thermal residual local area factor (Equation 6.11). Physical interpretations of each factor are as follows: (i) the combinatorial term (g^C) represents all the spatial configurations of the surface species in the absence of molecular interactions with each other, and (ii) the residual term (g^R) represents added effects of non-bonding molecular interactions.

$$\ln \gamma_{i,l}^{s} = g^{C} + g^{R} \qquad \textbf{Equation 6.9}$$

$$g^{C} = \ln\left(\frac{\Phi_{i,l}}{y_{i,l}}\right) + \left(\frac{z}{2}\right) s_{i,l} \ln\left(\frac{\theta_{i,l}}{\Phi_{i,l}}\right) + \lambda_{i,l} - \frac{\Phi_{i,l}}{y_{i,l}}\left(\sum_{\forall(j,m)} \lambda_{j,m} y_{j,m}\right) \qquad \textbf{Equation 6.10}$$

$$g^R = s_{i,l} - s_{i,l} \ln\left(\sum_{\forall(j,m)} \theta_{j,m}\tau_{ji,ml}\right) - s_{i,l} \sum_{\forall(j,m)} \left(\frac{\theta_{j,m}\tau_{ij,lm}}{\sum_{\forall(k,n)} \theta_{k,n}\tau_{kj,nm}}\right) \qquad \textbf{Equation 6.11}$$

The UNIQUAC equations are fairly complex and involve many different parameters including average area fraction ($q_{i,l}$), average volume fraction ($\Phi_{i,l}$), coordination constant (z = 10), adsorbate length factor ($\lambda_{i,l}$), adsorbate area factor ($s_{i,l}$), adsorbate volume factor ($r_{i,l}$), the adsorbed mole fraction of the i^{th} adsorbate ($y_{i,l}$), and a binary interaction parameter between the i^{th} and j^{th} adsorbates bound to the l^{th} and m^{th} ligands, respectively ($\tau_{ij,lm}$). Most all of these parameters can be estimated from known information about the adsorbing species.[33,39] For more detailed information on the calculation of the UNIQUAC parameters, please refer to APPENDIX B. Aqueous Adsorption Details.

6.4.5 Numerical Techniques

Collectively, each component of the model combines to form a fully coupled, non-linear system of equations. The primary unknowns in the system are the concentrations of the aqueous and adsorbed species, all of which must be solved simultaneously. Typically, the best approaches for solving these types of problems are gradient search or Newton methods. For our model, we utilize a Jacobian-Free Newton method[40] coupled with a backtracking line search algorithm[41] for efficiency and stability.

6.5 Results and Discussion

6.5.1 Estimation of Binding Constants

Reaction schemes and binding constants analyzed in this study for complexation between aqueous uranyl (UO_2^{2+}) and the acyclic (HAO^-) and cyclic ($HIDO^{2-}$) amidoxime ligands are summarized in Table 6.2. Although some experimental results on HAO^- and $HIDO^{2-}$ complexation with uranyl have already been reported,[42,43] the computational approach that was described in Section 6.3 enabled us to estimate the stability constants for the formation of $[UO_2(HAO)_3]^-$, $[UO_2(HAO)(CO_3)]^-$, $[UO_2(HAO)_2(CO_3)]^{2-}$, $[UO_2(HIDO)(CO_3)]^{2-}$, and $[UO_2(H_2IDO)(CO_3)]^-$ species. This additional work will provide a more detailed picture of uranium complexation in the presence of a high carbonate concentration, which is relevant to seawater conditions.[44]

Measuring formation constants and other thermodynamic parameters for amidoxime/vanadium systems can be very difficult. For instance, although the crystal structures of rare non-oxido vanadium complexes with two cyclic imide-dioxime ligands have been obtained, there were no reports on the stability constants of the corresponding complexes.[46] Challenges of this nature emphasize the utility and value of our computational protocols for predicting log *K* values of VO_2^+, as experimental parameters are not required. The calculated stability constant values for the VO_2^+/HAO^- and $VO_2^+/HIDO^{2-}$ complexes are summarized in Table 6.3.

Table 6.2 - Summary of reactions and stability constants for the UO_2^{2+}/HAO^- and UO_2^{2+}/$HIDO^{2-}$ complexes, at 25 °C and zero ionic strength.

Adsorption Reactions	log *K*
acetamidoximate (HAO^-) ligand:	
$UO_2^{2+} + H_2AO \leftrightarrows [UO_2(HAO)]^+ + H^+$	0.4[a]
$UO_2^{2+} + 2H_2AO \leftrightarrows [UO_2(HAO)_2] + 2H^+$	-2.7[a]
$UO_2^{2+} + 3H_2AO \leftrightarrows [UO_2(HAO)_3]^- + 3H^+$	-11.7[b]
$UO_2^{2+} + H_2AO + CO_3^{2-} \leftrightarrows [UO_2(HAO)(CO_3)]^- + H^+$	2.6[b]
$UO_2^{2+} + 2H_2AO + CO_3^{2-} \leftrightarrows [UO_2(HAO)_2(CO_3)]^{2-} + 2H^+$	-0.9[b]
glutarimidedioximate ($HIDO^{2-}$) ligand:	
$UO_2^{2+} + H_3IDO \leftrightarrows [UO_2(HIDO)] + 2H^+$	-4.6[a]
$UO_2^{2+} + H_3IDO \leftrightarrows [UO_2(H_2IDO)]^+ + H^+$	-0.3[a]
$UO_2^{2+} + 2H_3IDO \leftrightarrows [UO_2(HIDO)_2]^{2-} + 4H^+$	-18.7[a]
$UO_2^{2+} + 2H_3IDO \leftrightarrows [UO_2(H_2IDO)(HIDO)]^- + 3H^+$	-8.8[a]
$UO_2^{2+} + 2H_3IDO \leftrightarrows [UO_2(H_2IDO)_2] + 2H^+$	-3.5[a]
$UO_2^{2+} + H_3IDO + CO_3^{2-} \leftrightarrows [UO_2(HIDO)(CO_3)]^{2-} + 2H^+$	1.4[b]
$UO_2^{2+} + H_3IDO + CO_3^{2-} \leftrightarrows [UO_2(H_2IDO)(CO_3)]^- + H^+$	5.4[b]

[a]Taken from ref. 42, 43 and corrected to zero ionic strength with the Davies equation.[45]
[b]Predicted from the computation approach described in **Molecular Studies** section.

Table 6.3 - Summary of reactions and stability constants for the VO_2^+/HAO^- and VO_2^+/$HIDO^{2-}$ complexes, at 25 °C and zero ionic strength.

Adsorption Reactions	log *K*
acetamidoximate (HAO^-) ligand:	
$VO_4^{3-} + 3H^+ + H_2AO \leftrightarrows [VO_2(HAO)] + 2H_2O$	27.3
$VO_4^{3-} + 2H^+ + 2H_2AO \leftrightarrows [VO_2(HAO)_2]^- + 2H_2O$	21.9
$VO_4^{3-} + 3H^+ + 2H_2AO \leftrightarrows [VOOH(HAO)_2] + 2H_2O$	24.9
$VO_4^{3-} + 3H^+ + 3H_2AO \leftrightarrows [V(HAO)(AO)_2] + 4H_2O$	26.6
$VO_4^{3-} + 5H^+ + 3H_2AO \leftrightarrows [V(HAO)_3]^{2+} + 4H_2O$	22.7
glutarimidedioximate ($HIDO^{2-}$) ligand:	
$VO_4^{3-} + H^+ + H_3IDO \leftrightarrows [VO_2(IDO)]^{2-} + 2H_2O$	21.3
$VO_4^{3-} + 2H^+ + H_3IDO \leftrightarrows [VO_2(HIDO)]^- + 2H_2O$	24.6
$VO_4^{3-} + 3H^+ + H_3IDO \leftrightarrows [VO_2(H_2IDO)] + 2H_2O$	28.1
$VO_4^{3-} + 2H_3IDO \leftrightarrows [VO(IDO)_2]^{3-} + 3H_2O$	11.7
$VO_4^{3-} + 2H^+ + 2H_3IDO \leftrightarrows [V(IDO)_2]^- + 4H_2O$	28.5
$VO_4^{3-} + 3H^+ + 2H_3IDO \leftrightarrows [V(HIDO)(IDO)] + 4H_2O$	30.1
$VO_4^{3-} + 4H^+ + 2H_3IDO \leftrightarrows [V(HIDO)_2]^+ + 4H_2O$	26.9

6.5.2 Estimation of Maximum Capacity

Results from the capacity study are shown in Figure 6.4 below. This graph displays the equilibrium adsorbed concentration of uranium (U) on the AF1 fiber versus the final equilibrium aqueous concentration of uranium ($[U]_e$) in the batch solution. Data from these experiments show that as the aqueous concentration of uranium exceeds about 5 ppm, the adsorption capacity begins to level off and approach an asymptotic value. If this trend were then extrapolated beyond 8 ppm, then the maximum uranium capacity of the AF1 fiber would be approximately 785 g-U/kg-adsorbent or 3.3 mol-U/kg-adsorbent.

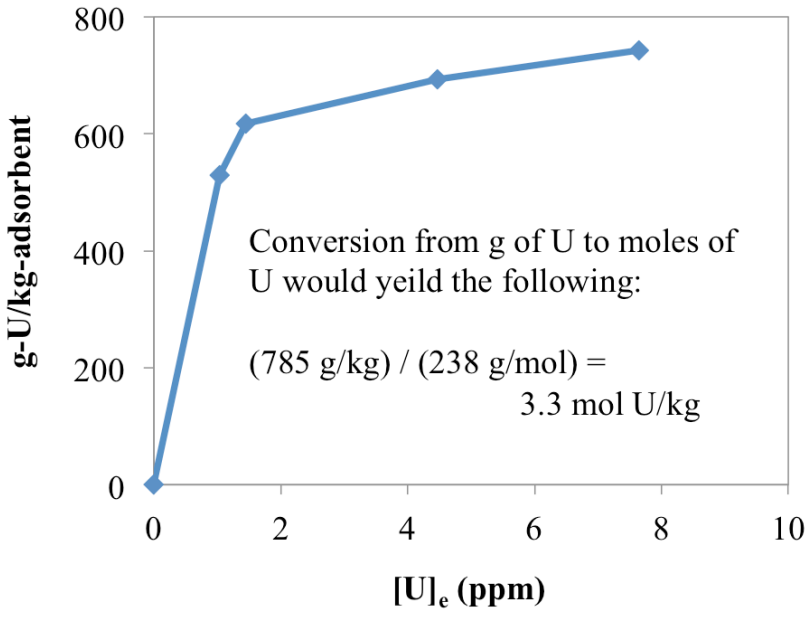

Figure 6.4 - Isotherm plot for uranium adsorption by AF1 at 20 ^{o}C. Extrapolation of this plot beyond 8 ppm of $[U]_e$ yields a maximum adsorption capacity of roughly 785 g-U/kg-adsorbent.

From the maximum uranium capacity, it is possible to make estimates of the surface concentration of the active ligand sites. For instance, if uranium binds to ligands in primarily a 1:1 ligand to uranium mode, then the surface ligand concentration would be around 3.3 mol/kg. However, uranium can also bind in 2:1 mode with the amidoxime ligands,[42,43] which means that the ligand surface concentration could be as high as 6.6 mol/kg according to the results of the capacity study (Figure 6.4). In addition, the capacity study itself does not provide information as to which ligands are most active (HAO^- or $HIDO^{2-}$), so a more in depth analysis of the surface composition is needed for adsorption modeling.

6.5.3 Estimation of Surface Composition

To get a clearer picture of how much of each ligand may be on the surface of the fiber, we can inspect the elemental analysis of the AF1 material performed by Das et al.[16] In this analysis, it was determined that after amidoximation of the fibers, and the KOH conditioning step, that the nitrogen content of the material comprised of 17.94 % of the weight. It should also be noted that before amidoximation the nitrogen content was less that 0.5 %. Based on this information, there is approximately 179.4 g-N/kg-adsorbent, which corresponds to 12.8 mol-N/kg-adsorbent.

If all of the nitrogen from the elemental analysis[16] can be contributed to the presence of the amidoxime ligands, then the estimate of the ligand surface concentration can be further refined. Based on Figure 6.2, it can be found that the HAO^- ligand contains 2 nitrogen atoms, while the $HIDO^{2-}$ ligand contains 3 nitrogen atoms. Combining this information with the 12.8 mol-N/kg-adsorbent from before, it can be concluded that if the

surface was entirely composed of $HIDO^{2-}$ ligands, then the ligand concentration would be 4.27 mol/kg. On the other hand, if the surface were entirely HAO^{-} ligands, then the ligand concentration would be 6.40 mol/kg. The actual ligand concentration should be somewhere between these two estimates.

To obtain a final estimate to the surface composition and concentration of each surface ligand, we need to consider some of the observations made in the pH studies and connect it back to the molecular studies. In the pH studies performed in this work, it was observed that vanadium uptake from the AF1 fiber peaks near a pH of 5 and reaches a capacity of 80 to 90 g-V/kg-adsorbent. This capacity yields a molar vanadium concentration of about 1.67 mol-V/kg-adsorbent. From prior molecular studies,[24] it was reported that vanadium did not bind favorably with the HAO^{-} ligand. As such, we might assume that nearly all of the vanadium is bound to $HIDO^{2-}$ ligands. Additionally, spectroscopic studies[46] of the binding between vanadium and $HIDO^{2-}$ ligands have demonstrated that the vanadium prefers to bind with $HIDO^{2-}$ in a 2:1 ligand to vanadium mode. Therefore, the surface concentration of $HIDO^{2-}$ ligands would be approximately 3.3 mol/kg.

The estimate of 3.3 mol/kg for $HIDO^{2-}$ ligands would account for 9.9 mol-N/kg-adsorbent from the elemental analysis, which leaves 2.9 mol-N/kg-adsorbent that must be accounted for by the HAO^{-} ligand. Based on that assessment, there must be 1.45 mol/kg of HAO^{-} ligands on the adsorbent, which would yield a total ligand concentration of 4.75 mol/kg. Table 6.4 provides a summary of the evaluation of the AF1 surface composition for HAO^{-} and $HIDO^{2-}$ ligands. These values, together with the uranium and vanadium

reactions and binding strengths (Table 6.2 and Table 6.3), will be provided to the adsorption model developed in this work to predict the outcome from the pH studies.

Table 6.4 - Summary of surface composition of ligands for the AF1 adsorbent

Model Parameter	Ligand Conc. (mol/kg)
L_{max} for HAO^-	1.45
L_{max} for $HIDO^{2-}$	3.30
L_{max} Total	4.75

6.5.4 Uranium Modeling

Parameters and reactions from Table 6.2 are utilized by the adsorption model developed in this work in an effort to predict the uranium adsorption observations made during the pH studies, which were also performed in this work. For this purpose, uranium adsorption was simulated across a wide range of pH values using the experimental parameters given in Table 6.1 together with the reactions in Table 6.2 and our approximation of the surface composition of the AF1 fibers (Table 6.4). Figure 6.5 shows the results of the model simulation compared to the data gathered in the uranium adsorption pH studies.

The simulation results in Figure 6.5 predicted the uranium adsorption data with reasonable accuracy, especially in the pH range of seawater (7.5 – 8.5).[30] At very high pH, both the data and the model show a secondary peak in uranium adsorption near a pH of 11 to 12. However, the model shows much higher adsorption than what was actually

observed in the data at pH 11. In addition, the model also overestimates the adsorption peak near a pH of 6, though the prediction is better than the result near pH 11. These discrepancies may be caused by minor errors in the aqueous speciation constants, errors in the binding strengths with the ligands, errors introduced from our approximation of the electrical surface potential (equation 7), or a culmination of all these factors. Regardless, the predictions of the model across a wide range of pH (3.0 – 10.0) are in fairly good agreement with experimental data and do show the appropriate trends (Figure 6.5).

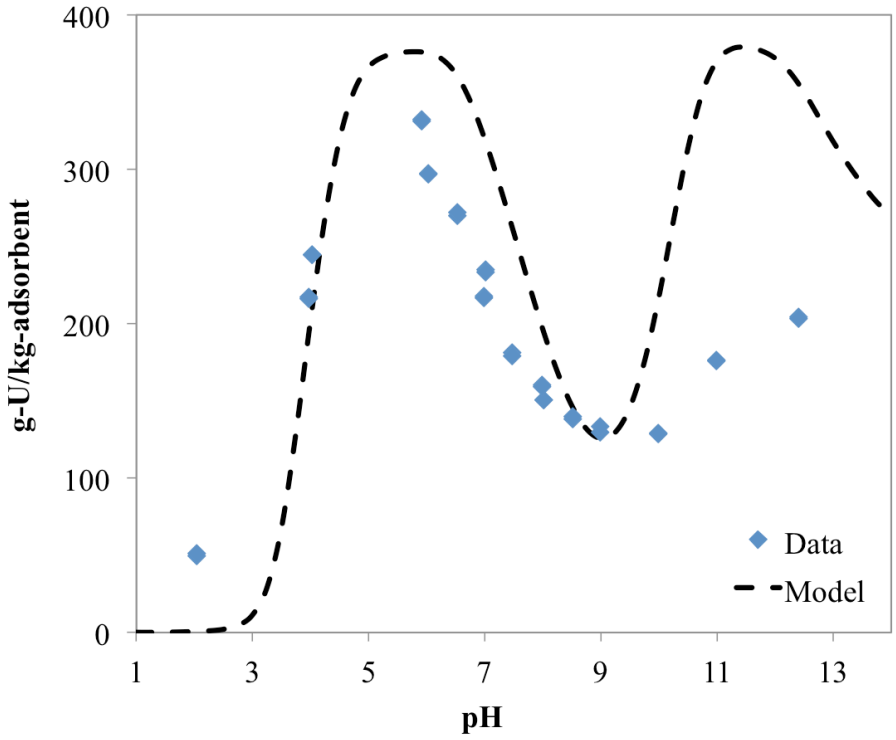

Figure 6.5 - Adsorption model simulation compared to adsorption data gathered from uranium pH studies.

6.5.5 Vanadium Modeling

As before, the reactions from molecular studies for vanadium binding with the amidoxime ligands (Table 6.3) were incorporated into the adsorption model to predict the vanadium adsorption from the pH studies (Table 6.1). Figure 6.6 shows the initial simulation results and compares them to the adsorption data gathered for vanadium. From the comparison, it is shown that the results from this simulation did not match the adsorption data. The model underestimates the adsorption of vanadium substantially across the entire pH range and never comes close to the vanadium capacity of ~90 g/kg.

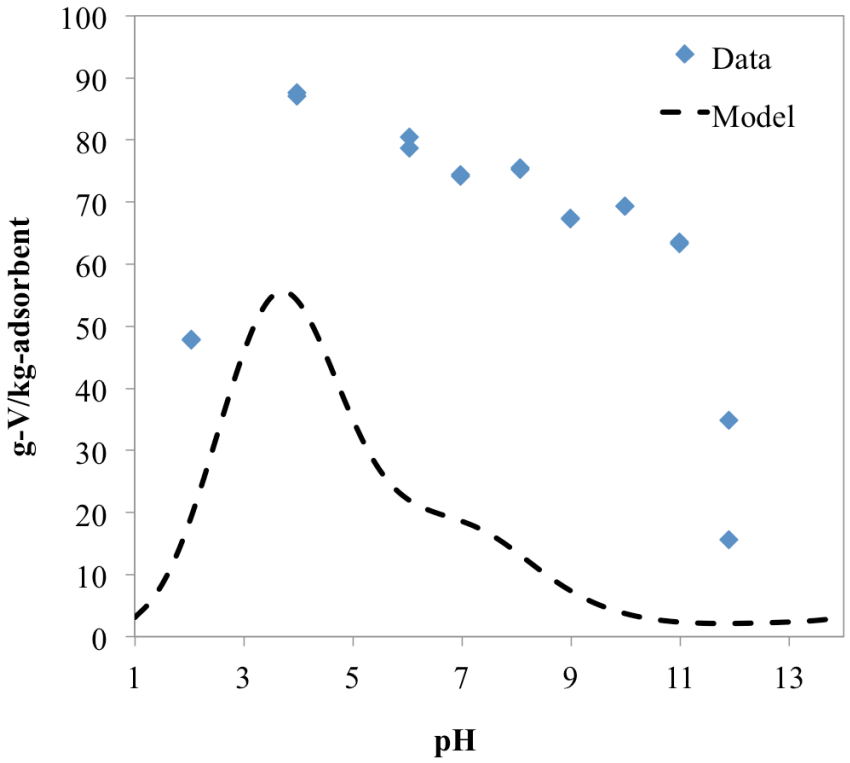

Figure 6.6 - Adsorption model simulation compared to adsorption data gathered from vanadium pH studies.

To investigate this discrepancy, we plotted the surface speciation of the vanadium and $HIDO^{2-}$ complexes in Figure 6.7. From this figure, it can be seen that the primary adsorbing vanadium species are [V(HIDO)(IDO)] at low pH and $[V(IDO)_2]^-$ in the neutral pH range. Note that it is in this range where the model performs worst at predicting the adsorption of vanadium (Figure 6.6). Because the primary species near neutral pH is charged (i.e., has a valence of -1), further adsorption of vanadium in the model is likely being suppressed due to the accumulation of negative surface charge density. In other words, as the adsorbent surface becomes negatively charged, additional adsorption of negatively charged ions will be stifled.

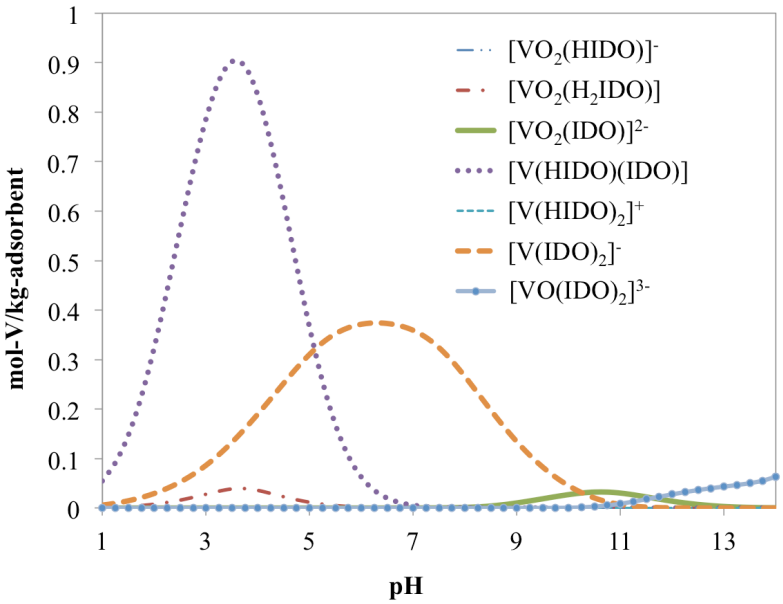

Figure 6.7 - Surface speciation for vanadium uptake on the AF1 fibers by $HIDO^{2-}$ ligands simulated from the adsorption model. The major species in the neutral pH range is the $[V(IDO)_2]^-$ complex, which is negatively charged. Accumulation of negative charge on the surface of the adsorbent would cause a repression of further adsorption of negative species.

In an attempt to correct the model discrepancy, we incorporated a counter-ion binding mechanism between Na^+ ions in solution and the $[V(IDO)_2]^-$ surface species.[34] It is known from Section 6.2 (Table 6.1) that the simulated seawater solutions used in the experiments contained 0.43 M of NaCl. This concentration adds not only a lot of ionic strength to the system, but also significant amount of Na^+ ions that may be attracted to the adsorbent surface as it accumulates negative charge from adsorption of vanadium. To account for this effect, the following reaction was added to the vanadium adsorption model:

$$VO_4^{3-} + 2H^+ + Na^+ + 2H_3IDO \leftrightarrows [Na\text{-}V(IDO)_2] + 4H_2O \quad \log K = 29.0 \qquad \textbf{Equation 6.12}$$

Equation 6.12 represents the counter-ion binding of Na^+ to produce $[Na\text{-}V(IDO)_2]$ as a neutrally charged surface species.[34] The binding strength of this reaction was computed from the $[V(IDO)_2]^-$ reaction constant (Table 6.3) and adjusted to account for the concentration of the Na^+ ions in solution.

Figure 6.8 below shows the results of running the adsorption simulation cases for vanadium with the addition of the counter-ion binding mechanism (Equation 6.12). From these results, we see that we have vastly improved the predictive capabilities of the model for vanadium uptake. The adsorption of vanadium predicted by the model now accurately represents the observations made in the vanadium adsorption experiments.

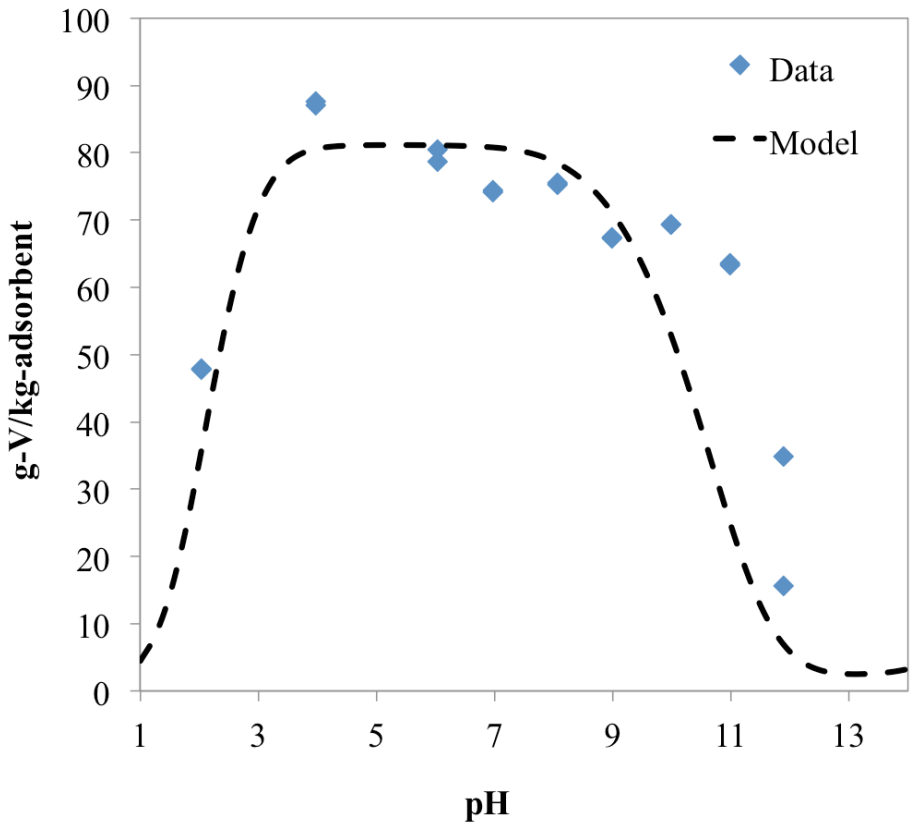

Figure 6.8 - Adsorption model simulation compared to adsorption data gathered from vanadium pH studies. The model utilized the counter-ion binding mechanism of Equation 6.12.

6.5.6 Uranium and Vanadium Selectivity

From Figure 6.5 and Figure 6.8, we have demonstrated that coupling molecular studies with process level adsorption modeling can accurately predict uptake of uranium and vanadium by amidoximated fibers. However, those experiments and simulations were done in the absence of any other competing metals for the active surface sites of the AF1 fiber. In real world applications, it is expected that the uranium and vanadium species are competing for the same ligands on the adsorbent surface.[13-15] Therefore, it is

vital that we can utilize our adsorption model to predict the U/V selectivity of the adsorbent materials.

To simulate the U/V selectivity experiments described in Section 6.2 (Table 6.1), we combined all uranium and vanadium reaction schemes and binding strengths (Table 6.2 and Table 6.3, respectively) from the molecular studies into the adsorption model. We also included the counter-ion binding reaction with Na^+ for vanadium adsorption (Equation 6.12), and then simulated the competitive adsorption between uranium and vanadium. Results from that simulation are shown below in Figure 6.9 and are plotted along side the adsorption data for both uranium and vanadium.

The simulation results shown in Figure 6.9 demonstrate that the model predicted well the adsorption of both uranium and vanadium. Simulation of the uranium adsorption matches the data observations with excellent accuracy in the pH range from 2 to 10, but performed relatively poorly at very high pH. This was also echoed in the uranium simulation from Figure 6.5, so it is possible that the errors that may have attributed to the model results at high pH in Figure 6.5 are also contributing to the errors from these simulation results (Figure 6.9). The vanadium results in Figure 6.9 show good agreement between pH 2 and 7, but then overestimate adsorption from pH 7 to 10 and underestimate adsorption from pH 10 to 12. However, overall both vanadium and uranium capacities are predicted with fairly good accuracy.

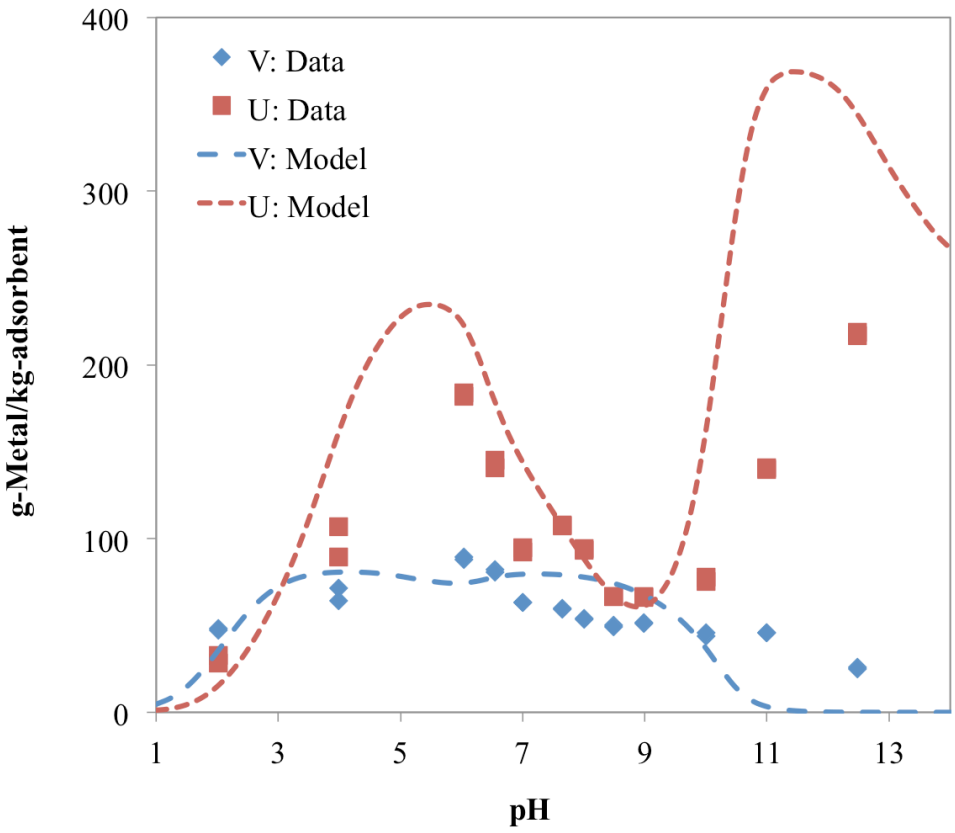

Figure 6.9 - Adsorption model simulation compared to adsorption data gathered from U/V selectivity pH studies. The model utilized the counter-ion binding mechanism of Equation 6.12.

One interesting outcome from the U/V selectivity studies was that the adsorption of vanadium seemed to be almost unaffected by the presence of uranium around pH 6 (Figure 6.10). In contrast, uranium adsorption near pH 6 from the U/V selectivity studies was reduced to 184 g-U/kg-adsorbent (Figure 6.9) from the previously observed 333 g-U/kg-adsorbent (Figure 6.5) in the uranium only study, nearly a 45% decrease in uranium capacity. This result would suggest that vanadium and uranium are not always competing for the same ligands, which may be the result of the presence of the HAO^- ligand on the adsorbent surface.

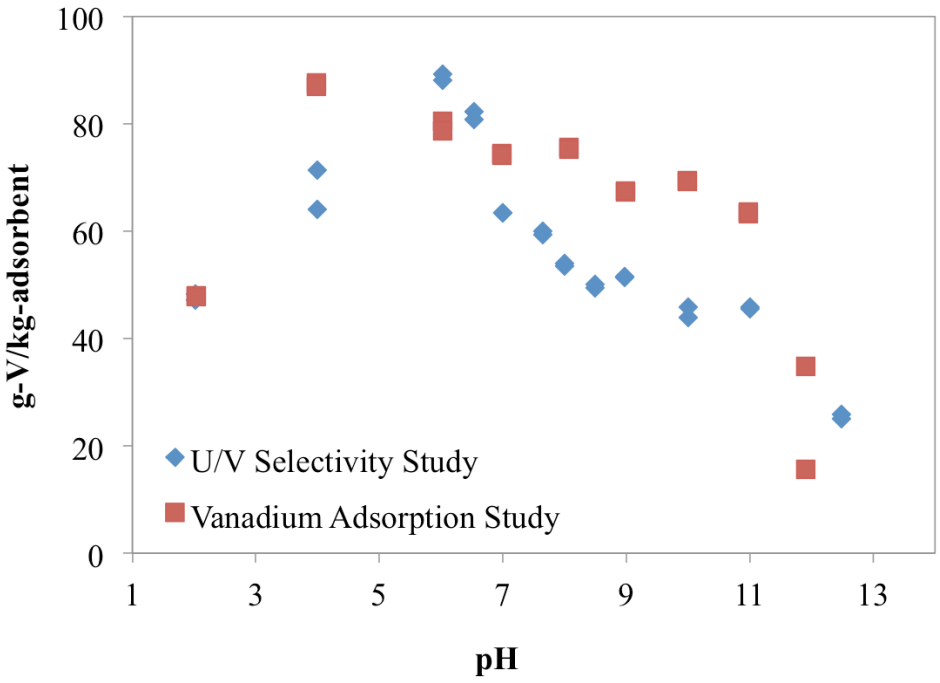

Figure 6.10 - Comparison between the vanadium adsorption data in the vanadium only study (red squares) and the U/V selectivity study (blue diamonds). Near pH 6 there is little to no difference in vanadium capacity for the two studies, and in the high pH range the maximum difference is only 25 g-V-kg-adsorbent (~36 % reduction in vanadium capacity from uranium adsorption). From these data, it appears that uranium adsorption is only impacting vanadium uptake at pH beyond the neutral region.

It was previously identified that vanadium does not have a high binding affinity towards HAO^-.[24] This conclusion is supported by the molecular studies' estimation of the vanadium binding constants for HAO^- (Table 6.3), which are several log units lower than the binding strengths with $HIDO^{2-}$ ligands, on average. Therefore, vanadium would not likely compete with uranium for these active sites. Conversely, vanadium does bind very favorably with the $HIDO^{2-}$ ligand, which would cause the suppression in the amount of

uranium that the fiber could adsorb. As such, uranium and vanadium are not competing for all the same surface sites, but there are surface sites that both of them do compete for.

6.6 Conclusions

The culmination of molecular studies and adsorption process modeling has produced a methodology wherein we can accurately predict the uptake of uranium by PAO-functionalized PE-fibers under laboratory conditions (Figure 6.5). This represents an important step forward in material design for future uranium adsorbents. By continuing to follow this multi-scale design approach, we can potentially utilize *ab initio* methods in chemistry to selectively screen ligands that have optimal uranium adsorption properties without needing to resort to extensive experimental work. This computational screening, coupled with adsorption modeling, will create an inexpensive design methodology for the development of future adsorbents.

In addition to predicting uranium capacity of adsorbent materials, our computational approach was also able to give a fairly accurate picture of the competition between uranium and vanadium for the AF1 fibers (Figure 6.9). However, a good agreement between experimets and prediciton was only accomplished after some modifications to the reaction schemes proposed through the molecular studies (Equation 6.12). In addition, the competitive adsorption modeling results suggested that vanadium and uranium are not in direct competition for all the same active sites of the fiber. This conclusion was also supported by the observations made in the vanadium adsorption experiments (Figure 6.10), which showed very little impact of uranium on the adsorption of vanadium. Based on the reactions and binding constants from the molecular studies

(Table 6.3), vanadium does not bind very well with the HAO^- ligand. Therefore, a potential strategy for future adsorbent design would be to functionalize the fiber surface with primarily HAO^- ligands, which only bind uranium, instead of $HIDO^{2-}$ ligands, which bind both uranium and vanadium.

While the adsorption model did perform well to predict the adsorption of uranium and vanadium in all cases studied, there were still some errors in those predictions that leave room for model improvement. For instance, surface charging was identified as a major mechanism that impacts the adsorption capacity of vanadium (Figure 6.6 through Figure 6.8). In our model, we utilize a very simple approximation to the electrical surface potential based on the Grahame model[37] (Equation 6.8). Errors introduced by this approximation may be partially responsible for some of the errors seen from the vanadium simulations shown in Figure 6.6. Developing a more accurate surface charging mechanism, along with other adsorption model improvements, should enhance the computational approach presented in this paper and provide a path forward for the creation of a closed-loop methodology that can be utilized to design the next generation of uranium adsorbents from seawater.

6.7 Acknowledgement

The development of this chapter was a collaborative effort between my co-authors and myself and was the main subject of a manuscript that is to be submitted for publication: A. Ladshaw, A. Ivanov, S. Das, V. Bryantsev, C. Tsouris, S. Yiacoumi, "Adsorption Modeling for Selective Capture of Uranium from Seawater," Under Internal Review, March 9th, 2017.

6.8 References

[1] D. L. Clark, D. E. Hobart, M. P. Neu, *Chem. Rev*. 95 (**1995**) 25.

[2] F. Endrizzi, L. Rao, *Chem. - Eur. J.* 20 (**2014**) 14499-14506.

[3] J. D. Wilson, R. K. Webster, G. W. C. Milner, G. A. Barrett, A. A. Smales, *Anal. Chim. Acta*, 23 (**1960**) 505.

[4] Y. Lu, *Nature*, 6 (**2014**) 175-177.

[5] I. Tabushi, Y. Kobuke, T. Nishiya, *Nature*, 280 (**1979**) 665.

[6] A. C. Q. Ladeira, C. A. Morais, *Minerals Eng.* 18 (**2005**) 1337.

[7] P. S. Kulkarni, S. Mukhopadhyay, M. P. Bellary, S. K. Ghosh, *Hydrometallurgy*, 64 (**2002**) 49.

[8] R. S. S. Murthy, D. E. Ryan, *Anal. Chem*. 55 (**1983**) 682.

[9] T. Takeda, K. Saito, K. Uezu, S. Furusaki, T. Sugo, J. Okamoto, *Ind. Eng. Chem. Res*. 30 (**1991**) 185.

[10] M. Tamada, N. Seko, N. Kasai, T. Shimizu, *Trans. At. Energy Soc. Japan*, 5 (**2006**) 358.

[11] M. J. Kanno, *Nucl. Sci. Technol*. 21 (**1984**) 1.

[12] J. Kim, C. Tsouris, Y. Oyola, C. J. Janke, R. T. Mayes, S. Dai, G. Gill, L.-J. Kuo, J. Wood, K.-Y. Choe, E. Schneider, H. Lindner, *Ind. Eng. Chem. Res.* 53 (**2014**) 6076.

[13] Idaho National Laboratory, *Fuel Cycle Technologies Annual Review Meeting Transactions Report,* INL/EXT-14–33501, FCRD-FCT-2015-000003, 2015.

[14] J. Kim, C. Tsouris, R. T. Mayes, Y. Oyola, T. Saito, C. J. Janke, S. Dai, E. Schneider, D. Sachde, *Sep. Sci. Technol.* 48 (**2013**) 367.

[15] T. Suzuki, K. Saito, T. Sugo, H. Ogura, K. Oguma, *Anal. Sci.* 16 (**2000**) 429.

[16] S. Das, Y. Oyola, R.T. Mayes, C.J. Janke, L.-J. Kuo, G. Gill, J.R. Wood, S. Dai, *Ind. Eng. Chem. Res.* 55 (**2016**) 4110-4117.

[17] L.-J. Kuo, C.J. Janke, J.R. Wood, J.E. Strivens, S. Das, Y. Oyola, R.T. Mayes, G.A. Gill, *Ind. Eng. Chem. Res.* 55 (**2016**) 4285-4293.

[18] K. Saito, S. Yamada, S. Furusaki, T. Sugo, J. Okamoto, *J. Mem. Sci.* 34 (**1987**) 307-315.

[19] M. J. Frisch, G. W. Trucks, H. B. Schlegel, G. E. Scuseria, M. A. Robb, J. R. Cheeseman, G. Scalmani, V. Barone, B. Mennucci, G. A. Petersson, H. Nakatsuji, M. Caricato, X. Li,

H. P. Hratchian, A. F. Izmaylov, J. Bloino, G. Zheng, J. L. Sonnenberg, M. Hada, M. Ehara, K. Toyota, R. Fukuda, J. Hasegawa, M. Ishida, T. Nakajima, Y. Honda, O. Kitao, H. Nakai, T. Vreven, J. A. Montgomery Jr., J. E. Peralta, F. Ogliaro, M. Bearpark, J. J. Heyd, E. Brothers, K. N. Kudin, V. N. Staroverov, R. Kobayashi, J. Normand, K. Raghavachari, A. Rendell, J. C. Burant, S. S. Iyengar, J. Tomasi, M. Cossi, N. Rega, M. J. Millam, M. Klene, J. E. Knox, J. B. Cross, V. Bakken, C. Adamo, J. Jaramillo, R. Gomperts, R. E. Stratmann, O. Yazyev, A. J. Austin, R. Cammi, C. Pomelli, J. W. Ochterski, R. L. Martin, K. Morokuma, V. G. Zakrzewski, G. A. Voth, P. Salvador, J. J. Dannenberg, S. Dapprich, A. D. Daniels, Ö. Farkas, J. B. Foresman, J. V. Ortiz, J. Cioslowski, D. J. Fox, *Gaussian 09 Revision D.01*, Wallingford, CT, Gaussian, Inc., 2009.

[20] A. D. Becke, *J. Chem. Phys.* 98 (**1993**) 5648.

[21] C. Lee, W. Yang, R. G. Parr, *Phys. Rev. B,* 137 (**1988**) 785.

[22] Y. Zhao, D. G. Truhlar, *Theor. Chem. Acc.* 120 (**2008**) 215.

[23] A. V. Marenich, C. J. Cramer, D. G. Truhlar, *J. Phys. Chem. B*, 113 (**2009**) 6378.

[24] A.S. Ivanov, V.S. Bryantsev, *Dalton Trans.* 45 (**2016**) 10744-10751.

[25] S. Vukovic, B.P. Hay, V.S. Bryantsev, *Inorg. Chem.* 54 (**2015**) 3995-4001.

[26] L. Astheimer, H.J. Schenk, E.G. Witte, K. Schwochau, *Sep. Sci. Technol.* 18 (**1983**) 307–339.

[27] S. Das, S. Brown, R. T. Mayes, C. J. Janke, C. Tsouris, L.-J. Kuo, G. Gill, S. Dai, *Chem. Eng. J.* 298 (**2016**) 125–135.

[28] M.M. Benjamin, *Water Chemistry*, Waveland Press Inc., Illinois, 2010.

[29] S. Yiacoumi, C. Tien, *Kinetics of Metal Ion Adsorption from Aqueous Solutions*, Kluwer Academic Publishers, Boston, MA, 1995.

[30] A. Ladshaw, S. Das, W. Liao, S. Yiacoumi, C. Janke, R. Mayes, S. Dai, C. Tsouris, *Ind. Eng. Chem. Res.* 55 (**2016**) 4241-4248.

[31] J.C. Westall, J.L. Zachary, F.M.M. Morel, *Abstracts of Papers of the American Chemical Society*, 172 (**1976**) 8-8.

[32] W.D. Schecher, D.C. McAvoy, *Computers, Environment and Urban Systems*, 16 (**1992**) 65-76.

[33] D.S. Abrams, J.M. Prausnitz, *AIChE J.* 21 (**1975**) 116-128.

[34] V.V. Kalinin, C.J. Radke, *Colloids and Surfaces*, 114 (**1996**) 337-350.

[35] T.W. Cochran, R.L. Kabel, R.P. Danner, *AIChE J.* 31 (**1985**) 268-277.

[36] O. Talu, I. Zwiebel, *AIChE J.* 32 (**1986**) 1263-1276.

[37] D.C. Grahame, *Chem. Rev.*, 41 (**1947**) 441-500.

[38] C. Tien, *Adsorption Calculations and Modeling*, Butterworth-Heinemann, Boston, 1994.

[39] A. Bondi, *J. Phys. Chem.* 68 (**1964**) 441-451.

[40] D.A. Knoll, D.E. Keyes, *J. Comp. Phys.* 193 (**2004**) 357-397.

[41] J.E. Dennis, R.B. Schnabel, *Numerical Methods for Unconstrained Optimization and Nonlinear Equations*, Prentice-Hall Inc., Englewood Cliffs, NJ, 1983.

[42] G. Tian, S. J. Teat, Z. Zhang, L. Rao, *Dalton Trans.* 41 (**2012**) 11579–11586.

[43] M. A. Lashley, N. Mehio, J. W. Nugent, E. Holguin, C.-L. Do-Thanh, V. S Bryantsev, S. Dai, R. D. Hancock, *Polyhedron*, 109 (**2016**) 81–91.

[44] R. Chester, T. D. Jickells, *Marine Geochemistry*. 3rd Edition, Wiley-Blackwell Publishing, New York, 2012.

[45] C. W. Davies, *Ion Association*, Butterworths, Washington, DC, 1962.

[46] C. J. Leggett, B. F. Parker, S. J. Teat, Z. Zhang, P. D. Dau, W. W. Lukens, S. M. Peterson, A. J. P. Cardenas, M. G. Warner, J. K. Gibson, J. Arnold, L. Rao, *Chem. Sci.* 7 (**2016**) 2775–2786.

6.9 Nomenclature

Latin Symbols

A	specific area of the adsorbent
e	elementary electric charge constant
F	Faraday's constant
g^C	combinatorial factor in UNIQUAC
g^R	residual factor in UNIQUAC
I	ionic strength of the solution
K	stability constant of a reaction
k_B	Boltzmann constant

L_{max} maximum surface concentration of ligands

m number of sites involved in a surface reaction

N net charge exchange term

n ionic charge of a species

q surface concentration of a species

R gas law constant

$\mathbf{r}$ location vector

r adsorbate volume factor

s adsorbate area factor

T system temperature

U uranium

V vanadium

y adsorbed mole fraction

z coordination constant

Greek Symbols

ΔG_{aq} change in free energy for an aqueous reaction

ρ volumetric ion charge density

γ^{aq} aqueous activity coefficient

γ^{s} surface activity coefficient

ε dielectric constant of a medium

ε_0 permittivity of free space

η Boltzmann factor

λ adsorbate length factor

τ binary interaction parameter

υ stoichiometric constant

Φ average volume factor

ψ electric surface potential

Sub/superscripts

i,j,k indices for species

l,m,n indices for ligands

Other Symbols

$[i]$ aqueous concentration of a species

$[L\phi]$ molar concentration of surface sites

$[U]_e$ equilibrium concentration of uranium

$\{i\}$ aqueous activity of a species

$\{q\}$ surface activity of a species

HAO^- acyclic acetamidoximate

$HIDO^{2-}$ cyclic glutarimdedioximate

CHAPTER 7. INFLUENCE OF FLOW RATES ON MASS TRANSFER

7.1 Introduction

Seawater represents a vast, untapped reservoir for uranium fuel as it contains 4.5 billion metric tons of dissolved uranium.[1] This unconventional supply could ensure centuries of uranium availability for worldwide growth in nuclear energy. As discussed in the previous chapters (CHAPTER 5 and CHAPTER 6), recovering uranium from seawater using adsorption is a challenging task due to its relatively low concentration (3.3 μg/L), high-salinity environment, and the presence of many competing ions/metals (e.g., Ca, Mg, V, Fe).

Prior has been focused on thermodynamics, kinetics, and structural characterization of amidoxime ligands,[2-7] laboratory testing and modeling of the amidoxime fibers,[8-12] and marine testing and performance assessment of adsorbent fibers.[13-16] In addition, the mechanisms of uranium uptake from simulated seawater were also investigated.[8,11] In those investigations, experiments were devised to quantify the reaction and intraparticle mass-transfer mechanisms of adsorption. However, the interphase and interparticle mass-transfer effects, which are largely controlled by fluid mixing and velocity, were neglected in those experiments.

In this study, the major focus is to investigate and quantify fluid velocity effects on mass-transfer kinetics of uranium adsorption from seawater onto amidoxime-based polymer fibers using natural seawater under realistic exposure conditions. The intent of

this work is to provide a relatively simple adsorption model that will couple reaction kinetics with mass-transfer effects to account for oceanic currents and their impact on the overall uptake rate of the adsorbents. Results obtained from this study will provide critical information in determining optimal marine locations for adsorbent deployment based on the local seawater currents of a particular region.

7.2 Experimental Methods

Two independent laboratory-based time series adsorption experiments were conducted using adsorbent fibers contained in flow-through columns and braided adsorbents in recirculating-flow channels (flumes) to assess the influence of linear velocity on the kinetic uptake of uranium by amidoxime-based adsorbent material. The experimental conditions used for these approaches were designed to overlap, allowing for comparison of the results.

7.2.1 Seawater Exposure System

Marine testing was conducted at the Marine Sciences Laboratory (MSL), a coastal-based marine laboratory within the Pacific Northwest National Laboratory (PNNL), using ambient seawater from Sequim Bay, WA. Details of the flow-through column and recirculating flume seawater exposure systems are given in Gill et al.[13] All seawater exposure experiments were conducted using ambient filtered (0.45 μm) seawater from Sequim Bay, with temperature controlled at 20 ± 1.5 ^{o}C. Filtration at 0.45 μm was necessary to eliminate organisms that would foul the adsorbents, resulting in loss of adsorption capacity.[17]

7.2.2 Flow-through Column Experiments

A critical feature in conducting flow rate experiments is how fibers are packed into the columns. Ideally, the fibers should be placed into the column having minimal contact with adjacent fibers. If they are in contact with each other (e.g., matted), exposure of their surface to seawater may be hindered, particularly for fibers in the interior of the matted adsorbent. For this reason, we mixed the fibers with glass beads, attempting to distribute the fibers as evenly as possible throughout the column. In practice, the fibers were very difficult to separate and the best that could be achieved was to break the fibers into several small clumps and distribute the clumps throughout the column.

The linear velocity (v) in the column is a function of the internal column diameter (d), flow rate (Q), and porosity (ε) of the column packing (Equation 7.1).

$$v = \frac{4Q}{\pi d^2 \varepsilon} \qquad \textbf{Equation 7.1}$$

The porosity is defined as the fraction of the total volume not occupied by solid matter. Random packing of spherical grains greater than 100 μm in diameter has a porosity >0.399 and is independent of grain size. Independent measurements of the porosity of 3-mm and 5-mm glass beads packed into the 1-inch internal diameter (nominal size) column used for adsorption studies gave porosities of 0.425 and 0.454, respectively.

Linear velocities in the flow-through columns ranging between 0.3 and 10 cm/s were achieved by using different diameter columns and seawater delivery flow rates ranging between 100 and 700 mL/min (Table 7.1). Each time-series experiment was

conducted for 56 days, with 7 time points (0, 7, 14, 21, 28, 42 and 56 days) each, and the final time point was replicated for a total of 8 samples per experiment. Additional details regarding the column experiments are given by Gill et al.[13] and Kuo et al.[14]

Table 7.1 - Linear velocities for flow-through column experiments using three different-diameter columns and flow rates ranging between 100 and 700 mL/min.

Flow Rate (mL/min)	Column Diameter (in)	Linear Velocity (cm/s)
100	1.50	0.29
250	1.50	0.73
120	1.00	1.08
400	1.50	1.18
120	0.75	1.75
320	1.00	2.88
275	0.75	4.01
700	1.00	6.30
700	0.75	10.2

7.2.3 Recirculating Flume Experiments

Recirculating flumes were used for conducting experiments with braided adsorbent materials under controlled temperature and flow rate conditions (Figure 7.1).[13] Different size recirculation pumps, flume dimensions, and internal water heights were used to create a range of linear velocities between 0.48 and 8.24 cm/s (Table 7.2). For example, a linear velocity of 5.52 cm/s was achieved in flume C, which was 6-foot (183 cm) long with a 7-inch (17.8 cm) water height using a high-capacity pump and setting the recirculation flow rate to 23 gal/min (87 L/min). There is a slight increase in linear

velocity (~3%) due to the fresh seawater flow of 2.5 L/min, which is small relative to the recirculation flow of 87 L/min.

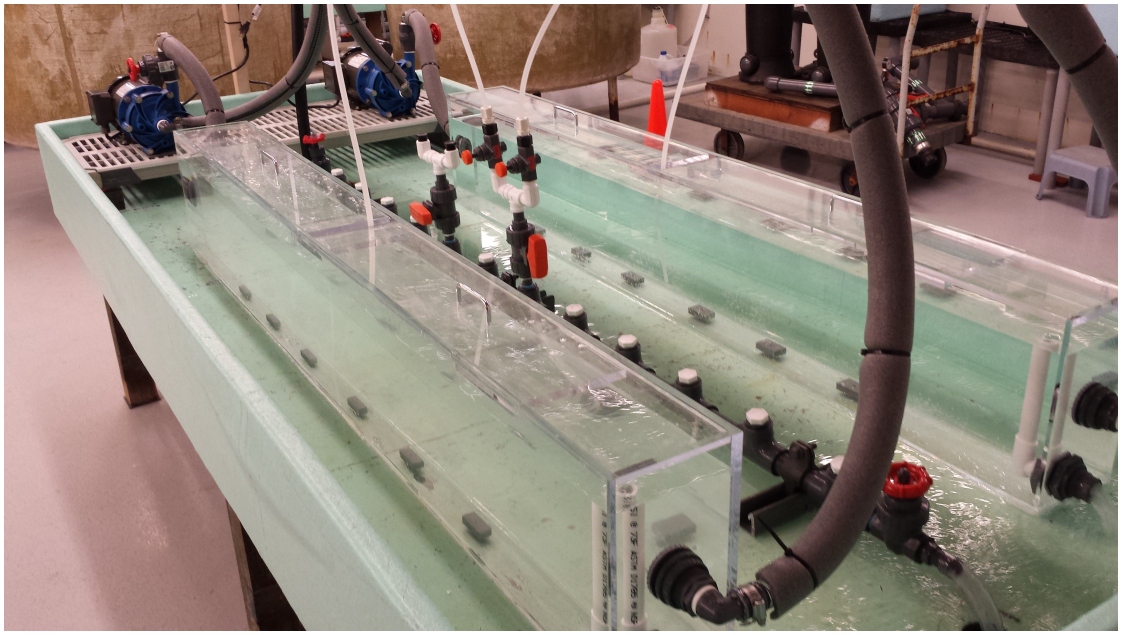

Figure 7.1 - Recirculating flumes for seawater exposure studies with braided adsorbent material. The pumps used to recirculate water in the flume and control the linear velocity of the flow are shown in the upper left side of the picture. The manifold that distributes fresh seawater into the flumes sits between the two flumes.

Table 7.2 - Flume configuration and associated water recirculation and input fresh seawater flow rates used to produce a range of linear velocities.

Experiment	Flume	Recirculation (L/min)	Seawater (L/min)	Linear Velocity (cm/s)
1	C	87.1	2.5	5.52
2	C	50.0	2.5	3.23
3	C	31.6	2.5	2.11
4	B	37.5	2.5	1.40
5	B	22.7	2.5	0.88
6	B	11.4	2.5	0.48
7	C	94.6	3.0	8.24

Two flume exposures were conducted simultaneously, starting with experiments 1 and 6, then 2 and 5, then 3 and 4, and finally experiment 7 was conducted separately (Table 7.2). Flume B, which had the larger cross sectional area, was used for the slower linear velocities and Flume C, with the smaller cross-sectional area, was used for the faster linear velocities (Table 7.2). The dimensions for each flume varied as follows: flume C was 183 cm long, 15.2 cm wide, and 17.8 cm deep, while flume B was 244 cm long, 20.3 cm wide, and 23.5 cm deep. Experiments consisted of 56-day time series exposures, with 8 sample time points (0, 7, 14, 21, 28, 35, 42 and 56 days). A replicate of the 21 day and 56 day sample time point was collected for a total of 10 samples per experiment.

The rate at which fresh seawater is fed into the system controls the residence time of seawater in the each flume. At a fresh seawater flow rate of 2.5 L/min through flume C, the water residence time is ~20 min. At a recirculation flow rate of 87 L/min, the water in the flume is recirculated once every 24 seconds, making the recirculation time much faster than the seawater residence time. For the lowest recirculation flow rate (11 L/min) through flume B, the flume seawater residence time is 10 minutes. Hence, even at the lowest recirculation rate, the water in the flume can be assumed well mixed.

7.2.4 Adsorbent Preparation

Linear velocity adsorption experiments were conducted with the Oak Ridge National Laboratory (ORNL) type AF1 amidoxime-based polymer adsorbent described previously in CHAPTER 5 and CHAPTER 6.[14,18] The AF1 adsorbent was prepared using hollow gear-shaped polyethylene fibers that were grafted using radiation-induced graft

polymerization.[18] All seven braided adsorbent materials used for this study came from a common batch. The adsorbents were conditioned immediately before use with 0.44 M KOH for 1 hour at 80°C.

7.2.5 Experimental Measurements

Adsorbent materials exposed to seawater were washed with deionized water to remove salts. Samples were then dried at 80 °C to a constant weight using a heated block (ModBlock™, CPI International). The dried fibers (50 to 100 mg) were weighed and then digested with 10 mL of a high-purity (Optima Grade, Fisher Scientific) 50% aqua regia acid mixture (3:1 hydrochloric acid: nitric acid) for 3 hours at 85 °C on a hot block. Analysis of uranium and other trace elements was conducted using either a Perkin-Elmer 4300 inductively coupled plasma optical emission spectrometer or a Thermo Scientific ICap™ Q inductively coupled plasma mass spectrometer. Quantification for both instruments is based on standard calibration curves.

Salinity was determined using a handheld YSI salinometer. The pH was measured with a standard pH meter and probe that was calibrated weekly using NIST-traceable buffers. Adsorption capacity measurements were normalized to a salinity of 35 psu using simple proportional relationships. The ability to normalize the uranium data to a common salinity for comparison purposes is possible because there is a well-defined relationship between the 238-U concentration in seawater and salinity of 3.187 μg U/kg of seawater.[19] This normalization removes the differences that result from exposures in seawater with varying salinity and hence uranium concentrations.

7.3 Modeling Methods

7.3.1 Model Development

The primary mechanisms governing the adsorption of uranium from seawater by the AF1 amidoxime-functionalized polymeric fibers involve reaction and mass-transfer effects.[11] Mass-transfer mechanisms include interparticle, interphase, and intraparticle transfer. We can simplify the analysis by lumping these individual mechanisms into a single mass-transfer coefficient to observe trends in velocity effects on adsorption. In these controlled experiments, only the flow rates in columns and flumes are changing; therefore, only the values of the mass-transfer coefficient are expected to change. It is assumed that uranium concentrations, and seawater pH and salinity do not vary significantly over the course of the experiments; therefore, the reaction parameters should remain unchanged.

To adequately describe the experimental data, we need to have an adsorption model that accounts for reaction and mass-transfer kinetics. Figure 7.2 depicts an idealized schematic of the system to be modeled. In this system, there is some linear velocity (v) calculated from the flow rate, which carries a bulk concentration of uranium (C_b) from seawater to an adsorption domain represented by a group of adsorbent fibers. The mass-transfer mechanism carries uranium from the bulk aqueous domain into the adsorption domain, which has its own uranium concentration level (c) and void volume (ε). The adsorption domain is an imaginary boundary that contains an assembly of adsorbent fibers, meant to represent either a woven braid of fibers in the flume or compacted fibers suspended between glass beads in columns. Within that adsorption

domain, reactions occur between the amidoxime ligands and aqueous uranium to form the adsorbed uranium (q). The fibers' density is represented by the ρ_f parameter.

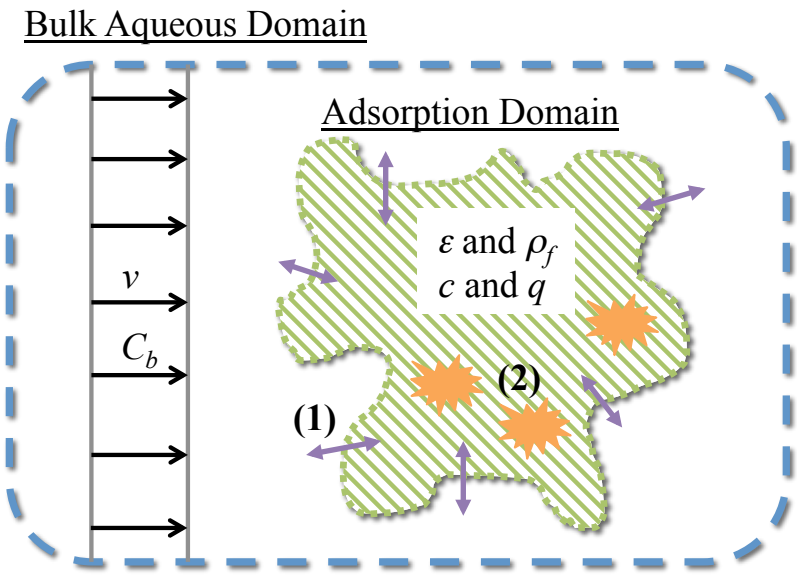

Figure 7.2 - Idealized view of modeled adsorption system. The mechanisms of adsorption considered are mass transfer from bulk domain to adsorption domain (1), and site-specific reactions (2).

This system is fairly complex, so the model will be simplified by making a few assumptions. First, it is assumed that the concentration distribution of uranium inside the adsorption domain (c) is relatively constant or evenly dispersed. In this way, the interior of the adsorption domain is treated as if it were completely mixed, which is a reasonable assumption given the amount of agitation that the fibers undergo and also given the fact that the rate of uranium adsorption from seawater is relatively slow. However, this is a simplification and may not capture all mass-transfer mechanisms that actually occur, such as interparticle and intraparticle diffusion.

It is also assumed that the reactions occurring inside the adsorption domain are Langmuir type reactions, typical for one-site ligand interactions in liquid-phase adsorption.[20] Equation 7.2 shows the basic Langmuir reaction considered. In this equation, L represents the number or concentration of available ligands, which can be expanded in Equation 7.3 as a function of the maximum sites (q_{max}) and the sites already in use (q). By combining Equation 7.2 and Equation 7.3, one can derive the kinetic expression for adsorption in the domain with the forward (k_1) and reverse (k_{-1}) rates of reaction (Equation 7.4).

$$c + L \Leftrightarrow q \qquad \textbf{Equation 7.2}$$

$$L = q_{max} - q \qquad \textbf{Equation 7.3}$$

$$\frac{\partial q}{\partial t} = k_1 c q_{max} - \left(k_1 c + k_{-1}\right) q \qquad \textbf{Equation 7.4}$$

Applying these assumptions to the system shown in Figure 7.2, one can then derive an expression for the concentration of uranium in the adsorption domain as a function of the adsorption reaction and mass transfer from bulk solution (Equation 7.5). Because a uniform distribution of uranium is assumed for the adsorption domain, diffusion effects are not included. Instead, transfer from the bulk to the interior is represented via a linear driving force mechanism. In this case, all the mass-transfer effects are lumped into a single parameter K, expected to vary with the flow rates (linear velocities) of the experiments.

$$\varepsilon \frac{\partial c}{\partial t} = \varepsilon K \left(C_b - c \right) - \rho_f \left(1 - \varepsilon \right) \frac{\partial q}{\partial t} \qquad \textbf{Equation 7.5}$$

7.3.2 Parameter Estimation

The formulated uranium adsorption model contains a number of parameters, many of which can be estimated based on the data collected through experiments, such as maximum capacity ($q_{\max}$) or average uranium concentration in seawater (C_b). The kinetic parameters (k_1 and K) must be determined through optimization of the experimental uptake curves from the column and flume experiments. Table 7.3 provides a list of all physical parameters determined experimentally before performing optimization for the kinetic parameter values.

Table 7.3 - Values of constants used in the adsorption model

Parameter	Value	Units	Information
$\boldsymbol{q_{max}}$	350	g/kg	Maximum capacity of fibers in seawater
$\boldsymbol{\rho_f}$	1.18	g/cm^3	Density of adsorbent fibers
$\boldsymbol{q_{sat}}$	5.17	g/kg	Extrapolated from flume data
$\boldsymbol{K_{eq} = k_1/k_{-1}}$	1.27E+6	L/mol	Estimated from seawater capacity
$\boldsymbol{C_b}$	2.80	μg/L	Uranium concentration in experiments
$\boldsymbol{\varepsilon}$	0.44	-	Average void volume of domain

The parameters q_{sat} and K_{eq} are the adsorption saturation and equilibrium constants, respectively, based on extrapolation of the flume adsorption data and the

average uranium concentration of the seawater used in these experiments. While these parameters are not directly used in the model, they are useful in reducing the complexity of the optimization scheme needed to determine the kinetic parameters. By determining the seawater saturation capacity (q_{sat}) through extrapolation, for example, there is no longer need to determine this value through optimization. Similarly, by estimating the K_{eq} value, which is the ratio of the reaction parameters (k_1 and k_{-1}), one can determine the value of k_{-1} after k_1 is estimated. Therefore, the only adjustable parameters that need to be optimized are k_1 and K, the forward reaction rate and the linear-driving-force (LDF) mass-transfer coefficient.

Optimization of the adjustable kinetic parameters must be carried out carefully, because the reaction parameter (k_1) must remain constant throughout the optimization, but the mass-transfer parameter (K) must be allowed to change with the changing flow rates. Additionally, it is known that without mass-transfer limitations, the kinetics of uranium adsorption for these amidoxime-functionalized fibers is very fast.[19] Therefore, the reaction parameter (k_1) must be large enough to allow variations in flow to impact the overall uptake rate, but small enough so that the model is still sensitive to changes in the reaction parameter. Through optimization, the following optimal reaction parameter value that works across all sets of column and flume data was obtained: $k_1 = 7.0 \times 10^3$ L/mol/hr. This value was determined iteratively through comparisons between model and data. Unlike the reaction parameter (k_1), which is the same for all data sets, the value of the mass-transfer coefficient (K) will vary with current velocities in the system. Therefore, it must be optimized independently for each individual data set.

7.4 Results

7.4.1 Column and Flume Observations

Little or no change in adsorption kinetics was observed in the flow-through column experiments across the range of linear velocities examined, from 0.29 to 10.2 cm/s (Figure 7.3). Typically, this result implies that the minimum linear velocity necessary to remove all external mass-transfer resistances, even for the lowest velocity of 0.29 cm/s, has already been achieved. In contrast, the flume experiments showed stark differences in adsorption capacity as a function of linear velocity (Figure 7.4). This suggests that for the flume experiments, the external mass-transfer resistance has not been successfully removed, even for the highest velocity of 8.24 cm/s.

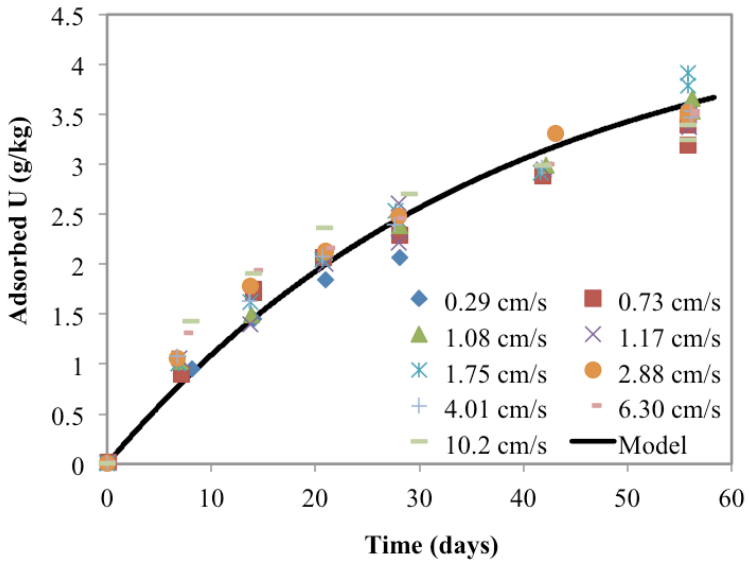

Figure 7.3 - Time series measurements of uranium adsorption capacity as a function of the linear velocity of seawater exposure in flow-through columns. The solid line is the result of the model using the optimal mass-transfer coefficient (*K*) for the data.

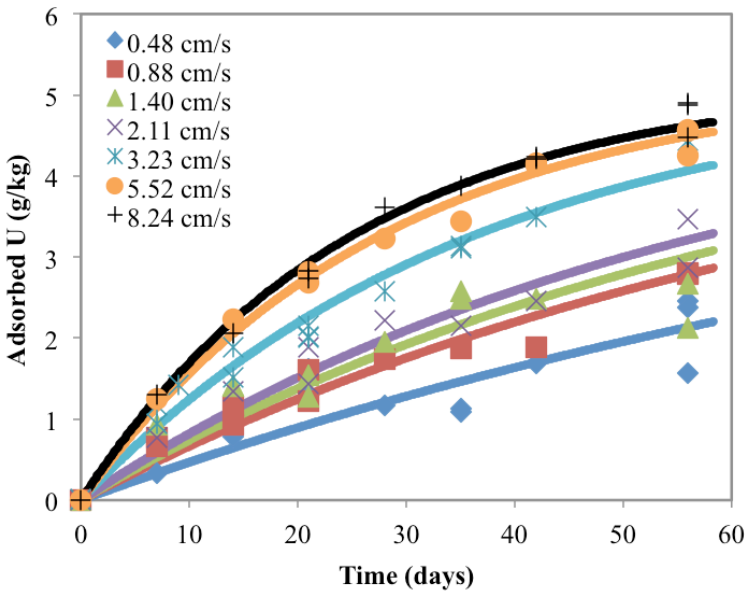

Figure 7.4 - Time series measurements of uranium adsorption capacity at a range of linear velocities using the ORNL AF1 braided adsorbent in a flume exposure. The lower three velocities were conducted in the 8-foot flume (Flume B) and the higher velocities were conducted in the 6-foot flume (Flume C). The solid lines show the results of the model using the optimal mass-transfer coefficients (*K*) found at each linear velocity.

7.4.2 Mass Transfer Parameterization

Quantification of the mass-transfer coefficient (*K*) for each experimental setup was carried out independently and plotted against the linear velocity for each experimental run. Recall from Equation 7.5 that the mass-transfer parameter represents the effects of interparticle and interphase transport and should theoretically vary with linear velocity.[20] Figure 7.5 shows the optimum mass-transfer coefficients versus the linear velocity in each experiment. For the flume data between 0.48 cm/s and 5.52 cm/s, this graph indicates that there is a strong, positive relationship between flow rate (linear velocity) and mass transfer (diamonds), as expected. Note that the highest flume velocity

of 8.24 cm/s does deviate from that trend. The flow-through column experiments (triangles) show no appreciable relationship between linear velocity and mass transfer, as indicated by the correlation coefficient (R^2) in the linear regression. Based on the observations in Figure 7.5, the entire set of all column data could be adequately described by an averaged mass-transfer coefficient, as shown by the solid line in Figure 7.3.

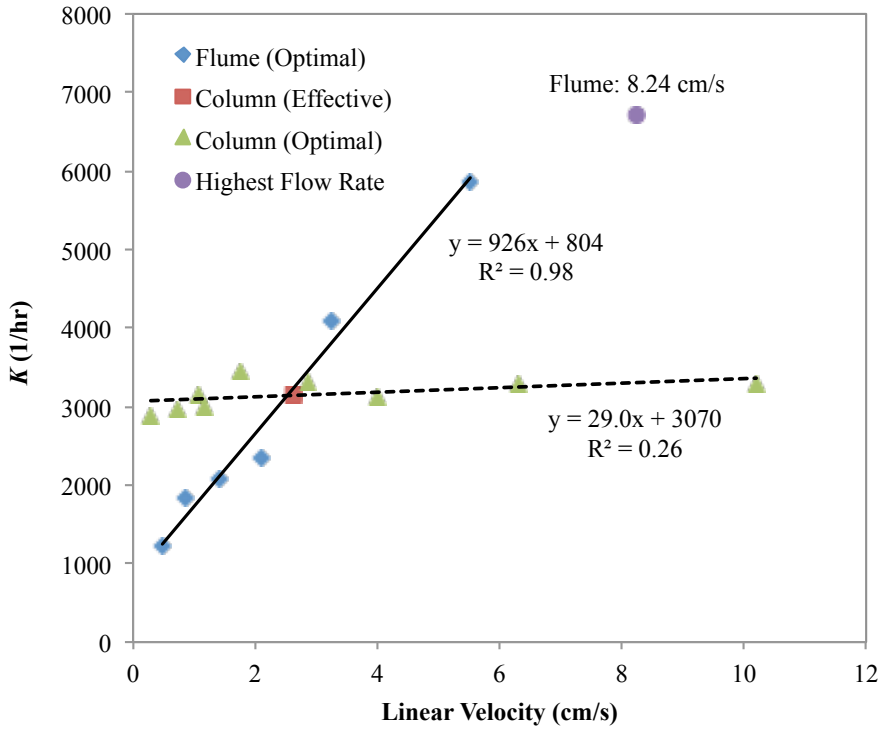

Figure 7.5 - Relationship between the optimal values of the mass-transfer coefficient and the linear velocities in the flume experiments (diamonds) and column experiments (triangles). No significant correlation can be made between linear velocity and mass-transfer rate for the column experiments, but a clear relationship does exist for the flume experiments. The solid square represents the effective linear velocity at the averaged mass-transfer-coefficient value for the column experiment. The solid circle represents the flume experiment with the highest linear velocity of 8.24 cm/s. The slope and intercept of the linear regression equation would represent the rate of change in *K* with linear velocity and the minimum *K*, respectively.

The solid lines in Figure 7.4 show the optimal model results plotted alongside the flume experimental data for each linear velocity. These model results agree very well with the experimental observations and clearly show the general trend of increasing uranium uptake rate with increasing linear velocity, as it is also shown in Figure 7.5. It should also be noted that the model lines for 5.52 cm/s and 8.24 cm/s in Figure 7.4 are very close to each other. This is an indication that the mass-transfer coefficient is reaching a plateau where it will no longer increase with increasing linear velocity. Figure 7.5 also mirrors this observation, which shows that the optimal flume mass-transfer coefficient at 8.24 cm/s (solid circle) deviates downward from the nearly linear trend formed by the other optimal mass-transfer coefficients determined for the flume (diamonds).

7.5 Discussion and Conclusions

The averaged mass-transfer coefficient used to model the flow-through column experiments in Figure 7.3 was approximately 3100 1/hr. Compared to the flume experiments, this mass-transfer rate corresponds to an effective linear flow velocity in the flume of 2.61 cm/s (solid square in Figure 7.5), which is significantly smaller than the 10.2 cm/s linear velocity achieved in the flow-through column experiments and less than half of the maximum mass-transfer rate seen in the flume studies (~6700 1/hr). These results suggest that, although high linear velocities can be achieved in a flow-through exposure, the column experimental procedure can only emulate the uranium uptake expected in flume currents of 2.61 cm/s. Therefore, the flume experiments provide a better quantitative measure of how ocean currents will affect uranium uptake kinetics, and are more representative of a marine deployment scenario.

There is an apparent lack of relationship between velocity and uranium uptake for the flow-through column experiments. This result may imply that the major mass-transfer resistances for that experimental setup are likely removed. On the contrary, the flume studies did show significant changes in adsorption rates with linear velocity (Figure 7.5) and likely provide a more realistic representation of the adsorption kinetics for seawater deployment. Since the mass-transfer coefficient did not plateau as the flume linear velocity increased, mass-transfer resistances must still be present in this system. However, the highest velocity of 8.24 cm/s in the flume does deviate from that linear trend (Figure 7.5), indicating that the system approaches the linear velocity necessary to remove the external mass-transfer resistances.

The inconsistencies between the column and flume experimental results are somewhat puzzling. While it is not expected that the uranium uptake kinetics mimic each other for the two experimental setups, it is expected that the trends be the same. However, the column data showed no relationship with linear velocity, while the flume data showed a strong linear relationship with linear velocity. To understand why this is the case, the fundamental differences between the two systems and how those differences impact mass-transfer resistances needs to be examined.

Variations in the mass-transfer coefficient depend on the linear velocity, as well as the *form-factor* (i.e., shape, style, and constraint) of the adsorbent braid. The difference between column flow tests and flume flow tests is two-fold: (i) the adsorbent *form-factor* and (ii) the constriction of the fluid phase. In the column test, the fibers are placed into a fixed volume enclosed bed filled with glass beads. Those beads are intended to hold the fibers in place, but they also restrict free movement in both the fluid and fibers.

Additionally, the packing material causes squeezing of the fibers, thus interaction between ligand and fluid at contact points is restricted leading to lower adsorption rates per unit mass of adsorbent in the column. In the flume tests, on the other hand, the fibers were assembled into a braid that was allowed to move and deform freely as the fluid passed over it.

Constriction of the fluid phase may have as much of an effect on the mass-transfer rate as the actual flow rate itself. When the fluid phase is confined, as in the column, the actual velocities of the fluid elements around the fibers are likely to be higher than the velocities around braid fibers in flumes for the same average velocities. This is because when the fluid is unconstrained as in the flume, the fluid elements may divert around the braid and take a path of least resistance, which would locally reduce the actual velocities near the fibers (Figure 7.6). This is likely the primary reason why the effect of flow velocity on uranium adsorption rates is more pronounced for the flume experiment than for the column. When flow rates are increased in the flume, mass transfer can be improved either by the additional mechanical mixing caused by the fluttering motion of the fibers or by forcing more fluid and/or uranium into the fiber domain. On the other hand, the higher effective fluid velocities experienced by the fibers in the column may explain why the mass-transfer coefficients for flow-through columns appear to already be at a plateau in Figure 7.5 (triangles).

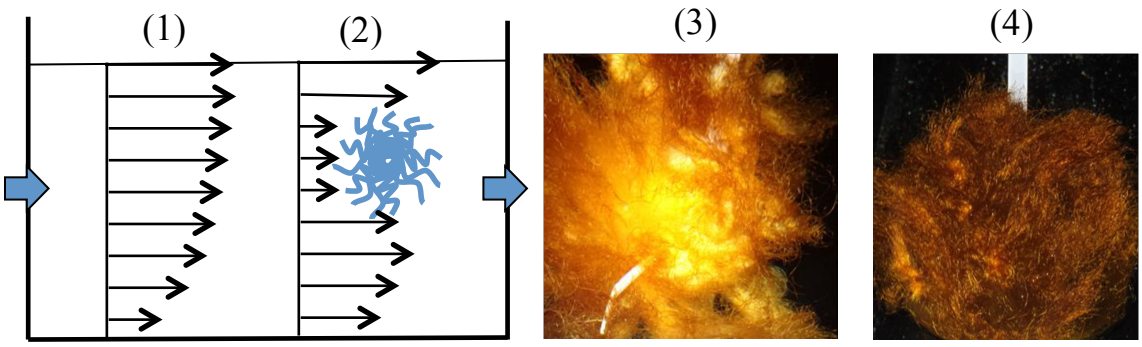

Figure 7.6 - Ideal velocity profile in the flume (1) and distorted velocity profile (2) due to flow restriction through the braid. Although the average linear velocity from profiles (1) and (2) may be the same, the velocities experienced by the braid in (2) may be less than the average linear velocity due to fluid elements diverting around the braid. This would cause lower mass-transfer rates, thus resulting in slower adsorption overall. Pictures on the right show the adsorbent after 56 days of seawater exposure at the lowest velocity (0.48 cm/s) used (3) and the 2nd highest velocity (5.52 cm/s) used (4). In general, darker color means higher adsorption capacity. Also, the color is less homogeneous in the low velocity braid (3), indicating poor transport through the braid.

In conclusion, differences in adsorption kinetics between the flow-through column and flume experiments could be explained based on the differences in the experimental setup and conditions. In the flumes, flow resistance provided by the adsorbent braid reduces the flow velocity through the braid and increases the velocity around the braid (Figure 7.6). Thus, the braid fibers experience less flow velocity than the average stream velocity. This can be seen visually in Figure 7.6 (image 3), which shows that the color change caused by adsorption is less homogenous for the lower velocity cases. Therefore, mass-transfer into the braids can be improved by deploying in high current or more turbulent flows or by reducing the density of the fiber braid to allow more seawater through the fibers. However, mass-transfer is also influenced by the *form-factor* of the adsorbent, as more tightly woven fibers are likely to have greater mass

transfer resistance. Based on the flume data with the adsorbent braid used in this study, it is recommended to deploy adsorbent in ocean currents greater than 8 cm/s, where mass-transfer resistances will be minimized and adsorption capacities will be maximized. Surface currents in the open ocean are primarily wind driven, moving at about 2% of the wind speed.[21] To produce a surface current velocity of 8 cm/s would require a mild wind speed of approximately 9 MPH (400 cm/s), which occurs over vast oceanic regions.

7.6 Acknowledgement

The development of this chapter was a collaborative effort between my co-authors and myself and was the main subject of the following publication: A. Ladshaw, L.-J. Kuo, J. Strivens, J. Wood, N. Schlafer, S. Yiacoumi, C. Tsouris, G.A. Gill, "Influence of Current Velocity on Uranium Adsorption from Seawater Using an Amidoxime-based Polymer Fiber Adsorbent," *Ind. Eng. Chem. Res.* 56 (**2017**) 2205-2211.

7.7 References

[1] J. Kim, C. Tsouris, R.T. Mayes, Y. Oyola, T. Saito, C.J. Janke, S. Dai, E. Schneider, D. Sachde, *Sep. Sci. Technol*. 48 (**2013**) 367–387.

[2] F. Endrizzi, A. Melchoir, M. Tolazzi, L. Rao, *Dalton Trans*. 44 (**2015**) 13763-14180.

[3] F. Endrizzi, C.J. Leggett, L. Rao, *Ind. Eng. Chem. Res.* 55 (**2016**) 4249-4256.

[4] C.J. Leggett, L. Rao, *Polyhedron.* 95 (**2015**) 54–59.

[5] C.J. Leggett, B. Parker, S. Teat, Z. Zhang, P. Dau, W. Lukens, S.J. Peterson, A.J.P. Cardenas, M.G. Warner, J. Gibson, J. Arnold, L. Rao, *Chem. Sci*. 7 (**2016**) 2775-2786.

[6] C.J. Leggett, F. Endrizzi, L. Rao, *Ind. Eng. Chem. Res.* 55 (**2016**) 4257-4263.

[7] C.W. Abney, R.T. Mayes, M. Piechowicz, Z. Lin, V. Bryantsev, G.M. Veith, S. Dai, W. Lin, *Energy & Environmental Science.* 9 (**2015**) 448 – 453.

[8] A.P. Ladshaw, S. Das, W.-P. Liao, S. Yiacoumi, C.J. Janke, R.T. Mayes, S. Dai, C. Tsouris, *Ind. Eng. Chem. Res.* 55 (**2016**) 4241-4248.

[9] S. Das, C. Tsouris, C. Zhang, J. Kim, S. Brown, Y. Oyola, C.J. Janke, R.T. Mayes, L.-J. Kuo, J.R. Wood, G.A. Gill, S. Dai, *Ind. Eng. Chem. Res.* 55 (**2016**) 4294-4302.

[10] S. Das, W.-P. Liao, M. Flicker Byers, C. Tsouris, C.J. Janke, R.T. Mayes, E. Schneider, L.-J. Kuo, J.R. Wood, G.A. Gill, S. Dai, *Ind. Eng. Chem. Res.* 55 (**2016**) 4303-4312.

[11] J. Kim, Y. Oyola, C. Tsouris, C.R. Cole, R.T. Mayes, C.J. Janke, S. Dai, *Ind. Eng. Chem. Res*. 52 (**2013**) 9433-9440.

[12] J. Kim, C. Tsouris, Y. Oyola, C.J. Janke, R.T. Mayes, S. Dai, G.A. Gill, L.-J. Kuo, J.R. Wood, K.-Y. Choe, E. Schneider, H. Lindner, *Ind. Eng. Chem. Res.* 53 (**2014**) 6076−6083.

[13] G.A. Gill, L.-J. Kuo, C.J. Janke, J. Park, R.T. Jeters, G.T. Bonheyo, H.-B. Pan, C.M. Wai, T. Khangaonkar, L. Bianucci, J.R. Wood, M.G. Warner, S. Peterson, D.G. Abrecht, R.T. Mayes, C. Tsouris, Y. Oyola, J.E. Strivens, N.J. Schlafer, R.S. Addleman, W. Chouyyok, S. Das, J. Kim, K. Buesseler, C. Breier, E. D'Alessandro, *Ind. Eng. Chem. Res.* 55 (**2016**) 4264-4277.

[14] L.-J. Kuo, C.J. Janke, J.R. Wood, J.E. Strivens, S. Das, Y. Oyola, R.T. Mayes, G.A. Gill, *Ind. Eng. Chem. Res.* 55 (**2016**) 4285-4293.

[15] J.R. Wood, G.A. Gill, L.-J. Kuo, J.E. Strivens, K.-Y. Choe, *Ind. Eng. Chem. Res.* 55 (**2016**) 4344-4350.

[16] H.-B. Pan, L.-J. Kuo, C.M. Wai, N. Miyamoto, R. Joshi, J.R. Wood, J.E. Strivens, C.J. Janke, Y. Oyola, S. Das, R.T. Mayes, G.A. Gill, *Ind. Eng. Chem. Res.* 55 (**2016**) 4313-4321.

[17] J. Park, G.A. Gill, J.E. Strivens, L.-K. Kuo, R.T. Jeters, A. Avila, J.R. Wood, N.J. Schlafer, C.J. Janke, E.A. Miller, *Ind. Eng. Chem. Res.* 55 (**2016**) 4328-4338.

[18] S. Das, Y. Oyola, R.T. Mayes, C.J. Janke, L.-J. Kuo, G.A. Gill, J.R. Wood, S. Dai, *Ind. Eng. Chem. Res.* 55 (**2016**) 4110-4117.

[19] S.A. Owens, K.O. Buesseler, K.W. Sims, *Marine Chem*. 127 (**2011**) 31-39.

[20] C. Tien, *Adsorption Calculations and Modeling*, Butterworth-Heinemann, Newton, MA, 1994.

[21] M.G. Gross, *Oceanography – A view of Earth*, Sixth edition, Prentice Hall Inc., Englewood Hills, NJ, 1993

7.8 Nomenclature

Latin Symbols

c	uranium concentration of adsorption domain (mol/L)
C_b	average uranium concentration of seawater (mol/L)
d	column diameter (cm)
v	linear velocity (cm/s)
K	mass-transfer coefficient (1/s)
K_{eq}	Langmuir equilibrium constant in seawater (L/mol)
k_1	Langmuir forward reaction rate constant (L/mol/s)
k_{-1}	Langmuir reverse reaction rate constant (1/s)
L	site concentration of available ligands on fibers (mol/kg)
Q	volumetric flow rate (mL/s)
q	uranium adsorption concentration on fibers (mol/kg)
$q_{\max}$	total maximum adsorption capacity of fibers (mol/kg)
q_{sat}	adsorption saturation of fibers for uranium in seawater (mol/kg)

Greek Symbols

ε	porosity or void volume of domain
ρ_f	fiber material density (kg/L)

Abbreviations

MSL	Marine Sciences Laboratory
ORNL	Oak Ridge National Laboratory
PNNL	Pacific Northwest National Laboratory

PART III. CLOSING REMARKS

CHAPTER 8. CONCLUSIONS AND RECOMMENDATIONS

8.1 Conclusions

Adsorption is a fairly complex process with wide ranging applications that occurs in a variety of different media. In this work, we have investigated and developed modeling tools for adsorption in both gaseous and aqueous systems. Developing specific models for each of these systems of interest was an arduous task, but taking as generalized of an approach as possible mitigated much of the complexitly of the specific problems. Additionally, by sticking to that comprehensive modeling approach we have successfully developed a framework off of which other adsorption models can be created and utilized (see APPENDIX C. Adsorption Software).

Although the particular models discussed in each chapter were very specific and seemingly narrow in their application, the greater impact of this work is in the development of the modeling framework. This framework provides an easy-to-use set of mathematical tools that are applicable to a variety of different adsorption systems and even useful beyond adsorption. At the base of the framework, there are very basic mathematical tools that are fundamental to just solving any types of linear and non-linear problems (see Appendix C.2 Members of the FLOCK). Therefore, the basic tools that were created in this work can be used in almost any scientific or engineering field.

Even in developing the specific models for adsorption, much care was taken to keep those models generalized or flexible. This is demonstrated very clearly in CHAPTER 4 when the bi-porous adsorption diffusion kinetics model was discussed. In

this chapter, a specific adsorption model was developed to simulate the multi-scale pore and surface diffusion in commercial zeolite pellets (Section 4.3.1). However, this same model was then also used to simulate adsorption kinetics in silver mordenite pellets, which have completely different physical structure and characteristics (Section 4.5.2: Figure 4.7). That same generality was also applied when developing the aqueous adsorption models. The same exact modeling tool (a.k.a., SHARK - see APPENDIX C. Adsorption Software) is used in both CHAPTER 5 and CHAPTER 6; the only difference is that CHAPTER 6 added new residual kernels into the existing non-linear model developed in CHAPTER 5.

The work developed in this thesis demonstrates the importance of using a fundamental modeling framework when developing specific models. This framework approach provides the platform off of which more complex models can be created. This capability was demonstrated in CHAPTER 2 through CHAPTER 4, wherein each adsorption model discussed in those chapters was utilized in subsequent chapters. The gas-solid isotherm model (CHAPTER 2) showed how application of a generalized isotherm could be used to describe a variety of different adsorption systems, so it served as the basis for the mixed-gas model (CHAPTER 3), which was used to accurately predict non-ideal adsorption behavior for various gas mixtures. Those equilibria models were then incorporated into the diffusion kinetic models investigated in CHAPTER 4.

The modeling results from CHAPTER 4 validated the fundamental modeling approach taken for adsorption kinetics in commercial adsorbents. By combing the isotherm models developed previously, with the pore and surface diffusion model based on the actual physical characteristics of the adsorbent, the models developed could

accurately predict the adsorption and desorption cycling behavior of water vapor on MS3A. In addition, without performing any curve fitting or parameterization, the same model could accurately predict the adsorption kinetics of iodine on Ag^0Z. This result reaffirms that fundamental model development is crucial to accurate predictive modeling and demonstrates the importance of framework development for model flexibility.

Beyond the common modeling framework that connects all the specific models discussed in this work, all of the adsorption models are also linked together through a common theme: adsorption applications in the Nuclear Fuel Cycle. The ultimate goal of developing the adsorption models in this work is to create a set of modeling tools that will aid in the design of the capture systems needed to enhance the availability of uranium for future generations. To that end, each of these models provides a necessary piece of information to achieve that objective: (i) off-gas models provide tools for predicting adsorption in gas mixtures and diffusion kinetics of the adsorbent materials, and (ii) uranium uptake models are useful for predicting uranium capacity of adsorbent fibers and mass transfer limitations in seawater deployment. There are steps, however, that can be taken to further enhance the models that have been created in this work.

8.2 Recommendations

One enhancement to this work could be through the exploration of a detailed sensitivity analysis of the specific adsorption models that were developed here. All of the models utilized and investigated in this research involved many different parameters for a variety of adsorption mechanisms. Some of these mechanisms and the parameters governing them, however, may not be as important as others. As such, including a

detailed sensitivity analysis with each model could provide scientists and engineers with information as to which adsorption mechanism is dominant in their particular system of interest. For instance, we know that surface charging is an important mechanism for uranium and vanadium adsorption in seawater (CHAPTER 6), but do not necessarily know the level of importance for this term relative to surface activity or the binding constants themselves. An indepth analysis of the parameters of this model and the associated significance of each mechanism could be very useful for individuals wishing to utilize the model for themselves by informing them about which parameters the model is most dependent on for accurate predictions.

In terms of more specific model enhancements, there is a need to design adsorption columns to remove the unwanted radioisotopic gases produced from reprocessing spent uranium. This gas stream is inherently a multi-species gas mixture and hence requires models that can predict adsorption behavior of such systems. In addition, the kinetics of adsorption in fixed-bed columns will dictate how and when the gas pollutant equilibriates with the adsorbents and breaks through the exit of the column. This information will be able to tell designers how large the column needs to be and for how long the column would need to be operated before the adsorbent material should be exchanged. Therefore, the final step for finalizing the off-gas models would be to incorporate our micro-scale equilibria and kinetic kernels into a macro-scale column model.

With regards to the recovery of uranium from seawater, the goal is to provide a predictive tool for engineers and scientists to aid in the development of new adsorbent materials and determination of the optimal deployment locations based on local ocean

conditions. For each of these objectives we have developed two separate adsorption tools: (i) a predictive adsorption model based on reaction schemes and binding constants from *ab initio* methods (CHAPTER 5 and CHAPTER 6) and (ii) an analytical model to determine impact of current velocity on mass transfer limitations of braided fiber adsorbents (CHAPTER 7). While each model on its own is useful, the combination of these separate models would make a powerful tool that could be used to predict uranium adsorption based on oceanic conditions such as pH, temperature, salinity, concentrations of competing metals, and local current velocities. Thus, the final step forward for creating a fully operational design tool for uranium from seawater is to incorporate the multi-ligand, competitive adsorption model of CHAPTER 6 with the mass transfer model of CHAPTER 7.

Beyond the design implications of the models developed in this work, there is the possibility that these modeling tools could be utilized on the control side of plant operations for engineered chemical processes. Similar to proportional-integral-derivative (PID) controls, there are a class of process controllers called model predictive controls (MPCs). With MPCs, an engineering model is used to predict future outcomes of a chemical process based on known past states and projecting those states forward in time. The controller can then use those predicted states to attempt to control the plant operations automatically. With modern day computers getting ever faster, MPCs are starting to become more popular than PIDs because the predictive capabilities of MPCs allow the controls to be proactive rather than reactive which is the case of PIDs.

Looking past the completion of the modeling tools for the Nuclear Fuel Cycle, there are other ways in which the models investigated in this work can be utilized in

science and engineering. For example, consider the chemi-sorption modeling framework that was developed in CHAPTER 5 and CHAPTER 6. While the discussion in both of these chapters was focused on adsorption of uranium and vanadium from brine solutions and seawater, the basic modeling framework that was developed can be applied to any aqueous or liquid system, with or without adsorption. As such, this framework has broad implications in the field of environmental and/or chemical engineering and has the potential to be utilized in groundwater chemistry, water treatment, or even aid in the design of new adsorbent materials for target metals. It was demonstrated in CHAPTER 6 that coupling *ab initio* methods in chemistry with fundamental adsorption modeling could be used to predict metal uptake by adsorbents functionalized by specific ligands. This approach to modeling could provide important insights to future materials development in order to obtain specific metal selectivity properties of new adsorbents.

Irrespectively of the adsorption process, the modeling framework that was created in this thesis can be either directly applied or modified to study that process. This is truly the power of the framework approach: modularity and flexibility. The framework at current has shown to be flexible enough to be applied to both gaseous (Part I) and aqueous systems (Part II). In addition, the modularity of the models has been demonstrated throughout the work by swaping out different pieces of physics or chemistry necessary for modeling a specific system. Therefore, moving forward it would be advantageous to continuing utilizing this framework, or at least a framework approach, when developing models to study systems of interest.

APPENDIX A. GSTA OPTIMIZATION FLOWCHART

A code was developed in C/C++ in order to apply all of the techniques discussed in Section 2.3.2 and to handle the variability that may be observed in the various input data, such as data set sizes and parameter units. The optimization routine for finding the parameters of the GSTA model uses a Levenberg-Marquardt non-linear least squares algorithm. Developed around that routine is the C/C++ code, which handles input/output and the various functions and data structures necessary to deal with the complications discussed in Section 2.3.2 above. A flowchart outlining the major code structure is provided below in Figure A. 1.

The main features of the code are in the three loops that make up the bulk of its structure. The inner most loop proceeds through each number of plausible parameters (n_par) for which the GSTA model may be valid, while the middle loop continues the solution searches for each number of isotherms (n_iso) that was given on input. For instances in which the value of the q_{max} parameter is unknown, the outer most loop will be executed twice in order to make a single estimate of this parameter for all isotherms.

Within the inner loop, there are three criteria that may force an early termination of the loop. These are put in place to reduce the total number of evaluations by eliminating unnecessary solution searches. The first criterion checks whether or not the current data set being evaluated is the first isotherm (iso = 0) given on input. If it is not, then it checks to see how many parameters the previous isotherm was allowed to have (max). The loop will terminate early when n_par is greater than that maximum.

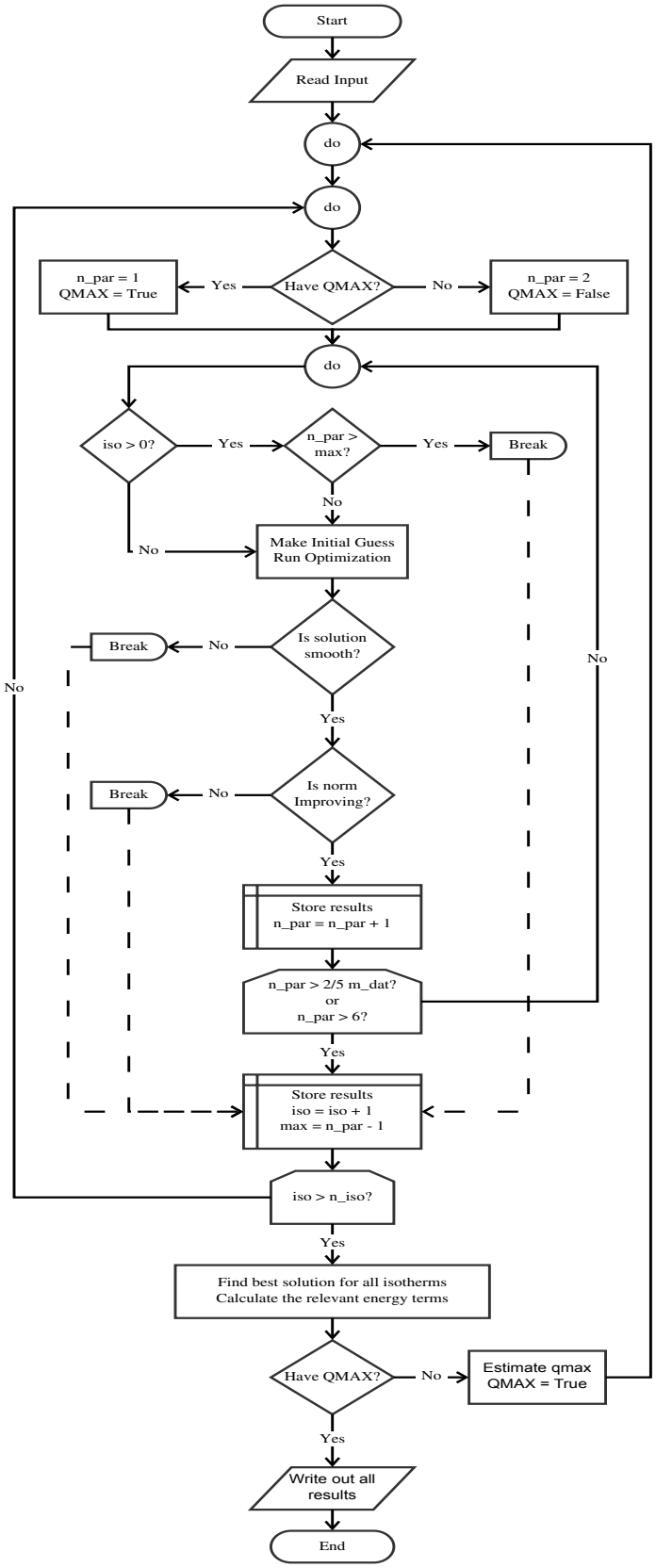
Start
Read Input
do
do
Have QMAX?
Yes
n_par = 1
QMAX = True
No
n_par = 2
QMAX = False
do
iso > 0?
Yes
n_par > max?
Yes
Break
No
No
Make Initial Guess
Run Optimization
Is solution smooth?
No
Break
No
Yes
Is norm Improving?
No
Break
Yes
Store results
n_par = n_par + 1
n_par > 2/5 m_dat?
or
n_par > 6?
Yes
No
Store results
iso = iso + 1
max = n_par - 1
iso > n_iso?
No
Yes
Find best solution for all isotherms
Calculate the relevant energy terms
Have QMAX?
No
Estimate qmax
QMAX = True
Yes
Write out all results
End

Figure A. 1 - Flowchart for the main functions within the GSTA optimization code. The logical path of the code flows down from the "Start" and follows the arrows. At each branch, a decision has to be made which determines the next process and/or the "Breaks" necessary to exit loops and reach the "End" of the program.

The next two criteria look at the obtained solution after the optimization has been completed. If the solution vector contains "noise" (i.e., the solution is non-smooth), then those results are kicked out and the loop is terminated. Also, if the Euclidean norm of the current solution were not improving from previous solutions, then the loop would also be terminated. The culmination of these criteria has reduced the total evaluations needed to reach a final solution by up to 80%.

APPENDIX B. AQUEOUS ADSORPTION DETAILS

B.1 Model Basics

The basics of the model are broken up into three parts: (i) aqueous reactions, (ii) mass balances, and (iii) electroneutrality. Aqueous reactions are represented in the model as shown in Equations B.1 and B.2. In this representation, υ is the stoichiometric constant for each species involved in the reaction, γ^{aq} is the aqueous activity coefficient of those species, $[i]$ is the aqueous molar concentration of the i^{th} species, $\{i\}$ is the aqueous activity of the i^{th} species, and K is the equilibrium constant for that reaction. The aqueous activity coefficients can be determined using the Davies or Debye-Hückel equations or similar models.[1]

$$\sum_{i}^{\text{reactants}} \upsilon_i \{i\} \Leftrightarrow \sum_{j}^{\text{products}} \upsilon_j \{j\} \tag{B.1}$$

$$K = \frac{\prod_{j}^{\text{products}} \left(\gamma_j^{aq}[j]\right)^{\upsilon_j}}{\prod_{i}^{\text{reactants}} \left(\gamma_i^{aq}[i]\right)^{\upsilon_i}} \tag{B.2}$$

Mass balances in the model are formed as the sums of the molar contributions and concentrations of each species in the system that contributes to a particular mass group. For instance, total carbonate in the system would be based on how much CO_3^{2-} was added to the system in total, and must equal the concentrations of each species containing CO_3^{2-} groups in their respective molar contributions (i.e., $UO_2(CO_3)_3^{4-}$ would contribute 3

moles of CO_3^{2-} to the carbonate mass balance). In addition, our model accounts for the mass removed from the aqueous phase via adsorption as shown in equation B.3 below:[2]

$$C_T - \frac{m_a}{V}\sum_j \delta_j q_j = \sum_i \delta_i [i] \tag{B.3}$$

where C_T is the total concentration of a particular species group, m_a is the total mass of an adsorbent in the system, V is the total volume of the system, δ_i is the molar contribution of species i to the total concentration, and q_i is the adsorbed molar concentration of species i.

The pH of the system is determined using the condition of electroneutrality in the aqueous phase (Equation B.4). This condition looks at the ionic charge (n) of each species in solution and requires that the total concentrations of positive and negative ions cancel out each other, such that there is no net charge in the system.[1,2] Alternatively, our model can consider the system at a constant pH by applying an equality constraint on the activity of the protons, $\{H^+\}$, in solution (Equation B.5).

$$0 = \sum_i n_i [i] \tag{B.4}$$

$$\mathrm{pH} = -\log\left\{H^+\right\} \tag{B.5}$$

B.2 UNIQUAC Parameters

The parameters of UNIQUAC include structural information about the adsorbing species, as well as reaction energies for the bonding of the adsorbates with their respective ligands. Shape factors ($s_{i,l}$ and $r_{i,l}$) for each adsorbed species are determined as a ratio of the van der Waals areas and volumes ($a_{i,l}$ and $v_{i,l}$) of the adsorbates to a standard segment area and volume (A_w = 2.5 x 10^9 cm^2/mol and V_w = 15.17 cm^3/mol) defined by Abrams and Prausnitz[3] (Equations B.6 and B.7). The van der Waals areas and volumes themselves can be calculated from the atoms that make up each adsorbate.[4]

$$r_{i,l} = {v_{i,l}}/{V_w} \tag{B.6}$$

$$s_{i,l} = {a_{i,l}}/{A_w} \tag{B.7}$$

After determining those shape factors, the remaining structural parameters of UNIQUAC are calculated as shown in Equations B.8 through B.11.[3] This procedure gives information on the surface mole fractions ($y_{i,l}$), average area fractions ($\theta_{i,l}$), volume fractions ($\Phi_{i,l}$), and length factors ($\lambda_{i,l}$). Once this information is determined, the only missing parameters from UNIQUAC are the binary interaction terms ($\tau_{ij,lm}$).

$$y_{i,l} = \frac{q_{i,l}}{\sum_{\forall(j,m)} q_{j,m}} \tag{B.8}$$

$$\theta_{i,l} = \frac{s_{i,l} y_{i,l}}{\sum_{\forall(j,m)} s_{j,m} y_{j,m}} \tag{B.9}$$

$$\Phi_{i,l} = \frac{r_{i,l} y_{i,l}}{\sum_{\forall(j,m)} r_{j,m} y_{j,m}} \tag{B.10}$$

$$\lambda_{i,l} = \left(\frac{z}{2}\right)\left(r_{i,l} - s_{i,l}\right) - \left(r_{i,l} - 1\right) \tag{B.11}$$

In the original UNIQUAC model,[3] the binary interaction terms were considered as adjustable parameters that needed to be obtained through optimization with adsorption data. It is possible, however, to provide approximations to those adjustable parameters from the binding energies of the individual adsorbing species. This can be accomplished by first considering the expansion of those binary parameters (Equation B.12) into a set of two energy terms: (i) a lateral interaction potential ($u_{ii,ll}$) and (ii) a cross-lateral interaction parameter ($u_{ji,ml}$).[3,5]

$$\tau_{ji,ml} = \exp\left[-\frac{u_{ji,ml} - u_{ii,ll}}{RT}\right] \tag{B.12}$$

The physical meaning of the lateral ($u_{ii,ll}$) and cross-lateral ($u_{ji,ml}$) interaction parameters can be interpreted as the interaction energy between the i^{th} adsorbate with another i^{th} adsorbate and the interaction energy between the i^{th} adsorbate with the j^{th} adsorbate, respectively. Since the j^{th} and i^{th} adsorbates may be bonded to different ligands, the secondary subscripts of m and l are used to denote which ligand each is bound to (e.g., in Equation B.12 above, j and m are paired and i and l are paired). The lateral interaction parameter can be calculated from the heat of adsorption ($\Delta H_{i,l}$) and the area factor of the adsorbate ($s_{i,l}$) as shown in Equation B.13. It is then possible to provide

an estimate to the cross-lateral term by taking the geometric average of each lateral interaction parameter (Equation B.14).[3,5]

$$u_{ii,ll} = -\frac{\Delta H_{i,l}}{s_{i,l}} \tag{B.13}$$

$$u_{ji,ml} = u_{ij,lm} = \sqrt{u_{jj,mm} u_{ii,ll}} \tag{B.14}$$

B.3 References

[1] M.M. Benjamin, *Water Chemistry*, Waveland Press Inc., Illinois, 2010.

[2] S. Yiacoumi, C. Tien, *Kinetics of Metal Ion Adsorption from Aqueous Solutions*, Kluwer Academic Publishers, Boston, MA, 1995.

[3] D.S. Abrams, J.M. Prausnitz, *AIChE J.* 21 (**1975**) 116-128.

[4] A. Bondi, *J. Phys. Chem.* 68 (**1964**) 441-451.

[5] O. Talu, I. Zwiebel, *AIChE J.* 32 (**1986**) 1263-1276.

APPENDIX C. ADSORPTION SOFTWARE

C.1 Introduction

All of the modeling and simulation results reported in this work were created from a software suite called Ecosystem, developed primarily by Austin Ladshaw. Ecosystem is a set of software kernels written in C and C++ to perform specific modeling tasks, such as matrix operations or parameter estimations. It also includes open-source libraries for performing the Levenberg-Marquardt non-linear least squares[1] and reading yaml structured input files.[2] As with the body of this work, the kernels are divided into two main categories: (i) the Fundamental Off-gas Collection of Kernels (FLOCK) and (ii) the Seawater Codes from a Highly Object-Oriented Library (SCHOOL). In this appendix, we will discuss what each of the kernels can do and how one can acquire and utilize this software for their own purposes.

C.2 Members of the FLOCK

The FLOCK is a collection of adsorption kernels designed primarily for use in simulating adsorption in gaseous systems. There is a fair amount of overlap between this set of kernels and the kernels of the SCHOOL, however, especially for some of the more generic mathematical objects that were developed under this category. Most of the following FLOCK kernels have been named after birds, hence why we call it the FLOCK. Provided below are the names of each member of the FLOCK and a short description of what it is responsible for doing in the Ecosystem software suite.

C.2.1 GSTA_OPT

The only kernel of the FLOCK not named as a bird is the GSTA_OPT kernel. This is the set of algorithms that is responsible for performing the GSTA isotherm parameterization of gas-solid adsorption systems. It takes in a set of data for a given adsorbate-adsorbent pair and estimates the maximum adsorption capacity parameter and optimum number of adsorption sites, as well as all the temperature independent energy terms associated with each of those sites. This kernel is discussed extensively in CHAPTER 2 and APPENDIX A. GSTA Optimization Flowchart.

C.2.2 MAGPIE

Our Multicomponent Adsorption Generalized Procedure for Isothermal Equilibria (MAGPIE) kernel was the primary subject of CHAPTER 3. This kernel performs all the necessary operations of the Generalized Predictive Adsorbed Solution Theory (GPAST) in order to simulate the gas-solid adsorption equilibria of a mixed-gas system. Those operations can be performed to either predict the adsorption based on the gas phase composition, or can predict the gas phase composition based on the adsorbed amounts of each species.

C.2.3 MACAW

MACAW stands for MAtrix CAlculation Workspace and is a C++ object for performing simple matrix operations on data. The object is templated so that it is possible for a user to create a matrix of doubles, strings, integers, or complex numbers. The primary use in Ecosystem, however, is to perform matrix math with double precision. In

addition to basic matrix operations, there are also subroutines built into MACAW to perform specific linear solutions to systems with special structure, such as triangular matrices or tri-diagonal matrices. Recently added to this suite of solver routines was a QR factorization algorithm to solve more general systems of linear equations.

C.2.4 LARK

The Linear Algebra Residual Kernel (LARK) set of subroutines is designed to solve very complex linear and non-linear systems using a variety of iterative techniques. Linear solvers in LARK are primarily from the Krylov Subspace[3] domain of algorithms for solving large sparse systems of equations. However, we also include a QR solver underneath LARK, which uses basis vectors to reform the matrix from a linear operator prior to calling the QR routine in MACAW. In addition to linear solvers, we have implemented a Picard method[4] and a Jacobian-Free Newton Krylov (JFNK) method[5] for non-linear systems. The JFNK method is also coupled with a backtracking line search algorithm[4] to improve the convergence of the Newton's method.

C.2.5 FINCH

The Flux-limiting Implicit Non-oscillatory Conservative High-resolution (FINCH) scheme framework is a modeling platform used to simulate conservation laws in a variety of different domains. It makes use of the existing objects and subroutines in MACAW and LARK in order to set up and solve the system of equations that is derived from the generalized 1-D conservation law model that was described in Section 4.2.1. Additional information regarding this framework is detailed in Section 4.2.

C.2.6 EGRET

This object is the Estimation of Gas-phase pRopErTies (EGRET) kernel and is responsible for calculating parameter information such as gas densities, viscosities, molecular diffusivities, and film mass transfer coefficients. All of the model details for each portion of this kernel have been discussed in Section 4.3.3 of this work.

C.2.7 SKUA and SCOPSOWL

These two kernels represent the modeling framework to simulate gas phase adsorption diffusion kinetics in spherical and cylindrical adsorbent particles. The Surface Kinetics for Uptake by Adsorption (SKUA) kernel performs the micro-scale surface diffusion simulation that is outlined in Equation 4.16 through Equation 4.18, while the Simultaneously Coupled Objects for Pore and Surface diffusion Operations With Linear systems (SCOPSOWL) kernel does the macro-scale pore diffusion and adsorption mass transfer simulation described in Equation 4.19 and Equation 4.20. Additional details regarding these models are provided in Section 4.3.1.

C.2.8 SKUA_OPT and SCOPSOWL_OPT

These two kernels are analysis tools that will take in a set of adsorption kinetic data, gathered at some constant exposure concentration for a single gas species, and produce what are the optimal surface diffusivities for each experimental run. Much like GSTA_OPT, each kernel makes use of the Levenberg-Marquardt non-linear least squares routine[1] to compare simulation results against actual data and optimize for the unknown surface diffusivity parameter.

C.3 Members of the SCHOOL

The SCHOOL is a collection of kernels developed specifically for simulating adsorption in aqueous systems. As such, each of its member kernels has been named after aquatic life to keep with the theme of naming kernels after animals. However, the SCHOOL does utilize some of the same kernels as the FLOCK, namely MACAW and LARK, because these contain subroutines that are valid regardless of the media we are simulating adsorption in. The remaining members of the SCHOOL are detailed in the subsections below.

C.3.1 EEL

The Easy-access Element Library (EEL) provides a C++ object for creating atoms from the periodic table. It contains all the necessary atomic information on those species for performing a variety of calculations, including the estimation of van der Waals volumes and molecular weights of polyatomic species. In general, this kernel is not very useful on its own, but is valuable as a component to building other modules for aqueous simulations.

C.3.2 MOLA

Built from the EEL kernel, the Molecule Object Library from Atoms (MOLA) module contains hundreds of molecular species of interest that are registered in a digital library for use in aqueous simulations. Each molecule is constructed from the individual atom objects of EEL and can use this information to implicitly determine the van der Waals volumes and molecular weights of the species in the system. In addition, MOLA

holds information regarding the valence charge and the standard state formation energies of the molecules. This information can then be utilized to determine aqueous activity coefficients and binding strengths of reactions.

C.3.3 SHARK

The Speciation-object Hierarchy for Adsorption Reactions and Kinetics (SHARK) kernel creates a suite of objects that are used to simulate speciation, adsorption, and kinetics in aqueous systems. In this kernel are objects for performing mass balances, steady-state aqueous reactions, unsteady aqueous reactions, single and multi-ligand adsorption reactions, and electroneutrality. Each object contributes a non-linear residual function that is compiled by SHARK and fed into LARK solvers to find the concentration of all species in a system as a function of temperature, pH, ionic strength, and other various parameters. Additional details on this kernel are discussed in Section 5.2 and 6.4, as well as APPENDIX B. Aqueous Adsorption Details.

C.4 Software Distribution

The Ecosystem suite of kernels is currently hosted on a private Bitbucket git repository at the following address:

https://bitbucket.org/gitecosystem/ecosystem

Access to the software can be granted to interested individuals through personal contact with myself (aladshaw3@outlook.com).

Computer requirements to run the software are simple. The software is distributed as source code that must be built using a compatible C/C++ compiler. For convenience, a Makefile is distributed with the source code that will automatically build the executable via the make utility using the gcc and g++ compiler. The gcc/g++ compiler must be version 4.7 or newer, or any other C++11 compatible compiler.

Installation on a linux or Mac computer will be very simple. Linux users should be just ready-to-go as is. For Mac users, you will need to install command line tools via the Xcode development software from Apple, which is free to download and install. To install the software on Windows will require some form of bash terminal, virtual box, or emulator. I recommend the use of Cygwin (http://cygwin.com/), which is a bash terminal application that provides the necessary functionality. As an additional step, Windows users must install the correct utilities when installing Cygwin. The minimum requirements are gcc, g++, git, and make. For additional information, see the README page of the Ecosystem source code directory.

C.5 License and Copyright

The software kernels developed in this work were written by Austin Ladshaw with contributions coming from contributor Alex Wiechert, as well as open-source algorithms for a Levenberg-Marquardt non-linear least squares routine[1] and a yaml document reader.[2] Austin Ladshaw retains full rights to use, copy, modify, merge, publish, distribute, sublicense and/or sell copies of the portions of this software that were developed under this work and are not directly dependent on the outside open-source libraries contained within. Portions of the software not developed during this work,

namely limfit[1] and LibYAML[2], are distributed under an LMFIT-BEER-WARE License and the MIT License, respectively. For additional licensing information, please refer to the LICENSE.txt file located in the Ecosystem source code directory.

C.6 References

[1] J. Wuttke, Version <lmfit-3.4>, <http://joachimwuttke.de/lmfit>, Accessed January 21, 2013.

[2] K. Simonov, Version <LibYAML-0.1.6>, http://pyyaml.org/wiki/LibYAML, Accessed June 30th, 2015.

[3] Y. Saad, *Iterative Methods for Sparse Linear Systems*, 2nd Edition, SIAM, Minneapolis, MN, 2003.

[4] J.E. Dennis Jr., R.B. Schnabel, *Numerical Methods for Unconstrained Optimization and Nonlinear Equations*, Prentice-Hall Inc., Englewood Cliffs, NJ, 1983.

[5] D.A. Knoll, D.E. Keyes, *J. Comp. Phys.* 193 (**2004**) 357-397.

VITA

Austin Pittman Ladshaw was born to Tom Ladshaw and Vicki Ladshaw on June 15th, 1988 in Snellville, Georgia. He attended and graduated from Shiloh High School in the spring of 2006 and started his undergraduate studies at Georgia College and State University (GCSU) in Milledgeville, Georgia. After completing his pre-engineering education from GCSU, he transferred to the Georgia Institute of Technology (GIT) in spring 2009 where he began studying Civil and Environmental Engineering. Austin finished his undergraduate work in December 2011 and was awarded a Bachelor's in Environmental Engineering from GIT and a Bachelor's of Science from GCSU.

Upon graduating college, he began to work for a construction company from his hometown of Snellville: E.R. Snell Contractor, Inc. After working off and on in construction over the course of the last few years, including a number of interships while an undergraduate student, Austin decided to continue his education by attending graduate school. In August of 2012, he started his PhD studies in adsorption modeling under the advisement of Dr. Sotira Yiacoumi. For the last five years, Austin has been leading the development of adsorption modeling tools and software for applications in Nuclear Energy through grants awarded by the U.S. DOE Nuclear Energy University Program.